UNIVERSITY of CALIFORNIA
Santa Barbara

Measuring the Cosmic Microwave Background with BOOMERANG

A dissertation submitted in partial satisfaction of the
requirements for the degree of

Doctor of Philosophy

in

Physics

by

Thomas Erhardt Montroy

Committee in charge:

John Ruhl, Chair
Deborah Fygenson
Mark Srednicki

June 2003

The dissertation of Thomas Erhardt Montroy is approved:

Chair

June 2003

Measuring the Cosmic Microwave Background with BOOMERANG

To my parents, for their unwavering support over these long years of graduate school.

Acknowledgements

A long time ago, the undergraduate engineering physics advisor at the University of Illinois let me substitute graduate physics courses for the required undergraduate lab classes based on my assertion that I would never become an experimentalist. Unfortunately with this thesis, I may be invalidating my undergraduate degree...

John Ruhl has been an excellent advisor over the years. He took me in when I knew nothing about experimental work; his patient advice and high standards have been a strong influence. Phil Farese, Ted Kisner, Eric Torbet, Jon Goldstein, Kim Coble, Jon Leong and Zak Staniszewski made time in the lab enjoyable and taught me quite a lot. I doubt very much I would have gotten to this point if not for Phil Farese; he has been an excellent friend and colleague through these years. I could not have asked for a better lab partner than Ted Kisner. We did not always agree on the right way to do things, but our different approaches insured that the right method would be found.

The support staff at UCSB has been excellent. Jeanie Cornet and Debbie Cedar eased the paperwork burden. The guys in the machine shop: Andy W., Andy S., Doug, Mike, Mark the Welder and Rudy always provided quality workmanship and taught me the art of good design. Art, Carrie and Craig in Physic purchasing always came through even with my near constant demand for next day delivery. Mike Deal (who is not paid nearly enough) kept things running smoothly in the presence of constant renovation.

My friends and former roommates especially Dave W., Ashish, Bryce, Natalie and Lauren have been a constant source of support. Also, the Friday frisbee games usually with Pete, Doron, Brian, Dave B., Ryan, Phil, Craig, Zeke and Jay provided a release from the tension that builds up over the course of a week.

Over the last decade, BOOMERANG has benefitted from the endless dedication of those who have brought it from acronym to reality. It is truly a team effort. For good or for bad, the scientific papers never quite capture the excitement and drama of building and launching such an experiment. I will always value the comraderie and friendship we shared during the long days in the field. Also, I would like to thank them for all they have taught me over the years. The current members of the BOOMERANG collaboration are listed on the following page.

Lastly, I would like to thank NASA for a GSRP fellowship.

BOOMERANG Collaboration

Case Western Reserve University J. Ruhl, T. Kisner, E. Torbet, T. Montroy

Universita' di Roma La Sapienza P. de Bernardis, S. Masi, F. Piacentini, A. Iacoangeli, G. De Troia, A. Melchiorri G. Polenta, S. Ricciardi, F. Nati

California Institute of Technology A. Lange, W. Jones, V. Hristov

University of Toronto B. Netterfield, C. MacTavish, E. Pascale

Cardiff University P. Ade, P. Mauskopf

IROE Andrea Boscaleri

ING G. Romeo, G. di Stefano

JPL J. Bock

CSU Dominguez Hills: B. Crill

IPAC K. Ganga, E. Hivon

CITA D. Bond, C. Contaldi

LBNL, UC Berkeley J. Borrill

Imperial College A. Jaffe

Institut d'Astrophysique S. Prunet

University of Alberta D. Pogosyan

Universita' di Roma Tor Vergata N. Vittorio, G. de Gasperis, P. Natoli, A. Balbi, P. Cabella

University of Pennsylvania M. Tegmark, A. de Oliveira-Costa

Curriculum Vitæ

Thomas Erhardt Montroy

Personal

Born	8 February, 1973 Sparta, IL USA

Education

1991–1995	B.S. Engineering Physics Univeristy of Illinois, Urbana, Illinois
1996	Non-degree graduate student Univeristy of Illinois, Urbana, Illinois
1996-1997	Teaching Assistant University of California, Santa Barbara, CA
1998-2002	Graduate Student Researcher University of California, Santa Barbara, CA
2002-2003	Graduate Student Researcher Case Western Reserve University, Cleveland, OH

Abstract

Measuring the Cosmic Microwave Background with BOOMERANG

by

Thomas Erhardt Montroy

In recent years measurements of the Cosmic Microwave Background (CMB), the remnant radiation from the Big Bang, have helped to open a new era of precision cosmology. BOOMERANG is a 1.3 m off-axis balloon-borne telescope designed for long duration (LDB) flights around Antarctica. It utilizes an AC-biased bolometer receiver operating in the frequency range 90-450 GHz. BOOMERANG has had two successful LDB flights (B98 and B00M03). We discuss the results of the B98 flight which measured the angular power spectrum of the CMB temperature anisotropies from $\ell = 25$ to $\ell = 1000$ and plays a strong role in providing strong constraints on cosmological parameters, namely Ω_{tot} and Ω_b. We also discuss the design and in-flight performance of the BOOM03 flight. BOOM03 was designed to measure CMB temperature and polarization anisotropies. It uses four pairs of polarization sensitive bolometers at 145 GHz. Polarizing grids provide polarization sensitivity for four 2-color photometers operating at 245 and 345 GHz.

Contents

List of Figures

List of Tables

Chapter 1

Introduction

Modern cosmology is based on the Big Bang paradigm. The idea that the universe began in hot, dense state, expanding and cooling as time passed on. Small initial perturbations in this nearly uniform state evolved into the stars and galaxies we see today. This paradigm is supported by the confirmation of three basic predictions: the fact that universe is expanding, the abundance ratios of certain light elements and the existence and properties of the Cosmic Microwave Background Radiation.

1.1 Expansion of the Universe

In the early 1920's, Einstein discovered that his General Theory of Relativity predicted that spacetime was fundamentally dynamic, meaning the universe is naturally expanding or contracting. Appalled by the idea, he introduced a cosmological constant (Λ) which could be fine-tuned to make a static universe. In 1929, Edwin Hubble observed that galaxies were in fact receding from Earth, finding that the recessional velocity increases with distance. His measurements showed that the recessional velocity obeyed the equation $v = H_0 R$, where R is the distance to the galaxy and H_0 is the value Hubble's constant today. This discovery forced Einstein to abandon the cosmological constant, but as we will discuss later it turns out that something like a negative cosmological constant may play a roll in the universe. Recent measurements using the Hubble Space Telescope show that $H_0 = 72 \pm 8\ km/s/Mpc$ [35].

Homogeneous and isotropic cosmologies can be described by the Friedman-Robertson-Walker (FRW) solutions to the equations of General Relativity. A homogeneous universe is one where the distribution of matter and energy are uniform while isotropy implies that there are no preferred directions in space. Even though galaxies and clusters of galaxies violate homogeneity and isotropy on small scales, the large scale distribution of structure appears to be homogeneous and isotropic. Therefore, FRW cosmologies are a good approximation for the large

scale dynamics of our universe.

In FRW universes the expansion of space is governed by an expansion factor $a(\tau)$, where τ is the proper time of isotropic observers. There are three classes of FRW solutions corresponding to three different geometries of the universe. There exists a critical density ρ_{crit} which determines the curvature of the universe,

$$\rho_{crit} = \frac{3H^2}{8\pi G}, \tag{1.1.1}$$

where H is the Hubble constant at time τ and G is Newton's gravitational constant. Taking H_0 from the Hubble Key Project, we find $\rho_{crit} = 1.35 \times 10^{-29}\ g\ cm^{-3}$, which corresponds to about 8 protons per cubic meter. Conventionally the density of the universe is expressed in terms of the ratio

$$\Omega_{tot} = \frac{\rho}{\rho_{crit}}, \tag{1.1.2}$$

where Ω_{tot} is the total mass-energy density of the universe. If $\Omega_{tot} < 1$ the space is negatively curved (open), if $\Omega_{tot} > 1$ the space has a positively curvature (closed), and if $\Omega_{tot} = 1$, then space is flat. In the absence of a cosmological constant, open and flat universes expand forever. Without a negative cosmological constant, closed universes eventually contract.

1.2 Nucleosynthesis and Light Element Abundances

The universe cools to about $10^9 K$ by the time it is three minutes old (for details on the first three minutes see Weinberg's *The First Three Minutes* [114]). At this time nucleosynthesis begins with protons and neutrons combining to form light nuclei. The modern view is that the present day abundances of Deuterium, Helium-3, Helium-4, and Lithium-7 are cosmological in origin [65] while other nuclei are formed in astrophysical processes, mainly in the interior of stars. The amount of Helium-4 is set primarily by the the proton-neutron ratio after the weak nuclear force freezes out; the mass ratio of Helium-4 to Hydrogen is about 0.25. The abundances of the other nuclei are more strongly dependent on the baryon density. The ratio of Deuterium nuclei to Hydrogen nuclei (free protons) is about 10^{-5}, for Helium-3 this ratio is 10^{-6} and for Lithium-7 it is approximately 5×10^{-9} [65]. Given the neutron-proton ratio (at freeze out) and the baryon density, the abundances of these nuclei can be calculated. Measurements of the Deuterium abundance provide a strong constraint on the baryon density $\Omega_b h^2 = 0.019 \pm 0.002$ [111] where h is defined so that $H_0 = 100h\ km/s/Mpc$.

1.3 The Cosmic Microwave Background

For the first 300,000 years, the universe was too hot to allow for the formation of atoms; it was filled with an ionized plasma. During this time, there was a large number of ionizing photons per proton (approximately 10^9 photons per baryon). Whenever a hydrogen atom formed, it was immediately ionized. The baryons and photons were strongly coupled which meant that the photon's mean free path was rather short (photons did not travel long distances before scattering again). Eventually expansion cooled the universe enough so that atoms become stable (the time of recombination). Recombination occurred when the temperature of the universe was 3000K. After recombination, the universe became transparent, meaning that the photon's mean free path is effectively the size of the universe. This radiation traveling since the time of recombination is the Cosmic Microwave Background.

As a photon travels through an expanding universe its wavelength increases, and the photon loses energy. The redshift factor z which characterizes the loss of energy relates the change in wavelength to the values of $a(\tau)$ at two times,

$$z + 1 = \frac{\lambda_2}{\lambda_1} = \frac{a(\tau_2)}{a(\tau_1)}. \tag{1.3.1}$$

For a blackbody the photon energy density is proportional T^4. As the universe expands, the photon energy density loses a factor of a^3 due to the expanding volume and a factor of a due to redshift. Therefore, the effective blackbody temperature scales as $T \propto 1/z$. Because the photon to baryon ratio is so high, the CMB retain its blackbody spectrum as the universe expands. However, Compton scattering in the intergalactic medium could produce small spectral distortions [90]. Today, the CMB has a temperature of 2.728 K, which peaks near 160 GHz (the microwave region of the radio spectrum). The present temperature of the CMB implies that recombination occured $z \sim 1100$.

The Cosmic Microwave Background was first observed in 1965 by Penzias and Wilson [91]. In an epic demonstration of experimental knowhow, they could not find an explanation for an excess noise of $\sim 3.5K$ they saw with their telescope (at one point they thought it might be due to pigeon crap on their antenna). Their observation was interpreted by Dicke, Peebles, Roll and Wilkinson [29] to be the relic radiation from the young universe, first predicted in 1948 by Gamow, Alpher, and Herman [1].

In the early 1990's, the FIRAS experiment on the COBE satelite showed that the CMB appears to be a perfect blackbody with a temperature of 2.728 ± 0.003 [78]. Soon afterward, the COBE-DMR released its first data showing that there were spatial variations in the CMB temperture with amplitude 1 part in 100,000 [5]. This was the first reported observation of cosmological anisotropies in the CMB. Before COBE many other experiments found that there was a dipole

anisotropy in the CMB signal ($\Delta T_{dipole} = 3.36mK$ [62]). This is due to Doppler shifting induced by the motion of our galaxy with respect to the CMB.

1.4 Modern Cosmology

Before moving on to describe the meaning of the CMB anisotropies, it is useful to discuss how recent measurements have modified the Big Bang paradigm.

The apparent isotropy of the CMB (or even it's small anisotropy) are somewhat inconsistent with with causality. In the FRW cosmology, the universe pops into being at $\tau = 0$. It can be shown that in a closed, dust-filled universe there is just enough time for a photon to travel around the universe and return to where it began [113]. In an FRW universe, one does not expect far separated regions of the sky to be in causal contact with one another. There is not enough time for light to travel between these regions. On the last scattering surface at $z \sim 1100$, causally connected regions had a size which subtends an angle of 2° (for a flat, dust-filled universe) when observed today. Within the standard FRW cosmology it is unlikely to expect that we would see the same CMB temperature when looking at widely separated regions. Only if those regions were in causal contact would we expect them to have the same value of T_{CMB}. To get around this, Guth introduced the idea of the inflationary universe [41], where the early universe experiences a brief period of exponential expansion. This period of exponential expansion makes it possible that widely separated regions could have been in causal contact before inflation leading to the observed CMB isotropy we see.

Based on the measurements of light element abundances, CMB temperature and the Hubble constant, we expect the baryon density Ω_b to be about 5% of the critical density. Measurements of the rotation curves of galaxies imply that galaxies are generally surrounded by massive dark halos which account for the majority of their mass [99]. In fact, the matter energy density for bright stars is roughly 0.5% of the critical density [110]. This in itself is not a terrible thing since it could be possible that most baryonic matter does not reside in stars. However, when coupled to cluster measurements which say that $\Omega_m = 0.16 \pm 0.05$ [3], we start to wonder if our cosmological model is complete. It becomes unlikely that our universe is composed of only baryons. Many ideas have been presented to account for this missing mass, but cold dark matter (CDM) has so far emerged as the leading candidate. Hot dark matter, composed of massive neutrinos, is disfavored because these models cannot account for the observed amount of small scale structure we see [23]. CDM models consist of particles which interact gravitationally but not electromagnetically. No evidence of such particles has been seen, but current experiments are probing interesting ranges of the parameter space of CDM models [103].

Another surprising development is that Einstein's scrapping of the cosmological constant may have been premature. Results from measuring the light

curves of Type 1A supernovae events show that it is likely that there is a negative cosmological constant meaning $\Omega_\Lambda > 0$ [97, 92]. Instead of making the universe static, a negative cosmological constant actually accelerates the expansion of the universe.

These non-baryonic components add to total energy density of the universe

$$\Omega_{tot} = \Omega_b + \Omega_{cdm} + \Omega_\Lambda + \Omega_\nu \tag{1.4.1}$$

where Ω_{cdm} is the contribution of CDM and Ω_ν represents the possible contribution of neutrinos to the mass of the universe. By themselves, large scale structure information and cosmological constant measurements imply that more than half of the mass/energy density of the universe is not baryonic and has an unknown orgin.

1.5 CMB Anisotropies

1.5.1 Basic Theory

In the inflationary paradigm, initial quantum fluctuations are blown up to large scales by the exponential expansion. These initial fluctuations are the seeds of the large scale structure we see today. Before recombination the photons and electrons are tightly coupled via Compton scattering and both are coupled to the protons through electromagnetic interaction. This creates a photon-baryon fluid [51]. Initial perturbations in the CDM distribution form the gravitational wells which provide the impetus for the evolution of photon-baryon fluid.

The relationship between the amplitude and spatial scale of the temperature anisotropies is determined in large part by the sound speed of the photon-baryon fluid [53, 51]. The sound speed is $c_s \simeq c/\sqrt{3(1+R)}$, where $R = 3\rho_b/4\rho\gamma$ is the baryon-photon momentum density ratio ($R \to 1$ when $\rho_b \ll \rho_{gamma}$). In this photon-baryon fluid, there are density oscillations. The gravitational potential causes mass to be drawn into potential wells. Photon pressure provides a restoring force, leading to an oscillation. When recombination occurs, the pattern of oscillations is frozen.

Modes larger than the sound horizon are not able to evolve before recombination. Temperature anisotropies from these modes are due only to the gravitational redshift of photons as they climb out of the potential well. For these modes $\Delta T(k) = \frac{1}{3}\Phi$ which is a negative number for an overdense region.

In a simplified Newtonian model with adiabatic initial conditions [53], oscillation modes smaller than the sound horizon produce a net temperature anisotropy $\Delta T(k) = \frac{1}{3}\Phi\cos(kc_s\eta_*)$ where Φ is the gravitational potential (a negative number), k is the wavenumber (Fourier-mode) of the oscillation and η_* is the conformal time at recombination. The oscillatory solution for $\Delta T(k)$ implies

that there will be a set of peaks in $k-space$ defined by $k_m = m\pi/c_s\eta_*$. The energy increase due to heating from photon pressure dominates the loss of energy from climbing out of a gravitational well. A mode which is fully compressed will be hot ($\Delta T > 0$) while a mode where the photon-baryon fluid is evenly distributed (rarefracted) will be cold. Therefore, compression peaks will have odd values of m, while rarefraction peaks will have even values.

This is not the whole story of anisotropy formation, but it is enough for us to have some intuition about it. On scales larger than the sound horizon, temperature anisotropies are due to gravitational redshift. For fluctuations with a characteristic size smaller than the sound horizon, acoustic oscillations are the dominant source of anisotropy. To keep the sign of the temperature fluctations straight, remember that for an overdense region acoustic oscillations produce $\Delta T > 0$ while gravitational redshift produces $\Delta T < 0$.

The statistics of the anisotropies as a function of spatial scale is determined by basic cosmological parameters, namely the previously introduced densities: Ω_{tot}, $\Omega_b h^2$, $\Omega_{cdm} h^2$, and Ω_Λ. Other parameters which affect anisotropy formation are n_s which is related to the power spectrum of primordial scalar perturbations of the gravitational potential, and τ_c which is the optical depth to reionization. The overall amplitude of the fluctuations is also a free parameter. See 7.8 for more details on cosmological parameters.

1.5.2 Measuring Anisotropies

Since we are only able to measure the anisotropy distribution on the celestial sphere, we need to compress the 3-dimensional Fourier space information (k-space) into something 2-dimensional which we can compare to our observations. Any scalar function on the sphere can be expanded into spherical harmonics, $Y_{\ell m}$,

$$T(\theta, \phi) = \sum_{\ell m} a_{\ell m} Y_{\ell m}(\theta, \phi), \tag{1.5.1}$$

where the $a_{\ell m}$'s are the expansion coefficients. Assumptions of isotropy imply that on average the $a_{\ell m}$'s are zero and that the we can parameterize our theory by

$$C_\ell = \langle a_{\ell m} a^*_{\ell m} \rangle \,, \tag{1.5.2}$$

the ensemble average of the $a_{\ell m}$'s. Fast Boltzmann codes like CMBFAST [100], can generate the C_ℓ spectra given a set of cosmological parameters. The transformation from 3 dimensions to 2 dimensions does come at a cost: a fundamental uncertainty which is worst for long wavelength (low-ℓ) modes. This uncertainty is due to the fact that the CMB fluctuations are random in nature; the uncertainty in the average power on a certain spatial scale depends on the number of spatial modes we measure (in statistics, this is called sample variance). Right now, we are measuring the CMB signal from approximately 14 billion light

years away. If we wait a few billion years, the CMB signal will be coming from a region much further away than it is now. Then we will have a new set of spatial modes to measure, which will decrease our uncertainty on the power spectrum at large angular scales.

Cosmological anisotropies have an amplitude $\Delta T \sim 30\mu K$; which is not an easy signal to measure. The COBE-DMR results came about 25 years after the discovery of the CMB. In the intervening years, many attempts were made to measure anisotropies, but experiments proved not sensitive enough. While the COBE-DMR did not fly with the most up to date technology, its low angular resolution and long integration time was enough to measure these small signals. Shortly after the release of the COBE-DMR data, improvements in detector technology helped to bring forth a number of other measurements on smaller angular scales. With the turn of the new century, CMB anisotropy measurments have entered a golden age with measurements spanning a large range of angular scales. Figure 1.1 shows results from some of the most recent experiments and the COBE-DMR result [98, 68, 7, 77, 42, 70, 39, 104]. In one decade, we have gone from initial detection to a measurement of the C_ℓ spectrum from $\ell = 2$ out to $\ell \sim 3000$.

The power spectrum measurements clearly show that there are at least 3 peaks in the power spectrum. Inflationary models with adiabatic perturbations generally predict such a series of peaks formed by the acoustic oscillations. The amplitude and position of the acoustic peaks can provide constraints on various comoslogy parameters. Most notably the position of the first peak can strongly constrain Ω_{tot}. With common sense priors on the age of the universe and Hubble constant, CMB anisotropy results are able to place strong constraints on Ω_{tot}, $\Omega_b h^2$, and n_s. With the age of the universe constrained to be greater that 10 billion years, $0.45 < h < 0.90$, and $\Omega_m > 0.1$, a combined analysis of the pre-WMAP data shows that $\Omega_{tot} = 1.04 \pm 0.04$ and $\Omega_b h^2 = 0.022^{+0.003}_{-0.002}$ [38]. The value of $\Omega_b h^2$ from CMB data is consistent with the result from Big Bang nucleosynthesis, $\Omega_b h^2 = 0.019 \pm 0.002$ [111]. If stronger constraints from Type 1A supernova and large-scale structure data are included in the analysis, Ω_Λ is found to be ~ 0.7.

These constraints on cosmological parameters are derived using from models which only include adiabatic perturbations (the prediction of the simplest inflationary models). Models based solely on isocurvature perturbations are unlikely to reproduce the pattern of acoustic peaks [33]. However, it is possible that structure formation was seeded by a mixture of adiabatic and isocurvature perturbations. Temperature anisotropy measurements alone are unable to constrain contributions from isocurvature perturbations. In we only have data on the temperature power spectrum, abandoning the assumption of adiabaticity can sharply reduce our ability to constrain cosmological parameters using temperature anisotropy data [17]. However, measuring the polarization of the CMB will allow

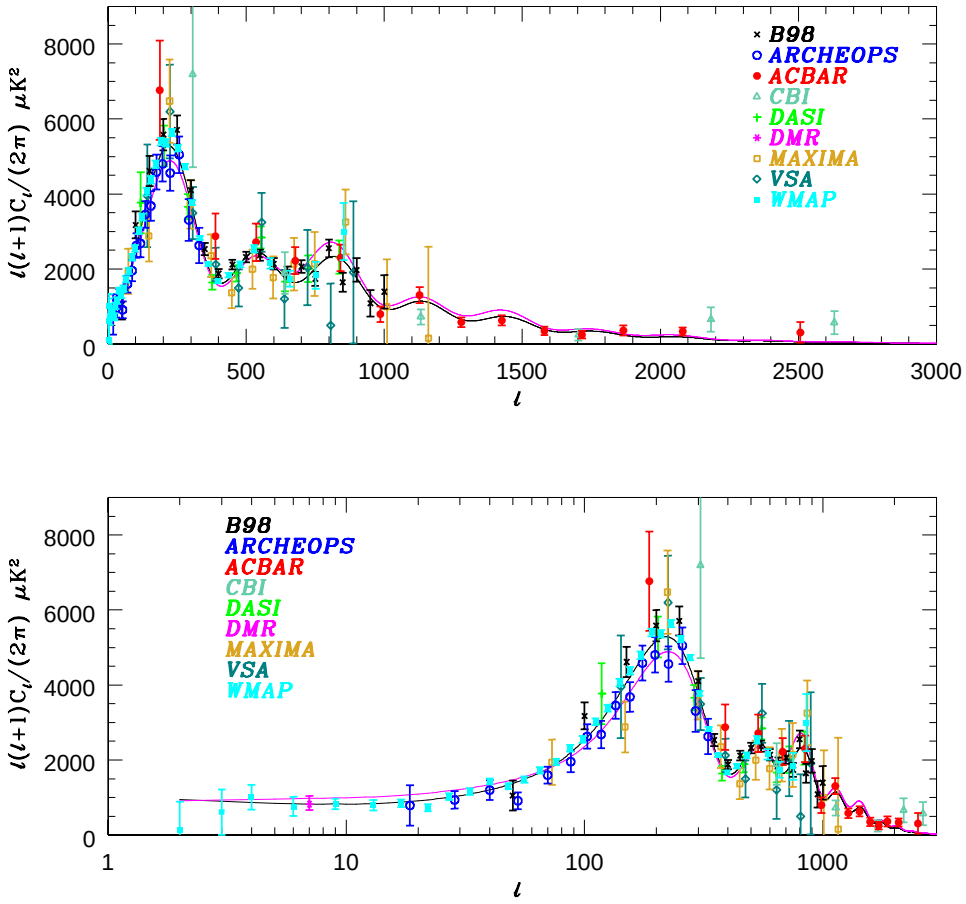

Figure 1.1: Recent measurements of the CMB Temperature power spectrum. Plots in ℓ and $\log \ell$ are shown to emphasize that the low-ℓ power spectra and the high-ℓ power spectrum both contain a important information. The black line is the best fit to a ΛCDM model using most of recent data before WMAP and the magenta line is the best fit to an $\Omega_\Lambda = 0$ model (from Goldstein et al.[38]). The amplitude of both models has been adjusted from the COBE normalization to the best fit value.

us to isolate the effects of isocurvature perturbations and verify the assumptions of adiabaticity.

1.6 CMB Polarization

Unpolarized radiation can be polarized through Thomson scattering with free electrons. Before recombination photons and electrons are tightly coupled. Constant scattering which prevents a net polarization from forming. As the optical depth decreases during recombination, photons scatter for the last time carrying away details of the last scattering surface in their polarization.

1.6.1 Stokes Parameters

Before describing Thomson scattering or CMB polarization, it is useful to describe how polarization is quantified. A monochromatic polarized electromagnetic wave with angular frequency ω ($\omega = 2\pi\nu$) can be described by

$$\vec{E} = E_x(t)sin(\omega t - \delta_x(t))\hat{x} + E_y(t)sin(\omega t - \delta_y(t))\hat{y}, \tag{1.6.1}$$

where $E_x(t)$, $\delta_x(t)$, $E_y(t)$ and $\delta_y(t)$ vary on times scales much longer than the period of the wave. The Stokes parameters: I, Q, U, and V completely describe the polarization state of a wave and can be calculated via time averages of combinations of wave's components

$$\begin{aligned} I &= \left\langle E_y^2 + E_x^2 \right\rangle, & (1.6.2)\\ Q &= \left\langle E_x^2 - E_y^2 \right\rangle, & (1.6.3)\\ U &= \left\langle 2E_yE_xcos(\delta_y - \delta_x) \right\rangle, & (1.6.4)\\ V &= \left\langle 2E_yE_xsin(\delta_y - \delta_x) \right\rangle, & (1.6.5)\\ \tau &= \frac{1}{2}\tan^{-1}(\frac{U}{Q}), & (1.6.6) \end{aligned}$$

where averaging is done on a time scale longer than the period of the wave. The total intensity of the radiation is described by I. Parameters Q and U describe the linear polarization, while V quantifies the degree of circular polarization ($V = 0$ when the radiation is linearly polarized). The angle of polarization is τ. To calculate U in a more intuitive way, we can represent the electric field in coordinate system rotated by $-45°$ in which $U = \left\langle E_{x'}^2 - E_{y'}^2 \right\rangle$. Thus Q measures intensity difference between the $\hat{x}$ and $\hat{y}$ axes while U is the intensity difference between the $\hat{x}'$ and $\hat{y}'$ axes which are rotated $-45°$ from the fiducial coordinate system.

What exactly does it mean for radiation to be polarized or un-polarized? If we just set $E_x = E_y$, then $Q = 0$, but we don't know about U or V until we consider the phases. In order to have un-polarized light, the phase difference $\delta_x - \delta_y$ must have a random distribution to insure that U and V are zero.

Under coordinate transformations Q and U rotate like spin-2 tensors

$$\begin{aligned} Q' &= Q\cos 2\theta + U\sin 2\theta, & (1.6.7)\\ U' &= -Q\sin 2\theta + U\cos 2\theta, & (1.6.8) \end{aligned}$$

while I and V are invariant. As we will see later, this makes measurements of the polarization spectrum somewhat more complicated than the temperature case.

1.6.2 Generating Polarization with Thomson Scattering

For Thomson scattering the differential scattering cross section can be written

$$\frac{d\sigma}{d\Omega} = \frac{3\sigma_T}{8}|\hat{\epsilon}\cdot\hat{\epsilon}'|^2, \tag{1.6.9}$$

where σ_T is the Thomson scattering cross section, $\hat{\epsilon}$ is the incident polarization vector and $\hat{\epsilon}'$ represents the outgoing polarization vector. Figure 1.2 shows the geometry of a single Thomson scattering event. In this case, the incoming and outgoing coordinate systems are defined so that the y-axis of each system is in the plane of scattering. The outgoing wave moves along the z' axis at an angle θ with respect to the incoming wave. If the incident radiation is unpolarized with intensity I, then $I_x = I_y = I/2$ and we can write the scattered intensities as

$$I'_x = \frac{3\sigma_T}{8\pi}\left[I_x(\hat{\epsilon}'_x\cdot\hat{\epsilon}_x)^2 + I_y(\hat{\epsilon}'_x\cdot\hat{\epsilon}_y)^2\right] = \frac{3\sigma_T}{16\pi}I, \tag{1.6.10}$$

$$I'_y = \frac{3\sigma_T}{8\pi}\left[I_x(\hat{\epsilon}'_y\cdot\hat{\epsilon}_x)^2 + I_y(\hat{\epsilon}'_y\cdot\hat{\epsilon}_y)^2\right] = \frac{3\sigma_T}{16\pi}I\cos^2\theta, \tag{1.6.11}$$

where $\hat{\epsilon}$ and $\hat{\epsilon}'$ represent unit vectors perpendicular to the direction of propagation in the incident and scattered coordinate systems, respectively. For the scattered wave the Stokes parameter are

$$I' = I'_x + I'_y = \frac{3\sigma_T}{16\pi}I(1+\cos^2\theta), \tag{1.6.12}$$

$$Q' = I'_x - I'_y = \frac{3\sigma_T}{16\pi}I\sin^2\theta, \tag{1.6.13}$$

where $U' = 0$ in this case. Thomson scattering cannot create circular polarization; therefore, $V = 0$.

For unpolarized radiation field with an incident angular distribution $I(\theta,\phi)$, we can calculate the Stokes parameters of the radiation scattered along the z-axis by integrating over the distribution on the sphere

$$I' = \frac{3\sigma_T}{16\pi}\int d\Omega(1+\cos^2\theta)I(\theta,\phi), \tag{1.6.14}$$

$$Q' = \frac{3\sigma_T}{16\pi}\int d\Omega\sin^2\theta\cos(2\phi)I(\theta,\phi), \tag{1.6.15}$$

$$U' = \frac{3\sigma_T}{16\pi}\int d\Omega\sin^2\theta\sin(2\phi)I(\theta,\phi), \tag{1.6.16}$$

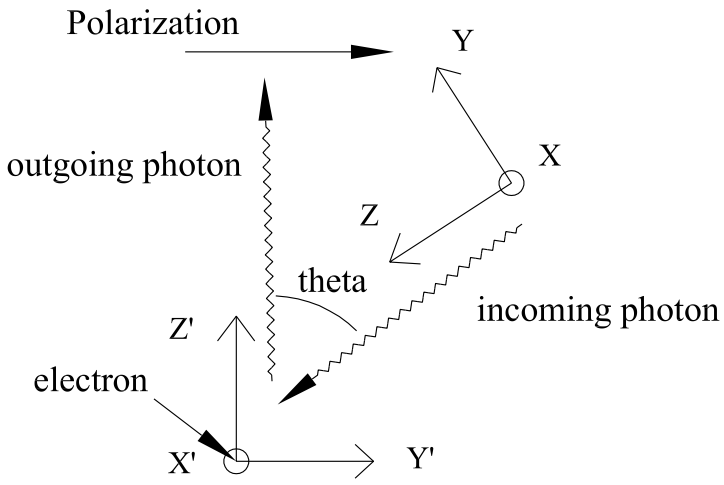

Figure 1.2: Geometry of Thomson scattering.

where we have defined Q and U in the outgoing coordinate system shown in figure 1.2. By expanding the incident radiation field in terms of spherical harmonics, we can write the Stokes parameters in terms of a_{lm}'s (equation 1.5.1)

$$I' = \frac{\sigma_T}{4\pi}\left[2\sqrt{\pi}a_{00} + \sqrt{\frac{\pi}{5}}a_{20}\right] \quad (1.6.17)$$

$$Q' = \frac{3\sigma_T}{4\pi}\sqrt{\frac{2\pi}{15}}\mathrm{R}e(a_{22}) \quad (1.6.18)$$

$$U' = \frac{3\sigma_T}{4\pi}\sqrt{\frac{2\pi}{15}}\mathrm{I}m(a_{22}). \quad (1.6.19)$$

This shows that Thomson scattering can induce polarization if the incoming radiation distribution has a non-zero component of Y_{22} (i.e. a quadrupole moment).

1.6.3 Polarizing the CMB

Measuring the polarization of the CMB provides a snapshot of the last scattering surface. Before recombination, at any given point, the only multipole moments which are stable are the monopole, which is the radiation temperature, and the dipole, which is induced by the flow of the photon-baryon fluid. The rapid rate of scattering causes any higher-order multipole moments to damp away. As the optical depth decreases, higher-order multipole moments begin to form and it is possible for the CMB to become polarized. The magnitude of the polarized signal depends on the duration of recombination which was $\Delta z \sim 200$.

The amplitude of the polarization signal is expected to be about 10% of the temperature anisotropy signal making it very difficult to detect.

To generate polarization, electrons on the Last Scattering Surface (LSS) must see a quadrupole radiation moment. Scalar, vector and tensor perturbations in the photon baryon fluid lead to such quadrupole moments. Cosmologically we don't expect significant contributions from vector perturbations, so here we only consider scalar and tensor perturbations.

Scalar modes are associated with density perturbations in the photon-baryon fluid. These perturbations give rise to fluid flows into gravitational wells on scales larger than the sound horizon but smaller than the causal horizon. On scales smaller than the sound horizon there are acoustic oscillations. To understand why these are the scalar modes, we need to think about the forces which govern the flows. The gravitational potential and the photon pressure are the main driving components; their effects can each be written as the gradient of a potential. For a function $\phi(\vec{x})$, $\nabla \times \nabla\phi(\vec{x}) = 0$. This means that this flow is irrotational, which is the definition of a scalar mode.

The development of a local quadrupole can be understood by moving to the reference frame of an electron flowing between an overdense region (large gravitational potential) and an underdense region (small gravtational potential) in the photon-baryon fluid. Figure 1.3 shows the velocity fields for an electron falling into a gravitational well. In its reference frame (the right panel of figure 1.3, the electron sees a radiation quadrupole as a the result of Doppler shifting induced by the velocity quadrupole of the plasma. Photon pressure counteracts the gravitational infall and can reverse the flow near an overdense region. Similarly it can push the fluid into an underdense region. To be precise, the velocity directions in the quadrupole moment depend on whether the photon-baryon fluid is converging or diverging, not whether the electron is near an overdense or underdense region. The left side of figure 1.4 shows the radial polarization orientation for a converging flow. By reversing the velocity vectors, the polarization orientation is found to be tangential for a diverging flow.

These polarization directions can be understood rather simply. From equations 1.6.10 and 1.6.11, we see that $I_y = 0$ at $\theta = 90°$, meaning that the polarization is polarized perpendicular to the scattering plane. For an electron falling into an overdense region (figure 1.3), the radiation perpendicular to the flow is hotter. Radiation scattered from that direction to an observer out of the page if polarized along the direction of the flow (radially). Cooler radiation reaching the electron from radial directions is polarized perpendicularly to the flow (tangentially). In this case there is more intensity polarized in the radial direction than in the tangential direction; therefore, the net polarization is radial for electrons flowing into an overdense region.

Since scalar fluctuations in the photon-baryon fluid induce velocity fields which in turn induce polarization, there is a correlation between temperature

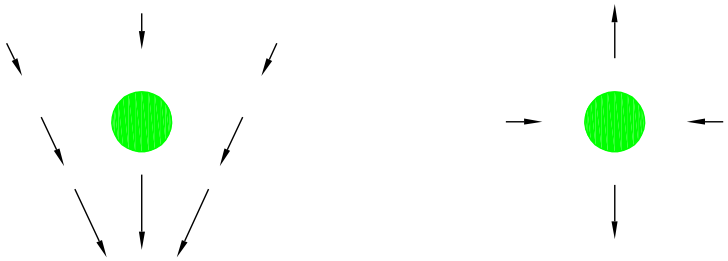

Figure 1.3: Velocity field of the photon-baryon fluid flowing into an overdense region. The green circle represents and electron in the fluid. The arrows represent the flow with the length of the arrow corresponding to velocity. The left picture shows the velocities in the overdense region's frame of reference; the plasma is flowing towards the maximum of the gravitational potential with increasing velocity. The right picture show the velocities in the electron's reference frame. In this reference frame the velocity field has a quadrupole distribution which turns into a radiation quadrupole through Doppler shifting. The velocity directions in the quadrupole depend only on the direction of the flow. Photon pressure can push the fluid out of an overdense region; this results in quadrupole moment similar to flow out of an underdense region.

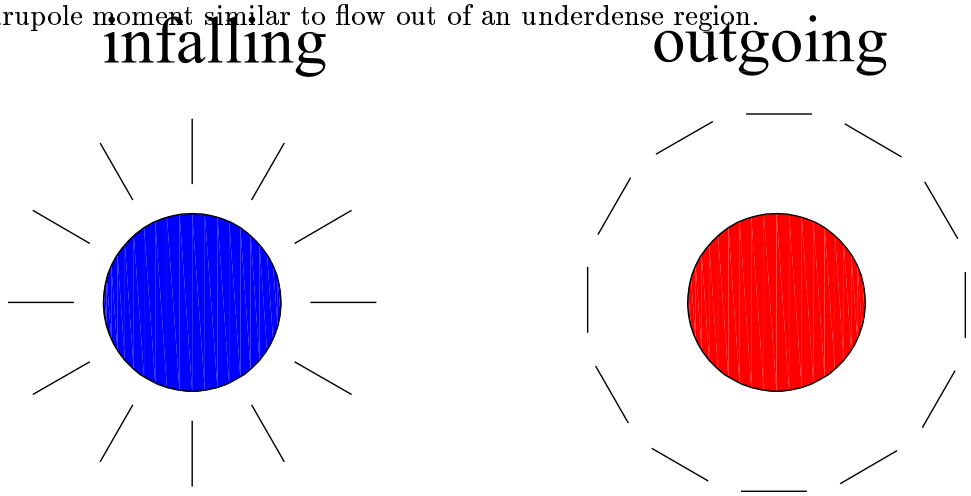

Figure 1.4: Polarization patterns generated for a converging and diverging flow. For a converging flow, the polarization orientation is radial. The orientation is tangential when the flow is diverging.

anisotropies and polarization. For temperature anisotropies, the acoustic oscillations lead to a series of peaks corresponding to compression and rarefraction. For scalar polarization modes, the amount of polarized signal depends on the velocity field; the polarization power spectrum will peak on angular scales where there are valleys of the temperature spectrum (corresponding to scales where the velocity is maximal). The cross-correlation between temperature and polarization will peak between neighboring peaks of the individual spectra. The sign of the cross-correlation can change depending on whether the temperature fluctuation is dominated by gravity or photon pressure, or if the acoustic oscillation is compressing or rarefracting [52].

Tensor perturbations are caused by gravity waves. Perturbations from gravity waves distort spacetime in a elliptical way causing a radiation quadrupole via stretching of photon wavelengths. Measuring the polarization signal from gravity waves would allow us to place constraints on the energy scale of inflation. As we will discuss in the next section, the polarized pattern generated by gravity waves has a different character than that produced by scalar perturbations. In principle this allows us to distinguish between the contributions from gravity waves and scalar perturbations. Unfortunately the gravity wave signal is expected to be $\leq 10\%$ of the polarization signal from scalar modes [61].

Lastly, from the Gunn-Peterson test, we know that the universe reionized before $z \simeq 5$ [40]. Reionization re-populates the universe with free electrons which will scatter CMB photons. This has the effect of damping temperature anisotropies on all scales, but introduces new anisotropies on scales larger than the horizon size at decoupling [120]. Cosmic variance makes it hard to distinguish between the effect of reionization and the overall amplitude of the temperature power spectrum. Fortunately, reionization causes an increase in the polarization signal on large angular scales which should not be hidden by cosmic variance. This reionization signature has been seen by WMAP [64].

1.6.4 Measuring CMB Polarization

As we will discuss in section 6.6.2, the spin-2 nature of the Stokes parameters requires that the description of polarization on the sphere be an expansion in spin-weighted spherical harmonics [118]. By taking appropriate linear combinations of the spin-2 coefficients, we can define coefficients $a_{E,\ell m}$, and $a_{B,\ell m}$ which represent E-mode and B-mode polarization respectively (see definitions in section 6.6.2). These modes are rotationally invariant and therefore can be expanded in terms of normal spherical harmonics. With these coefficients, three new power spectra

can be defined

$$C_\ell^E = \left\langle a_{E,\ell m} a^*_{E,\ell m'} \right\rangle \delta_{mm'}, \tag{1.6.20}$$

$$C_\ell^B = \left\langle a_{B,\ell m} a^*_{B,\ell m'} \right\rangle \delta_{mm'}, \tag{1.6.21}$$

$$C_\ell^{TE} = \left\langle a_{E,\ell m} a^*_{T,\ell m'} \right\rangle \delta_{mm'}, \tag{1.6.22}$$

where C_ℓ^{TE} is the cross spectrum between temperature anisotropies and E-mode polarization.

The transformation from Q, U to E-modes and B-modes separates the polarization information into two different geometrical basis. The rotational properties of Q and U are identical to those of the independent components of a second rank symmetric trace-free (STF) tensor. Any STF can be decomposed into E-modes and B-Modes analogous to the way vectors are separated into curl-free and divergence-free components. The E-modes represent the analog of the gradient of a scalar function, while B-modes represent the analog of the curl of a different scalar function [58, 18]. E-modes transform as a scalar quantity, while B-modes are pseodoscalars which means that they change sign under a parity transformation. Since B-modes are not invariant under a parity transformation C_ℓ^{TB} and C_ℓ^{EB} are identically zero.

Zaldarriaga provides an intuitive introduction to the geometrically nature of the E and B modes [117]. The rotational properties of Q and U require that the transformation to E and B modes be a non-local linear transformation. One way of calculating the value of E and B at a point P is to integrate the values of Q_r and U_r in concentric circles around P weighting each integral by the inverse square of the angular radius of that circle. Q_r and U_r are the Stokes parameters at one point on the circle in a coordinate system defined by the radius from P to that point. The integral can be written as

$$E(\theta) = \int d^2\tilde{\theta} w(\tilde{\theta}) Q(\theta + \tilde{\theta}) \cos(2\tilde{\phi}) - U(\theta + \tilde{\theta}) \sin(2\tilde{\phi}), \tag{1.6.23}$$

$$B(\theta) = \int d^2\tilde{\theta} w(\tilde{\theta}) U(\theta + \tilde{\theta}) \cos(2\tilde{\phi}) + Q(\theta + \tilde{\theta}) \sin(2\tilde{\phi}), \tag{1.6.24}$$

where $w(\tilde{\theta}) = -1/\tilde{\theta}^2$ is a conventional weighting. This way of writing the integrals accounts for the necessary rotation of Q and U at each point.

Physically scalar perturbations only produce E-modes, while tensor modes produce approximately equal amounts of E and B [52]. By measuring B, we could hope get some handle on the tensor perturbations and the gravity waves which cause them. This is not an easy task. Unfortunately, E-modes can be gravitationally lensed into B-modes as the photons travel from the last scattering surface to our detectors [119]. Luckily only the high-ℓ part of the C_ℓ^B spectra is contaminated.

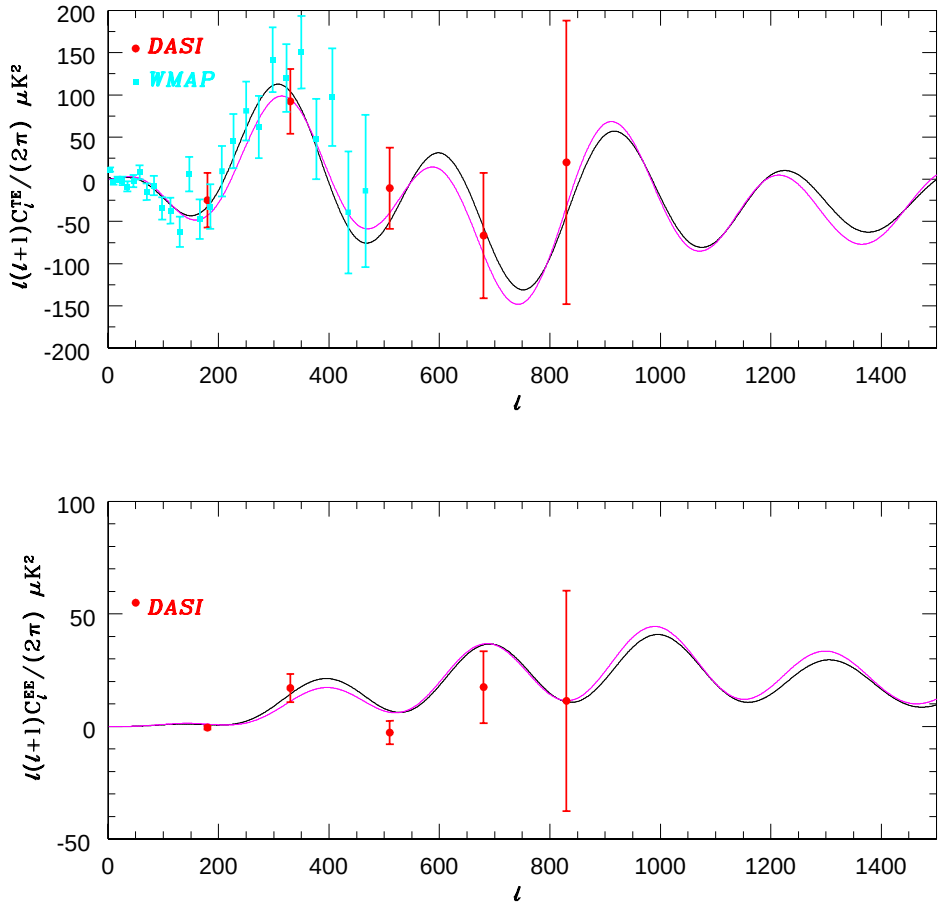

Figure 1.5: CMB polarization measurements from DASI and WMAP. The black and magenta curves show the expected polarization signals for the models shown in Figure 1.1. The models are the best fits for ΛCDM models (black) and $\Lambda = 0$ (magenta) models calculated using pre-WMAP data [38].

Recent and currently deployed experiments have sensitivities which are within range of detecting E-mode polarization, while the B-mode signal is still out of range. The E-mode polarization is 10% of the temperature anisotropy signal, making it a significant challenge. A measure of the E-mode power spectrum will allow us to test whether the primordial perturbations are primarily adiabatic or a mixture of adiabatic and isocurvature modes. In recent years experiments such as POLAR [59], PIQUE [45] and COMPASS [34] have pushed down the upper limits on the CMB polarization signal. In the fall of 2002, DASI published the first detection of CMB polarization [67] with measurements of C_ℓ^{EE} and C_ℓ^{TE}.

More recently WMAP [64] released a measurments of C_ℓ^{TE} clearly showing the in-print of reionization on large angular scales. Figure 1.5 shows the WMAP and DASI results overplotted with the expected polarization signal for the the best-fit ΛCDM and $\Omega_\Lambda = 0$ models (based on analysis of the pre-WMAP temperature anisotropy data [38]).

1.7 BOOMERANG

There are several approaches to measuring CMB anisotropies and polarization. Experiments can be done on the ground, on a balloon or in space. Detectors systems are usually constructed from High Electron Mobility Transistors (HEMT's) or bolometers. The observing strategy can involve interferometry, a correlation receiver or simply scanning back and forth in azimuth. For CMB observations, HEMT's have been used at frequencies from 10-100 GHz, while bolometers have been used at 90 GHz and above. Here we give a quick introduction to BOOMERANG. A more detailed discussion is in Chapter 2.

BOOMERANG is a balloon-borne telescope designed for long duration flights (LDB) around Antarctica. It is an off-axis telescope with a 1.3 m diameter primary mirror. It has cryogenically cooled secondary and tertiary mirrors which re-image the prime focus onto the detector focal plane. Its detector system consists of AC-biased bolometers cooled to < 0.3K by a large cryostat capable of keeping the detectors cold for more than 14 days. The general observation mode is to scan in azimuth leaving the elevation constant for at least an hour. Sky rotation turns a one-dimensional scan in azimuth (at fixed elevation) into a crosslinked two-dimensional map on the celestial sphere.

BOOMERANG has made three flights: a North American test flight in 1997, an LDB flight starting in late 1998, and a second LDB flight in January 2003. The 1997 flight helped to make the first CMB based constraints on Ω_{tot} [84]. The 1998 flight (known hereafter as B98) provided striking high signal-to-noise maps of CMB anisotropies (see figure 7.3) and a measure of the temperature power spectrum from $\ell \sim 25$ to $\ell \sim 1025$ [98] (see also figure 1.1). For the 2003 flight (known hereafter as BOOM03), the receiver was designed for polarization sensitivity. The analysis of the data from this flight is ongoing, but we hope to measure C_ℓ^T, C_ℓ^{TE}, and C_ℓ^E.

The operating frequencies is one of the most important decision made in the design of the experiment. The frequencies should be chosen to maximize sensitivity to the CMB in the presence of contaminants, namely atmospheric and galactic foreground emission. The amount of atmospheric emission depends on the location of the experiment. The atmospheric spectrum rises with frequency. Different galactic foregrounds scale differently with frequency: free-free and synchrotron emission dominate at $\nu < 100GHz$, while dust is the primary foreground for $\nu > 100GHz$.

Figure 1.6 compares the frequency spectra of atmospheric emission (at balloon altitudes) and galactic foregrounds to the CMB signal. Since the CMB anisotropy and polarization signals are deviations from a blackbody spectrum, their frequency dependence is described by the derivative of the Planck blackbody function (dB_ν/dT) evaluated at T_{CMB} which peaks at 217 GHz. In the 1998 flight, we operated with bands centered at 90, 150, 240 and 410 GHz to maximize our lever arm on foregrounds. In Masi et al. [74] (and summarized in chapter 7), it is shown that the high-latitude dust emission in our maps is negligible ($\sim$ 2%) at 150 GHz when compared to the the CMB anisotropy signal. For BOOM03 , we chose bands centered at 145, 245 and 345 GHz with the 245 and 345 GHz channels having nearly 100 GHz of bandwidth. The polarized foreground signal at these frequencies is unknown. Synchrotron radiation is expected to be strongly polarized, but its signal is sub-dominate above 90 GHz. Galactic magnetic fields could cause polarized dust emission, but the dust would need to be 50% polarized in order to cause even a 10% contamination in the expected polarization signal at 145 GHz.

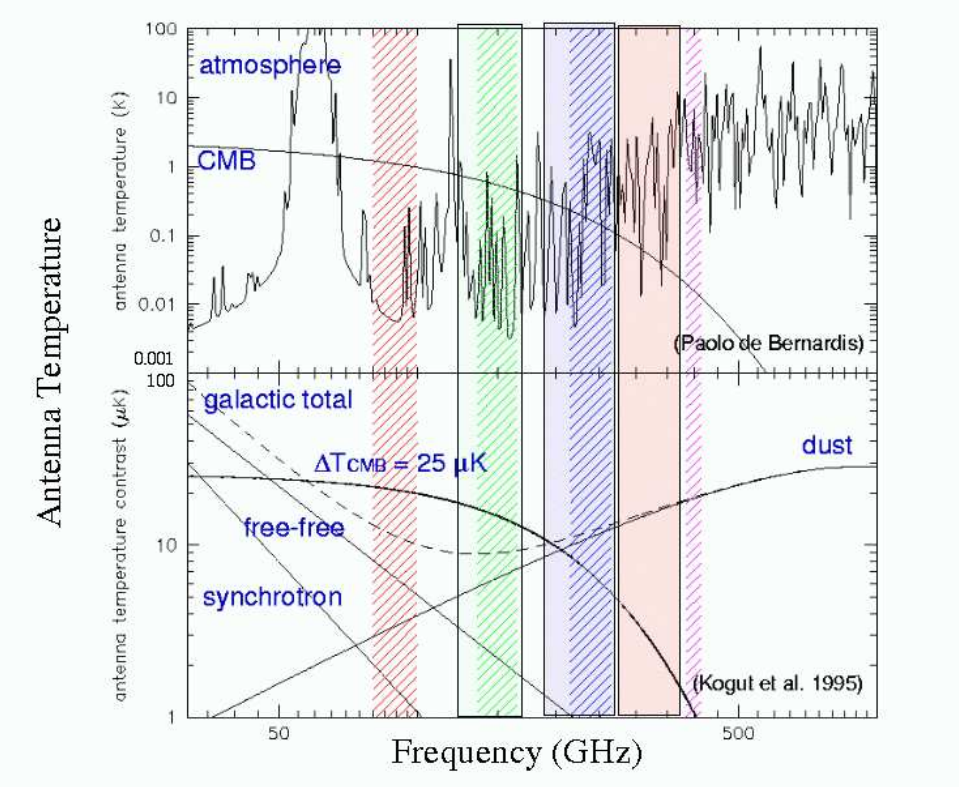

Figure 1.6: A comparison of atmospheric emission and galactic foregrounds to the level to the expected CMB signals. The top panel compares the contribution to the antenna temperature from the atmosphere at float altitude ($\sim 120,000$ft) to the antenna temperature contribution from the CMB (thick solid line). The atmospheric emission is computed using the HITRAN model (http://www.hitran.com). The bottom panel compares the expected foreground emission at high galactic latitudes (based the COBE results [63]) to the expected signal from CMB anisotropy. The BOOMERANG bands are overlayed on these plots with the B98 bands represented by diagonal cross-hatching and the BOOM03 bands repesented by lightly colors boxes.

Chapter 2

The BOOMERANG Telescope

During the Austral summer, stratospheric winds form a vortex centered on the Antarctic continent. BOOMERANG is designed to operate at stratospheric altitudes ($\sim 120,000ft$) over the Antarctic continent for periods of 10-16 days. During the course of a Long Duration Balloon (LDB) flight, a balloon payload can circumnavigate the continent at $\sim 78^\circ$ South latitude in a time period of 10 to 24 days.

The Antarctic LDB environment is quite harsh and special care must be taken to insure proper operation and to prevent contamination of the data. Proper thermal design and shielding are vital, because constant sunlight and the low ambient pressure at stratospheric altitudes allow for extreme temperature variations (-50° C in the shade to +50° C in the sun). Since we are trying to measure very small signals (1 part in 10^6), we need shielding to ensure the telescope is immune to contamination from stray Sunlight and Earthshine. High-bandwidth communications with the telescope are possible only when the payload is near enough to the launch site for line of sight radio communication; therefore, the telescope must be designed to operate autonomously for long periods of time. The flight duration requires a cryogenic system which can keep the detectors at < 0.3K for 10 days or longer. Also more ominously, the cosmic ray flux is about 10 times greater at balloon altitudes over Antarctica than it is at comparable altitudes in North America (cosmic rays can contaminate data from bolometric detectors). Reconstructing the pointing of the telescope can also be a problem. The constant sunlight makes it very difficult to use fixed star sensor systems (which are relatively easy to work with and very accurate); therefore, alternate pointing sensors must be used. Planets are very bright point sources; they are ideal for measuring the calibration and beam response of microwave telescope. Unfortunately, at polar latitudes the planets are at a low elevation making observation difficult.

In spite of all the difficulties, Antarctic ballooning is well worth the effort. The long duration flight allows for deep integration, and ample time to check for systematic effects. The high latitude allows us to integrate on a small regions

of sky without having to make large changes in the elevation of the telescope. Even though the Sun is above the horizon 24 hours a day and moves 23 degrees in elevation, the polar summer is second only the the polar winter in terms of diurnal thermal stability. During the Antarctic summer, we are able to integrate on a region of sky which has very low galactic foreground emission. At this time region is in a direction about 150 degrees away from the sun in Right Ascension.

The telescope has been described extensively in [93, 22, 21]. Here we provide an overview of the fundamental design focusing more on details about the changes made for the BOOM03 flight. See [22, 21] for details on the B98 receiver design, thermal design details and B98 in-flight performance.

2.1 Telescope and Gondola

In comparison to earlier balloon-borne CMB experiments, BOOMERANG is relatively simple. Figure 2.1 shows 2 pictures of the telescope pointing out some of the important subsystems and the protective shielding. BOOMERANG is designed to scan back and forth in azimuth at speeds around 1 degree per second while the elevation fixed for long periods of time. The azimuth of the telescope is controlled by two torque motors [16]. One motor torques a large flywheel for fast time scale control. The other corrects for the random rotation of the balloon by applying a torque to the steel cables connecting the payload to the balloon, thereby dumping angular momentum on long time scales. The elevation of the telescope is controlled by tipping the inner frame with a linear actuator driven by a DC gear motor.

The azimuth and elevation motors are controlled by a pair of redundant 386 computers. These read data from the pointing sensors and use it in a feedback loop for controlling the scan of the telescope. Similar to the 1998 flight, BOOM03 used a differential GPS array, an azimuthal sun sensor and three orthogonal rate gyros. The azimuthal gyro provides feedback for controlling the speed of the scan. The GPS and sun sensor both provide absolute pointing information which is used to set the center and limits of the scan. To improve post-flight pointing reconstruction for BOOM03 , we added a pointed sun sensor and tracking star camera The star camera was properly filtered and baffled to allow for tracking of stars in the daytime. It was able to see stars with a magnitude as low as 4, but in practice there are enough accessible stars brighter than magnitude 2.5 for tracking purposes. With these new sensors we hope to be able to reduce the pointing reconstruction error to $< 1'$ rms.

2.2 Cryogenics

The BOOMERANG cryogenic system was custom built to keep the detectors at a temperature of < 0.3 K for as long as two weeks. The system consists of a

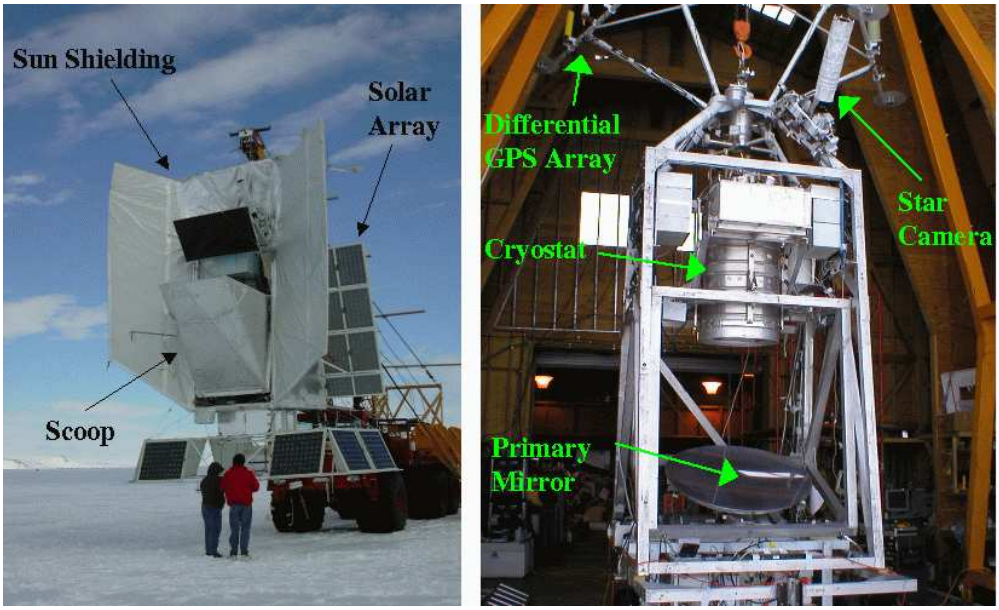

Figure 2.1: The left side shows a picture of BOOMERANG on the day BOOM03 was launched. The right side shows some of the vital components which reside underneath the shielding.

large ^{4}He cryostat and a powerful closed-cycle sorption-pumped ^{3}He refrigerator [76, 75]. The ^{3}He refrigerator contains $\sim$48 liter STP of ^{3}He and runs at 0.275 K with a heat load of $\sim 27\mu$W. The cryostat holds 65 liters of liquid nitrogen and 60 liters of liquid helium. Both tanks are toroidal in shape. They are suspended with Kevlar cord (1.6 mm diameter) which provides adequate mechanical support and has a low enough thermal conductivity to ensure a 16 day hold time. The 77 K stage is protected from 300 K thermal radiation by 30 layers of aluminized mylar superinsulation. A shield cooled to < 20 K by the vapor from the evaporating liquid Helium provides radiative protection for the ^{4}He stage. Inside the toroid of the ^{4}He tank, there is a 60 L volume, where the re-imaging optics and focal plane are inserted. The optics are held at the same temperature as the ^{4}He stage, while the focal plane is isolated from the ^{4}He stage by 4 thin walled Vespel legs and cooled to 0.275 K.

Once liquids have been added to the cryostat and the focal plane has thermalized to 4 K, the ^{4}He stage and the focal plane can be further cooled to 1.65 K by pumping on the liquid helium bath. Due to flow impedances and the complex geometry of the ^{4}He vent tubes, thermo-acoustical oscillations prevent a fast pumpdown. It is necessary to pump down the system slowly over the course of 12 to 16 hours. Once the ^{4}He pressure is less than 5 Torr, the cryopump on the sorption refrigerator is heated to 40 K. This expels all the ^{3}He from the charcoal

in the pump causing the ^{3}He to condense in the evaporator. At this point, a heat switch can be closed connecting the cryopump to 1.65 K. As the cryopump cools, it begins the pump on ^{3}He cooling the evaporator to 0.275 K.

BOOMERANG is launched with the helium bath already pumped down. A mechanical valve between the ^{4}He bath and ambient pressure is closed during the launch and ascent. The valve is opened once the package reaches float altitude where the ambient pressure is about 3 Torr. This pressure is low enough to keep the ^{4}He stage at the proper temperature.

For BOOM03 , thin ($1\mu m$) reflective infrared blocking filters were placed in front of the 18 cm^{-1} and 15 cm^{-1} filters in order to reduce excess emission possibly caused by heating of the filters. Room temperature radiation coming in through the window could heat the 18 cm^{-1} filter and 77 K (or hotter) radiation from the 18 cm^{-1} filter could heat the 15 cm^{-1} filter. Both cases could lead to excess optical load on the detectors and the ^{4}He stage. The impetus for adding these filter was that we noticed the ^{3}He and ^{4}He stages were overly sensitive to external optical load. This effect was most drastic when we made a test run with an 18 cm^{-1} filter which was highly emissive in the infrared. When we switched from a 77 K external load to 300 K, we found that the temperature of the ^{4}He stage rose by approximately 0.15 K and the ^{3}He stage temperature rose by 10 mK. As discussed earlier, the addition of these filters increased our ^{4}He hold time by approximately 25%.

During the B98 flight, the cryogenic system was still cold when the flight was terminated after 10 days. For BOOM03 , the addition of the infrared blocking filters on the 77 K and 1.65 K optical apertures increased the ^{4}He hold time by roughly 25% to about 18 days. During the pre-flight runs, we measured the LN_2 to have a hold time of about 16 days. This made the ^{3}He refrigerator the limiting factor, since it was able to keep the focal plane cold for about 13 days. For the BOOM03 flight, we added a telemetry command that would allow us to cycle the ^{3}He refrigerator during flight. During the BOOM03 flight, the ^{3}He ran out after 10.9 days. We were able to cycle the refrigerator and gain another 19 hours of data before the telescope was turned off at the end of day 13.

2.3 Optics

The BOOMERANG primary mirror is an off-axis parabola with a diameter of 1.3 m. It is 45° degrees off axis and has a focal length of 1280 mm. The primary feeds the secondary and tertiary mirrors which are kept at 1.65 K inside the cryostat. The primary mirror and the cryostat are mounted on the inner frame of the gondola which has an elevation range of 33° to 55°; the cryostat being level when the elevation is 45°. When BOOMERANG is pointed away from the sun the primary has a temperature of about −20° C. Radiation from the sky reflects off the primary mirror and enters the cryostat through a thin (50 μm) polypropylene

window which is near the prime focus. The radiation then passes through low pass filters mounted on the 77 K and 1.65 K stages which reject radiation with frequencies above 18 cm−1 and 15 cm^{-1} respectively [71].

The fast off-axis secondary and tertiary mirrors re-image the prime focus onto the focal plane correcting for aberrations induced by the primary. The secondary and tertiary are mounted in a box which has absorbing walls and baffles to prevent stray light from reaching the focal plane. An overview of the BOOMERANG optics can be seen in Figure 2.2. The secondary mirror is an ellipsoid, while the tertiary mirror is a paraboloid. They have effective focal lengths of 20 cm and 33 cm respectively. The surface shapes of these mirrors were optimized using Code V software [81] to provide diffraction limited performance at 1 mm over a $2^\circ \times 5^\circ$ field of view. These two mirrors and the primary mirror can be described by

$$z(r) = \frac{r^2}{R\left[1+\sqrt{1-(1+k)\frac{r^2}{R^2}}\right]} + Ar^4 + Br^6, \qquad (2.3.1)$$

with parameters R, k, A, B as in Table 2.1.

The re-imaging optics form an image of the primary mirror at the tertiary. Therefore, the tertiary acts as a Lyot stop for the system. The feed horn illumination spills over the edge of the tertiary and sees the 1.65 K blackbody inside the optics box. The tertiary is 10 cm in diameter which corresponds to an effective 85 cm diameter aperture on the 1.3 m primary. Under-illumination of the primary helps to control the sidelobe response.

Mirror	R (mm)	k	A (mm^{-3})	B (mm^{-5})
Primary	2560	-1.0	0.0	0.0
Secondary	363.83041	-0.882787413818	1.3641139×10^{-9}	1.8691461×10^{-15}
Tertiary	545.745477407	-1.0	4.3908607×10^{-10}	-3.2605391×10^{-15}

Table 2.1: Ideal parameters for the three BOOMERANG mirrors (equation n2.3.1)

2.4 Receiver

The BOOM03 receiver consists of 8 pixels, and each pixel has two detectors. Four of the pixels contain pairs of polarization sensitive bolometers (PSB's) operating with a band centered at 145 GHz. The two bolometers in a pair view orthogonal polarizations. The other four pixels are 2-color photometers operating with bands centered at 245 and 345 GHz. The photometers become polarization sensitive by placing a polarizing grid on the entrance aperture of the cryogenic feed horn. Both the PSB's and the photometers use corrugated feed horns.

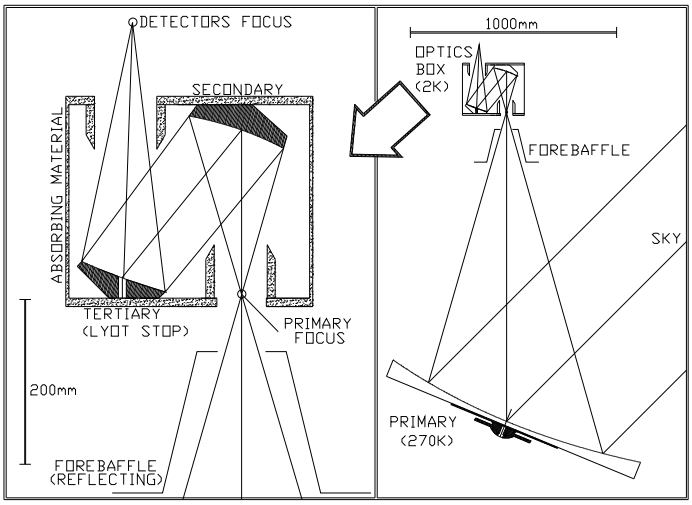

Figure 2.2: An overview of the BOOMERANG optics. Radiation from the primary reflects off the secondary, to the tertiary and then to the focal plane. The secondary and tertiary correct aberrations induced by the primary. They are kept at 1.65 K in a box coated with absorbing material. The tertiary acts as the Lyot stop for the system, controlling the illumination of the primary. Spillover off the edge of the tertiary sees a 1.65 K blackbody.

2.4.1 Detectors

In BOOM03 we used two types of silicon nitride micromesh bolometers. All of our detectors are fabricated at NASA's Jet Propulsion Laboratory. In the photometers, "spider web" bolometers are used. They were designed to operate in environments with high cosmic ray flux [83] and used in B98 . The absorber consists of a silicon nitride mesh which is covered in a layer of gold. Incident radiation heats the absorber and a Neutron Transmutation Doped (NTD) thermistor is used to measure this temperature change. Seven of the eight photometer bolometers were also used in B98 ; Table 2.2 lists the correspondence between B98 channel and BOOM03 channel.

The polarization sensitive bolometers are a variation on the original micromesh design [56]. Instead of a spider web design, the mesh is grid, however the grid is only metallized in one direction (see figure 2.4). This makes it sensitive to only one component of the incoming electric field. A pair of these with metallized directions oriented 90°apart are mounted with a 60 μm separation at the end of a corrugated feed structure. This allows for simultaneous intensity measurements in both polarizations at the same point on the sky through the same feed optics.

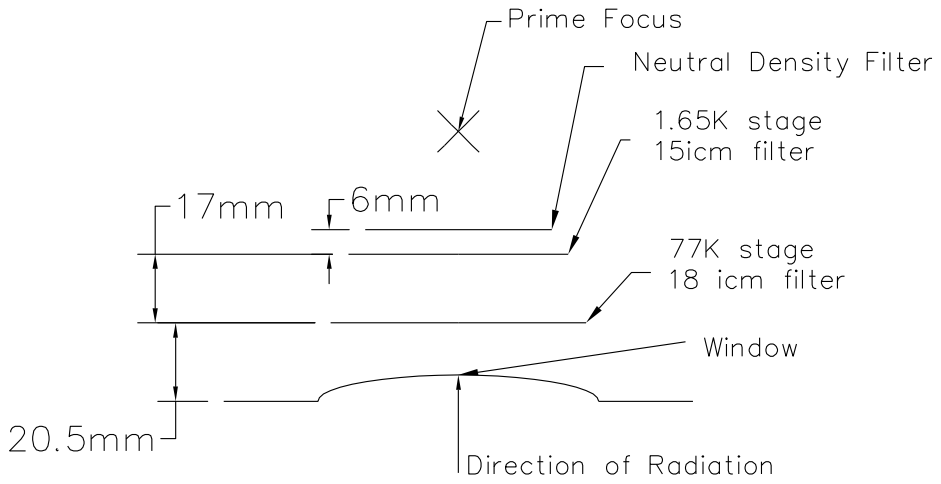

Figure 2.3: Schematic of the window and cold filtering inside the cryostat. Incoming radiation passes through window, the 18 icm filter (mounted at 77 K), the 15 icm filter (mounted at 1.65 K) and perhaps the neutral density filter (also at 1.65 K) before arriving at prime focus. The neutral density filter could be moved in and out of the beam; it was used to simulate a low background during lab testing.

2.4.2 PSB Feed Structure

In principle one can build a receiver without using any feed horns (e.g. CCD arrays or the 350 μm SHARC camera [31]) and let the mirrors decide the beam pattern. The primary advantages of the feed horns are that they control the illumination pattern on the mirrors (providing protection against sidelobe contamination) and that they protect against excess loading inside the cryostat.

Figure 2.5 shows the feed structure for a PSB pair. Light enters into a corrugated back-to-back feedhorn (mounted at 1.65 K), travels out across the thermal break and into the filter stack which is mounted on the front of the corrugated reconcentrating feed (mounted at 0.275 K). The filter stack consists of 4 filters in the following order: a Yoshinaga/Black-poly filter (which blocks infrared radiation above 1650 GHz), a 540 or 740 GHz lowpass, a 255 GHz lowpass and a 168 GHz lowpass. The last three lowpass filters are hot pressed metal mesh filters [71]. The 168 GHz filter decides the upper edge of the band and the lower edge of the band is set to 122 GHz by waveguide cut-off of the back-to-back feed. Metal mesh filters can sometimes have leaks above the cut-off (especially at the harmonics of the cut-off); this prompted the addition of the two extra metal mesh filters. The cut-off frequency of the extra filters is not that important; instead we need to make sure the leaks do not overlap. Once the radiation passes through the filter stack, it enters the reconcentrating feed which optimally couples to the

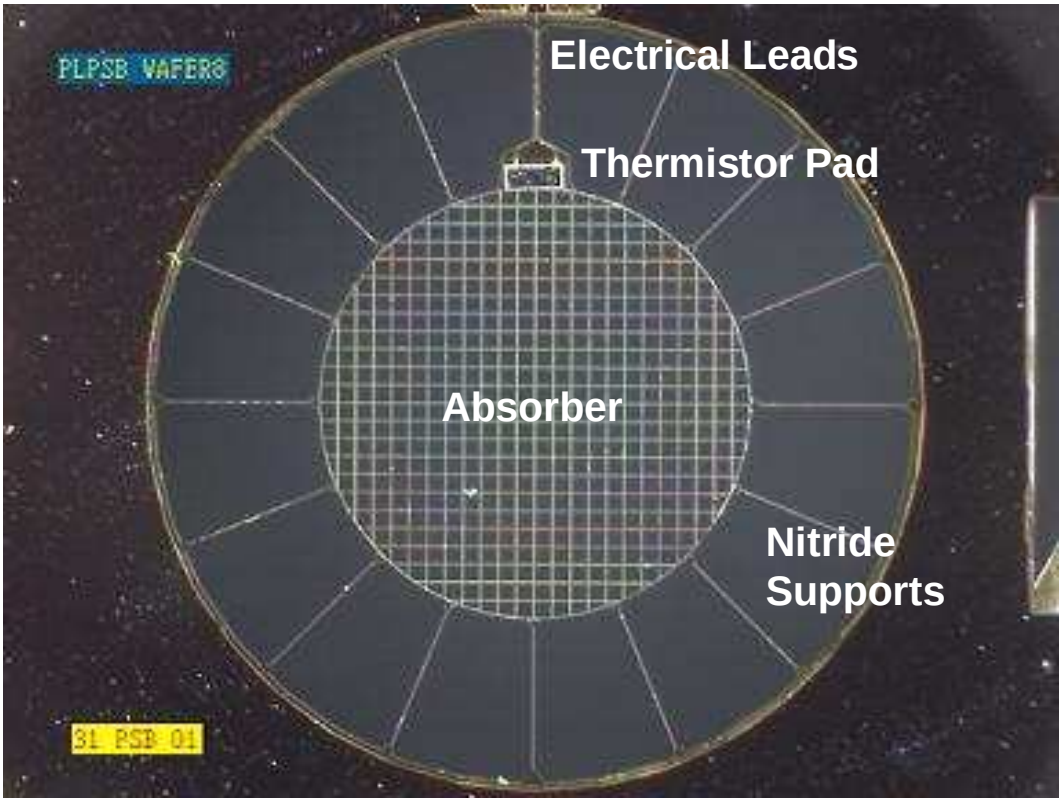

Figure 2.4: A Polarization Sensitive Bolometer. Photo courtesy of W. Jones.

pair of PSB's sitting at the exit aperture and separated by $60\mu m$.

Since the polarization discrimination is done at the exit aperture of the feed structure, the feed structure must be designed so that polarization is preserved as the radiation travels through [56]. Corrugated feeds have beam pattern which is symmetric when viewing a polarized source. A corrugated feed preserves the polarization of incident radiation. The back-to-back feed has a -11 dB Gaussian edge taper on the tertiary. Based on the effective primary illumination one would naively expect a beam full width half max (FWHM) of 11 arcminutes. The measured beams are $9' - 10'$ which agrees with physical optics calculations.

The gap between the exit aperture of the back-to-back feed and the entrance aperture of the reconcentrating feed is also an important consideration. The coupling between the feeds starts to diminish when the apertures are separated by more than 0.5 ". The filter stack is about 0.4 " thick leaving a maximum gap of 0.1" between the 0.275 K and 1.65 K stages. Thermal contraction shrinks the copper feeds, so one would expect the gap to expand when we cool down from room temperature. However, the Vespel legs which separate the 0.275 K stage from the

B98 channel	BOOM03 channel
B150A	B245X
B150B1	B245W
B150B2	B245Z
B220A2	B345W
B220B1	B345Z
B220B2	B345X
Dark B	B245Y
B400A1	Dark B

Table 2.2: Correspondence between bolometers used in both B98 and B00M03.

1.65 K stage have a significant thermal contraction which will pull the stages together (a contraction of roughly 0.04" for a 3" Vespel leg). During preparations for the early test runs, we set the room temperature distances between the stages to be 0.020" which most likely lead to a slight touch between the 1.65 K and 0.275 K stages. Diabolically it turns out that our ^{3}He refrigerator was strong enough so that the cold stage could cool to 0.290 K even with slight touch between the stages. We could not tell that the stages were touching until we made the gaps so small that the ^{3}He refrigerator could only cool to 0.350 K. In other words: **Mind the Gap!**

2.4.3 2-color Photometer

The 2-color photometer (Figure 2.6) design has evolved from the 3-color photometer of B98 which was derived from photometers used by SuZIE, MAX and the FIRP on IRTS. The feed horn is mounted on the ^{4}He stage while the photometer body is mounted on the 0.275 K stage. The photometer is made polarization sensitive by placing a polarizing grid in front of feed horn.

The photometer operates with bands centered at 245 GHz and 345 GHz. Each is fed by a back-to-back corrugated shaped feed which was designed to be single-moded from 180 GHz to nearly 400 GHz. In principle, the beams should be diffraction limited (6 arcminutes at 245 GHz and 4 arcminutes at 345 GHz) over this range. The edge illumination on the tertiary is -6.5 dB at 245 GHz and -15 dB at 345 GHz (for a single mode). Beam measurements and the optical efficiencies imply that the horn may have more than one mode at higher frequencies. The 345 GHz beam has been measured to be $\sim$ 7 arcminutes (Table 4.14, and the optical efficiency of the 345 GHz channels is $\sim$ 75% when compared to a single mode (Table 4.5). The entrance horn of the feed is designed to maximally couple to the re-imaging optics and the exit horn is designed to couple to the 0.5 inch light pipe inside the photometer body.

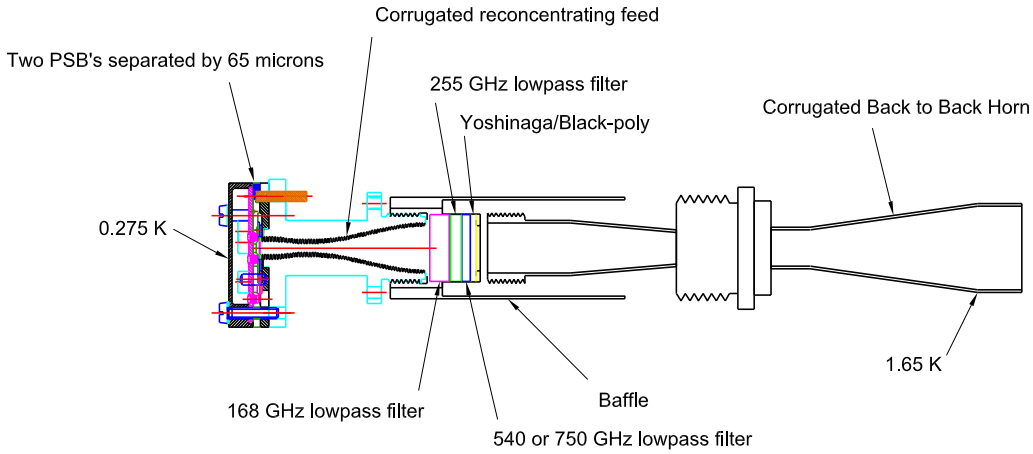

Figure 2.5: The PSB feed structure.

At the entrance to the photometer body is a high-frequency blocking filter with a cut-off at 420 GHz and a Yoshinaga/Black-poly filter to block leaks at higher frequencies. After the blocking filters, the radiation comes to a dichroic which is oriented at 22.5°to the axis of the light pipe. Radiation above 295 GHz is reflected off the dichroic toward to a 410 GHz low pass filter in front of the 345 GHz bolometer. Radiation below 295 GHz is passed through the dichroic and to a 360 GHz low pass filter in front of the 245 GHz bolometer. The low edge of the 245 GHz band is determined by the waveguide cut-off of the feedhorn. The 420, 410 and 360 GHz filters are hot pressed metal mesh filters. The bolometers are fed by shaped reconcentrating feeds which maximally couple to the light pipe and have an exit aperture of about the same size as the bolometer absorber.

The thermal gap for the photometers was not as well engineered as it was for the PSB's. Due to some modifications during testing, the gaps were about 0.15" for two of the photometers and 0.30" for the other two. This difference does not seem to effect the optical efficiency (Table 4.5).

2.5 Calibration Lamp

In order to track the calibration stability of the bolometers, a an infrared-emitting lamp was installed behind a 1 cm hole in the tertiary mirror. The calibration lamp for B98 had a spider web style similar to the bolometers.

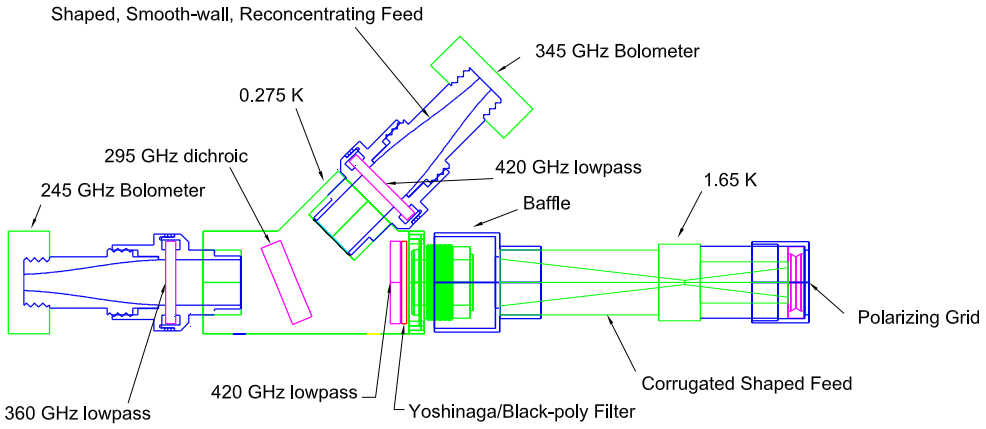

Figure 2.6: The photometer feed structure.

For BOOM03 , we used an NiCr coated sapphire chip from Haller-Beeman (http://www.haller-beeman.com/).

2.6 Readout Electronics

Because the telescope scans slowly in azimuth (1°/s), the detectors and readout electronics need to be stable from the bolometer thermal cutoff frequency ($\sim$ 10Hz) down to the time scale of a few scans ($\sim$ 10 mHz). To achieve this stability BOOMERANG employs an AC modulation/demodulation scheme which moves the signal bandwidth to well above the 1/f knee of the cold JFETS and the warm electronics.

The bolometers are voltage biased with a 143 Hz sine wave. Dual load resistors on each side of the bolometer (10 MΩ pairs for the photometer bolometers and 30 MΩ pairs for the PSB's) provide an approximate current bias. The load resistors are on the bolometer wiring module and therefore kept at 0.275 K. The bolometer signal then passes through an offset-matched dual JFET follower circuit on the 1.65 K stage. The signal from the JFETs has a low output impedance which decreases susceptibility to microphonics as the signal travels out of the cryostat. The JFETs are selected for low power dissipation and packaged by Infrared Laboratories (IR labs TIA). Figure 2.7 shows a diagram of the readout electronics.

The cold JFET signal then is passed out of the cryostat to a differential preamplifier stage which has a gain of 375 and is AC coupled in order to roll off the DC offset from the JFET stage. The output of the preamplifier is passed to a bi-quad bandpass filter which limits the bandwidth of the signal to 40 Hz. The sine

wave is then demodulated by multiplying the the filtered signal by a reference square wave. The demodulated signal is filtered with a 4-pole Butterworh low pass filter with a cutoff at 20Hz. This is the primary anti-aliasing filter for the Data Aquisition System (DAS). At this point, the signal is supposed to be proportional to the resistance of the bolometer, but as we discuss in section 4.4 parasitic capacitance can distort the meaning of this signal. This "DC" output is sampled at 5 Hz by the DAS. Because of the 16 bit resolution of the DAS, this resolution of this signal ($2-5$V) is bit-noise limited. In order to make the signal noise greater than the input noise of the DAS, we amplify the signal by a factor of 100 after highpass filtering with a cutoff of 16 mHz (5.6 mHz) for B98 (B00M03) (this problem could also be solved by having more bits in the A/D conversion). Theses AC-coupled signals are sampled by the DAS at 60Hz. For B00M03, we added extra anti-aliasing into the AC-coupling stage on the lock-in boards (see section 4.8 for more discussion).

The cold JFETs are the dominant noise source in the readout electronics chain contributing 8-10 $nV_{rms}/\sqrt{Hz}$ to total readout noise. The AC bias and warm readout electronics contribute less than 6 $nV_{rms}/\sqrt{Hz}$. Therefore, the white-noise level of the readout chain should be less than 12 $nV_{rms}/\sqrt{Hz}$.

The readout electronics also need to be stable on long time scales. The bias waveform and the warm readout are especially sensitive to 1/f noise. This is most often caused by thermal instability of the electronic components or bad electrical connections. The capacitors used on the AC waveform generator and the bi-quad bandpass filter need to be very stable. In B98 , polycarbonate film capacitors were used. For the BOOM03 flight we replaced some of the polycarbonate capacitors with ultra stable NPO capacitors, but found that the dominate source of 1/f was the trimpots which tune the resonate frequency of bi-quad bandpass filter (see section 4.8).

2.7 Rejection of RF and Microphonic Pickup

Bolometric signals can be contaminated by radio frequency interference (RFI) or microphonic pickup. RFI can dissipate heat in the bolometer's thermistor, while microphonic pickup can take place in the bolometer itself, or in the wiring inside the cryostat.

The BOOMERANG payload carries several microwave transmitters for communication with satellites and the ground station. The most worrisome transmitters are an ARGOS transmitter at 400 MHz and a 2.3 GHz TDRSS transmitter.

Figure 2.7 shows the three separate Faraday cages which protect the detectors from RFI. At 0.275 K the bolometers are placed in an integrating cavity which is electrically sealed except for the feed horn aperture and the readout wiring. The waveguide cutoff of the feed horn rejects long wavelength radiation. For

the BOOM03 photometer channels and all the B98 bolometers, there are 20 pF feed-through capacitors connecting the readout wires to ground. These filter RFI which tries to enter the cavity through the wiring. For the PSB's, an LC circuit is used with an inductance of 47pH and a capacitance of a few picoFarads.

The second Faraday cage is at 1.65 K. All signals traveling from the outside of the cryostat to the 1.65 K stage (and vice versa) pass through RF filters mounted on the 1.65 K stage. These filters are stripline cables potted in cast eccosorb (EV Roberts CR-124) and have significant attenuation above a few GHz. RF can also enter the cryostat through the window and travel through the optics path to the feedhorns. Since the optics box is sealed with aluminum tape, the only path to the detectors is through the feedhorns; where the waveguide cutoff prevents radio frequency signal from passing through.

The warm electronics reside in an RF tight box (Backpack) which forms an extension to the outer shell of the cryostat (the third Faraday cage). Between the Backpack and cryostat, the signal wires are run inside a stainless steel KF-40 hose which is electrically sealed on both ends. Indium was used to seal the connections to the KF-40 hose, and all joints were sealed with metal tape. Copper tape was found to provide the best rejection of RFI, but conductive adhesive aluminum tape was useful as well. We also placed ferrite RF chokes around the cables where they connect to the vacuum feedthrough on the cryostat. Amplified output signals exit the Backpack through in-line 37 pin d-connector filters (Spectrum Control part number SCI-56-735-005) on the way to the DAS.

Micromesh bolometers have a low suspended mass. This reduces microphonic response when compared to old-style composite bolometers. Care was taken to securely tie down the high impedance wires connecting the the bolometers to JFET follower stage as well as the bias wires which travel from the 1.65 K RF feedthrough to the bolometers. The 0.275 K wires were strapped down using nylon cord. Between 0.275 K and 1.65 K, low thermal conductivity 50 μm manganin wires were secured to the Vespel posts using teflon tape. Since the wires were a bit longer than necessary, there was some excess length which was covered in teflon tape and carefully aluminum taped to the cover of JFET box.

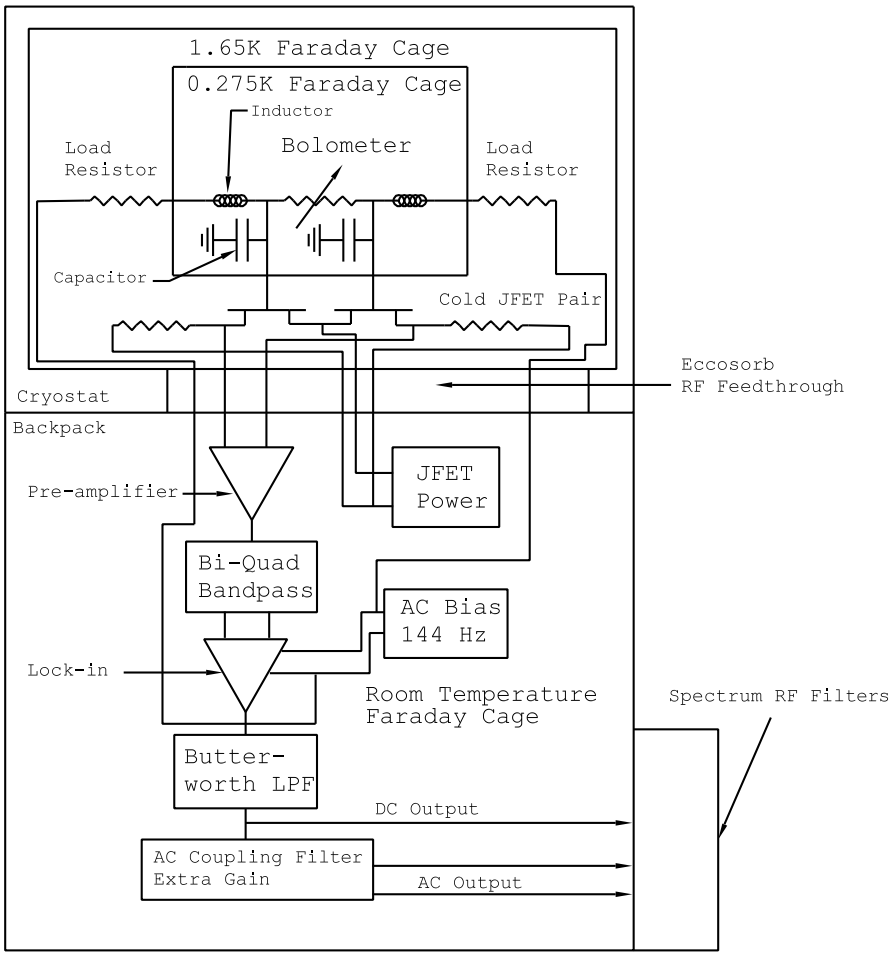

Figure 2.7: Diagram of the readout electronics. The AC waveform is generated in the backpack running into the cryostat to the bolometers. The voltage across the bolometer travels to the JFET stage at 1.65 K. The signals travel from the JFET stage back to the backpack where it is amplified and filtered before going through a lock-in amplifier. Manganin wires run between the 0.275 K stage and the 1.65 K stage, while stainless steel wires go between 1.65 K and 300 K. There are three stages of radio frequency (RF) filtering in the electronics chain. For the photometer bolometers, capacitive filters prevent RFI from entering into the integrating cavity. For the PSB's an LC circuit provide RFI protection. All signals going into and out of the 1.65 K stage pass through RF filters made from cast eccosorb (EV Roberts CR-124).

Chapter 3

BOOM03 focal plane optics design

The B98 optics were designed with 2 sets of 4 pixels with the centroids of each set separated by 3.5°. This was done so that different pixels would repeat observations of the same patch of sky on different time scales. The B98 CMB scans were 60°peak to peak. With this scan strategy we had approximately 330 samples per 7 arcminute pixel, which gives a sensitivity of 85 μK per pixel per detector (assuming a a CMB sensitivity of 200 μK $\sqrt{s}$). The main scan region was nearly 1700 sq. degrees.

Because the CMB polarization signal is $\sim 10\%$ of the temperature anisotropy signal, we need a higher sensitivity per pixel (10 μK per pixel is a good estimate). This requires an enormous increase in detector sensitivity or a smaller map. Since the sensitivty per detector for BOOM03 is similar to what we had in B98 , we chose to concentrate more than half of our observation time on a 120 sq. degree region in order to increase our sensitivity to C_ℓ^E (see chapter 8).

Since each detector is only sensitive to one polarization and sky rotation tilts the scans by only $\pm 11°$, we need to combine information from different channels to measure the Stokes parameters. Each PSB pairs can measure Q or U simultaneously in the same pixel; we need to consider at least three detectors to fully characterize the linear polarization of a pixel [20]. The photometer channels are each sensitive to only one polarization; to measure Q or U, we need to combine signals from different pixels. To avoid wasting integration time, it is best that the receiver pixels have as much overlap on the sky as possible.

In order to do this with smaller azimuth scans, we need place the pixels as close together as possible. The physical size of the elements in the focal plane limits the pixel spacing to 0.5°. Figure 3.1 shows the layout of the pixels in the focal plane and the orientation of the polarization sensitivity. The polarization orientations are distributed evenly over 180° to maximize our ability to discriminate between Q and U [20].

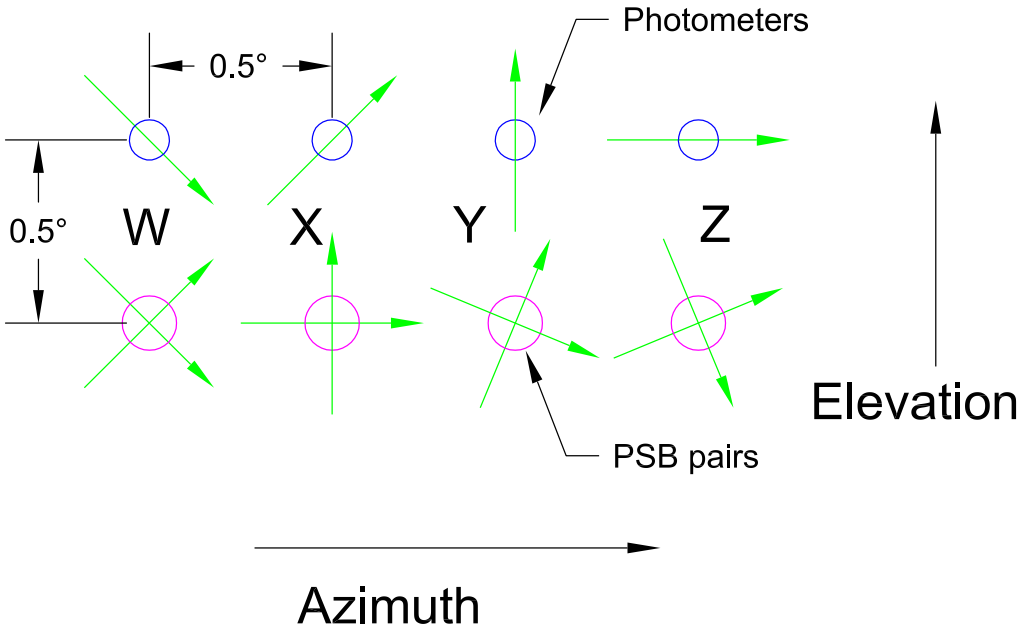

Figure 3.1: Focal Plane Schematic. 2-color photometers with band centers at 245 GHz and 345 GHz populate the upper row. Each photometer is only sensitive to one polarization. The lower row has 4 pairs of PSB's, each PSB pair is sensitive to both polarizations. The circles representing the pixels show relative beams sizes: 7' for both photometer channels and 9' for the PSB's. The green arrows through the circles show the orientation of the polarization sensitivity. The photometer and PSB rows are separated by 0.5° in elevation, while the pixels in a row are separated 0.5° in cross-elevation. W, X, Y, and Z correspond to channels names: for example a PSB pair would be B145W1 and B145W2, and in the photometer we have B245W and B345W.

3.1 Focus Positions

The location of the feed horns in the focal plane was determined by geometric ray tracing using Zemax (Focus Software, Inc.). The feed is pointed towards the center of the tertiary mirror; ideally the location of the feed horn is chosen so that its phase center is located at the point where the spot size (locus of the traced rays) is smallest. Figure 3.2, shows the spot diagrams at the optimal positions. In order to avoid having the PSB horns shadow the photometer horns, the final position of the feed horns was moved a few millimeters away from optimal. Figure 3.3 shows that the spot size does not change too much when the focus is moved a few millimeters. As long as the spot size is smaller than the Airy disk, performance will be nearly diffraction limited. Appendix A has a description of the conventions for mapping the focal plane in Zemax and table A.1 lists the optimal positions of the objects in the focal plane with respect to the tertiary center.

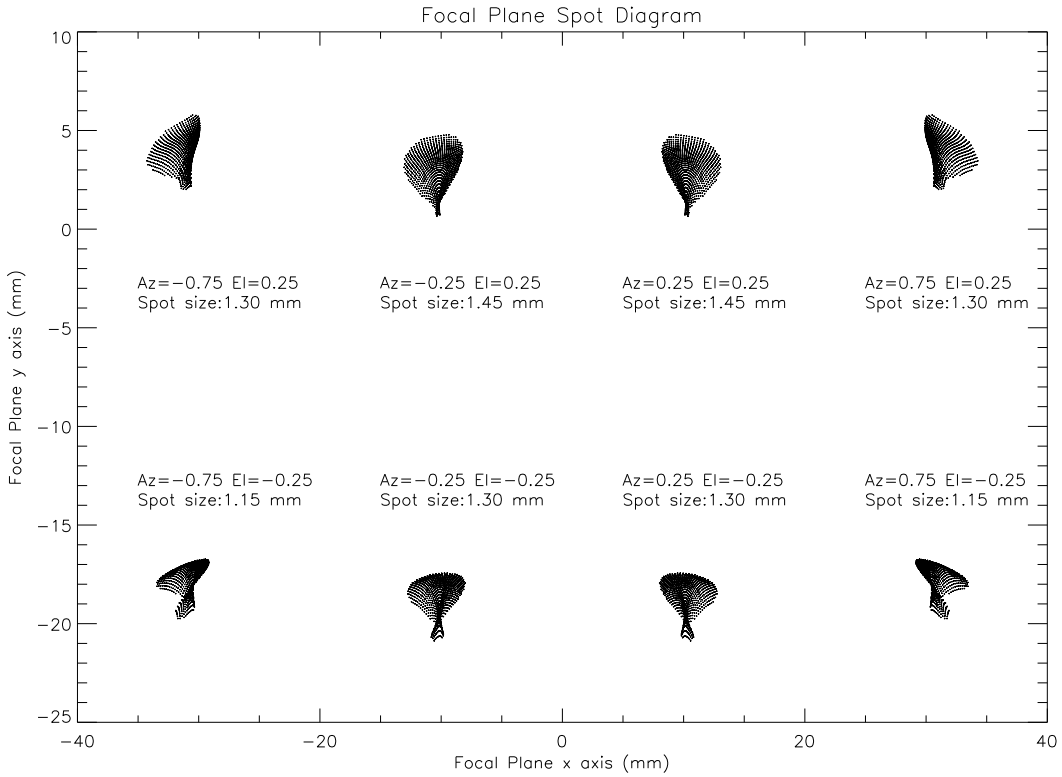

Figure 3.2: Spot diagrams for all the pixels. Each element is at its optimal distance from the tertiary. The focal length of the primary of 2560mm. Assuming the effective illumination has a diameter of 80 cm, the Airy disk has a radius of 8 mm at 145 GHz, 4.7 mm at 245 GHz, and 3.3 mm at 345 GHz.

3.2 Window and Filter Designs

As the beam passes from the primary mirror into the cryostat it passes through the polypropylene window, the 77K blocking filter, and the 1.65 K blocking filter. During ground tests a 1.65 K neutral density filter (ndf) is sometimes placed in the beam. Since the tertiary is supposed to determine the primary illumination, these apertures must be large enough so they do not to vignette the beam, but not too large, otherwise the cryogens would face an extra radiative load.

In B98 , the 2 sets of 4 pixels were arranged so that the window, blocking filters, and NDF could all be circular with one circle for each set of pixels. For BOOM03 , the 4×2 arrangement of the pixels and the set-up of the cryostat make it difficult to use circular apertures. The aperture sizes were determined by looking at the ray distributions at the surfaces where the window and filters were to be mounted. Allowances were made so that apertures would be large enough even if the mounting surfaces were shifted 2 cm relative to the primary mirror. This could happen if the position of cryogen tanks was changed due to tightening

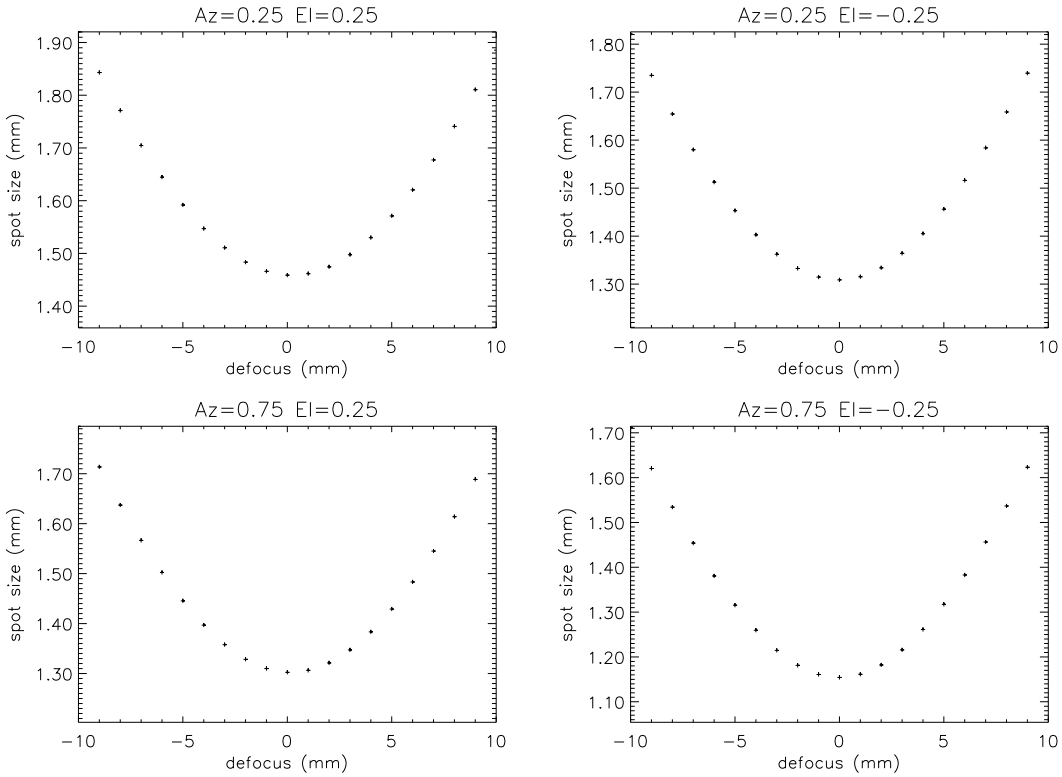

Figure 3.3: Spot size as a function of defocus.

or loosening of the supporting Kevlar ropes or if the entire cryostat was shifted relative to the primary mirror. Figure 3.4 shows the shapes of the apertures and the ray distribution across the aperture for the half the focal plane where the azimuth relative to the boresight is negative.

Mechanical constraints inside the cryostat and the limitations of the filter technologies required creative solutions. In B98 the blocking filters were metal mesh vacuum gap filters which consist of layers of thin film stretched on a steel ring (304L stainless is used, because its thermal contraction coefficient is small). A non-circular ring would have asymmetric stresses which could cause problems when the filters are cooled down. To solve this problem, we switched to hot-pressed filters which use the same metal mesh principles. Layers of thin film are heated and pressed together with plastic spacers to form the filter. These filters can then be cut to any shape. The NDF filter is a metallized filter; it has only 1 layer of mylar film mounted between two 304L stainless steel rings. a hot-pressed filter. We mounted the filter in a elliptical frame which could cause asymmetric stresses, leading to a degradation of performance. We tested a prototype by cooling it down

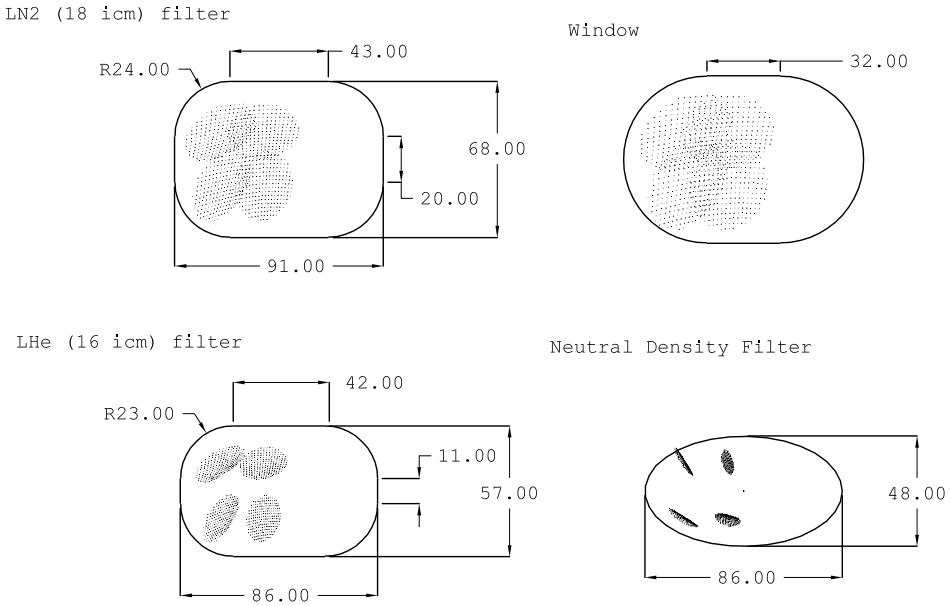

Figure 3.4: Ray distribution on the apertures in the case where the apertures are 2 cm closer to the primary than expected (aperture sizes are in millimeters). The distributions are only for the side of the focal plane where the azimuth is negative relative to the boresight. Azimuthal symmetry implies that the ray distribution for the other half of the focal plane can be found by reflecting the distribution about a vertical line at the center of the aperture.

to 90 K in a vacuum chamber. Looking into the chamber we did not observe any crinkling of the filter which would be indicative of asymmetric stresses.

The window is where the radiation enters into the cryostat. All that stands between success and terrible failure is a sheet of 50 μm thick polypropylene. In B98 the window consisted of two close circles each with a diameter of 73 mm. The BOOM03 window was designed to be like a race track consisting of two 73 mm diameter semi-circles separated by 32 mm. This design has the disadvantages of being non-circular and larger than the individual B98 windows. The non-circularity introduces asymmetric stresses which can be seen when the window is under vacuum. The larger size causes the window to make a larger depression under vacuum which could prove disastrous if the window stretches enough to come in contact with the 77K filter. The window never burst, but we always made a new window for each run of the cryostat.

Chapter 4

BOOM03 Pre-flight Instrument Characterization

Since balloon experiments carry a certain amount of risk, a second chance is never guaranteed. Also there is a good probability that the receiver will be damaged in the landing. With this in mind, it is of vital importance to understand the properties of the receiver before launch in order to be certain it will work as advertised and that one has all necessary information for post-flight analysis. In this chapter, we describe many of the techniques and results used in the characterization of BOOM03 receiver.

4.1 Introduction to Bolometry

A bolometer is basically just a thermometer. It absorbs incident radiation and heats up, causing the resistance to change. In the steady state, the relationship between the power dissipated in the bolometer and the thermal conductance to the temperature reservoir can be expressed as

$$Q + P_{elec} = \int_{T_0}^{T_{bolo}} G(T)dT, \tag{4.1.1}$$

where Q is the incident optical power, $P_{elec} = I_{bias}^2 R_{bolo}$ is the electrical power dissipated in the bolometer, T_{bolo} is the bolometer temperature, T_0 is the cold stage temperature, and $G(T)$ is the thermal conductance of the link between the cold stage and the bolometer. Variations in the input power lead to variations in T_{bolo},

$$\delta Q + \delta P_{elec} = G(T_{bolo})\delta T_{bolo} + C(T_{bolo})\frac{dT_{bolo}}{dt}, \tag{4.1.2}$$

where we have introduced the heat capacity $C(T_{bolo})$ and also assumed that $dG(T)/dT$ is small compared to the other terms. A change in bolometer

temperature results in a change in the bolometer resistance, leading to a change in electrical power on the bolometer. As discussed in section C.2, this change in electrical power (called electro-thermal feedback) can increase the effective thermal conductivity. This leads to a loss of sensitivity, and an increase in the bandwidth.

If an oscillating radiation intensity with angular frequency $\omega = 2\pi f$ has the form

$$Q = Q_0 + \Delta Q e^{i\omega t}, \tag{4.1.3}$$

the resulting bolometer thermal response is given by

$$T_{bolo} = T_{avg} + \Delta T e^{i\omega t}. \tag{4.1.4}$$

From equation C.2.6, we find the following solution for ΔT

$$\Delta T = \frac{\Delta Q}{G - \frac{dP_{elec}}{dT_{bolo}} + i\omega C}, \tag{4.1.5}$$

where the effective bolometer time constant is $\tau = C/(G - dP_{elec}/dT_{bolo})$ (the physical time constant of the bolometer is $\tau = C/G$). If $dP_{elec}/dT_{bolo} < 0$, then electro-thermal feedback reduces ΔT and the time constant.

The optical power absorbed by the bolometer is a function of the incident optical power, the spectral response of the bolometer and the optical efficiency of entire system. For a beam filling source we have

$$Q = \eta A \Omega \int B(\nu) e(\nu) d\nu, \tag{4.1.6}$$

where A is the aperture area, Ω is the beam solid angle, $e(\nu)$ is the normalized spectral response of the telescope), η is the spectral efficiency (i.e. $\eta e(\nu)$ is the actual spectral response), and $B(\nu)$ is the spectrum of the input source.

Since we actually measure bolometer voltage, the voltage responsivity is important,

$$\Delta V_{bolo} = S \Delta Q. \tag{4.1.7}$$

where S (Volts/Watt) is the voltage responsivity of the detector to a change in optical power. This is derived in section C.2 to be

$$S = \frac{dV_{bolo}}{dT_{bolo}} \frac{dT_{bolo}}{dQ} = \frac{dR_{bolo}}{dT_{bolo}} \frac{dV_{bolo}}{dR_{bolo}} \frac{1}{G - \frac{dP_{elec}}{dT_{bolo}} + i\omega C}. \tag{4.1.8}$$

The responsivity with respect to CMB fluctuations can be written as

$$\frac{dV_{bolo}}{dT_{cmb}} = S \eta A \Omega \int d\nu \; e(\nu) \frac{dB_\nu}{dT}\bigg|_{T=2.73K}, \tag{4.1.9}$$

where dB_ν/dT is the derivative of the Planck blackbody spectrum.

The bolometer noise is the sum of contributions from amplifier noise, Johnson noise, phonon noise, and photon noise. The amplifier noise is naturally expressed as a noise voltage. For a resistor, the Johnson noise term is also naturally a noise voltage

$$e_{Johnson} = \sqrt{4kTR}, \tag{4.1.10}$$

with units $V/\sqrt{Hz}$ and T and R are the temperature and resistance. However, bolometers are fundamentally dynamic. Johnson noise dissipates power in the bolometer leading to changes in the bolometer temperature. Mather [79] shows that the effective Johnson noise contribution must be modified,

$$e'_{Johnson} = \sqrt{4kTR}\frac{1+i\omega\tau}{i\omega\tau + \frac{2R}{R+Z}}, \tag{4.1.11}$$

where $\tau = G/C$ and $Z = dV_{bolo}/dI_{bias}$ is the dynamical impedance.

The phonon and photon noise terms are naturally calculated in terms of a Noise Equivalent Power (NEP) with units $W/\sqrt{Hz}$. In the equilibrium case (see Mather [79] for detailed calculation of the non-equilibrium case), the phonon contribution to the NEP is

$$NEP_{phonon} = \sqrt{4kT^2G}. \tag{4.1.12}$$

The photon noise can be written as function of radiation frequency

$$NEP_{photon}(\nu) = \sqrt{2Q(\nu)h\nu}\left(1 + \frac{\eta e(\nu)\epsilon(\nu)}{e^{h\nu/kT}-1}\right), \tag{4.1.13}$$

where $Q(\nu)$ is the spectral density of absorbed radiant power, $\eta e(\nu)$ is the spectral response of the system, and $\epsilon(\nu)$ is the emissivity of the source [79].

The NEP's are related to noise voltage by the responsivity

$$NEP_i = \frac{e_i}{S}, \tag{4.1.14}$$

and the total NEP of the bolometer is the sum of all noise components

$$NEP^2_{tot} = NEP^2_{phonon} + NEP^2_{photon} + NEP^2_{Johnson} + NEP^2_{amp}. \tag{4.1.15}$$

The Noise Equivalent Temperature (NET) has units of $K\sqrt{s}$. It represents the uncertainty in the amplitude (temperature) of a signal which has been observed for one second, or the signal required to have a signal-to-noise ratio equal to one with one second of observation. In general, the uncertainty is

$$\delta T = \frac{NET}{\sqrt{t_{obs}}}, \tag{4.1.16}$$

where t_{obs} length of observation. The NET with respect to CMB anisotropies is calculated as

$$NET = \frac{1}{\sqrt{2}} \frac{e_{bolo}}{dV_{bolo}/dT_{cmb}}, \tag{4.1.17}$$

where e_{bolo} is the total voltage noise of the bolometer in $V/\sqrt{Hz}$, dV_{bolo}/dT_{cmb} is the calibration with respect to CMB anisotropies and the factor of $1/\sqrt{2}$ is because one second of integration time corresponds to 0.5 Hz of bandwidth.

4.2 Receiver Model

Given the thermal conductivity G_0 (defined at the base temperature, T_0), the spectral normalization η, and spectral response $e(\nu)$, we can calculate some of the intrinsic parameters of the receiver. With these parameters and the value of $R(T)$ for the thermistor, it is possible to calculate the bolometer's expected responsivity and noise for a given optical load. Table 4.1 summarizes the results of these calculations.

4.3 Load Curves

Load curves contain a wealth of information about the bolometers and and the conditions under which they operate. The most important things which can be learned are the optical power incident on the bolometer, the optical efficiency of system, and the responsivity of the bolometer to changes in power. From this an independent value of the lab calibration can be inferred.

Many authors have gone described bolometer theory in great detail especially the relationship between the bolometer properties and loadcurve data [55, 73, 79, 80]. Here we describe some of the necessary methods for relating loadcurve data to bolometer properties.

4.3.1 R(T)

Our bolometers use NTD Germanium thermistors which have a characteristic temperature dependence

$$R_{bolo}(T_{bolo}) = R_0 e^{\sqrt{\frac{\Delta}{T_{bolo}}}}, \tag{4.3.1}$$

with $T_{bolo} = T_0 + \delta T$, where T_0 is the temperature of the cold stage, and δT is the change in temperature caused by the bias current and incident radiation. For our detectors, R_0 ranges from approximately $10 - 300\ \Omega$ and Δ goes from from $30 - 80\ K$. At $0.3\ K$ the bolometer resistance is usually $5 - 10\ M\Omega$. Knowing $R(T)$ is vital to calculating detector properties especially the optical load and G.

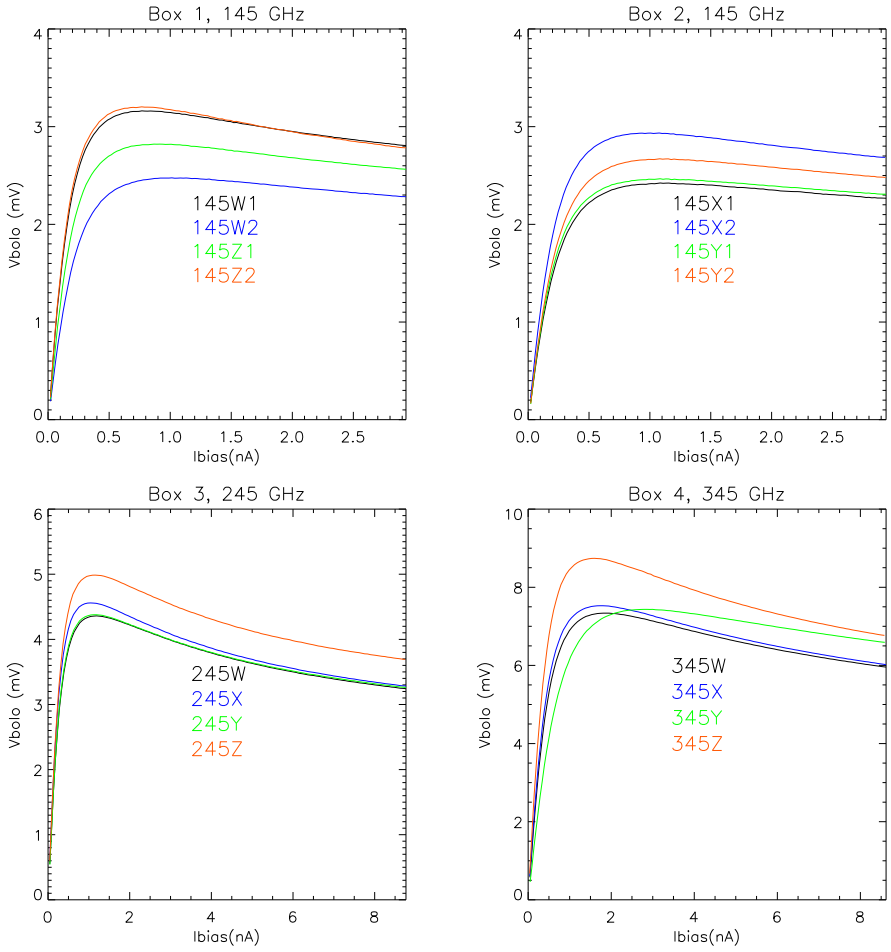

Figure 4.1: Plot of raw bolometer voltage versus bias current from loadcurves taken with an external liquid nitrogen load (77 K) and the neutral density filter (ndf) in the beam. The ndf transmission is 1.5%; therefore, the effective load in this case is approximately 1.2 K. The cold stage temperature was 0.275 K.

We made measurements of $R(T)$ by taking dark loadcurves at temperatures from 0.285 K to 1.0 K. $R(T)$ is then determined by extrapolating R_{bolo} to zero bias current, or by fitting a line to the first part of the loadcurve where R_{bolo} is nearly constant. The resulting data is fit to

$$\log(R_{bolo}(T)) = \log(R_0) + \sqrt{\frac{\Delta}{T}} \tag{4.3.2}$$

in order to find R_0 and Δ.

4.3.2 Deriving Bolometer Parameters from Load Curves

Raw loadcurve data consists of the bias voltage and the output bolometer voltage. Our load curves our done using a DC ramp generator. DC loadcurves are preferable because phase shifts caused by parasitic capacitances can contaminate AC loadcurves. From this data, we can directly calculate the dynamic impedance (Z), the responsivity S, and the thermal conductivity (G)

$$Z = \frac{dV_{bolo}}{dI_{bias}}, \tag{4.3.3}$$

$$S = \frac{1}{2I}\frac{Z/R_{bolo}-1}{Z/R_{load}+1}, \tag{4.3.4}$$

$$G = -\frac{dR_{bolo}}{dT_{bolo}}R_{bolo}^{-1}P_{elec}\frac{R_{bolo}+Z}{R_{bolo}-Z}, \tag{4.3.5}$$

showing that only G depends on knowing R(T) precisely.

The thermal dependence of G can be parametrized by the two numbers g_0 and β with

$$G(T) = g_0(\frac{T}{T_0})^{\beta}. \tag{4.3.6}$$

Using equation 4.1.1, we find

$$Q + P_{elec} = g_0\int_{T_0}^{T_{bolo}} dT(\frac{T_{bolo}}{T_0})^{\beta}, \tag{4.3.7}$$

$$= g_0\frac{T_{bolo}^{\beta+1}-T_0^{\beta+1}}{T_0^{\beta}(\beta+1)}. \tag{4.3.8}$$

In a load curve, only P_{elec} is changing, so if we take the derivative of both sides with respect to T, we get

$$\frac{dP_{elec}}{dT} = g_0(\frac{T}{T_0})^{\beta}. \tag{4.3.9}$$

If we have knowledge of the bolometer's $R(T)$, we can extract T_{bolo} from R_{bolo}. Then we can calculate dP_{elec}/dT and fit for g_0 and β.

Armed with knowledge of $G(T)$, $R(T)$, and P_{elec} we can in principle calculate Q using 4.1.1. In principle, we can calculate Q at every point of the load curve, and the value should be the same at every point. In practice this does not work very well. Part of the reason could be due to the "electric field effect". This effect is dependent on the NTD thermistor material and causes the bolometer resistance to also be a function of bias voltage [48],

$$R_{bolo} = R_0\exp\left(\sqrt{\frac{\Delta}{T}} - \frac{BV}{T^{m+1}}\right). \tag{4.3.10}$$

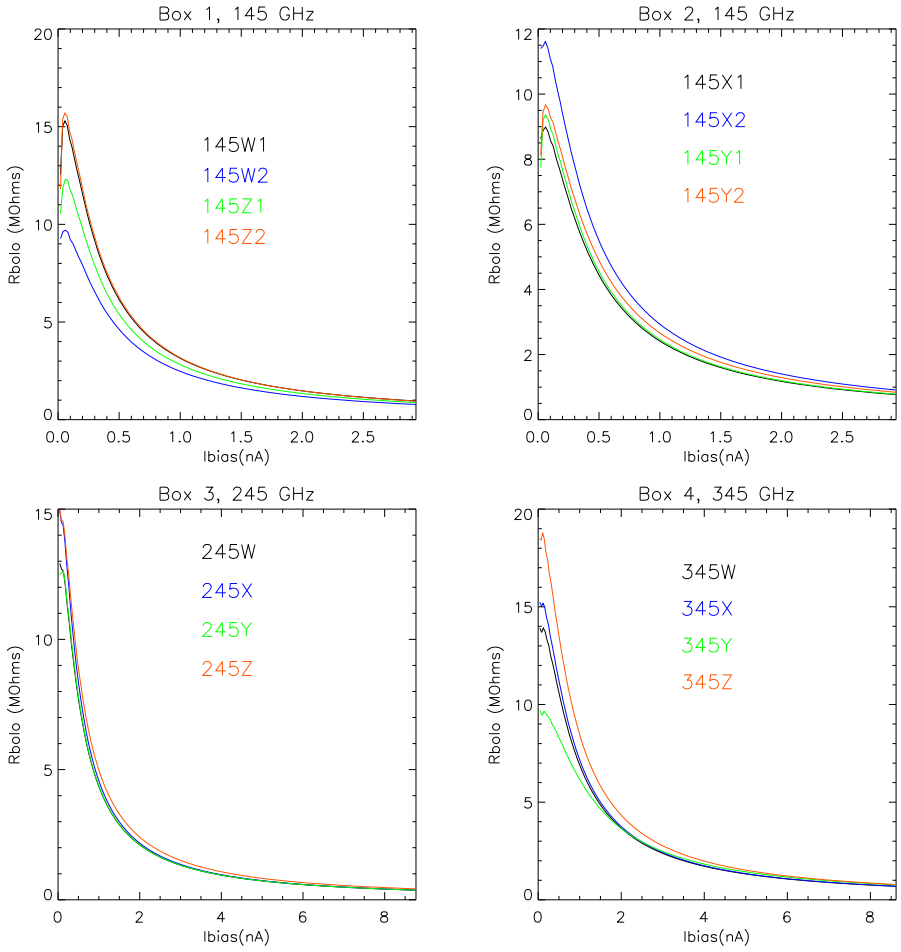

Figure 4.2: Plot of bolometer resistance versus bias current from loadcurves taken with a liquid nitrogen load (77 K) and the neutral density filter (ndf) in the beam. Note that the apparent peaks at low bias current are not really peaks but due to noise at low bias. The cold stage temperature was 0.275 K.

Also, this method is very sensitive to how well $R(T)$, $G(T)$ and T_0 are known. An error in these numbers could throw off the balance needed for the Q vs. I_{bias} curve to be flat. Better methods have been developed which can calculate Q using likelihood methods to simultaneously estimate g_0, β and Q once $R(T)$ is known [106].

If one is able to calculate the Q for a given load, then one can easily calculate the spectral normalization by

$$\eta = \frac{Q}{A\Omega \int d\nu \; e(\nu) B_\nu(T_{load})} \tag{4.3.11}$$

A more robust method for determining the optical efficiency is to take

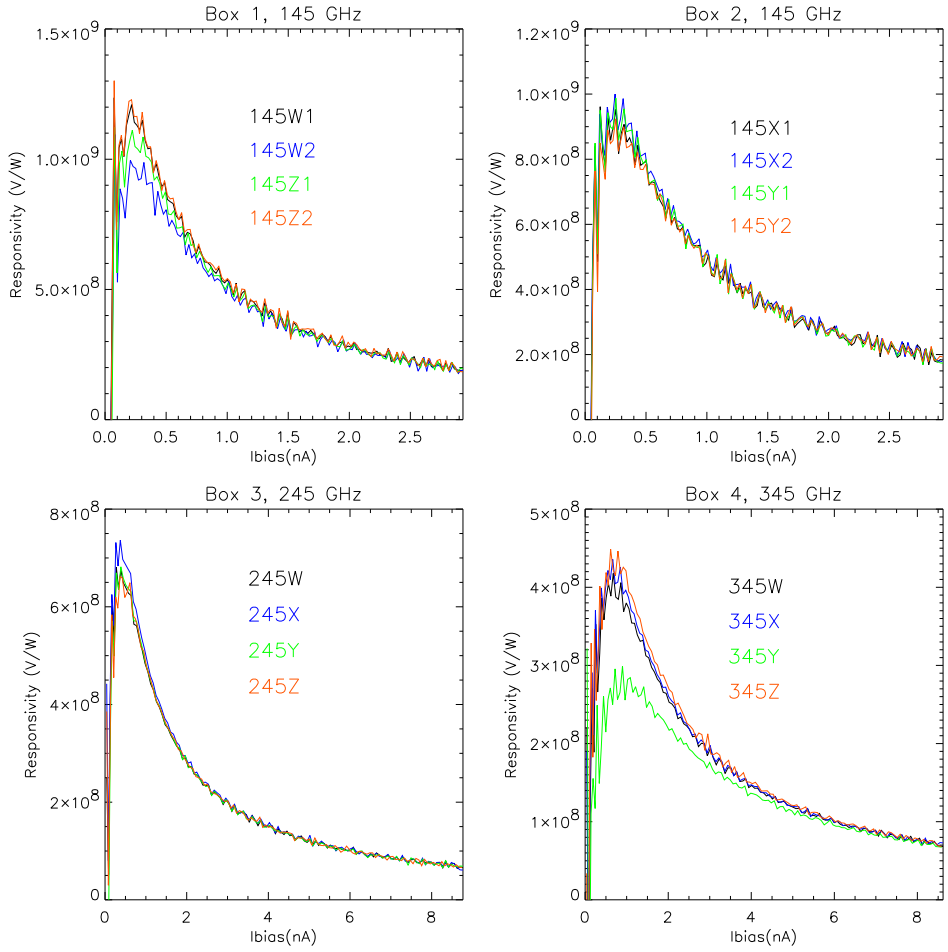

Figure 4.3: Plot of DC voltage responsivity versus bias current from loadcurves taken with a liquid nitrogen load (77 K) and the neutral density filter (ndf) in the beam. The cold stage temperature was 0.275 K.

loadcurves with 2 different optical loads. If the "electric field effect" is not significant, we can assume that equal R_{bolo} implies equal temperature and equal input power,

$$P_{elec}(I_{bias1}) + Q^{load1} = P_{elec}(I_{bias2}) + Q^{load2}, \tag{4.3.12}$$

where $R(I_{bias1}) = R(I_{bias2})$. By plotting P_{elec} vs. R_{bolo} for two different loads, we can read off the difference in incident optical power:

$$\Delta P = P_{elec}(I_{bias1}) - P_{elec}(I_{bias2}) = Q^{load2} - Q^{load1}. \tag{4.3.13}$$

We can check for the "electric field effect" by making sure that ΔP is constant over the range where the R_{bolo} values overlap.

From this data, we can calculate the spectral normalization

$$\eta = \frac{\Delta P}{A\Omega \int d\nu \; e(\nu)(B_v(T_{load2}) - B_v(T_{load1}))}, \tag{4.3.14}$$

where we set $A\Omega = \lambda^2_{center}$ (λ_{center} is the central wavelength in the single-mode approximation) and the spectral response $e(v)$ was determined using a Fourier Transfrom Spectrometer (section 4.5). When operating with loads in the Rayleigh-Jeans regime we can simplify this to

$$\eta = \frac{\Delta P}{\lambda^2_{center} \Delta T k \int d\nu \; \frac{e(\nu)\nu^2}{c^2}}, \tag{4.3.15}$$

where k is Boltzmann's constant and we expect a signal from one polarization only.

Using this power difference method, one can also calculate the transmission of the neutral density filter (ndf). Assuming the attenuation of the filter is independent of frequency, the transmission can be measured by comparing power differences measured with the ndf out of the beam (up) and power differences measured with the ndf in the beam (down):

$$\Delta P_{ndfup} = \eta \Delta T_{ndfup} \lambda^2_{center} k \int d\nu \; \frac{e(\nu)\nu^2}{c^2}, \tag{4.3.16}$$

$$\Delta P_{ndfdown} = \eta_{ndf} \eta \Delta T_{ndfup} \lambda^2_{center} k \int d\nu \; \frac{e(\nu)\nu^2}{c^2}, \tag{4.3.17}$$

$$\eta_{ndf} = \frac{\Delta P_{ndfdown}}{\Delta P_{ndfup}} \frac{\Delta T_{ndfup}}{\Delta T_{ndfdown}}. \tag{4.3.18}$$

4.3.3 Load Curve Data

In order to characterize our receiver, we took load curves under a wide variety of conditions. We used 4 different loads: liquid nitrogen (77K), liquid oxygen (90K), ice water (273K), and room temperature (285-300K). For each load, we did load curves with and without the ndf in the beam. The ndf up load curves were used to measure the optical efficiency of the cold optics and detectors, while the ndf down load curves are used to characterize the detectors under more realistic flight loading conditions. The ndf transmission is roughly $1.5\% - 1.8\%$ (Table 4.6) and the ndf down load curves have roughly 50 times more voltage responsivity. Figures 4.1, 4.2 and 4.3 respectively show the bolometer voltage, resistance, and voltage responsivity as a function of bias current. for ndf down loadcurves with a 77K load (which is effectively a 1.2K Rayleigh-Jeans load). This is somewhat smaller than the expected flight load; we expect a flight load $T_{RJ} \geq 5$ K as shown in table 4.1. A room temperature ndf down load may have been more accurate. The 77K ndf down data is presented because the room temperature ndf down

loadcurves were taken with a larger spacing between bias levels, which makes it hard to make a good calculation of the DC responsivity. For an estimate the responsivity change between a 77K ndf down and a room temperature ndf down load see Figure 4.6. Table 4.2 shows the properties of the bolometers at peak voltage responsivity for the 77K ndf down load.

As described in the previous section, we can use power differences to measure the optical efficiency of our system and the ndf transmission. Measuring the power differences is a bit of a black art. Besides the electric field effect, the measurements can be contaminated by drifting temperatures on cold stage or a drift in the temperature of the optical loads. One must also measure the loadcurves to a high enough bias current so that the two loads will have overlapping values of R_{bolo}.

With our 8 sets of loadcurves (table 4.3) we can take 6 useful power differences (table 4.4). The optical efficiency can be calculated from the measured $P^u_{77K} - P^u_{90K}$ and $P^u_{273} - P^u_{Room}$ power differences. The ndf transmission can be calculated by combining any of the 4 ndf down power differences and either of the 2 ndf up power differences. Using all combinations give a check on systematic errors.

Figure 4.4 shows the various power differences for channel B145W2. With the exception of the $P^u_{273} - P^u_{Room}$ case, the curves are relatively flat. For each load we took 3 loadcurves, so for each pair of loads there are 9 difference curves. For each difference curve, we take the average of the data which is to the left of the vertical line in Figure 4.4, then we calculate the power difference as the average of the results from the 9 curves. In order to gauge the errors, two methods were employed. One was to use the standard deviation of the 9 difference curves as the error. The second method was to take the standard deviation of all the points in a single power difference curve, and then average these 9 standard deviations. The errors calculated by these 2 methods are roughly the same and correspond to a 5% error on the final optical efficiencies and ndf transmission values.

Table 4.5 shows the measured spectral normalizations and optical efficiencies. The spectral normalization is calculated using the measured frequency bands (where the highest point is normalized the unity). The optical efficiency is calculated assuming flat bands defined by the half power points from the FTS measurments (Figure 4.9): 125-165 GHz for the 145 GHz channels, 210-280 GHz for the 245 GHz channels and 295-395 GHz for the 345 GHz channels. This calculation assumes the channels are single moded. The 345 GHz channels have a very high optical efficiency which could be due to the presence of an extra mode. Only the $P^u_{77K} - P^u_{90K}$ measurement was used because the $P^u_{273} - P^u_{Room}$ data gives an efficiency which is unphysically high. Normally the 2 methods agree pretty well (at least in the lab in Santa Barbara). The results from the $P^u_{273} - P^u_{Room}$ power difference would be consistent if the load temperature was higher than what we thought it was.

Table 4.6 shows calculations of the ndf transmission using 4 different ndf down power differences and the $P^u_{77K} - P^u_{90K}$ power difference. The ndf was also measured

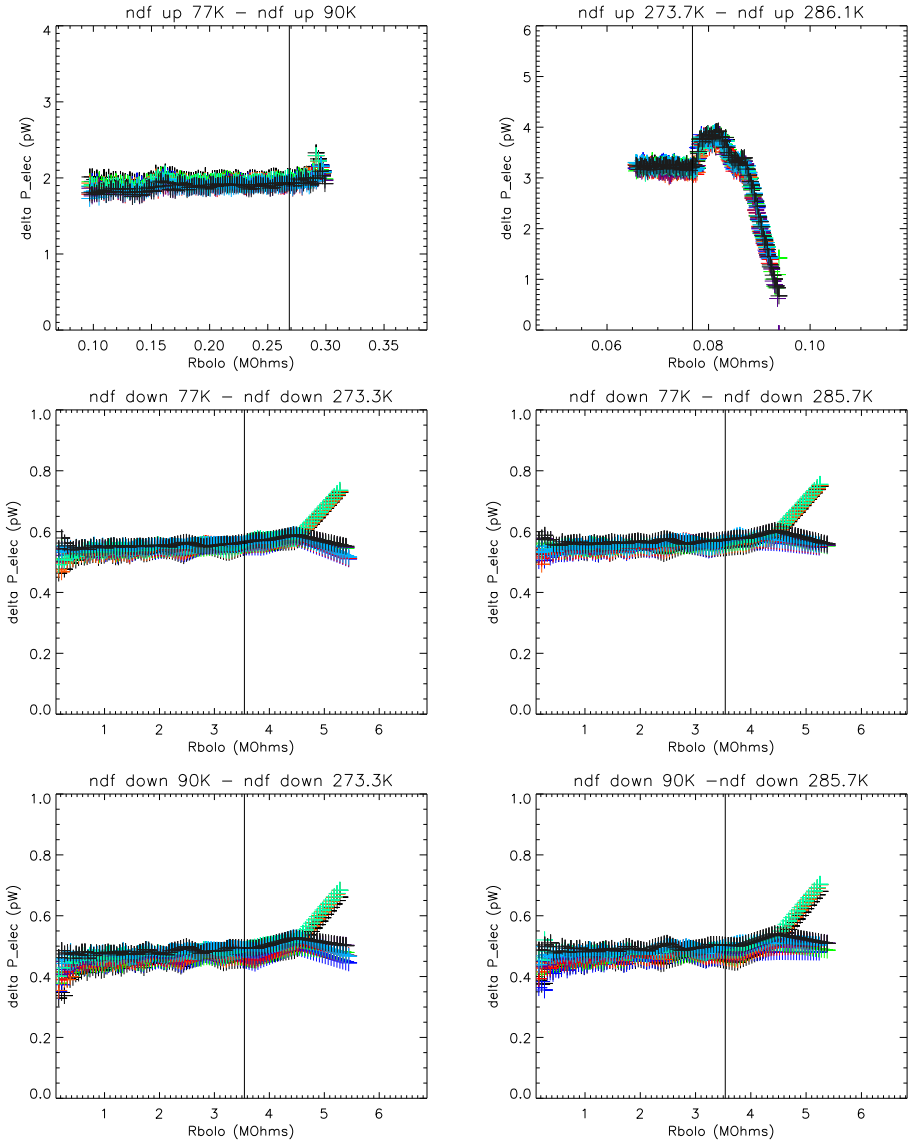

Figure 4.4: Plots of the P_{elec} difference betweens various loads for channel B145W2. For each load we took 3 loadcurves, so for each pair of loads there are 9 individual differences. Data to the left of the vertical line was used for the power difference analysis. For the individual differences, we average all the data left of the vertical line. The final number for the power difference is calculated as the average of the individual differences.

at room temperature to have a transmission of 1.5% at 150 GHz using a Gunn oscillator as a source and a Gunn diode as a detector (in good agreement with the data presented here). Previous cold measurements put the ndf transmission between 2.0% and 2.5%. For the 245 GHz and 345 GHz channels, the results are

pretty consistent across the focal plane. At 145 GHz, it is pretty obvious that the ndf transmission seems to decrease as we move from the W PSB channels to the Z PSB channels. Nonetheless, one can quote an average for each frequency band: 145 GHz = 1.58%, 245 GHz = 1.45% and 345 GHz = 1.41%.

It is possible that addition of the $1\mu m$ infrared blockers had an effect on this (It was not present when previous measurements were made.). Without the infrared blockers, it is possible that the 77 K and 1.65 K filters were heated by incoming radiation. This means that the internal contribution to optical power could differ depending on what the external load was. Excess emission could also heat the ndf causing the ndf to have a load dependent contribution emission. Such differential emission could cause excess signal in the power difference measurements and lead to a higher measured transmission for the ndf.

Channel → Parameter ↓	145 GHz	245 GHz	345 GHz	Units
Center Freq	146	241	345	GHz
Bandwidth	44	72	120	GHz
Beam FWHM	9	6.5	7	arcminutes
G_0	21	65	160	pW/K
Opt Eff	0.250	0.330	0.491	
Q	0.8	1.8	6.1	pW
Q_{CMB}/Q	0.113	0.032	0.006	
Q_{atmos}/Q	0.021	0.169	0.423	
Q_{prim}/Q	0.357	0.333	0.242	
Q_{filt}/Q	0.510	0.466	0.330	
T_{RJ}	5.2	5.5	7.5	K
P_{elec}	0.8	2.7	6.6	pW
G_{phys}	27	75	188	pW/K
G_{eff}	37	95	241	pW/K
T_{bolo}	0.346	0.342	0.352	K
R_{bolo}	7.0	7.4	6.3	MΩ
S_{bolo}	9.0	5.5	3.2	10^8V/W
Time Constant (τ)	48	20	8	ms
V_{bias}	22.3	16.4	27.0	mV
NEP	2.08	3.62	6.93	$10^{-17}W/\sqrt{Hz}$
NEP_{photon}	1.23	2.40	5.29	$10^{-17}W/\sqrt{Hz}$
NEP_{phonon}	1.12	1.91	3.07	$10^{-17}W/\sqrt{Hz}$
$NEP_{johnson}$	0.89	1.30	2.15	$10^{-17}W/\sqrt{Hz}$
NEP_{amp}	0.87	1.42	2.45	$10^{-17}W/\sqrt{Hz}$
NEP_{bolo}/NEP_{blip}	1.2	1.0	0.7	$10^{-17}W/\sqrt{Hz}$
NET_{cmb}	164	289	656	$\mu K\sqrt{s}$
NET_{RJ}	97	78	60	$\mu K_{RJ}\sqrt{s}$
NET_{inst}	58	145	328	$\mu K\sqrt{s}$
Voltage noise	18.7	19.9	21.8	$nV/\sqrt{Hz}$

Table 4.1: Model for the BOOM03 bolometers (parameters calculated by W. Jones). The parameters are derived using data from the pre-flight characterization of the detectors and estimations of the in-flight optical load. The expected optical load is the sum of the expected contributions from atmospheric emission, the primary mirror and the internal filters. G_0 ($G(T_0)$) comes from loadcurve data. This requires knowledge of the thermistor's $R(T)$, which can be derived from loadcurves taken at different base temperatures. The center frequency and bandwidth come from measurements taken with a Fourier Transform Spectrometer. The optical efficiency is calculated using the bolometer's spectral response and loadcurve data. With these numbers, it is possible to calculate the bolometer's responsivity and noise.

Channel	$V_{bias}(mV)$	$I_{bias}(nA)$	$V_{bolo}(mV)$	$R_{bolo}(M\Omega)$	$S(10^8 V/W)$
B145W1	15.4	0.22	2.4	11.1	12.0
B145W2	14.0	0.21	1.6	7.8	9.9
B145X1	15.0	0.23	1.6	7.0	9.6
B145X2	16.9	0.25	2.1	8.6	10.0
B145Y1	15.4	0.23	1.7	7.3	9.0
B145Y2	15.0	0.23	1.8	7.7	8.8
B145Z1	15.4	0.22	2.1	9.3	11.1
B145Z2	15.4	0.22	2.5	11.3	12.3
B245W	10.0	0.35	3.4	9.3	6.6
B245X	11.0	0.37	3.8	10.1	7.4
B245Y	11.2	0.39	3.5	9.2	6.8
B245Z	11.2	0.37	3.9	10.7	6.6
B345W	21.0	0.74	6.3	8.6	3.9
B345X	20.0	0.66	6.4	9.6	4.3
B345Y	24.0	0.90	5.9	6.5	2.9
B345Z	24.0	0.79	8.1	10.2	4.4

Table 4.2: Properties of the bolometer at peak voltage responsivity for a 77K ndf down load curve ($T_{RJ} \sim 1.2K$).

Load Temperature	ndf state	symbol
Room Temperature	up	P^u_{Room}
273 K	up	P^u_{273K}
90 K	up	P^u_{90K}
77 K	up	P^u_{77K}
Room Temperature	down	P^d_{Room}
273 K	down	P^d_{273K}
90 K	down	P^d_{90K}
77 K	down	P^d_{77K}

Table 4.3: List of loadcurves, which can be used for power difference measurements.

ndf up	ndf down
$P^u_{273} - P^u_{Room}$	$P^d_{90} - P^d_{Room}$
$P^u_{77K} - P^u_{90K}$	$P^d_{90} - P^d_{273K}$
	$P^d_{77} - P^d_{Room}$
	$P^d_{77} - P^d_{273K}$

Table 4.4: List of useful power differences. When the ndf is up, differences like $P^u_{77} - P^u_{Room}$ are impossible to calculate because the two loadcurves do not overlapping values of R_{bolo}. For small power differences such as $P^d_{77K} - P^d_{90K}$, the signal-to-noise is too low for accurate calculations. It is also possible to use differences between ndf up and ndf down loadcurves, e.g. $P^d_{77K} - P^u_{77K} \sim \eta(1 - \eta_{ndf})$, for these calculations.

	77K - 90K	
Channel	Spec Norm	Opt Eff
B145W1	0.35	0.26
B145W2	0.35	0.26
B145X1	0.37	0.28
B145X2	0.33	0.25
B145Y1	0.38	0.29
B145Y2	0.38	0.31
B145Z1	0.26	0.19
B145Z2	0.21	0.14
B245W	0.38	0.33
B245X	0.36	0.28
B245Y	0.33	0.27
B245Z	0.32	0.27
B345W	0.81	0.70
B345X	0.89	0.77
B345Y	0.82	0.72
B345Z	0.87	0.68

Table 4.5: Spectral normalizations and flat band optical efficiencies measured using ndf up loadcurve power differences. The results are calculated using $P^u_{77K} - P^u_{90K}$ loadcurve power differences and the Rayleigh-Jeans band integral is calculated from the spectral response measurements (Table 4.7).

	ndf transmission (percentage)				
Channel	77K-273.3K	77K-285.7K	90K-273.3K	90K-285.7K	average
B145W1	1.88	1.79	1.74	1.65	1.77
B145W2	1.88	1.79	1.71	1.63	1.75
B145X1	1.75	1.64	1.62	1.51	1.63
B145X2	1.72	1.60	1.58	1.47	1.59
B145Y1	1.67	1.55	1.54	1.43	1.55
B145Y2	1.63	1.53	1.52	1.41	1.52
B145Z1	1.55	1.46	1.42	1.33	1.44
B145Z2	1.51	1.44	1.35	1.28	1.40
B245W	1.49	1.38	1.36	1.25	1.37
B245X	1.57	1.44	1.43	1.30	1.43
B245Y	1.78	1.62	1.62	1.45	1.62
B245Z	1.47	1.39	1.35	1.27	1.37
B345W	1.52	1.40	1.40	1.28	1.40
B345X	1.59	1.47	1.44	1.32	1.45
B345Y	1.60	1.46	1.46	1.32	1.46
B345Z	1.48	1.39	1.35	1.26	1.37

Table 4.6: Calculated ndf transmission (percentage) using the $P^u_{77K} - P^u_{90K}$ power difference and four different ndf down power differences.

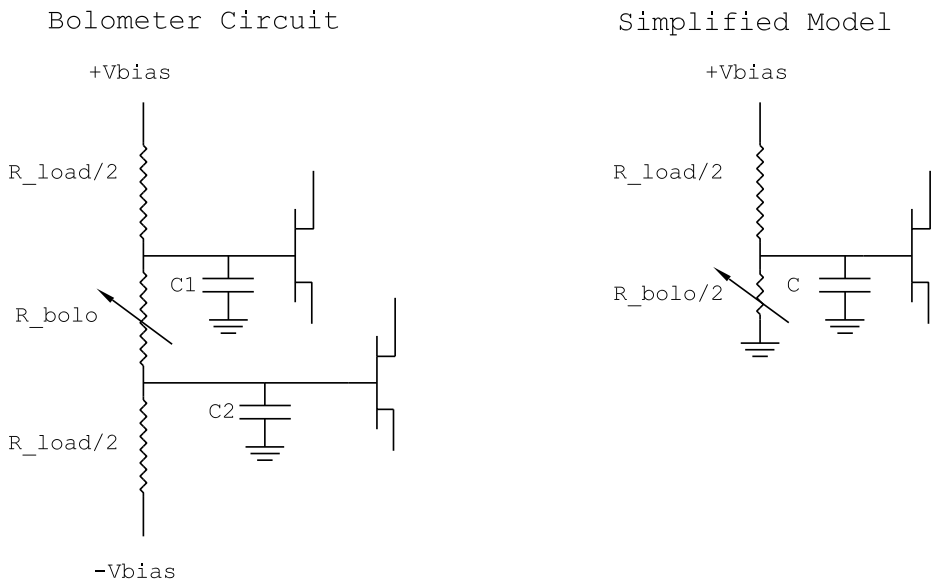

Figure 4.5: Cold bolometer circuit from load resistors to JFETs. The left diagram shows the cold bolometer circuit including parasitic capacitances. The right diagram shows a simplified model which can be used to model the effect of the stray capacitance on the signal (here we assume $C_1 = C_2$).

4.4 AC Bias and Parasitic Capacitance

In an ideal world, there is no stray capacitance. In our case, with large load resistors (20-60 $M\Omega$) and $R_{bolo} \sim 10M\Omega$, it does not take much stray capacitance (100 pF) to have an effect on the AC signal coming from across the bolometer. The parasitic capacitance is damaging where the output impedance is greatest. Here the bolometer resistance and the load resistors can combine with the capacitance to make a low pass filter. This can reduce the voltage responsivity of the circuit and also cause phase lag which can lead to signal loss at the lock-in amplifier.

The right side of 4.5 shows a simplified model which assumes that $C_1 = C_2$ and the bias is symmetric. This model is much easier to use for modeling. First

it is convenient to combine ($R_{bolo}/2$ and C) into a single impedance,

$$Z = \left(i\omega C + \frac{1}{\frac{R_{bolo}}{2}} \right)^{-1}, \tag{4.4.1}$$

$$Z = \frac{R_{bolo}}{2 + i\omega C R_{bolo}}, \tag{4.4.2}$$

with $\omega = 2\pi f_{bias}$. The complex transfer function can be written.

$$T = \frac{V_{out}}{V_{in}} = \frac{Z}{R_{load}/2 + Z}, \tag{4.4.3}$$

$$= \frac{R_{bolo}}{R_{load} + R_{bolo} + i\omega C R_{bolo} R_{load}/2}. \tag{4.4.4}$$

The magnitude and phase of the transfer function can be written.

$$|T| = \frac{R_{bolo}}{\sqrt{(R_{load} + R_{bolo})^2 + (\omega C R_{bolo} R_{load}/2)^2}}, \tag{4.4.5}$$

$$\phi_T = tan^{-1}\left(\frac{-\omega C R_{bolo} R_{load}/2}{R_{load} + R_{bolo}} \right). \tag{4.4.6}$$

The CMB signal we are looking for will cause small deviations in R_{bolo} from it's base level. Ideally, we would like to know the complex AC-biased responsivity (dV_{bolo}/dP) of the bolometer. This turns out to be a difficult to determine analytically (at least for this author). In order to get a handle on this we can start by looking at how the transfer function changes when R_{bolo} changes slightly (neglecting bolometer feedback effects which are necessary to understand the effect on the amplitude of the bolometer responsivity)

$$\frac{dT}{dR_{bolo}} = \frac{R_{load}}{(R_{load} + 2Z)^2} \frac{dZ}{dR_{bolo}}, \tag{4.4.7}$$

$$\frac{dZ}{dR_{bolo}} = \frac{2}{(2 + i\omega C R_{bolo})^2}. \tag{4.4.8}$$

Expanding this out we get

$$\frac{dT}{dR_{bolo}} = \frac{R_{load}}{(R_{load} + R_{bolo} + i\omega C R_{bolo} R_{load}/2)^2}, \tag{4.4.9}$$

$$\left| \frac{dT}{dR_{bolo}} \right| = \frac{R_{load}}{(R_{load} + R_{bolo})^2 + (\omega C R_{bolo} R_{load}/2)^2}, \tag{4.4.10}$$

$$\phi_{\frac{dT}{dR_{bolo}}} = tan^{-1}\left(\frac{-2(R_{load} + R_{bolo})\omega C R_{bolo} R_{load}/2}{(R_{load} + R_{bolo})^2 - (\omega C R_{bolo} R_{load}/2)^2} \right). \tag{4.4.11}$$

For small changes in R_{bolo}, this should give us a good approximation to the phase shift.

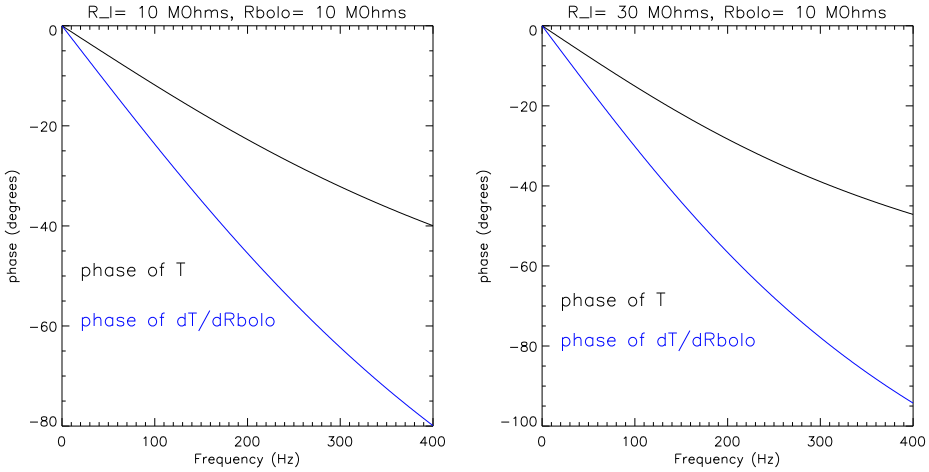

Figure 4.6: Comparison of the phase shifts from T (eq. 4.4.6) and dT/dR_{bolo} (equation 4.4.11) with a parasitic capacitance of 100 pF.

The phase of dT/dR_{bolo} has a subtle but important effect on the signal traveling into the warm electronics chain. When biasing a bolometer with a sine wave, the sine wave coming out of the cryostat will have phase described by equation 4.4.6. However small changes in the bolometer resistance will generate signal with phase defined by 4.4.11. Figure 4.6 shows the difference in the two phase shifts for each load resistor case.

In our lock-in detection scheme, the incoming signal is multiplied by a square wave reference. The gain of the lock-in stage is

$$G_{lock-in} = \frac{2}{\pi} cos(\delta\phi) \tag{4.4.12}$$

where $\delta\phi$ is difference in phase shift between the reference and the bolometer signal. As can be seen in the right panel of figure 4.6, it is possible for the phase shift of dT/dR_{bolo} to be 90° or greater. If one is operating a bolometer in this regime (with an unshifted reference), it is possible that an input optical signal might be nulled or inverted by the lock-in.

To characterize the phase shifts, we measured AC-biased loadcurves (with $f_{bias} = 145\ Hz$) using a spectrum analyzer to read out the data straight from the JFET's. With the spectrum analyzer, we were able to record the magnitude of the bolometer signal and the phase with respect to the the input bias waveform. We took load curves using a 77K ndf down load and a room temperature (290K) ndf down load. The complex difference of the loadcurves gives the vector in the complex plane which (for a given bias voltage) connects a point on the 77K loadcurve to a point on the room 290K loadcurve. As can be seen in Figure 4.7, the phase shift of the difference is larger than the phase shift of the signal.

This qualitatively agrees with equation 4.4.11. Although the bolometer response is probably non-linear between 290K and 77K (even with the ndf down), this method gives a rough estimate of the phase shift of the bolometer response. In Appendix B, we calculate the capacitance from the complex AC loadcurve data. We find capacitances of roughly 235 pF for the 145 GHz channels and 180 pF for the 245 and 345 GHz channels.

In order to avoid signal loss at the lock-in, we need to add a phase delay to the lock-in reference. Although it would be possible to individually shift the reference for each channel, it was decided (for simplicity and 1/f stability) that it was best to apply a uniform phase delay in each of the four electronics boxes. If the phase shift is off the optimal one by 10°, the signal loss is only $1.5\%(\cos(10°) \simeq 0.015)$. Also, there is no guarantee that the R_{bolo} in flight will be the same as on the ground with the ndf in the beam. To chose the phase shift we tested the responsivity to the internal calibration lamp with four different phase shifts (17.6°, 25.3°, 34.6° and 45.7°) under both a 77K ndf down load and a 290K ndf down load. Figure 4.8 shows the results of this test. We chose 34.6° as the best phase shift for each channel. This seemed to provide the best compromise between loading changes, bias levels, and total responsivity. In retrospect, 45.7° might have been best for the box 1 channels (B145W1, B145W2, B145Z1 and B145Z2).

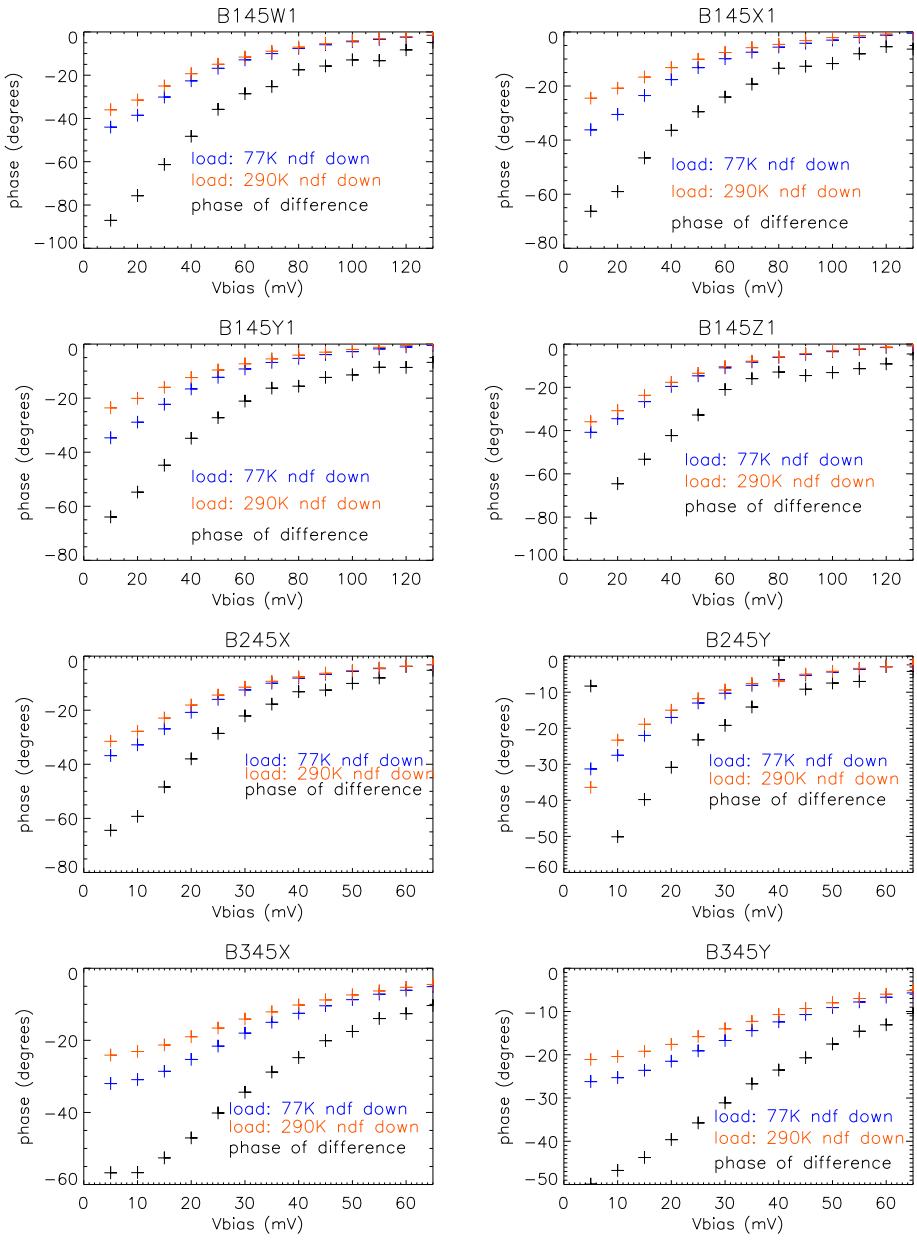

Figure 4.7: Phase measurements from AC-biased load curves. The blue curve is for 77K load with the ndf down, the red curve if for a 290K load ndf down, and the black curve represents the phase shift of the difference between bolometer voltages at a given bias voltage.

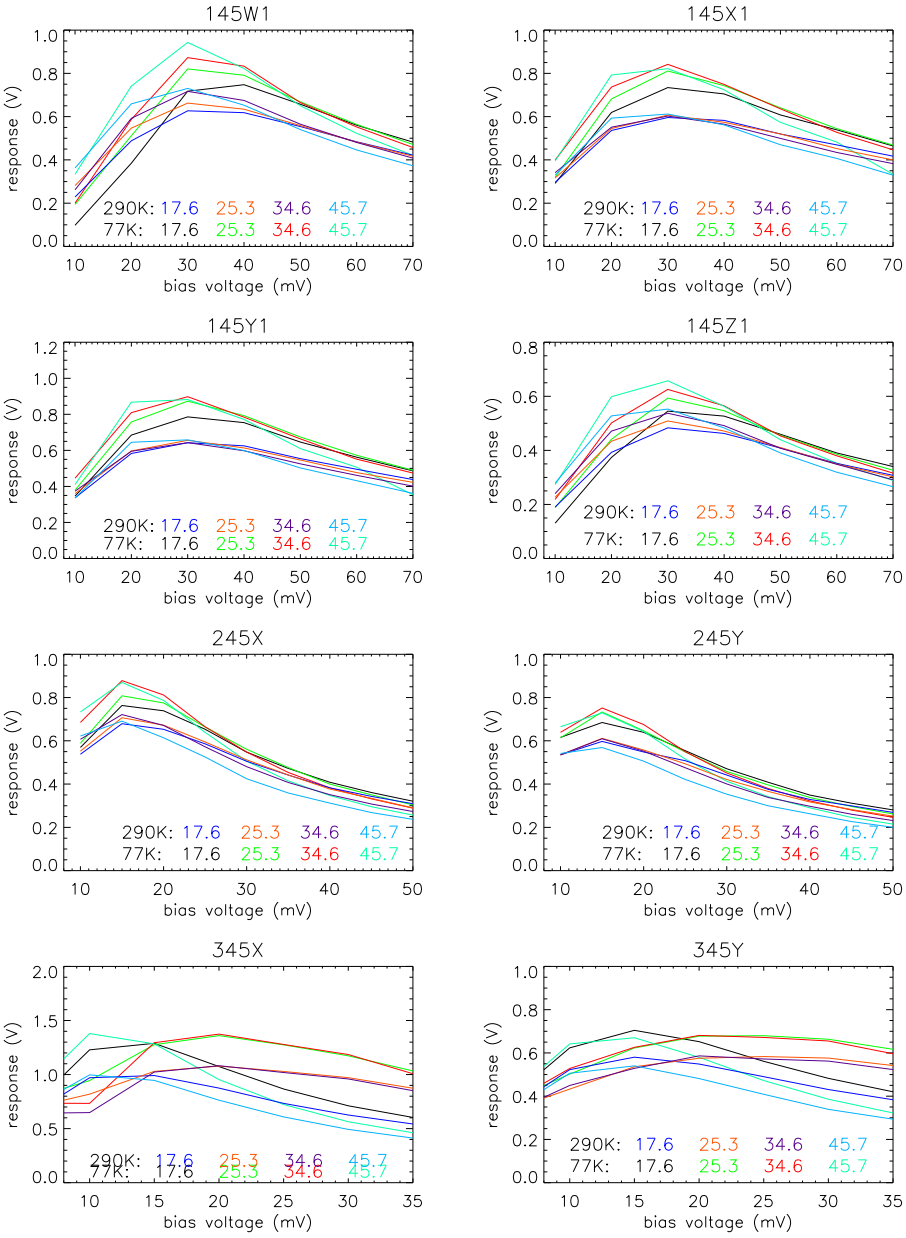

Figure 4.8: Test of responsivity versus phase and bias using the calibration lamp. For each loading and each phase delay, response vs. bias voltage was measured.

4.5 Bandpass

The spectral bandpass was measured using a Fourier transform spectrometer with a Martin-Puplett interferometer (built by Eric Torbet). The beam-splitter is a wire grid polarizer (6-inch diameter, 0.7-mil wire, 2.5-mil spacing), which has a flat broad-band response. Two other polarizers are required: one to polarize the input radiation and one to select the output polarization. The output signal is the sum of the signals travelling down the 2 arms of the interferometer. A moving mirror modulates the interference.

Figure 4.9 shows plots of the measured spectral bandpasses. Channel B245X has a dip in the spectra at 210 GHz. This feature is most likely caused by the particular feed horn which feeds the X photometer (i.e. Similar behavior has been seen when this feed was used with other photometers). Table 4.7 contains relevant band integral calculations. Column 2 is the CMB anisotropy band integral and column 3 is the Raleigh-Jeans band integral. The band integrals are done for only 1 polarization.

Channel	$\int d\nu\ e(\nu)\frac{dB_\nu}{dT}\|_{T=2.73K}$ $10^{-8}W/(K\ m^2\ sr)$	$k\int d\nu\ \frac{e(\nu)\nu^2}{c^2}$ $10^{-8}W/(K\ m^2\ sr)$	Center Frequency GHz
B145W1	6.100	10.372	146.3
B145W2	5.921	10.049	146.1
B145X1	6.022	10.194	145.6
B145X2	5.949	10.092	146.0
B145Y1	6.153	10.477	146.5
B145Y2	6.477	11.013	146.3
B145Z1	5.861	9.974	146.4
B145Z2	5.399	9.205	146.5
B245W	14.460	58.049	247.0
B245X	12.844	52.773	249.6
B245Y	13.587	52.486	243.2
B245Z	14.325	57.291	246.5
B345W	14.381	158.273	341.6
B345X	14.687	155.825	338.3
B345Y	14.217	162.301	344.9
B345Z	13.079	140.020	339.2

Table 4.7: Useful band integral data calculated from spectral bandpasses. The first column is the band integral over the spectrum of CMB fluctuations. The second column is the band integral for the Rayleigh-Jeans spectra with temperature $T_{RJ} = 1$.

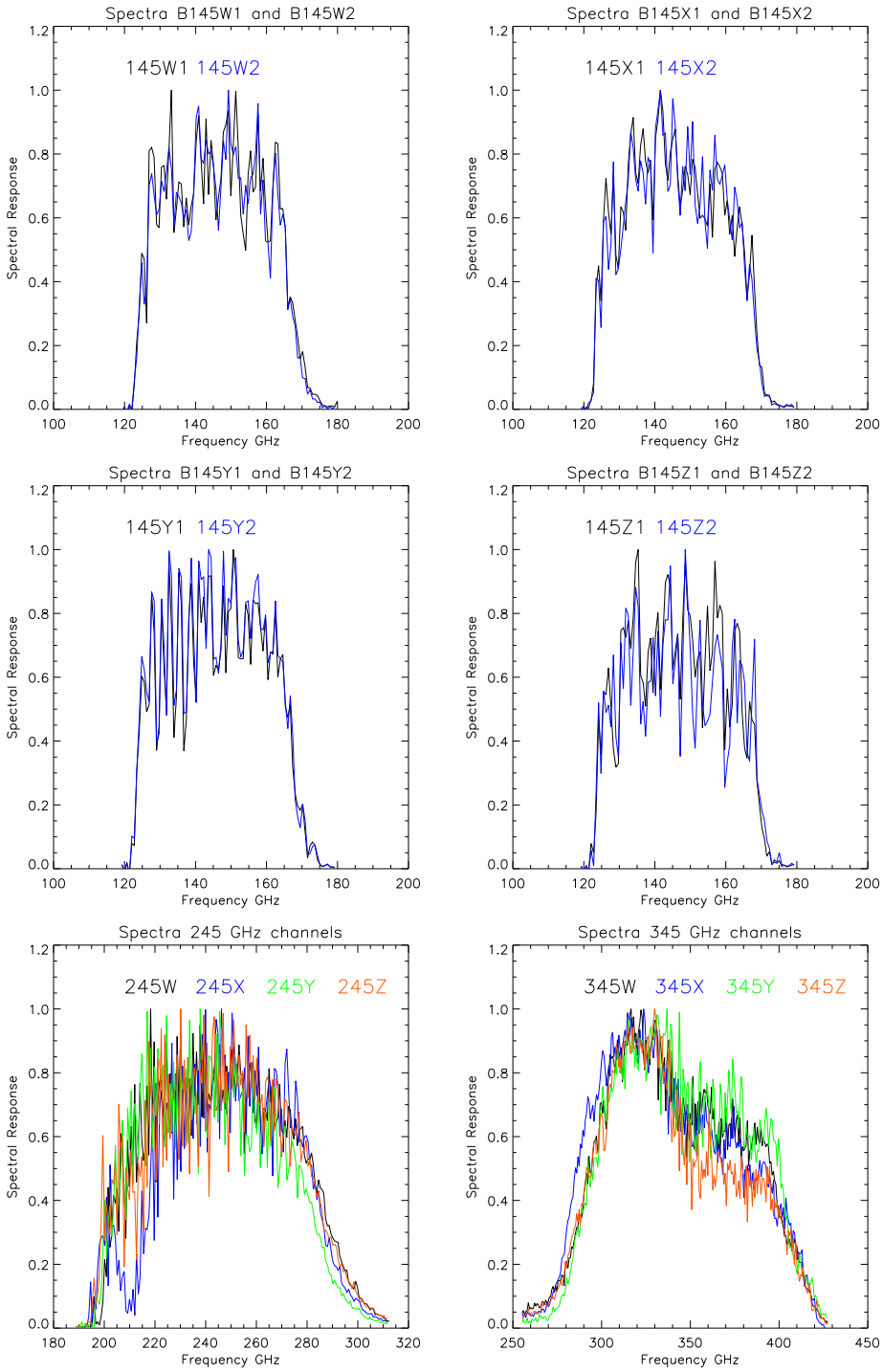

Figure 4.9: Measured spectral bandpasses. The spectra are normalized so that the maximum point is 1.0. The Rayleigh-Jeans spectrum of the source is divided out of the final results.

4.6 High Frequency Leaks

We are only interested in radiation in the frequency band 120 GHz to 400 GHz. A high frequency leak could make a channel more sensitive to galactic and zodiacal dust than it is to CMB signals. We quantify our sensitivity to such spectral leaks using high pass thick grill filters [107]. This is a more stringent test than the FTS, because the thick grill filter test is sensitive to the integrated leak above its cut-off frequency.

The measurement is performed using a chopped 77K source, with and without a thick grill filter in the source aperture. We used three filters with cut-off frequencies 250 GHz, 350 GHz and 450 GHz (each about 50 GHz above each of our bands). The result of this test is the ratio of the out-of-band to in-band response for a Rayleigh-Jeans source:

$$R_{leak} = \frac{\int (B_\nu^{300} - B_\nu^{77}) e_{leak}(\nu) d\nu}{\int (B_\nu^{300} - B_\nu^{77})(e_{band}(\nu) + e_{leak})(\nu) d\nu}. \tag{4.6.1}$$

We want to measure the ratio of out-of-band to in-band power from a dust source

$$R_{dust} = \frac{\int B_{dust} e_{leak}(\nu) d\nu}{\int B_{dust} e_{band}(\nu) d\nu}. \tag{4.6.2}$$

To solve for R_{dust}, we first need to solve for $e_{leak}(\nu)$. Since we don't have a model for our leak or spectroscopic measurements to that high of a frequency, the best we can do is assume the leak is flat from the cut-on of the grill filter (ν_{grill}) up to some cut-off. In our case, $\nu_c = 1650\ GHz$ ($55\ cm^{-1}$) is a good choice, because the Yoshinaga/Black-poly filter in each filter stack should stop anything with $\nu > \nu_c$. With this assumption we can solve for e_{leak},

$$e_{leak} = \frac{R_{RJ} \int_{band} (B_\nu^{300} - B_\nu^{77}) e_{band}(\nu) d\nu}{\int_{\nu_{grill}}^{1650\ GHz} (B_\nu^{300} - B_\nu^{77}) d\nu}, \tag{4.6.3}$$

where we assuming e_{leak} is small enough that the e_{leak} term in the denominator of equation 4.6.1 is negligible (this is valid approximation if $e_{leak} \ll e_{band}$).

For simplicity we assume a single-component dust model with a frequency dependent emissivity.

$$B_{dust} \approx \nu^\alpha B_v(T) \tag{4.6.4}$$

Choosing a 'favored' dust model, with $\alpha = 1.7$ and $T_{dust} = 20\ K$ [24], we can calculate R_{dust}.

Table 4.8, shows the results of our thick grill tests. For all channels, R_{RJ} column is an upper limit of signal in the leak band. The 145 GHz channels had no detectable signal above 250 GHz, and the 245 GHz and 345 GHz channels had no detectable signal above 450 GHz. R_{RJ} is adjusted for the aperture loss of the

thick grill hole coverage, which was conservatively taken to be 50%. Similarly, the R_{dust} column (column 3), is also an upper limit for all channels. For the 145 GHz channels, the leak band was taken to be 250-1650 GHz. For 345 GHz, we used 450-1650 GHz. The 245 GHz channels are more complicated. For 245 GHz, columns 2 and 3 of the table are for the leak band 450-1650 GHz. There was actually a finite amount of signal in the 245 GHz channels when the 350 GHz grill was in place. The R_{RJ} with the 350 GHz grill in place is about twice the number in Column 2. Column 4, shows the R_{dust} for the amount of dust in the band 350-450 GHz relative to the dust in the 245 GHz band. Even though the 245 GHz signal might have some signal between 350 and 450 GHz, the signal there is too small to cause any problem.

Channel	R_{RJ}	R_{dust}	R_{dust} 350-450 GHz
B145W1	0.0031	0.0206	
B145W2	0.0046	0.0309	
B145X1	0.0046	0.0308	
B145X2	0.0030	0.0203	
B145Y1	0.0066	0.0443	
B145Y2	0.0051	0.0345	
B145Z1	0.0027	0.0183	
B145Z2	0.0019	0.0130	
B245W	0.0019	0.0060	0.0075
B245X	0.0018	0.0056	0.0075
B245Y	0.0018	0.0058	0.0062
B245Z	0.0015	0.0046	0.0075
B345W	0.0031	0.0064	
B345X	0.0030	0.0061	
B345Y	0.0021	0.0042	
B345Z	0.0030	0.0062	

Table 4.8: Thick grill results. R_{dust} is calculated assuming the leak spectrum is flat from the thick grill cut-off to 1650 GHz. Except for the column labeled "R_{dust} 350-450 GHz", all the values in this table are upper limits. No detectable signal is seen above 250 GHz in the 145 GHz channels or above 450 GHz in the 245 GHz and 345 GHz channels. For the 145 GHz channels, the R_{RJ} values are measured with the 250 GHz grill in place. For 245 GHz and 345 GHz, the values are from the 450 GHz grill measurement. The 245 GHz channels had some signal when the 350 GHz grill is in place; the signal amplitude leads to a value of R_{RJ} which is twice the value in column 2. For the 245 GHz channels, the ratio of dust in the 350-450 GHz band to the in-band contribution is given in column 4.

4.7 Time Constants

Because of its heat capacity and finite thermal link, a bolometer is not able to respond instantaneously to a change in incident power. For the most part, it's frequency response can be modeled by a single pole RC filter with $\tau = C/(G - \alpha P_{elec})$ where C is the heat capacity. Knowing the time constant gives the effective bandwidth of the experiment which is important for designing the scan strategy.

We made a variety of measurements in order to get a handle on our time constants before the flight. Measurements were made using both AC-bias and DC-bias and with 2 different loads : 77K and a room temperature loads (both with ndf down). Both measurements used a chopper wheel to modulate the signal. The DC-biased measurements were done using a commercial lock-in to measure the amplitude and phase of the chopped signal directly, while the AC-biased measurements were done using the flight electronics and the chopped signal was demodulated in software. The AC-biased measurement have the disadvantage that the filtering on the lock-in boards will have some effect on the output signals. Since the 4-pole Butterworth does not seriously cut-off until about 20Hz, the only significant effect is the induced phase shift from the Butterworth. This does not severely affect a fit for τ using the magnitude of the output voltage.

Table 4.9 shows the results of AC-biased measurements. The data was fit to a single time constant model. For the 145 GHz channels, at frequencies greater than 5 Hz there is some extra attenuation which is better fit by a double time constant model. One interesting thing to note is that the many of 145 GHz channels actually got faster when the loading went down. Figure 4.10 shows the results of the measurements and fits for B145W1. The 245 and 345 GHz channels are basically unaffected by the load temperature. It is likely that the flight time constants will be different in flight (especially for the 145 GHz channels); we will need another method to measure the time constants from the flight data. One good way to do this is to use cosmic rays (see section 6.1.3).

Channel	77K ndf down load	290K ndf down load
	msec	msec
B145W1	70	84
B145W2	41	52
B145X1	50	56
B145X2	39	44
B145Y1	81	83
B145Y2	77	81
B145Z1	62	58
B145Z2	126	109
B245W	21	22
B245X	19	21
B245Y	18	19
B245Z	25	26
B345W	15	14
B345X	15	15
B345Y	12	13
B345Z	21	21

Table 4.9: Pre-flight time constant measurements, done with the AC bias. Values are in milliseconds. For this analysis, the effect of the 4-pole Butterworth lowpass was not removed, so the true time constants 245 and 345 GHz channels could be slightly different from what is shown here.

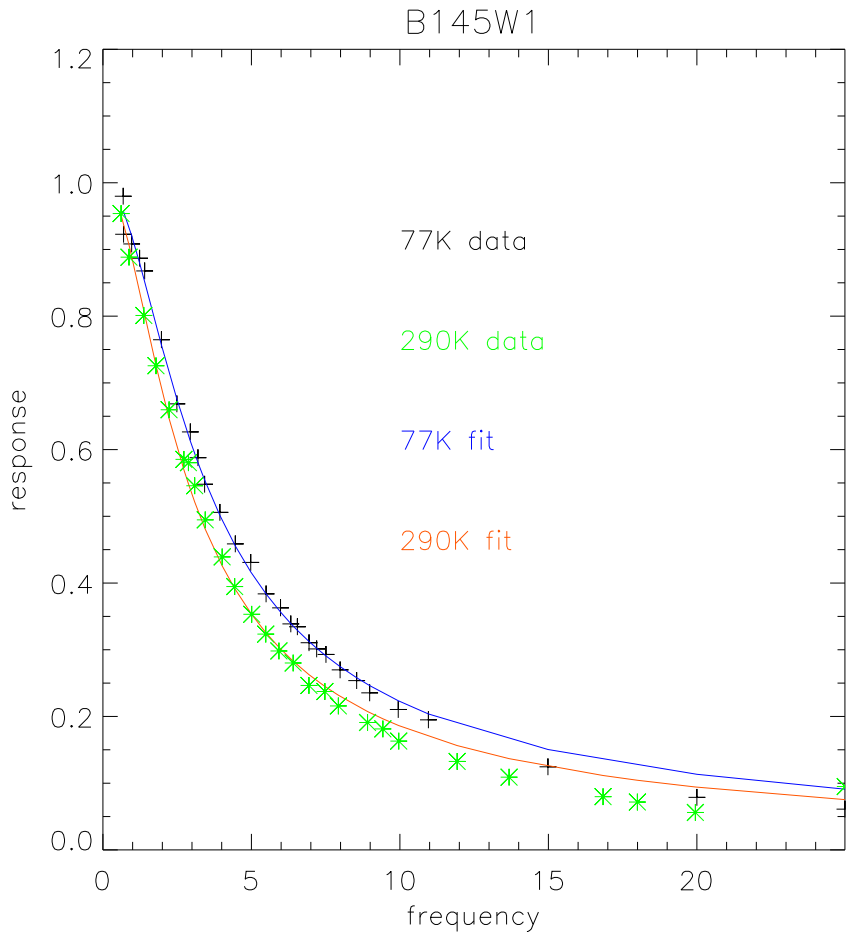

Figure 4.10: B145W1 time constant measurements. At frequencies greater that 5 Hz, it is apparent that a single tau model does not fit very well. The deviation from a single tau model could be due to the fact that we did not account for the roll-off of the Butterworth filter. It could also be due to a second time constant.

4.8 Noise Characterization

In the signal chain, there are many sources of noise, each of which needs it's own special brand of love and care in order to insure optimal operational. We are concerned both with the level of the white noise and the long term (1/f) stability. Starting at the detectors our signal chain looks like this.

- Bolometers
- Cold wiring
- JFET's
- Warm Electronics
- Data Aquisition System

Each of these has its own possible contribution to unwanted noise. Below we will detail some of the pitfalls we found and the measures taken to alleviate unwanted effects.

To fully understand the noise sources, we need to understand how noise can propagate through the signal chain. With our lock-in method, there are two paths for noise to make it into our output signal: additive and multiplicative. The AC-bias generator sends a sine wave into the cryostat. The signal output from the bolometer is proportional to $R_{bolo}/(R_{load} + R_{bolo})$. This is sent through the JFET's to the warm electronics where it is amplified, demodulated and filtered. An additive noise source is one which adds a voltage noise to the AC waveform. It must have frequency $f_{bias} - f_{cutoff} < f < f_{bias} + f_{cutoff}$ where f_{cutoff} is the cutoff of the Butterworth anti-aliasing filter. A multiplicative source is one which causes a variation in amplitude of the output AC waveform (e.g. fluctuations in R_{bolo} or JFET gain drift). Its effect on the waveform can be represented as a signal at $f_{bias} + f$ and $f_{bias} - f$. It must have a frequency $f < f_{cutoff}$.

4.8.1 Bolometers

There is a great deal of literature on bolometer noise theory [79, 80] (see also section 4.1). The three unavoidable sources of noise are Johnson noise, phonon noise and photon noise. The Johnson noise is primarily dependent on the bolometer resistance; it is almost a pure voltage noise and almost independent of frequency. There is a slight dependence on the responsivity of the bolometer due to the possibility of self-heating through dissipation of noise power in the bolometer. The phonon and photon noise represent fluctuations in incident power on the bolometer which lead to fluctuations in R_{bolo}. Since the phonon and photon noise induce fluctuations in R_{bolo}, the white noise scales with voltage responsivity. However, it is possible to get 1/f noise, namely popcorn or contact noise, if the thermistor does not have good electrical contacts.

4.8.2 Cold Wiring

Bad solder joints and bad wires in the cold stage are potential sources of 1/f noise. One of our requirements before cooling the cryostat was that there were no anomalous shorts ($R_{short} < 100M\Omega$) in bolometer wiring. Independent of the electrical quality of the wiring is the possibility of microphonic resonances. The high impedance wires were tied down to constrain vibration. While lock-in boards are designed to filter spurious signals outside our signal bands ($f_{bias} - f_{cutoff} < f_{signal} < f_{bias} + f_{cutoff}$), it is still possible for the filtered signals above the signal band to alias down into the band, especially signals near odd-harmonics of the bias frequency. Originally, we had set the bias frequency to 317 Hz. At this frequency, we had noise lines in the 245 GHz channels which we could not trace to anything outside the cryostat. Changing the bias frequency to 144 Hz helped all these channels, but B245W still had some noise lines.

4.8.3 JFET's

The JFET stage uses TIA's packaged by Infrared Laboratories. The FET die is stood off on glass posts. This isolates the critical electrical components from the 4K stage so that the JFET itself can operate at 77K-100K (with heat applied to it). This makes them very convenient to use: we don't need to thermally isolate the entire readout board, they can be easily replaced, and the heater power can be tuned individually for each JFET. Besides fragility and cost, the only drawback to these JFET's is that the noise level is often sensitive to the amount of heater power applied (especially for newer devices). We made a large number of tests (with the cold stage at 4K) and found that at 330 Hz those with serial number < 700 were largely immune to the amount of heat applied. In the testing before flight, we found that the 4K noise at 144 Hz was somewhat worse for three of channels compared to the 4K noise at 330Hz (even for the low serial number devices). Applying more heat helped 2 of the 3 affected channels.

4.8.4 Warm Electronics

With modern instrumentation amplifiers, it is trivial to achieve input noise levels of 4-6 $nV/\sqrt{Hz}$ (one can even get to 1 $nV/\sqrt{Hz}$ easily if need be). The hard part about the warm electronics is long term stabilty. Most stabilty problems are thermal in orgin resulting from temperature variation of integrated circuit components, resistors and capacitors. As much as possible we tried to use components which had strong immunity to thermal variations. For fixed resistors, we mainly used Vishay-Dale RN55C. For most of the critical capacitors, we used Vishay-Sprague polycarbonate film capacitors or Kemet NPO capacitors (NPO has the lower temperature coefficient, but they are hard to find in values above 100nF).

In order to test the stabilty of the electronics, we made tests using warm resistor dividers which simulated the effective bolometer circuit (except for the JFET's). The circuit used two $10K\Omega$ as load resistors and one $5K\Omega$ as the "bolometer". Low resistance values were used so that the input white noise would be low and we could resolve the 1/f knee.

The most thermally critical parts of the electronics chain are the bias oscillator, the bandpass filter, and the AC-coupling filter. The oscillator's frequency is determined by a pair of matched resistors and capacitors. Over long time periods the oscillator frequency was seen to drift, but this was not the cause of most of the 1/f noise. If the oscillator were significant source of 1/f noise, it would manifest itself as correlated drifts in all channels.

The AC-coupling filter proved problematic in a few instances. The AC-coupling cut-on frequency is defined partly by Tantalum capacitors. These are not a good choice for thermal stability, but for a low cut-on ($f_c < 50mHz$) frequency, large capacitors ($C > 50\mu F$) are necessary. These high capacitances are not easily available (if at all) in a more thermally stable packages. In pre-deployment testing, we found that the level of 1/f noise correlated quite well with the amount of leakage current through these capacitors. The leakage current manifests itself as a DC offset at the AC bolometer output.

In the end, the bandpass filters were the most troublesome. The bandpass filters use a bi-quad design whose transfer function is not quite flat over the passband nor is the phase shift zero. The center of the passband is set by a 2 resistances and a capacitor (one of the resistances is built from a trimpot and a fixed resistor). The non-flat passband could be troublesome. A small variation in the oscillator frequency or the passband center could lead to drifts since the input signal would be moved to a different part of the passband.

After many tests and many crackpot theories, most of the electronic stability issues were traced to the trimpots which help set the center frequency. The effect was most pronounced because we were doing the tests with the reference phase shifters installed. Using 4.4.12, we can calculate derivative of the lock-in gain with respect to a change in the phase difference between the reference and the signal,

$$\frac{dG_{lock-in}}{d\phi} = -\frac{2}{\pi}\sin\phi. \tag{4.8.1}$$

If the lock-in reference and the signal have zero phase difference then the lock-in output is stable to small deviations in phase. In our test, the reference was delayed by about 35° (there was no phase delay in the bolometer simulator circuit). Here, the effects of the phase changes would be much more pronounced. This lead us to replace the trimpots with groups of parallel fixed resistors whose values added to the value needed to set the proper bandpass.

In case the previous paragraph was not clear enough: **trimpots are pure evil** (Horowitz and Hill point this out as well [49].). In our experience, we found

that wire-wound trimpots work well (we use those to set the bias voltages), but they are very bulky and will not fit well on a circuit board. However, the small trimpots which fit on a board are suspect (at least if you are worried about thermal stability).

4.8.5 Data Aquisition System

Having survived the cold wiring, JFET's and backpack electronics, one might hope that the worst is over (well actually it is). There is only one systematic issue with the Data Aquisition System (DAS) and it's not all bad. The Butterworth stage on the lock-in boards was our original anti-aliasing filter. The main reason for having an anti-aliasing is to kill off signals far from the signal band (e.g. harmonics of the bias frequency).

The signal coming out of the lock-in chip is a rectified sine wave whose dominate component is at $f = 2f_{bias}$. This signal moves to the Butterworth filter which rolls off most of the signal above the cut-off (20 Hz in our case). However, even if the attenuation of the filter is a factor of 250 at $f = 2f_{bias}$, the bias residual is still roughly the same size as the output noise from 1-20 Hz. If the sample rate of the DAS is less than $2f_{bias}$ it is possible to for the bias harmonic to alias down into the signal band with a frequency

$$f_{alias} = nf_{sample} - 2f_{bias}, \tag{4.8.2}$$

where n is any integer. The AC-coupled data is sampled at 60 Hz. With our bias frequency at 144 Hz, we would expect an aliased signal at 12 Hz. This is exactly what we get, and it is out of our signal band (this was part of the consideration when we moved the bias frequency from 317 Hz to 144 Hz. In the end, we had to add some extra anti-aliasing filtering to the AC-coupled output because moving the bias from 317 Hz down to 144 Hz led to less attenuation at $2f_{bias}$ by the Butterworth (whose cutoff was kept at 20 Hz). This meant that time stream plots were dominated by the aliased bias signal. The extra filtering does not completely remove the signal, but leaves it at a value roughly twice the bolometer noise. This so-called "DAS line" has one great advantage in that it allows us to track the bias frequency.

4.8.6 Pre-flight Noise Data

Table 4.10 shows the noise levels at 1 Hz for the 4K JFET test, a 290K ndf down load, and a 77K ndf down load. At 4K, the bolometers have a small resistance and a very small responsivity; the noise is dominated by the JFETs. For the 77K noise test, a shiny metal place covered the cryostat window. Internal reflections inside the cryostat make this an effective 77K load. The 290K test was done with an sealed eccosorb load mounted on the bottom of the cryostat. All tests were done

during pre-flight integration in Antarctica. We had 3 channels with excess noise. Dark A and B345Z showed noise which looked liked contact noise. B245W was very weird. Sometimes it had a forest of noise lines and sometimes it worked very well. For these channels, the problems could not be found outside of the cryostat and their 4K JFET noise was fine. In the past, the wires for these channels have all performed better than they did here. It is hard to say for sure what caused these problems.

Figure 4.11 shows measured noise spectra from the final configuration of the electronics at flight bias. In this case the bolometers were staring at a sealed reflective plate which meant that most of the loading was reflecting from inside the dewar. The sealed room temperature eccosorb load was not thermally stable enough for 1/f tests. In this case, the shiny plate was further from the window than it was during the white-noise tests described in 4.10. The effective load is somewhere between 300 K and 77 K.

The 145 GHz spectra are quite interesting. On a log scale, the spectra have a nearly constant slope from 10 mHz until the anti-aliasing filter kicks in. After 1 Hz, most of the slope is due to the fact that the long time constant rolls off much of the phonon and photon noise above 1 Hz. If one defines the 1/f knee as the point where the noise level is twice the 1 Hz noise level, then all of the 145 GHz channels have 1/f knees below 10 mHz. For the 245 and 345 GHz channels, the 1/f knees are generally between 10 and 30 mHz. The problems in B245W and B345Z are readily apparent. The astute reader might notice that in this test the white noise level in B345X is a somewhat higher than reported in Table 4.10. The cause for this is not clear.

Channel	$T_0 = 4$K	$T_0 = 275$mK 290K load	$T_0 = 275$mK 77K load
	$nV/\sqrt{Hz}$	$nV/\sqrt{Hz}$	$nV/\sqrt{Hz}$
B145W1	9.4	21.7	22.0
B145W2	8.6	18.0	18.2
B145X1	8.7	20.0	21.4
B145X2	8.1	19.9	20.5
B145Y1	9.0	19.2	19.7
B145Y2	10.4	18.5	19.0
B145Z1	8.4	18.8	18.6
B145Z2	9.4	18.6	20.6
B245W	11.4	35.9	42.2
B245X	9.7	24.4	24.6
B245Y	10.6	23.6	24.6
B245Z	10.3	23.2	25.8
B345W	8.9	22.1	22.3
B345X	8.0	23.1	23.2
B345Y	9.2	20.2	19.4
B345Z	14.8	NA	52.5
DARK A	8.4	277.3	269.9
DARK B	9.1	19.4	19.8
GNDFET	12.1	11.5	11.5
LRES	26.7	13.4	13.3

Table 4.10: Lab noise measurements, made during pre-flight integration. Results shown are the level of the noise at 1 Hz. The $T_0 = 275$ mK noise was taken with the ndf in the beam for greater responsivity. At 4 K, the bolometers have a small resistance and a very small responsivity; the noise is dominated by the JFETs. For the 77 K noise test, a shiny metal place covered the cryostat window, creating an effective 77 K load because of internal reflections in the cryostat. The 290K test used a room temperature eccosorb load.

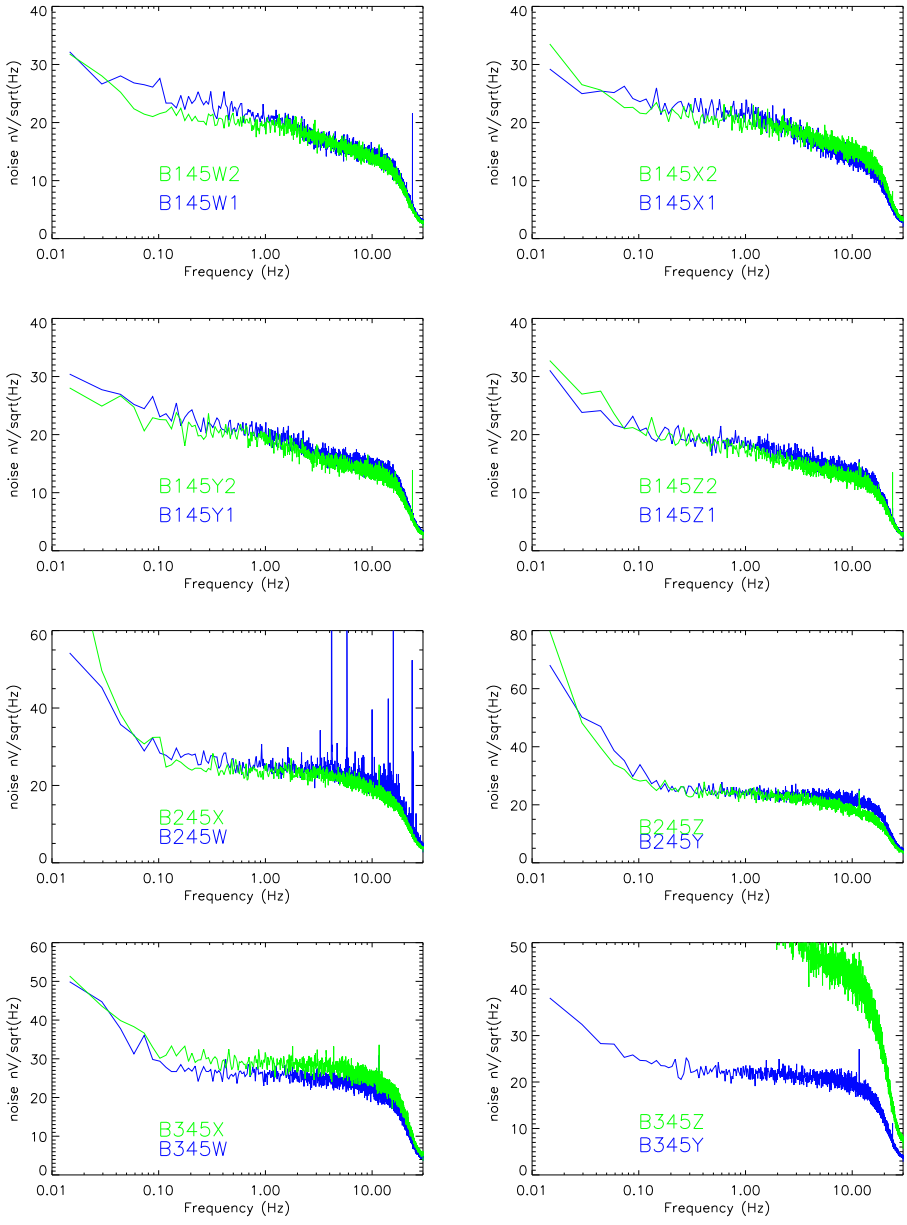

Figure 4.11: Noise spectra measured before flight in final electronics configuration. The detectors were looking at a shiny plate through the ndf. The shiny plate was found to be a more stable load than room temperature eccosorb. The plate was about 10 inches from the window, so the effective load on the bolometers was somewhere between 300 K and 77 K. The ndf was down so that the responsivity would be similar to flight conditions.

4.9 Signal to Noise and Flight Bias levels

In order to choose the flight bias, we made a comparison of signal-to-noise versus bias voltage. The signal measurement was done using the calibration lamp and the measured noise was taken to be the noise at 1 Hz. For the 145 GHz channels, we set the bias at the following levels: 5, 10, 15, 20, 25, 30, 35, 40, 45, 50, 55, 75 and 120 mV_{rms}. For the 245 and 345 GHz channels we set the bias at: 5, 10, 15, 20, 25, 30, 35, 40, 45, 50, 55, 75 and 95 mV_{rms}. Both signal and noise were measured with a 290K ndf down load. Conventional wisdom says that the bias where signal to noise peaks is slightly higher than the bias where the signal peaks. As the bias voltage is increased, the noise should decrease faster than the signal. Table 4.11 shows the bias levels corresponding to where the signal, noise and signal to noise values peaked. In our case, we found that the signal-to-noise peak was pretty close to the signal peak. This could be partly due to the AC phase shift issues. Figure 4.12 shows plots of signal, noise and signal-to-noise for selected channels. From this data, we selected our flight biases to be 30 mV for the 145 GHz channels, 20 mV for the 245 GHz channels, and 25 mV for the 345 GHz channels.

Channel	Signal	Noise	Signal to Noise
B145W1	30	30	30
B145W2	25	30	20
B145X1	30	20	40
B145X2	30	40	30
B145Y1	30	20	40
B145Y2	30	20	30
B145Z1	30	40	20
B145Z2	40	30	40
B245W	15	10	30
B245X	15	10	20
B245Y	15	0	20
B245Z	15	20	10
B345W	25	20	30
B345X	25	30	20
B345Y	25	30	30

Table 4.11: Peak AC bias voltages for signal, noise and signal-to-noise. The flight phase shift (35°) was installed. Below 55 mV_{rms}, the bias was ramped 5 mV_{rms} at time. The next point was 75 mV_{rms}. The last point was 120 mV_{rms} for the 145 GHz channels and 95 mV_{rms} for the 245 and 345 GHz channels.

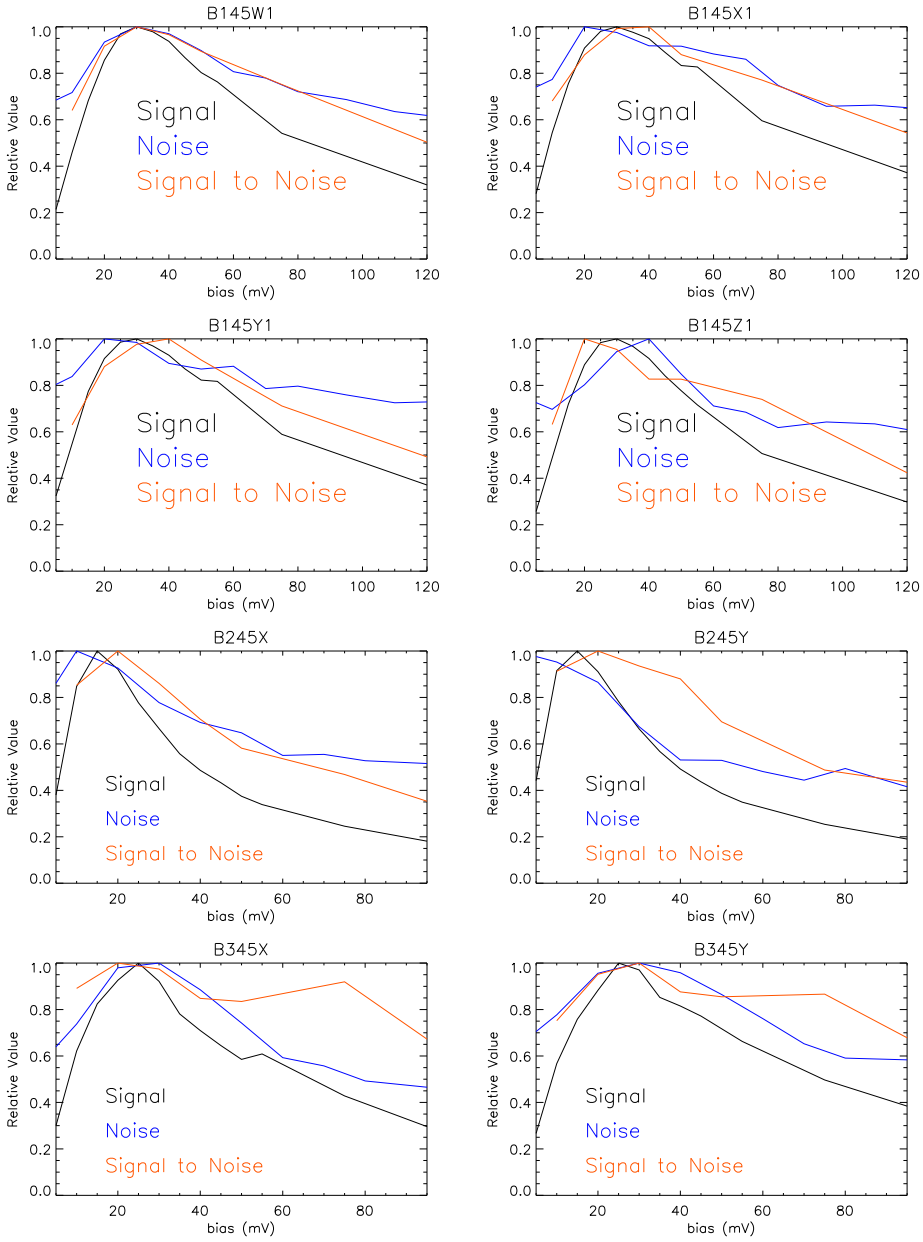

Figure 4.12: Signal, noise, and signal-to-noise as a function of bias for selected channels.

4.10 Calibration

The pre-flight calibration of the receiver was done by measuring the response to chopped thermal loads. We used beam-filling chops between liquid nitrogen (77K) and liquid oxygen (90K) as well as chops between ice water and "room temperature". Traditionally, we had used a hollow, inverted, polyethylene cone to cut down on reflections when using the ice water load; however, we've found that the chopped signal did not change significantly when then cone was not used. The chop was done with the AC bias frequency at 144 Hz and the final lock-in reference phase shift (35°) was installed. For the 145 GHz and 345 GHz channels, we measured the response with AC-bias levels between 10 and 70 mV_{rms} with increments of 10 mV_{rms}. For the 245 GHz channels, we used 5 mV_{rms} increments and made the measurements with bias levels between 5 and 35 mV_{rms}. The chopped loads measure the Raleigh-Jeans responsivity. This allows us to measure the quantity $S\eta A\Omega$ which from 4.1.7 is

$$S\eta A\Omega = \frac{\Delta V_{chop}}{\eta_{ndf}\Delta T_{chop}\int d\nu\ \frac{e(\nu)\nu^2}{c^2}} \tag{4.10.1}$$

where $\eta_{ndf}T_{chop}$ is the effective Raleigh-Jeans temperature difference of the chop. Plugging this into 4.1.9 we get

$$\frac{dV_{bolo}}{dT_{cmb}} = \frac{\Delta V_{chop}\int d\nu\ e(\nu)\frac{dB_\nu}{dT}|_{T=2.73K}}{\eta_{ndf}\Delta T_{chop}\int d\nu\ \frac{e(\nu)\nu^2}{c^2}} \tag{4.10.2}$$

We can also measure of the calibration by using the responsivity measured from the DC loadcurves, the spectral normalization and $A\Omega = \lambda^2_{center}$ (equation 4.1.9).

Table 4.12 shows the results for the 77K-90K chops, the 273K-293K chops and the 77K ndf down loadcurve. This calibration uses the ndf transmission reported in table 4.6, and is linearly proportional to that value. Also the value of the temperature difference in the 273K-293K chop is uncertain since the room temperature was not well known. The difference in responsivity between the DC loadcurve based result to AC-biased chops might be explained by voltage responsivity loss due to parasitic capacitance or by uncertainty in the ndf calibration.

With these calibration values and the noise data from 4.10, we can calculate a Noise Equivalent Temperature (NET) using equation 4.1.17. Table 4.13 shows the results of this for a 77K ndf down load.

Channel	AC-biased chops 77K-90K	273K-293K	DC Responsivity 77K loadcurve
	$\mu V/K_{cmb}$	$\mu V/K_{cmb}$	$\mu V/K_{cmb}$
B145W1	77.8	71.7	107.2
B145W2	68.4	59.1	86.2
B145X1	68.4	55.1	91.2
B145X2	65.3	56.0	83.0
B145Y1	75.8	62.6	88.9
B145Y2	78.7	64.4	90.9
B145Z1	59.4	52.8	72.1
B145Z2	38.4	41.6	57.7
B245W	13.7	7.4	54.2
B245X	41.2	34.2	49.4
B245Y	39.8	29.4	47.0
B245Z	38.6	37.2	45.0
B345W	33.0	23.9	35.1
B345X	38.1	27.3	44.1
B345Y	23.3	17.5	25.7
B345Z	36.1	28.7	39.3

Table 4.12: Lab calibration results.

Channel	NET ($\mu K\sqrt{s}$)
B145W1	199.8
B145W2	188.0
B145X1	221.2
B145X2	222.1
B145Y1	183.8
B145Y2	170.8
B145Z1	221.4
B145Z2	379.7
B245W	NA
B245X	421.9
B245Y	437.5
B245Z	472.1
B345W	477.4
B345X	431.1
B345Y	588.8
B345Z	NA

Table 4.13: Pre-flight NET estimates. The calibration is from using the 77K-90K AC-biased results in table 4.12. The noise comes from the data taken with 77 K ndf down load, reported in Table 4.10.

4.11 Polarization Efficiency

In Chapter 5, we discuss the effect of cross-polarization on our measurements of the CMB polarization. Off-axis telescopes and off-axis pixels in on-axis telescopes can induce or rotate polarization. Generally the polarized signal induced by the telescope should be pretty small. Polarized offsets can also be generated by the geometry and emissivity of the mirrors; for example, a polarized offset can be induced if the mirror temperature has a quadrupole moment [34]. For the BOOM03 receiver, our cross-polarization component is mainly from the intrinsic cross-polarization of PSB's and the polarizing grids on the photometers (i.e. a detector nominally sensitive to E_x^2 is sensitive to a small amount of E_y^2). As shown in sections 5.2 and 6.4.1, the polarization efficiency of the detectors enters into the calculation of Q and U showing that the polarization efficiency must be measured accurately in order to prevent intensity signal from leaking into polarized maps.

We can measure polarization efficiency in 2 different situations. In the first situation the cryostat is on the ground and we place a polarized source beneath the window. This tests the polarization efficiency looking through the filters, feed optics, and re-imaging optics. In the second situation, the cryostat is mounted on the telescope and we simulate a far field polarized source.

As we rotate a polarizing grid in front of a partially polarized detector, we see a signal

$$S_{det} = \alpha + \beta \cos^2(\theta_{det} - \theta_{grid}), \tag{4.11.1}$$

where α is the cross polarization contribution (i.e. α is the signal seen when the source has an orientation 90° from the detector). In a properly normalized way, we can write

$$\gamma = \alpha + \beta, \tag{4.11.2}$$

$$\rho = \frac{\beta}{\alpha + \beta}, \tag{4.11.3}$$

$$S_{det} = \gamma(1 - \rho \sin^2(\theta_{det} - \theta_{grid})), \tag{4.11.4}$$

where ρ is the polarization efficiency.

4.12 Cold Optics Test

Figure 4.13 shows the configuration for the cold optics polarization efficiency test. A rotating polarization grid is placed directly beneath the cryostat. It sits above a cold load (liquid nitrogen) which is modulated by a chopper wheel. The chopper wheel is rotated at 2 Hz and the grid has a rotation period of approximately 10 minutes. When the transmission axis of the grid is aligned with the polarization axis of the detector, the detector sees whatever is behind the grid (i.e. the chopper wheel or the cold load). When the grids are 90° out

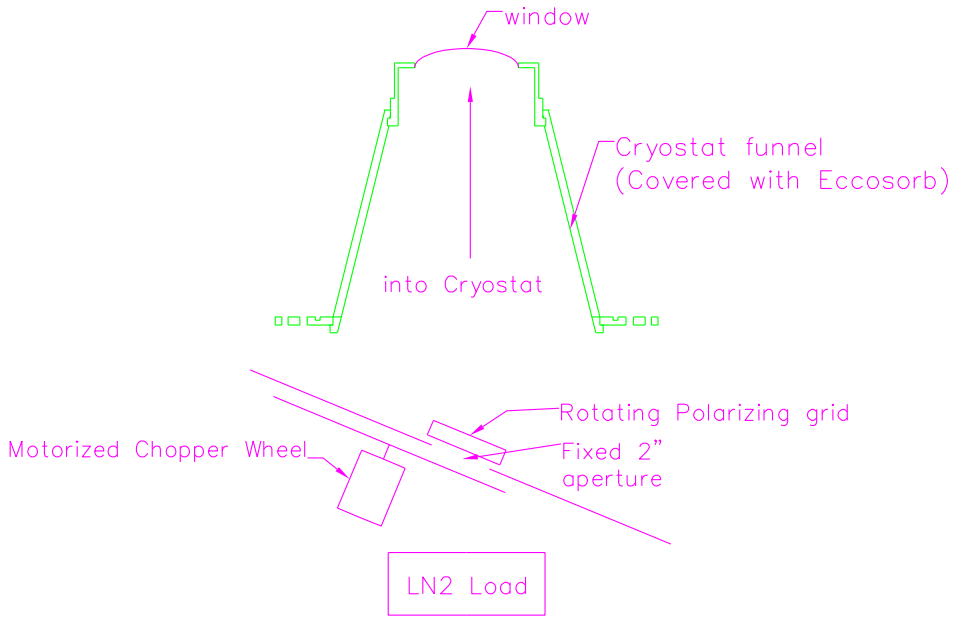

Figure 4.13: The source used for characterizing the polarization efficiency of the cold optics. The system is tilted at 22.5° so that rays reflecting off the grid go to 300 K eccosorb. The aperture of the system is $\sim$ 2 inches. The chopper wheel chops between 77 K and 300 K, while a belt drive rotates the polarizing grid. The chopper wheel rotates at 2 Hz, while the grid has a rotation period of about 10 minutes.

of alignment the detector sees radiation reflected off the grid. This is why it is necessary to tilt the grid. The detector sees 300K when is rotated 90° from the axis of the polarization grid; otherwise if the grid were flat the detector would see internal reflections from the cryostat which could contaminate the measurement. For the cold optics tests we used a tilt angle of 22.5°. The general equation for the signal can be written

$$S_{det} = X_{chop} S_{cold} \cos^2(\theta_{det} - \theta_{grid}) + S_{300K} \sin^2(\theta_{det} - \theta_{grid}), \qquad (4.12.1)$$

where $X_{chop} = 0$ when the chopper wheel is blocking the aperture and $X_{chop} = 1$ when the aperture is clear. This measurement can be done without the chopper wheel; however, it would be far more sensitive to contamination by stray light and spurious reflections. Any signal not synchronous with the chopper can be ignored. As the grid rotates, contributions from the $S_{300K} \sin^2(\theta_{det} - \theta_{grid})$ term show up as long term drifts.

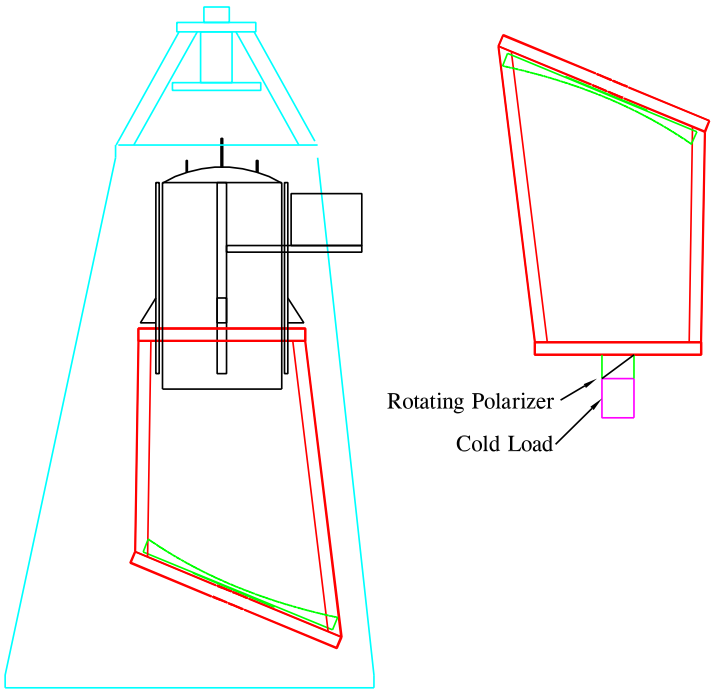

Figure 4.14: Diagram of polarization measurement method using simulated far-field polarization source. A copy of the BOOMERANG primary is used as the collimator. At the focus of the collimator is a polarizing grid and chopper wheel combination similar in spirit to that used in the cold optics test.

4.13 Polarized Far-Field Simulator

To measure the far-field polarization efficiency, we used the spare BOOMERANG primary mirror as a collimator to approximate a far-field polarized source. As shown in figure 4.14, the spare primary was mounted on a copy of the inner frame and inverted. A variable aperture was placed at the focus. Behind the aperture sits a polarizing grid (tilted at 28°) and a chopper wheel which are in front of a cold load. The signal in this situation is basically the same as for the grid rotator used under the cryostat. We did the measurements with two apertures: a beam filling source with FWHM 3° and a pencil beam source of size $\sim 4'$ (plus diffractive effects). The pencil beam source also allowed us to make polarized beam measurements.

4.14 Effect of a Tilted Grid

In the end, our polarization angles should be referenced to the plane tangent to the beam center for each channel. The plane parallel to the bottom of the cryostat and the horizontal plane at the focus of the collimator should be roughly equivalent to the plane of the beam projected onto the sky. When using a tilted grid, there is a small difference between the polarization angle referenced in the plane of the grid and the polarization angle referenced to a horizontal plane. The effective angle in the horizontal plane is determined by projecting the electric field vector from the grid plane

$$\tan\theta_H = \tan\theta_G \cos\phi, \tag{4.14.1}$$

where θ_H is the angle in the horizontal plane, θ_G is the angle in the grid plane and ϕ is the tilt angle with respect to horizontal. Some care must be taken in the definition of the coordinate system. If we let the $\hat{y}$ axis be the axis of symmetry of the telescope, θ_H and θ_G angle are defined with respect to the $\hat{x}$ axis and the tilt is done about the $\hat{x}$ axis. If we tilt the grid about the $\hat{y}$ while keeping the angle definition the same, then we have

$$\tan\theta_H = \frac{\tan\theta_G}{\cos\phi}, \tag{4.14.2}$$

which is equivalent to rotating the coordinate system by 90°. This property of a titled grid can also be found in solutions to Maxwell's equations for a polarizing grid [50].

4.15 Results

The analysis of the polarization efficiency tests is ongoing. The results from the far-field simulator are not as straight forward as we might hope. The general situation is that the PSB's have a polarization efficiency between of $90-95\%$ and the photometer channels have a polarization efficiency $> 98\%$. Figure 4.15 shows the results of the pencil beam test with the far field polarization simulator.

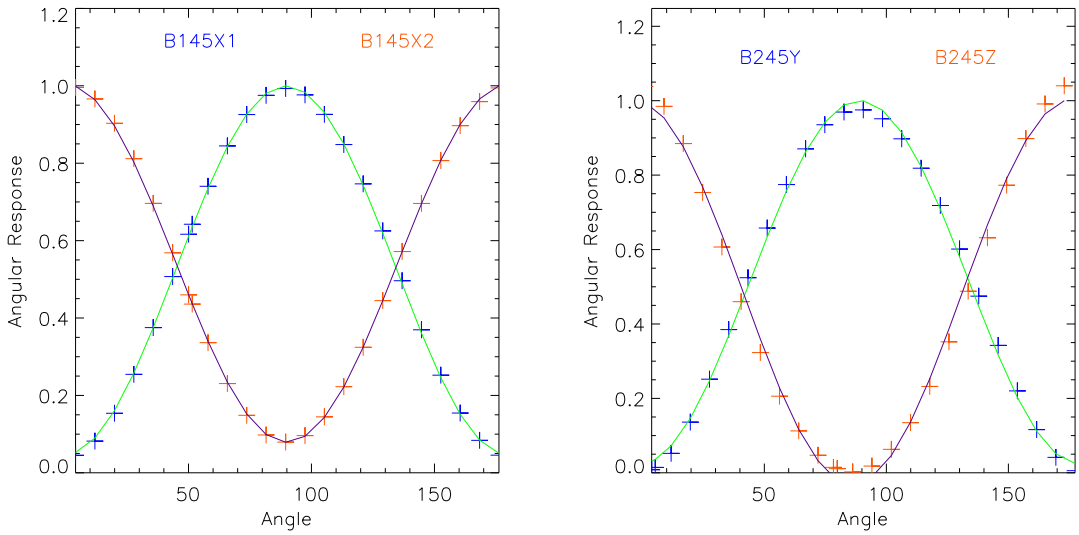

Figure 4.15: Normalized polarization response from the pencil beam test using the far-field polarization simulator. The left panel shows the PSB pair B145X1 and B145X2. The right panel shows the results from channels B245Y and B245Z. These fits have not been adjusted for the angle distortion due to the tilting of the grid. This could explain deviations from the fit seen in the right panel.

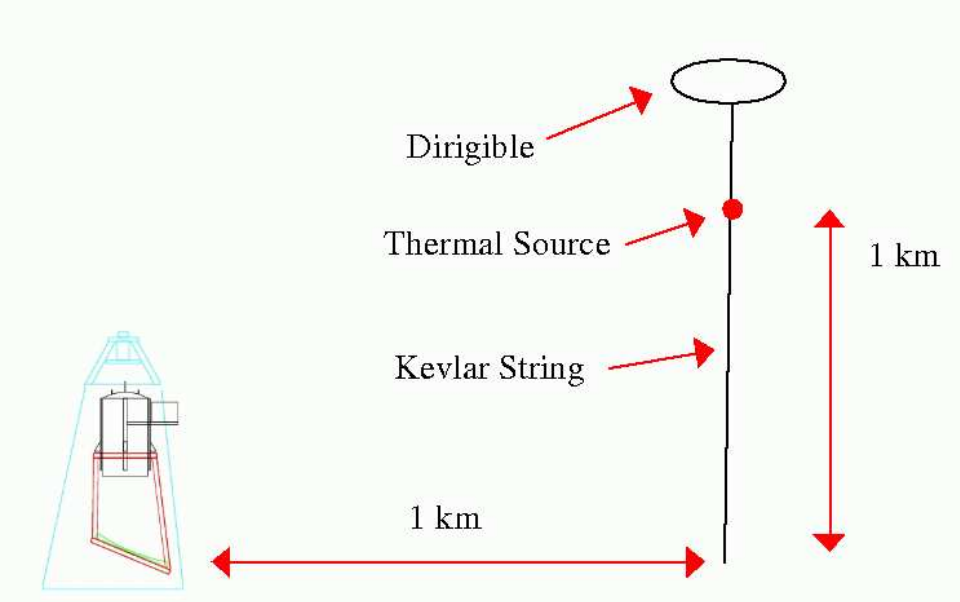

Figure 4.16: Diagram of the pre-flight beam mapping process.

4.16 Pre-Flight Beam Measurement

Because they are bright and compact, planets are the best way to make beam measurements. However, one of the disadvantages of Antarctic ballooning is that the planets are at a low elevation ($\leq 30°$) which is out of the accessible elevation range of BOOMERANG. During flight, we are able to observe galactic sources and three quasars. These observations help to estimate the beam widths, but low signal-to-noise and confusion with other celestial sources makes it is hard to discriminate low amplitude sidelobes.

As discussed earlier, the focal plane is attached the ^{4}He tank inside the cryostat. The tank is suspended by Kevlar ropes. Any tightening or loosening of the ropes moves the focal plane with respect to the cryostat shell. BOOMERANG is focused by raising and lowering the cryostat on the inner frame, changing the distance between the cryostat and the fixed primary.

Our pre-flight beam mapping process consisted of two steps. The focusing of the telescope was done using the far-field polarizing source (figure 4.14) which allowed us to map the beam quickly and easily while making focus adjustments. The second part of the beam measurement involved a tethered eccosorb source (figure 4.16). The source was raised to an altitude of 1 km by a Helium filled dirigible and launched 1 km away from the telescope. With an effective primary illumination of 80 cm, $d^2/\lambda = 320$ m at 150 GHz meaning that 1 km is pretty well into the far field of the telescope. We used two different tethered sources for the

Channel	FWHM (arcminutes)
B145W1	9.8
B145W2	9.8
B145X1	9.6
B145X2	9.7
B145Y1	10.0
B145Y2	10.0
B145Z1	9.9
B145Z2	9.6
B245W	6.2
B245X	6.4
B245Y	6.2
B245Z	6.2
B345W	7.0
B345X	6.7
B345Y	8.0
B345Z	6.9

Table 4.14: Beam sizes calculated from the pre-flight mapping of the tethered thermal source. Measurements are done by fitting to scans over the small eccosorb source.

measurement. A small ball of size ~ 18 inches (giving a $1.5'$ at a 1 km distance) was used for mapping the main lobe of the beam. To map the near sidelobes, we used a large cylinder, 3 ft tall with a 30 inch diameter, which saturated the main beam. A full beam map can be made from the combination of the two measurements. The tracking star camera was used to monitor the location of the source, while the pointing of the telescope was monitored by the gyroscopes and the fixed Sun-sensor (which was viewing a collimated Sun simulator). The beam measurements will ultimately be limited by the uncertainties in the location of the source and sky noise which is a major effect at 345 GHz. Nevertheless, we should be able to measure our sidelobes to less than -25 dB. Table 4.14 shows preliminary full width half maximum (FWHM) beam widths calculated from fits to the small ball data.

Chapter 5

Measuring Polarization

In this chapter we introduce some of the issues involved in making polarization measurements. Unlike the correlation receivers used in POLAR [59], COMPASS [34] and PIQUE [45], where the output of their amplifier chain is a combination of Q and U, each of our detectors measures the total power in one polarization. For example, the signal received by a detector sensitive to the x-component of the electric field would be proportional to E_x^2. In order to measure Q and U, we must combine data from different channels. This issue is complicated by the fact that each of our detectors has a finite cross-polarization ($1\% - 10\%$) meaning that our x-polarized detector is be contaminated with a small amount of E_y^2.

5.1 Definition of Calibration

Before discussing how estimate Q and U from our detectors, it is useful to discuss calibration conventions. CMBFAST [100] is the standard code for determining CMB power spectra, so it is best to use the same conventions for calibrating our detectors. Since our detectors are sensitive to both temperature and polarization signals it makes sense to calibrate our detectors in terms of response to unpolarized CMB temperature anisotropies

$$C = \frac{\Delta V_{bolo}}{\Delta T_{CMB}}, \tag{5.1.1}$$

where C is the calibration factor in V/K_{cmb}. (this is similar to what is done in equation 4.1.9). Consider a PSB pair with no cross-polarization and oriented along the $\hat{x}$ and $\hat{y}$ axes; the signal seen by each detector is T_x and T_y calibrated in terms of CMB anisotropies. Combining the detectors, we have

$$T = \frac{T_x + T_y}{2}, \tag{5.1.2}$$

$$Q = \frac{T_x - T_y}{2}, \tag{5.1.3}$$

where T and Q are calculated in the same units K_{CMB}.

In order to project errors on the CMB power spectra, we need to understand how the NET changes for a polarization experiment. If we have n detectors, the total NET to temperature anisotropies can be defined by

$$NET_T^2 = \left(\sum_i^n \frac{1}{NET_i^2} \right)^{-1}, \tag{5.1.4}$$

with $NET_T = NET/\sqrt{2}$ for a pair of detectors with identical sensitivity. Describing the total polarization error is a bit more tricky. Using equations 5.1.3 and 5.1.4, we find that $NET_Q = NET/\sqrt{2}$ for a pair of identical detectors. In order estimate errors on the power spectra, we need to account for the errors on Q and U

$$\sigma_P^2 = \frac{(\sigma_Q^2 + \sigma_U^2)}{2}, \tag{5.1.5}$$

where $\sigma_P = NET_P/\sqrt{t_{obs}}$, and t_{obs} is the amount of observation time[118, 28]. Since we are only describing 2 detectors in this case, we are not able to measure U. However, if our experiment was set up so that we could spend half our time observing Q and the other half measuring U ($t_Q = t_U = t_{obs}/2$), then we have

$$\sigma_P^2 = \frac{NET_Q^2 + NET_U^2}{t_{obs}}. \tag{5.1.6}$$

If we let $NET_Q = NET_U$, then we get

$$NET_P = \sqrt{2}\ NET_Q = \sqrt{2}\ NET_T. \tag{5.1.7}$$

5.2 Measuring Stokes Parameters by Differencing Detectors

With calibration issues out of the way we can now effectively describe how to measure the Stokes parameters by differencing detectors. The effect of the polarization efficiency (ρ) on one detector is described by equation 4.11.4. In section 6.4.1, the method for combining detectors into I, Q and U maps is described. Here we focus on understanding how cross-polarization, relative calibration and detector orientation affect the measurement of Stoke parameters.

A single linearly polarized detector with no cross-polarization measures a combination I, Q and U in pixel p

$$V_i = \gamma_i (I_p + Q_p \cos(2\alpha) + U_p \sin(2\alpha)) \tag{5.2.1}$$

where α is the polarization orientation of the detector and γ_i is the calibration in V/K_{CMB}. For the case here it is easier for now to just consider the case of a pair

of detectors viewing the same point on the sky with polarizations oriented in the $\hat{x}$ and $\hat{y}$ directions. The general case can be described by applying equations 1.6.8 and 1.6.8 for the rotation of the Stokes parameters. Including the effects of cross polarization we have

$$V_x = 2\gamma_x(E_x^2 + (1-\rho_x)E_y^2), \tag{5.2.2}$$
$$V_y = 2\gamma_y(E_y^2 + (1-\rho_y)E_x^2), \tag{5.2.3}$$

where factor of 2 provides the same normalization used in equations 5.1.2 and 5.1.3. This equation can be rewritten as

$$V_x = 2\gamma_x((1-\frac{\rho_x}{2})I + \frac{\rho_x}{2}Q), \tag{5.2.4}$$
$$V_y = 2\gamma_y((1-\frac{\rho_y}{2})I - \frac{\rho_y}{2}Q). \tag{5.2.5}$$

Solving for I and Q using these equations, we get

$$I = \frac{1}{2}\frac{\frac{V_x}{\gamma_x}\rho_y + \frac{V_y}{\gamma_y}\rho_x}{\rho_x + \rho_y - \rho_x\rho_y}, \tag{5.2.6}$$
$$Q = \frac{1}{2}\frac{\frac{V_x}{\gamma_x}(2-\rho_y) - \frac{V_y}{\gamma_y}(2-\rho_x)}{\rho_x + \rho_y - \rho_x\rho_y}. \tag{5.2.7}$$

If we left $\rho_x = \rho_y = \rho$, then things are a bit simpler

$$I = \frac{1}{2}\frac{\frac{V_x}{\gamma_x} + \frac{V_y}{\gamma_y}}{2-\rho}, \tag{5.2.8}$$
$$Q = \frac{1}{2}\frac{\frac{V_x}{\gamma_x} - \frac{V_y}{\gamma_y}}{\rho}, \tag{5.2.9}$$

illustrating that the cross-polarization creates a loss of efficiency in measuring Q. Since the polarization signal is 10% of the temperature signal, the above equations illustrate the importance of high-precision measurements of the gains and polarization efficiencies in each channel.

5.3 Relating Q and U on the Celestial Sphere

Since Q and U are not rotationally invariant, some care must be taken to ensure that they are properly defined. Figure 5.1 shows the definitions of Q and U used by the IAU [43] and Healpix [36]. They have the identical definition for Q, but $U_{Healpix} = -U_{IAU}$.

Sky rotation changes the orientation of the detector with respect to the celestial sphere. In order to compare observations of Stokes parameters of the same point

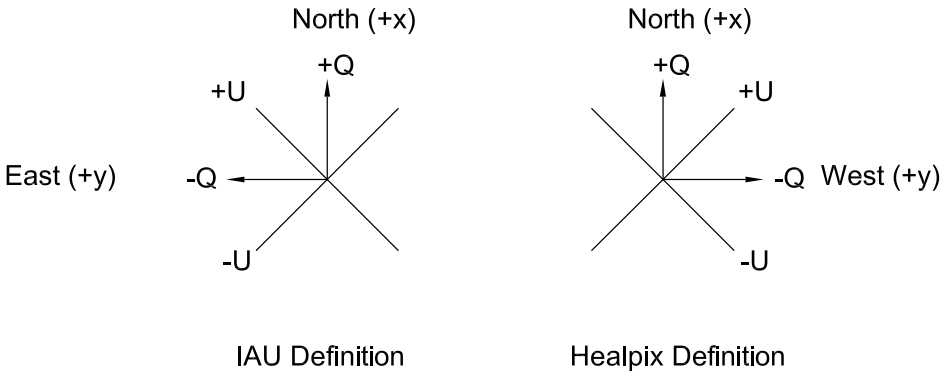

Figure 5.1: Definitions of Q and U on the sky. The left side is the IAU convention [43] and the right side is the Healpix convention [36]. Both coordinate systems are right-handed and are shown from the point of view of an observer looking south (north is overhead). These definitions are identical for Q, but $U_{Healpix} = -U_{IAU}$.

at different times, it is best to transform the Stokes parameters from the local horizon coordinate system to the celestial sphere. This rotation is defined by the angle between 2 great circles which intersect at the observation point. One circle goes through local zenith, and the other runs through the North Celestial Pole (NCP). In spherical geometry [115], this angle (the parallactic angle) can be calculated by

$$\sin(\phi) = \pm \frac{\cos(Latitude)\ \sin(Azimuth)}{\cos(Declination)}, \tag{5.3.1}$$

where the negative sign is chosen if the hour angle (H = (Local Sidereal Time)-(Right Ascension)) is between 0 and 12, and the positive sign is chosen if H is between 12 and 24. A more intuitive but less compact way involves the use of unit vectors on the sphere [109]. These rotation techniques can be used for any rotations of parallactic angle. When calculating the pixel-pixel correlations for Q and U (section 6.6.2), the polarization orientation of each pixel must be rotated so that the coordinate system is defined by the great circle connecting the two pixels.

Chapter 6

Analysis of Flight Data

6.1 From Raw data to CMB maps

Processing the raw flight data so that it can be used for CMB analysis is a long and arduous task. Except for the polarization sensitivity of B00M03, B98 and BOOM03 produce very similar raw data streams. Therefore, there is a lot of overlap in the techniques used for processing the raw data. For the B98 and BOOM03 the following tasks must be completed before we can make maps or measure the power spectrum of the CMB:

- Pointing reconstruction
- Cleaning and deconvolving the bolometer timestream
- Calculate the in-flight transfer function
- Measure the beam shape of each channel
- Determine the calibration
- Calculate the in-flight noise characteristics

In this chapter we give a brief overview of how these issues are dealt with. For more detail see [21, 22, 86, 98].

6.1.1 Pointing Reconstruction

For B98 attitude reconstruction was done using a combination of three sensors: an azimuth Sun sensor, a three-axis rate gyro system, and a differential GPS system. The gyros and GPS were used to calibrate the azimuth Sun sensor. Then the gyros were integrated using the calibrated sun sensor to prevent long term drifts. The pitch and roll are constrained to be zero on long time scales. The pointing offset of each detector was determined by using maps of galactic sources.

From the gyro noise we expect a $2.7'$(1-σ) uncertainty, from the scatter of the galactic source offset measurements we measure an error of $2.5'$ (1-σ).

For BOOM03 , we made number of improvements which should help reduce our pointing reconstruction uncertainty. A tracking star camera and a pointed sun sensor were added to give additional pointing information. The GPS performed much better in this flight. Gyro noise was reduced by adding an integral preserving filter. We hope to achieve a pointing reconstruction uncertainty of less than $1'$ rms.

6.1.2 Spike and Glitch Removal

The bolometer timestream data is contaminated with transient events which must be flagged and removed; these include cosmic ray hits, thermal events in the cold stage, calibration lamp signals, and short periods of electromagnetic interference (EMI). These glitches are found using spike detection and pattern matching algorithms. Also, elevation changes cause long term drifts in the bolometer data which are removed by fitting an exponential to the data.

At the last stage an iterative binning scheme is used: the data is binned into pixels on the sky and individual samples which are more than 4σ from the average value of the pixel were cut. In B98, we found that after 4 iterations, a negligible number of new glitches are found. In B98, approximately 5% of the data is flagged in each channel. This flagged data is replaced by a constrained realization of the noise which preserves noise correlations across gaps (this is vital for map making).

There is a question as to whether it is better to deconvolve the data before finding spikes or to try to find them by using the raw data. Proper deconvolution removes all electronic time delays in the data stream. The electronics and bolometer transfer function could delay a spike by a few samples. This is probably not a big effect since usually 10-100 samples are cut depending on the size of the spike. Another issue is that the AC-coupling filter forces the signal to average to zero on long time scales. Cosmic rays cause the signal to have a long recovery time; $t \sim 1/f_{AC}$, where f_{AC} is the cutoff of the AC-coupling filter. Deconvolution automatically corrects for this, otherwise a decaying exponential may need to be subtracted from the data after a large spike.

There is a disadvantage to deconvolving before searching for spikes. At high frequencies where the transfer function has a small magnitude, the noise can be very large after deconvolution. Since most of the cosmic ray signal is at high frequency, the signal to noise ratio should be roughly the same. However, it may be harder to look for long timescale glitches.

In the B98 analysis, for the most part deconvolution was done before trying to find spikes. However there was one exception to this rule. Any spike which saturated the DAS ($V_{das} > 10\ V$) was cut before deconvolution and replaced with a local average of the data.

6.1.3 In-flight Transfer Function

Cosmic rays hits are surprisingly useful in our data stream. The cosmic rays act like a delta function in power input. This makes them almost ideal for measuring the bolometer transfer function. The system transfer function depends on the AC coupling filter, the anti-aliasing filter, and the bolometer thermal time constant. The properties of the AC-coupling filter and the anti-aliasing filter can be determined on the ground before flight. However, the bolometer time constant is very sensitive to the input optical load which will most likely be different in-flight than on the ground.

The bolometer transfer function can be modeled as a single or double pole RC filter. Since the sampling rate of the bolometer signal is not fast enough to adequately sample the response to the cosmic ray, each cosmic ray is simultaneously fit for an amplitude and phase with respect to the model impulse response function. This method works well for the higher frequencies of the transfer function, but has trouble at very low frequencies (< 100 mHz) since celestial signals and 1/f noise can cause contamination.

For B98 , we used the measured electronics transfer function and the cosmic rays to find the bolometer time constants. With the BOOM03 data, we are able to measure the full transfer function (electronics plus bolometer time constant) using just the cosmic ray data. Figure 6.1 shows the impulse response for three BOOM03 channels. The impulse response is Fourier transformed to give the system transfer function. By dividing out the measured electronics' transfer function, we can recover the bolometer time constant.

6.1.4 Producing the Cleaned/Deconvolved Bolometer Timestream

The raw bolometer timestream needs to be cleaned and deconvolved before it can be used for mapmaking. As described above, cosmic ray events and other glitches need to be found and flagged. We also deconvolve the timestream to remove the effects of the bolometer and electronics transfer.

For the B98 data the deconvolution/despike code pipeline was organized in the following manner:

- Cut the regions where cosmic rays saturate the DAS.
- Deconvolve data.
- Cut and flag spikes and glitches. The spikes and glitches were already found by a different program.
- Remove drifts after elevation changes.

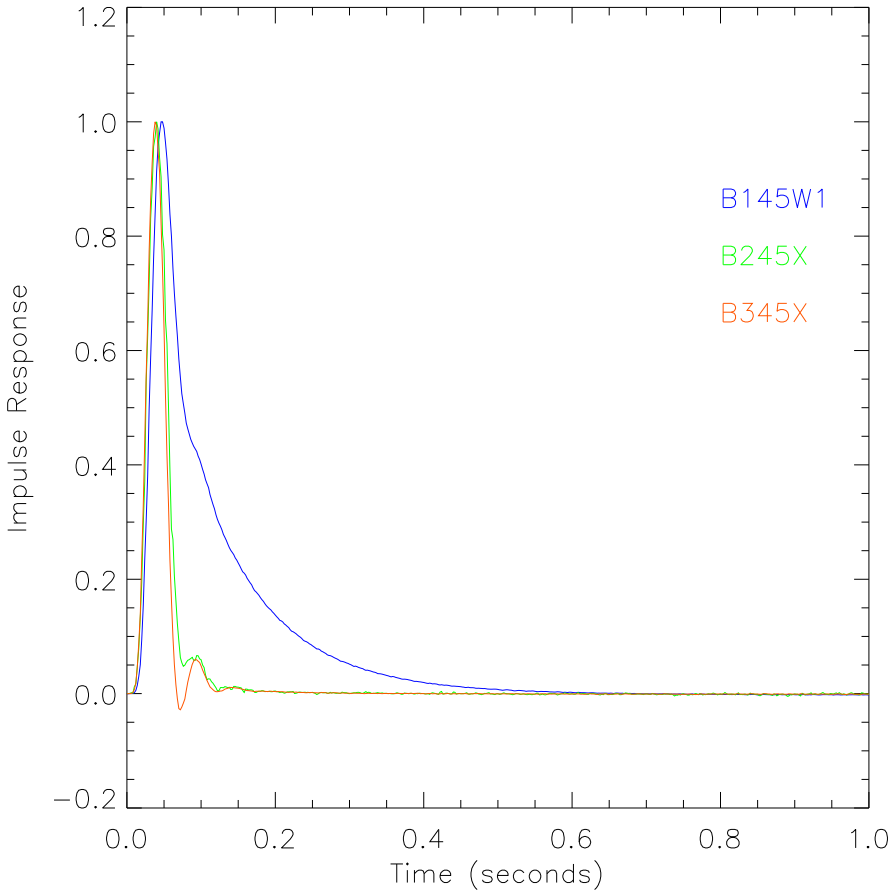

Figure 6.1: Impulse response for three BOOM03 channels B145W1, B245X, and B345X, calculated using cosmic rays. For an individual cosmic ray, the 60 Hz bolometer samples are shifted so that the cosmic ray signal lines up with the more discretely sampled model.

- Linearly interpolate accross the gaps.
- Digitally high-pass filter the data.
- Cut and flag a few more samples around each flagged gap. This removes ringing caused by the filtering. Also, small islands of good data between big gaps are cut.
- Fill gaps with a constrained realization of the noise.

The removal of saturated samples is done because the saturation causes us to lose track of the effect of the AC-coupling filter. Perhaps this not the best thing

to do. The large cosmic rays have a large recovery time. By just cutting the samples where the DAS is saturated, we are unable to make any compensation for the loss of the AC-coupling information. This means that the recovery will not be properly deconvolved. It's hard to say what the best method is for dealing saturated spikes. One easy method is to leave the data in and deconvolve it. This way the recovery is somewhat accounted for. Another legitimate method would be to cut the spike and subtract an exponetial from the recovery. This basically makes it seem like the cosmic ray never happened.

Digital high-pass filtering was done with a transfer function

$$F(f) = \begin{cases} 0.5(1 - \cos(\pi f/0.01)) & f < 0.01\ Hz \\ 1.0 & f > 0.01\ Hz \end{cases} \tag{6.1.1}$$

A cut-off of 0.01 Hz is a pretty good choice since the 3dB point of the analog AC-coupling filter is about 16 mHz in B98 . The digital high pass filtering was necessary because we used a time domain integral to deconvolve the AC coupling filter. This integral method was not very stable and often led to big drifts in the data which were taken care of by the digital high pass filter. Another problem was that the linear interpolation across the gaps sometimes led to problem when we applied the digital high-pass filter. This manifests itself as low frequency contamination in the good data near some of the gaps. This problem was solved by identifying the problem gaps and cutting more data before and after filtering.

6.1.5 Beam Measure

The beam shape of each channel is the combined effect of the mirrors, the spectral response, the feed and the feed's location in the focal plane. When measuring the beam, the source spectrum, and the source distance are also important. Additionally the effective beam is enlarged by the pointing reconstruction error which to first order can be approximated by an isotropic Gaussian contribution to the beam size.

For B98 , beam sizes were determined using 3 methods: in-flight galactic source and quasar observations, pre-flight observations of an eccosorb target in the near field (at a distance of $\approx 300\ m$), and software modelling. The galactic source observations were used to estimate the full width half maxima (FWHM) of the beam, but did not have the sensitivity to map the near sidelobes or deviations from Gaussianity. The eccosorb target measurements had a senstivity of $-20dB$ compared to beam center, but we were not in the far-field. To model the beam, we used the ZEMAX ray-tracing code and a physical optics code written explicitly for our telescope. Both methods provide results compatible with the tethered source measurements.

The galactic sources are not ideal for beam measurement since they have a finite width ($3'$-$5'$ FWHM). However, we are able to get reasonable estimates of

FWHM of our beam by deconvolution. Quasars in our CMB scan region provide a confirmation of our beam FWHM, but in B98 we did not have the signal to noise for a definitive measurement.

For the B98 150 GHz and 90 GHz channels the results from the physical optics code was used to scaled to match the near-field measurements and then extrapolated out to the far field where the FWHM was consistent with the FWHM observed in with scans of the galactic sources. This was convolved with the pointing uncertainty (a $\sigma = 2.5'$ Gaussian) to make the effective beam from which the window function is calculated.

For B00M03, we improved our tethered source measurement by using a helium filled dirigible which allowed us to raise the source to 1 Km in altitude and launch it 1 Km from the telescope (section 4.16). The dirigible allowed for source stability in windy conditions. This puts us well into our far field ($d^2/\lambda = 320\ m$) at 145 GHz. Also, our deep scan region was chosen so that we could integrate deeply on a quasar which should give us a good in-flight beam measurement.

6.2 Calibration

In previous releases of B98 results [26, 86, 98], the CMB dipole was the primary calibrator for the 90, 150, and 240 GHz channels. It was mapped to high precision (0.7%) by COBE/DMR [62]. It an almost ideal calibrator because its spectrum is identical to the spectrum of degree-scale anisotropies and fills the beam for our channels. This makes the calibration independent of both the spectral bandpass and the beam pattern.

Alas, not everything is ideal. Because the dipole is a large scale effect, its signal appears at very low frequency (0.008 Hz in 1 deg/sec and 0.016 Hz in 2 deg/sec scanning modes). On these time scales, the data is plagued by 1/f noise and scan synchronous pickup. Uncertainties in the AC-coupling transfer function and the galactic dust emission can also contaminate the results.

Nonetheless, we are able to make a reasonable calibration using maps made from the data. For the 1 deg/sec data, these maps are fit to a dipole template. This is made from a data stream we get by sampling a dipole map with our pointing timestream then filtering the map with the same filters we used on the real data. For the 2 deg/sec data, the scan synchronous signal dominates the dipole; here a simultaneous fit is made to the dipole template and to a scan synchronous noise template made from a map of a 400GHz channel. To minimize galactic contamination, we only use data with a galactic latitude $b < -15°$ (cutting more data does not make a significant change). At 90 and 150 GHz the 1 deg/sec and 2 deg/s responsivities agrees within about 10% providing a check of both the uncertainty in the AC-coupling transfer function and on the contamination by scan synchronous noise. We assigned a 1σ systematic error of 10% to our calibration due to this 10% agreement between the two scan modes.

For the B98 90 and 150 GHz channels, the calibration was confirmed using galactic source measurements. In January 2000, NGC3576 and RCW 38 were observed at 90 and 150 GHz with the SEST telescopes located at La Silla Observatory in Chile. Due to the small size of the SEST beams and it's $11'$ chop, we could not make extended maps of the sources. We made $4' \times 4'$ maps of the cores of each source, a $10' \times 10'$ map of NGC3576 and a $6' \times 6'$ map of RCW38. From this data we find the source fluxes to be consistent with the dipole calibration to about 6% at 150 GHz and 8% at 90 GHz. The SEST observations and other aspects of the B98 source observations are described in Coble et al.[57].

With the release of the WMAP data [6], absolute calibration is a great deal easier. The WMAP maps allow us to calibrate directly to degree scale CMB anisotropies. In this case, our calibration error could in principle limited by the noise in the WMAP maps. To get an accurate calibration for BOOM03 , we can to cross-calibrate both with WMAP and B98 maps.

Calibrating using CMB maps is not as straight forward as it might seems. It depends both on the mapmaking process and on the relative resolutions of the maps used. The precision of map based calibrations is an important issue in polarization analysis since the relative calibration of elements of a PSB pair must also be known very well. In order to account for different beam sizes, it is probably more convenient to do the relative calibrations using spherical harmonics (C_ℓ's or a_{lm}'s), which allows for easy inclusion of beam effects.

6.3 Mapmaking

To measure the angular power spectrum of the CMB, it is not always necessary to make a map of the data. In principle one could estimate the CMB power spectrum directly from the time-ordered data; however this would probably be extremely costly in terms of computation time. A map allows us to compress the data into a more tractable format for power spectrum estimation. Also it allows for nice pictures. For a scanning experiment such as BOOMERANG, a map is a natural basis. Experiments which employ interferometers [42, 77, 39] tend to work in Fourier space which is the natural basis for their data.

6.4 Temperature Maps

With a cleaned, calibrated, and pointed time stream in hand, we can now begin to make maps. CMB mapmaking has been discussed by many authors. A summary of various methods is described in [108]. The time-ordered data can be described by:

$$d_t = P_{tp}\Delta_p + n_t, \tag{6.4.1}$$

where Δ_p is the pixelized version of the observed sky signal (the true sky signal convolved by the experimental beam), and n_t is the noise timestream after deconvolution of the instrumental filters (e.g. bolometer time constant and/or electronic readout filters). P_{tp} is the pointing matrix which maps pixels from map to the time stream. $P_{tp} = 1$ if sample d_t is observing pixel p, otherwise it is zero.

The simplest map to make is to average all the samples which fall into each pixel. In formal notation this can be written:

$$\Delta_{naive} = (P^\dagger P)^{-1} P^\dagger d, \tag{6.4.2}$$

where $P^\dagger P$ is a diagonal matrix whose elements are the number of samples in each pixel. This method is exactly correct when the noise is white. However, when the time-ordered data (TOD) has 1/f or noise correlations something more is required. Long term drifts can lead to striping along the scan direction and perhaps destroying small scale information. By applying an appropriate high-pass filter to the data, sensible naive maps can be made with the cost of losing information on long wavelength modes in the map. In matrix terms this can be represented by

$$\Delta_{naive} = (P^\dagger P)^{-1} P^\dagger M d, \tag{6.4.3}$$

where $M = F^\dagger F$ is a matrix representation of the filter function and F is the time domain representation of the filter.

Because high-pass filtering requires the data to average to zero on long time scales, artifacts can be introduced into the map. This is especially a problem near the galactic plane where the brightness of the galaxy can cause shadows in the regions directly off the plane. Similarly the filtering introduces path dependence to the data. The filtered value of d_t at pixel p depends on the signal in pixels the detector has recently passed through. For a noiseless TOD, this introduces a non-zero variance in each pixel.

To alleviate these problems an unbiased method is called for. We can make a minimum variance (or maximum likelihood) map by minimizing the equation $\chi^2 = (d - P\Delta)^\dagger N^{-1} (d - P\Delta)$ where $N \equiv N_{tt'} = < n_t n_{t'} >$ is the time-time noise correlation matrix. The solution to this equation is:

$$\Delta = (P^\dagger N^{-1} P)^{-1} P^\dagger N^{-1} d, \tag{6.4.4}$$

where the matrix $N_{pp'} \equiv P^\dagger N^{-1} P$ is the pixel-pixel noise correlation matrix (It is diagonal when the noise is white.). The operation $N^{-1} d$ (often called a pre-whitening filter) decorrelates the data. In principle, this map should be unbiased and free of stripes along the scan direction. In practice it may still be necessary to cut out the low frequency signal. This can be done by de-weighting the long time scale modes in $N_{tt'}$. However, if 1/f noise is correlated (e.g. scan synchronous) then it is more appropriate to filter the data. The filtering can be accounted for

by replacing P by FP, where F is the filter, or more transparently by replacing N^{-1} with $F^{\dagger}N^{-1}F$ [94].

The downside of the brute force maximum likelihood method is that the matrix $N_{pp'}^{-1}$ must be inverted. This matrix has a size of N_{pix}^2 and the inversion is a N_{pix}^3 process. At $7'$ pixelization, the B98 maps have about 100,000 pixels in the main CMB region. Direct inversion of this matrix requires a fair chunk of time on a large parallel machine. Iterative methods [94, 85, 30] have been developed to make this process run on a single PC in less than 1 hour for a B98 map. These techniques are based on conjugate gradient solvers. These iterative methods can solve for the map, but are not able to output $N_{pp'}$ which is necessary for likelihood based C_l estimation.

Another way to make maps is to use the noise-shaping techniques described in [34]. In this case, the noise was white except for a stable scan synchronous component. By fitting out the scan synchronous signal, the noise was effectively whitened and maps could be made by binning the data. The computational price for this is that one must use constraint matrices to keep track of the modes which are lost by fitting out the scan synchronous component [13]. The constraint matrices play a role similar to $N_{pp'}^{-1}$ in the C_l estimation.

6.4.1 Making Polarization Maps

To make a polarization map, we can use most of the machinery described in the previous section. We just need to increase the number of pixels by a factor of 3 (maps for I, Q, and U) and keep track of the polarization orientation of the detector.

6.4.2 Case of No Cross-polarization

As stated in section 5.2, the output of a polarized detector (with no cross-polarization) viewing a pixel p is a combination of I, Q, U and instrument noise

$$d_t = (I_p + Q_p \cos(2\alpha_t) + U_p \sin(2\alpha_t)) + n_t, \tag{6.4.5}$$

where α_i is the orientation of the polarizer with respect to a fixed coordinate system (section 5.3). Also note that in this case the detector is implicitly assumed to calibrated with respect to its response to an unpolarized source.

To make maps of polarized data, we can still use the maximum likelihood mapmaking equation 6.4.4, we just need to modify our definition of the map (Δ) and the pointing matrix (P). We can redefine Δ as a $3N_{pix}$ long vector which is the concatenation of the I, Q and U maps:

$$\Delta = \begin{pmatrix} I \\ Q \\ U \end{pmatrix}. \tag{6.4.6}$$

For temperature maps, the pointing matrix is a $N_{sample} \times N_{pix}$ matrix. To account for the polarization orientation we can redefine P as a $N_{sample} \times 3N_{pix}$ matrix

$$P = \left(P^I P^Q P^U\right), \tag{6.4.7}$$

where P^I, P^Q and P^Q are the individual pointing matrices for the I, Q and U maps. P^I is identical to the pointing matrix used in the temperature map making section. To calculate P^Q, the non zero values of P^I are replaced by $\cos(2\alpha_t)$, and for P^U the nonzero values are replaced by $\sin(2\alpha_t)$.

Now we can solve for the map $\Delta = (P^\dagger N_{tt'}^{-1} P)^{-1} P^\dagger N^{-1} d$. To illustrate some of the complexities of polarization measurements it is useful at this point to assume that $N_{tt'}$ proportional to the identity matrix (white noise). Now we just have to compute $\Delta = (P^\dagger P)^{-1} P^\dagger d$. Expanding $P^\dagger P$, we get 9 $N_{pix} \times N_{pix}$ matrices

$$P^\dagger P = \begin{pmatrix} P^{I\dagger}P^I & P^{I\dagger}P^Q & P^{I\dagger}P^U \\ P^{Q\dagger}P^I & P^{Q\dagger}P^Q & P^{Q\dagger}P^U \\ P^{U\dagger}P^I & P^{U\dagger}P^Q & P^{U\dagger}P^U \end{pmatrix}. \tag{6.4.8}$$

As discussed in the previous chapter $(P^{I\dagger}P^I)_{pp'} = n_p \delta_{pp'}$, the number of times pixel p is observed. Calculating the other elements (which are all diagonal matrices) we get

$$(P^{I\dagger}P^Q)_{pp} = n_p \langle \cos(2\alpha_t) \rangle, \tag{6.4.9}$$

$$(P^{Q\dagger}P^Q)_{pp} = n_p \left\langle \cos(2\alpha_t)^2 \right\rangle, \tag{6.4.10}$$

$$(P^{U\dagger}P^U)_{pp} = n_p \left\langle \sin(2\alpha_t)^2 \right\rangle, \tag{6.4.11}$$

$$(P^{I\dagger}P^U)_{pp} = n_p \langle \sin(2\alpha_t) \rangle, \tag{6.4.12}$$

$$(P^{Q\dagger}P^U)_{pp} = n_p \langle \cos(2\alpha_t) \sin(2\alpha_t) \rangle, \tag{6.4.13}$$

where $\langle x \rangle$ denotes the average of the values of x which land in pixel p. The terms $P^{I\dagger}P^Q$, $P^{I\dagger}P^U$ and $P^{Q\dagger}P^U$ are zero if the observation angles (α_t) are distributed uniformly between 0° and 180°.

In $P^\dagger P$ there are no elements which relate pixels viewing different points on the sky. Taking advantage of this fact, we can rearrange the matrix so that we are solving for I, Q, and U in each pixel. Defining S as the vector of Stokes parameters

$$S = \begin{pmatrix} I \\ Q \\ U \end{pmatrix}, \tag{6.4.14}$$

we can write

$$S = (A^\dagger A)^{-1} A^\dagger m, \tag{6.4.15}$$

where m is the vector of n_p time samples which are in pixel p. Next we find

$$A = \begin{pmatrix} 1 & \cos 2\alpha_1 & \sin 2\alpha 1 \\ \vdots & \vdots & \vdots \\ 1 & \cos(2\alpha_n) & \sin(2\alpha n) \end{pmatrix}.$$

Expanding $A^\dagger A$ we get the inverse of the Stokes parameter covariance matrix

$$A^\dagger A = \begin{pmatrix} n_p & \sum_1^{n_p} \cos(2\alpha_t) & \sum_1^{n_p} \sin(2\alpha_t) \\ \sum_1^{n_p} \cos(2\alpha_t) & \sum_1^{n_p} \cos^2(2\alpha_t) & \sum_1^{n_p} \cos(2\alpha_t)\sin(2\alpha_t) \\ \sum_1^{n_p} \sin(2\alpha_t) & \sum_1^{n_p} \cos(2\alpha_t)\sin(2\alpha_t) & \sum_1^{n_p} \sin^2(2\alpha_t) \end{pmatrix}. \quad (6.4.16)$$

Writing it this way. we see that I, Q, and U can be solved for by inverting a 3×3 matrix for each pixel; however, I, Q, and U may be highly correlated.

Because the polarization orientation is fixed, the change in α is small for the BOOM03 detectors. Sky rotation causes a variation of approximately 10°. For B00M03, it will almost impossible to make useful polarization maps using only 1 detector.

To add an additional channel, we can add the new channels data stream to the end of d, making a new time-ordered vector of length $2 * N_{samples}$

$$d^{new} = \begin{pmatrix} d \\ e \end{pmatrix}, \quad (6.4.17)$$

where d and e represent the timestreams of the individual detectors. Similarly the pointing matrix can be adjusted

$$P^{new} = \begin{pmatrix} P^I & P^Q & P^U \\ R^I & R^Q & R^U \end{pmatrix}, \quad (6.4.18)$$

where P is the pointing matrix for timestream d, and R is the pointing matrix for timestream e. This way of adding additional channels shows that is relatively easy to make maps of multiple channels. If we add in an additional channel with the same pointing but an orthogonal polarization orientation (assuming the same white noise level), it measures

$$e_t = (I_p - Q_p \cos(2\alpha_t) - U_p \sin(2\alpha_t)) + n'_t, \quad (6.4.19)$$

and we have $P^I = R^I$. For the combined map, the Stokes parameter matrix now takes the form

$$A^\dagger A = \begin{pmatrix} 2n_p & 0 & 0 \\ 0 & \sum_1^{n_p} 2\cos^2(2\alpha_t) & \sum_1^{n_p} 2\cos(2\alpha_t)\sin(2\alpha_t) \\ 0 & \sum_1^{n_p} 2\cos(2\alpha_t)\sin(2\alpha_t) & \sum_1^{n_p} 2\sin^2(2\alpha_t) \end{pmatrix}, \quad (6.4.20)$$

where the full matrix can be understood as the sum of $A_d^\dagger A_d + A_e^\dagger A_e$. The addition of the orthogonal detector decorrelates the polarization information from the intensity, but we don't get an unambiguous measurement of Q and U.

In general it takes at least three detector orientations to determine the all three Stoke parameters. Couchot et. al [20] show that $A^\dagger A$ becomes diagonal when there are three or more detectors whose polarization orientations are distributed uniformly over 180°.

6.4.3 Including Cross-polarization

As discussed in section 5.2, cross-polarization requires a bit of extra work. In the spirit of equations 5.2.4 and 5.2.5, we can write the general solution for signal seen by a polarized detector with polarization efficiency ρ

$$d_t = 2C\ (I_p(1-\frac{\rho}{2}) + \frac{\rho}{2}(Q_p\cos(2\alpha_t) + U_p\sin(2\alpha_t))) + n_t, \tag{6.4.21}$$

where C is the ratio measured calibration to the true calibration. This reduces to equation 6.4.5 if $\rho = 1$ and $C = 1$. Following the techniques of the previous section, we can derive an expression for $A^\dagger A$ for a single detector

$$A^\dagger A = 2C \begin{pmatrix} n_p(1-\frac{\rho}{2})^2 & \frac{\rho}{2}(1-\frac{\rho}{2})\sum_1^{n_p}\cos(2\alpha_t) & \frac{\rho}{2}(1-\frac{\rho}{2})\sum_1^{n_p}\sin(2\alpha_t) \\ \frac{\rho}{2}(1-\frac{\rho}{2})\sum_1^{n_p}\cos(2\alpha_t) & (\frac{\rho}{2})^2\sum_1^{n_p}\cos^2(2\alpha_t) & (\frac{\rho}{2})^2\sum_1^{n_p}\cos(2\alpha_t)\sin(2\alpha_t) \\ \frac{\rho}{2}(1-\frac{\rho}{2})\sum_1^{n_p}\sin(2\alpha_t) & (\frac{\rho}{2})^2\sum_1^{n_p}\cos(2\alpha_t)\sin(2\alpha_t) & (\frac{\rho}{2})^2\sum_1^{n_p}\sin^2(2\alpha_t) \end{pmatrix}. \tag{6.4.22}$$

If we add an orthogonal polarized detector with an independent value of ρ, the resulting matrix will still have a non-zero coupling between intensity and polarization. This does not mean that it is impossible to separate I, Q and U cleanly, just that the cross-polarization introduces an extra coupling which must be accounted for.

6.5 Noise Estimation

In the old days, CMB experiment had such low signal to noise that one could estimate the noise by taking the power spectrum of the timestream voltage. With more sensitive detectors, the CMB anisotropy signal in the raw timestream cannot be neglected. This requires the noise estimation to be an iterative process [94]. In each iteration a maximum likelihood map is made and the noise spectrum for the next iteration is calculated by subtracting the map from the time stream. In the first iteration, the timestream is assumed to be all noise. The noise spectrum converges after 3-5 iterations. This process was used for all three B98 power spectrum releases [26, 86, 98].

The noise estimation method is described schematically below. The iterations are labeled by α. $\mathbf{d}$, $\mathbf{P}$, $\mathbf{n}^{(\alpha)}$,$\mathbf{N}^{(\alpha)}$, and $\mathbf{\Delta}^\alpha$ are the bolometer timestream, pointing matrix, noise time stream, noise times-time correlation matrix, and sky map respectively.

1. Given the bolometer timestream and estimated map, solve for the noise-only timestream with $\mathbf{n}_t^{(\alpha)} = \mathbf{d}_t - \mathbf{P}_{tp}\mathbf{\Delta}_p^{(\alpha)}$.

2. Use $\mathbf{n}_t^{(\alpha)}$ to construct the noise times-time correlation matrix, $\mathbf{N}_{tt'}^{(\alpha)} = \langle \mathbf{n}_t^{(\alpha)}\mathbf{n}_{t'}^{(\alpha)\dagger}\rangle$.

3. Solve for a new version of the map using $\mathbf{\Delta}^{(\alpha+1)} = (\mathbf{P}^\dagger\mathbf{N}^{(\alpha)-1}\mathbf{P})^{-1}\mathbf{P}^\dagger\mathbf{N}^{(\alpha)-1}\mathbf{d}$.

4. Return to step 1, using the new version of the map, and repeat. Iterate until the map $\mathbf{\Delta}$ and the noise correlation matrices $\mathbf{N}_{tt'}$ are stable.

In step 3, the maximum likliehood map ($\mathbf{\Delta}^{(\alpha+1)}$) is solved for using a conjugate gradient method [30]. The noise is assumed to be stationary over subsets of the time stream. This means that $\mathbf{N}_{tt'}$ is diagonal in Fourier space. The operation $\mathbf{N}^{(\alpha)-1}\mathbf{d}$ can be done in Fourier space. A separate $\mathbf{N}_{tt'}$ is computed for each subset of the data.

Figure 6.2 shows the noise for channel B150A during the flight. The noise spectra are calculated for the two scan modes (1 deg/s and 2 deg/s), and are compared to the expected CMB signal. This shows that the CMB contributes a significant portion of the signal, especially at low frequency.

Figures 6.3, 6.4, and 6.5 show the noise stability of B150A over the course of the B98 flight. The plots are made by averaging the power spectra taken each minute during a 72 minute chunk. Figure 6.3 shows the power spectrum from $f = 1 - 9$ Hz while Figure 6.4 shows the variation in low frequency portion of the power spectrum ($f = 0.1 - 1$ Hz). Figure 6.5 shows the average over the spectral bins for frequencies $f = 1 - 9$ Hz (top panel) and $f = 0.1 - 1$ Hz (bottom panel). Between 1 Hz and 8 Hz, the power spectrum is quite stable. Above 8 Hz, there is a line which migrates from 8 Hz to 9 Hz over the course of the flight. This is likely to be related to aliasing of the bias frequency into the signal band, as discussed in 4.8.5.

6.6 Estimating the Power Spectrum

6.6.1 General Considerations and the Temperature Spectrum

If the CMB can be described by a Gaussian random field, then its statistical properties can be completely described by its power spectrum [10]. Temperature anisotropies are scalar quantities which can be expanded into spherical harmonics on the celestial sphere

$$a_{\ell m} = \int d\Omega \; T(\theta,\phi) Y_{\ell m}(\theta,\phi), \tag{6.6.1}$$

with

$$T(\theta,\phi) = \sum_{\ell,m} a_{\ell m} Y_{\ell m}(\theta,\phi). \tag{6.6.2}$$

If the $T(\theta,\phi)$ is Gaussian random field then the ensemble average $\langle a_{\ell m} \rangle = 0$ and

$$\langle a_{\ell m} a_{\ell' m'} \rangle = \delta_{\ell\ell'}\delta_{mm'} < C_\ell > . \tag{6.6.3}$$

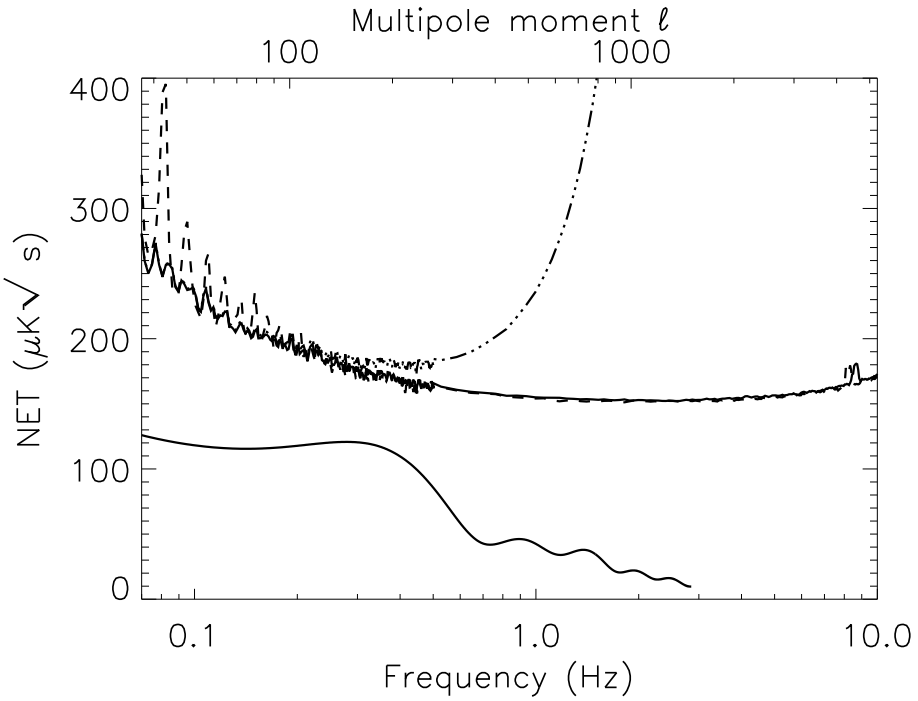

Figure 6.2: Noise spectra from the B98 flight for channel B150A (from Crill et al. [22]). The two noise spectra are for 1 deg/s (solid line) and 2 deg/s (dashed line) scan modes. The lines at $f < 0.1$ Hz are harmonics of the scan frequency. The noise increase at high frequency is due to the bolometer time constant, $\tau = 10.8$ ms. The top x-axis shows the corresponding spherical harmonic multipole mode for the 1 deg/s scan rate ($\ell \sim 180/\theta$). The dot-dashed line is the 1 deg/s noise spectrum convolved with a $10'$ beam giving the effective sensitivity as a function of frequency and multipole. The smooth solid line at the bottom of the plot is the expected CMB signal.

We can estimate C_l from the a_{lm}'s:

$$C_\ell = \frac{1}{2l+1} \sum |a_{\ell m}^2|. \tag{6.6.4}$$

If the $a_{\ell m}$'s are Gaussian then C_ℓ contains all the information in the map. In real space C_ℓ is related to the angular correlation function

$$C(\theta) = \sum \frac{(2l+1)}{4\pi} C_\ell P_\ell(\cos\theta), \tag{6.6.5}$$

where $P_l(\cos\theta)$ is a Legendere polynomial.

The C_ℓ spectrum relates the theory of primordial perturbations to the CMB signal we can measure on the sky. Given values for various cosmological parameters (Ω_{tot}, Ω_{baryon}, Ω_Λ, Ω_{cdm}, H_o etc...) and some assumptions about the

form of the primordial perturbations, it is possible to calculate the expected C_l spectra [100]. Since the C_l's only provide information in 2 spatial dimensions, a measurement of C_l over the full sky at one point in the universe will be subject a fundamental uncertainty known as cosmic variance. For each multipole the cosmic variance can be written as

$$(\Delta C_\ell)^2 = \frac{2C_\ell}{2l+1}. \tag{6.6.6}$$

Generally it is very hard to make a CMB map of the full sky. Only sattelite experiments are able to map the full sky, but even their maps will be contaminated by galactic foreground emission. With maps at many different frequencies, this contaminating emission near the galactic plane can in principle be removed leaving only CMB. Also, full sky coverage is not always optimal; the optimal sky coverage depends on the sensitivty and the angular scales of interest.

A number of techniques have been developed for C_ℓ estimation in the case of partial sky coverage and in the presence of instrument noise [13, 87, 47]. Here we describe general methods for C_l estimation.

In map space we can model the data as

$$\Delta_{obs} = \Delta_{sky} + \Delta_{noise}, \tag{6.6.7}$$

where the signal map (which is convolved with the experimental beam) and the noise map are both independent and have zero mean. The correlation matrices are given by

$$C_T = < \Delta_{sky} \Delta_{sky}^T >, \tag{6.6.8}$$

$$C_N = < \Delta_{noise} \Delta_{noise}^T >, \tag{6.6.9}$$

where $C_N = N_{pp'}$ (the noise correlation matrix as defined in section 6.3). The theory covariance matrix can be written as

$$C_{Tpp'} = \sum_\ell \frac{2\ell+1}{4\pi} B_\ell^2 C_\ell P_\ell(\chi_{pp'}), \tag{6.6.10}$$

where $\chi_{pp'}$ is the angle separating the 2 pixels and B_ℓ is the beam window function. This is the angular correlation function weighted by the beam. As described in section 6.3, the process of mapmaking can introduce correlations or mode loss (more generally called constraints) which need to be accounted for in the C_ℓ estimation. The constraints can be accounted for with an extra correlation matrix (C_C). The form of the constraint matrix depends on the mapmaking process. O'dell et al.'s discussion of the POLAR analysis [88] provides detailed examples of how to build constraint matices.

When building the theory correlation matrix it is usually more efficient to combine the multipoles into a small number of bands. For a non-full-sky

experiment, individual mulitpole moments will be highly correlated with their nearest neighbors. Combining multipoles decreases correlation while increasing the signal to noise. This also decreases the number of free parameters in the likelihood estimation; thereby reducing computation time.

In a particular bin, $C_\ell = C_b C_\ell^{shape}$ where C_ℓ^{shape} is an optimal shape function for the spectrum expected across the bin and C_b is the power in the bin. The effect of binning can easily be accounted for in parameter estimation and for narrow bins the choice of shape does not matter very much. For the B98 results, we chose $\ell(\ell+1)C_\ell^{shape} = \text{constant}$. The traditional way of calculating the power spectrum involves the transformation $\mathcal{C}_\ell = \ell(\ell+1)C_\ell/2\pi$ which sets $\mathcal{C}_\ell$ to be roughly constant on large scales. Although the standard convention may be to use $\mathcal{C}_\ell$, we will keep everything in terms of C_ℓ for the rest of this section.

For the latest release of B98 (Ruhl et al.) [98], we used 22 bins. The first bin ($\ell \leq 25$) and the last bin ($\ell \geq 1026$) are used as junk bins to prevent power from being aliased into the other bins. The middle 20 bins had a width $\Delta\ell = 50$ and centered at $\ell = 50, 100, 150, 200, ...1000$.

The likelihood of a given set of C_ℓ's given our data and noise is

$$P(\Delta|C_\ell) = \frac{1}{(2\pi)^{n_p/2} Det(C_T(C_\ell) + C_N + C_C)^{1/2}} \exp[-\frac{1}{2}\Delta^T (C_T(C_\ell)+C_N+C_C)^{-1}\Delta)] \tag{6.6.11}$$

where n_p is the number of pixels in the map and $C_\ell = C_b C_\ell^{shape}$ where C_b is the bandpower. The best fit power spectrum is determined by maximizing the likelihood $P(\Delta|C_\ell)$. The most likely power spectra can be computed using brute force likelihood evaluation [87], quadratic estimator methods [13], or Monte Carlo methods [47]. Quadratic estimators, for example, work by assuming the likelihood is Gaussian (which is a good approximation near the likelihood peak) and then Taylor expanding the likelihood. Given an initial guess, the maximum likelihood can be found by correcting the initial bandpowers by

$$\delta C_b = -\sum_{b'} \left[\frac{\partial^2 ln P(\Delta|C_\ell)}{\partial C_{b'} \partial C_b}\right]^{-1} \frac{\partial P(\Delta|C_\ell)}{\partial C_{b'}}. \tag{6.6.12}$$

After a few iterations the bandpowers should converge on a most likely value.

The uncertainty in the estimate of C_ℓ is related to the inverse curvature of the log likelihood about the maximum likelihood point.

$$(\Delta C_\ell)^2 = -\left(\frac{\partial^2 ln P(\Delta|C_\ell)}{\partial C_\ell^2}\right)^{-1}. \tag{6.6.13}$$

The curvature of the likelihood can be parametrized by

$$(\Delta C_\ell)^2 == f_{sky}^{-1} \frac{2}{2\ell+1}\left(C_\ell + \frac{N_\ell}{B_\ell^2}\right)^2, \tag{6.6.14}$$

where f_{sky} is a fudge factor to account for the increase in error due to loss of sky coverage and N_ℓ is the noise power as a function of ℓ. In practice, the curvature of the likelihood is used to estimate the error, because it is often difficult to calculate N_ℓ from the C_N. Equation 6.6.13 is strictly correct only if C_ℓ had a Gaussian probabilty distribution. In general, the probability distribution of (usually done in terms of $\mathcal{C}_\ell = \ell(\ell+1)C_\ell/2\pi$) is better parametrized as an offset log normal distribution [14]. This error estimate is also related to the Fisher information matrix for the bandpowers

$$F_{bb'} = -\frac{\partial^2 ln P(\Delta|C_\ell)}{\partial C_b \partial C_{b'}}, \tag{6.6.15}$$

where the diagonal ($b = b'$) terms are the inverse uncertainties for each bin and the off-diagonal terms describe correlations between multipole bins.

For the Ruhl et al. results [98], we used two power spectrum estimation pipelines: MADCAP [15] (a matrix quadratic estimator method), and MASTER/FASTER [47, 19] (a Monte Carlo based method).

MADCAP computes a maximum likelihood map and noise correlation matrix, and then estimates C_l spectra using a Newton-Raphson method to find the maximum likelihood spectrum. MADCAP is able to solve for the most likely power spectra using map based constraints which allow for marginalization over galactic foreground templates and any other contaminated modes in the map. Its drawback is that the number of operations scales as N_{pix}^3 and the memory requirements scale as N_{pix}^2. In the lastest release of B98 , $92,000$ $7'$ pixels were used in the MADCAP analysis.

The Master/Faster method uses naively binned maps which are made by highpass filtering the data. For the B98 data, we used a brickwall filter with $f_c = 0.1\ v_{az}$ Hz. The power spectrum on the cut sky is calculated using a fast $O(N_{pix}^{1/2}\ell)$ spherical harmonic transformation based on the Healpix pixelization method [37]. When calculating the spherical harmonic transform, a non-uniform weight can be applied to the map. We tried a variety of weightings including $1/N$ (inverse noise weighting), $1/(S+N)$ (a total variance filter) and $S/(S+N)$ (which is like a Weiner filter). S is the pixel signal variance calculated from Monte Carlo simulations. It is nonzero when a highpass filter is applied to the data. N is the noise variance in a pixel. We found that $1/(S+N)$ gave the best results [98].

Because the maps cover only part of the sky, the power spectra calculated with this method ($\widetilde{C}_\ell$) is not the true power spectrum; individual multipoles are correlated. The time domain filter and any spatial filters can also introduce bias. Timestream noise must also be accounted for. These affects can be accounted for by writing the cut sky power spectrum as a function of these effects and the real power spectrum,

$$\left\langle \widetilde{C_\ell} \right\rangle = \sum_{\ell'} M_{\ell\ell'} F_{\ell'} B_{\ell'}^2 \left\langle C_{\ell'} \right\rangle + \left\langle \widetilde{N_\ell} \right\rangle. \tag{6.6.16}$$

C_ℓ is the full sky power spectrum. $M_{\ell\ell'}$ is the mode coupling matrix which accounts for correlations induced by the cut sky; it is computed analytically using Clebsch-Gordan coefficients. B_ℓ is the full window function which is the effective experimental window function convolved with the Healpix pixel window function. F_ℓ is the transfer function which accounts for modes lost to time domain and spatial filtering; it can be calculated using roughly 600 Monte Carlo simulations of signal-only maps. $\widetilde{N_\ell}$ is cut sky noise power spectrum from roughly 750 noise-only Monte Carlos. In the Monte Carlo simulations, the pointing and flag information from the channel under consideration is used with the fake noise and/or fake signal to create the simulated maps.

The great advantage of the Master/Faster technique is that the signal and noise are represented in a basis where they are simultaneously diagonal. This allows for the construction of a fast quadratic estimator (FASTER) which works in the basis of the cut sky variables. It converges on the maximum likelihood power spectrum with its output expressed in terms of the full sky power spectra C_ℓ. The uncertainties on the measured bandpowers come from the curvature of the likelihood at it's peak.

6.6.2 The Polarization Power Spectrum

Although the polarization power spectrum is a more complicated than the temperature case, the same basic tools used for estimating the temperature power spectrum can be used for the polarization spectrum.

The Stokes parameters Q and U transform as

$$Q' = Q\cos(2\alpha) + U\sin(2\alpha), \tag{6.6.17}$$
$$U' = -Q\sin(2\alpha) + U\cos(2\alpha), \tag{6.6.18}$$
$$\tag{6.6.19}$$

which means that the combinations $Q \pm iU$ transform like spin-2 quantities. These quantities need to be expanded in terms of spin-weighted spherical harmonics ${}_{\pm 2}Y_\ell^m$ [118]

$$(Q+iU)(\theta,\phi) = \sum_{lm} a_{2,\ell m}\ {}_2Y_{\ell m}(\theta,\phi), \tag{6.6.20}$$
$$(Q-iU)(\theta,\phi) = \sum_{lm} a_{-2,\ell m}\ {}_{-2}Y_{\ell m}(\theta,\phi). \tag{6.6.21}$$

By taking linear combinations of $a_{2,\ell m}$ and $a_{-2,\ell m}$ we can define

$$a_{E,\ell m} = -(a_{2,\ell m} + a_{-2,\ell m})/2, \tag{6.6.22}$$
$$a_{B,\ell m} = -(a_{2,\ell m} - a_{-2,\ell m})/2i, \tag{6.6.23}$$

where $a_{E,\ell m}$ are components of E-mode polarization which transforms evenly under parity and $a_{B,\ell m}$ represent the B-mode polarization which changes sign under a parity transformation. This linear combination allows us to treat E and B in a similar manner to temperature in that we can use $a_{E,\ell m}$ and $a_{B,\ell m}$ to expand the E and B modes in terms of spherical harmonics and characterize them in terms of their power spectra

$$C_\ell^E = \left\langle a_{E,\ell m} a^*_{E,\ell m'} \right\rangle \delta_{mm'}, \tag{6.6.24}$$

$$C_\ell^B = \left\langle a_{B,\ell m} a^*_{B,\ell m'} \right\rangle \delta_{mm'}, \tag{6.6.25}$$

$$C_\ell^{TE} = \left\langle a_{E,\ell m} a^*_{T,\ell m'} \right\rangle \delta_{mm'}, \tag{6.6.26}$$

where C_ℓ^{TB} and C_ℓ^{EB} are zero by parity.

When polarization is included the theory correlation matrix has $3N_{pix} \times 3N_{pix}$ elements. The correlation function for two pixels separated by an angle χ can be written as a 3×3 matrix

$$M_{pp'} = \begin{pmatrix} \langle TT \rangle & \langle TQ_r \rangle & \langle TU_r \rangle \\ \langle TQ_r \rangle & \langle Q_r Q_r \rangle & \langle Q_r U_r \rangle \\ \langle TU_r \rangle & \langle Q_r U_r \rangle & \langle U_r U_r \rangle \end{pmatrix}, \tag{6.6.27}$$

where Q_r and U_r are the Stokes parameters calculated in a reference frame chosen such that one axis is the great circle connecting the pixels (section 5.3). U_r changes sign under a parity transformation while T and Q_r are invariant. Because of this $\langle TU_r \rangle$ and $\langle Q_r U_r \rangle$ are identically zero. Equation 6.6.10 shows the correlation function for $\langle TT \rangle$. Zaldarriaga [116] shows that the correlation functions can be written as

$$\langle Q_r(\theta,\phi) Q_r(\theta',\phi') \rangle = \sum_\ell \frac{2\ell+1}{4\pi} C_\ell^E F_{1,\ell 2}(\chi) - C_\ell^B F_{2,\ell 2}(\chi), \tag{6.6.28}$$

$$\langle U_r(\theta,\phi) U_r(\theta',\phi') \rangle = \sum_\ell \frac{2\ell+1}{4\pi} C_\ell^B F_{1,\ell 2}(\chi) - C_\ell^E F_{2,\ell 2}(\chi), \tag{6.6.29}$$

$$\langle T_r(\theta,\phi) Q_r(\theta',\phi') \rangle = \sum_\ell \frac{2\ell+1}{4\pi} C_\ell^{TE} F_{1,\ell 0}(\chi). \tag{6.6.30}$$

By defining $z = \cos\chi$, the functions $F_{1,\ell 0}$, $F_{1,\ell 2}$, and $F_{2,\ell 2}$ can be written (when $z \neq \pm 1$) as

$$F_{1,\ell 0}(z) = 2 \frac{\frac{\ell z}{(1-z^2)} P_{\ell-1}(z) - \left(\frac{\ell}{1-z^2} + \frac{\ell(\ell-1)}{2} \right) P_\ell(z)}{[(\ell-1)\ell(\ell+1)(\ell+2)]^{1/2}}, \tag{6.6.31}$$

$$F_{1,\ell 2}(z) = 2 \frac{\frac{(\ell+2)z}{(1-z^2)} P^2_{\ell-1}(z) - \left(\frac{\ell-4}{1-z^2} + \frac{\ell(\ell-1)}{2} \right) P^2_\ell(z)}{(\ell-1)\ell(\ell+1)(\ell+2)}, \tag{6.6.32}$$

$$F_{2,\ell 2}(z) = 4 \frac{(\ell+2) P^2_{\ell-1}(z) - (\ell-1) z P^2_\ell(z)}{(\ell-1)\ell(\ell+1)(\ell+2)(1-z^2)}, \tag{6.6.33}$$

where $P_\ell(z)$ is a Legendre polynomial and $P_\ell^2(z)$ is the associated Legendre polynomial $P_\ell^m(z)$ for $m = 2$. If $z = \pm 1$ then the functions take the form

$$F_\ell^{10}(z) = 0 \text{ if } |z| = 1, \tag{6.6.34}$$

$$F_\ell^{12}(z) = \begin{cases} \frac{1}{2} \text{ if } z = 1, \\ \frac{1}{2}(-1)^\ell \text{ if } z = -1, \end{cases} \tag{6.6.35}$$

$$F_\ell^{22}(z) = \begin{cases} -\frac{1}{2} \text{ if } z = 1, \\ \frac{1}{2}(-1)^\ell \text{ if } z = -1. \end{cases} \tag{6.6.36}$$

This corresponds to a correlation between the pixel and itself or one separated by 180°.

With a suitable definition of the correlation function, we can use the techniques described in the previous section to estimate C_ℓ^E, C_ℓ^B and C_ℓ^{TE}. Although we expect the the B mode signal to be too small to detect with BOOM03 , maps with partial sky coverage can have an ambiguity between the E mode and B mode signals. This mainly affects the largest scales of the map [117]. Bunn et al. [18, 109] show how to minimize the effects of this contamination. For BOOM03 we are developing matrix based and Monte-Carlo based pipelines for power spectrum estimation.

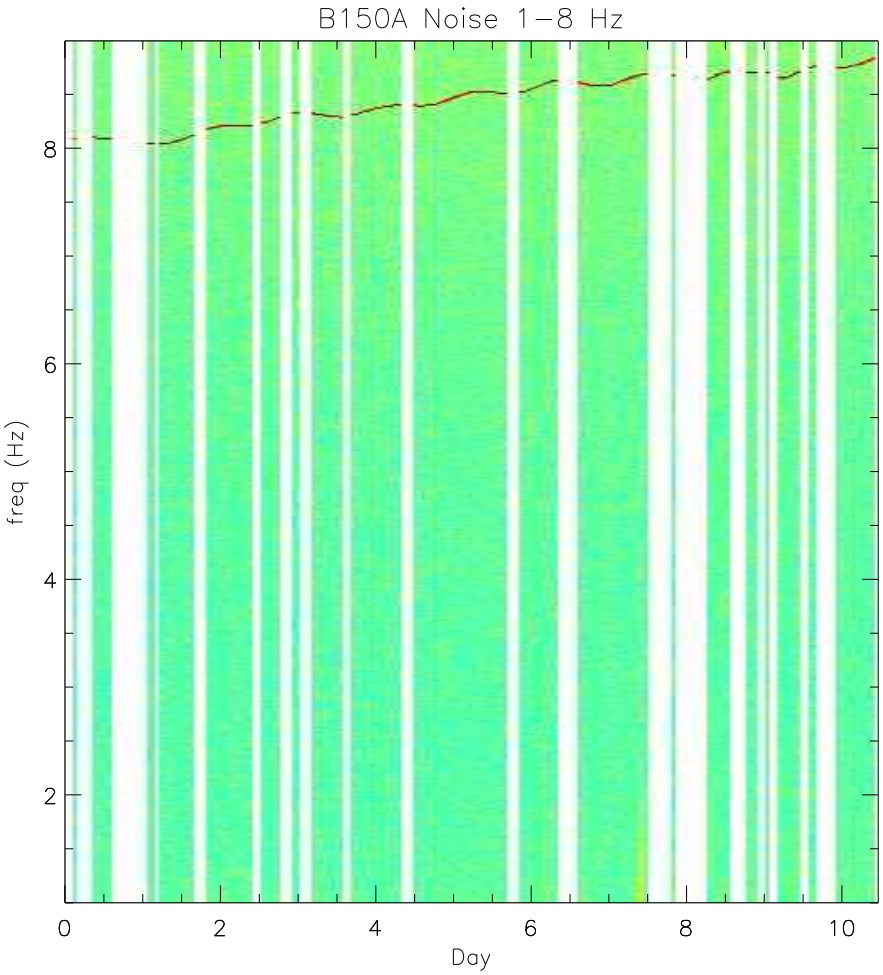

Figure 6.3: Power spectrum over the course of the B98 flight for channel B150A (for frequencies 1-9 Hz). The data was divided into chunks 72 minutes long. The spectra are a mix of sky signal and noise, and are taken only when the telescope was scanning CMB regions away from the galaxy (the blank spaces are when the telescope was observing the galaxy). For each chunk, the average power spectrum is calculated from individual power spectra taken for each minute of data. Above 8 Hz, there is a line in the power spectra (this is also visible in figure 6.2). It migrates from 8 Hz to 9 Hz over the course of the flight. This is probably due to aliasing of the bias frequency into the signal band (discussed in section 4.8.5).

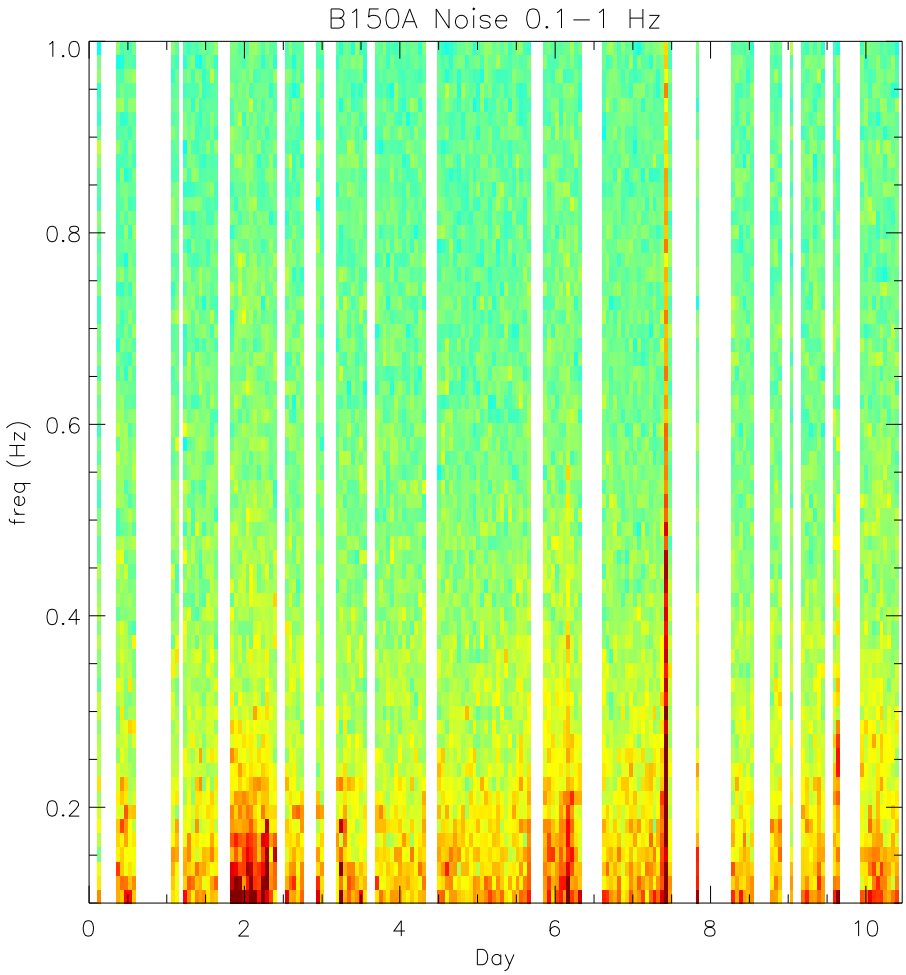

Figure 6.4: Plot of the low frequency part of the power spectrum for B150A over the course of the B98 flight.

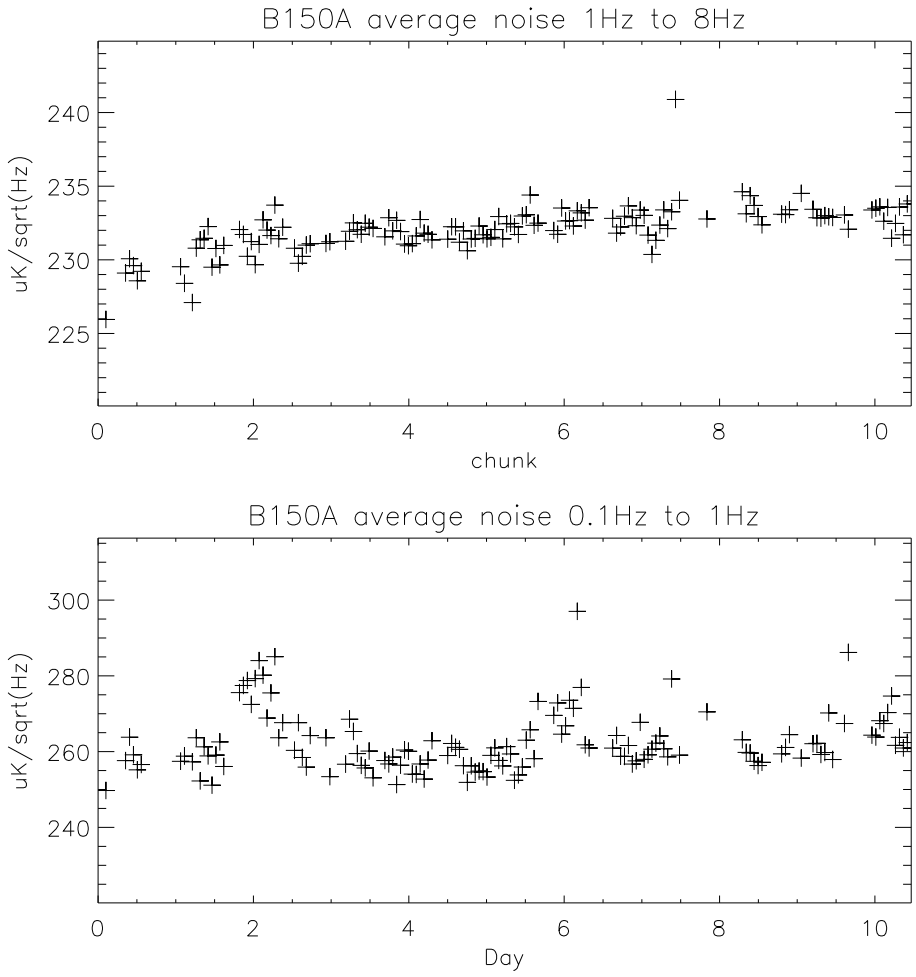

Figure 6.5: Average noise for B150A over the course of the B98 flight. The top panel shows the average of the spectral bins (in $\mu K/\sqrt{Hz}$) for $f = 1 - 8$ Hz, and the bottom panel shows the average noise for $f = 0.1 - 1$ Hz. These averages are calculated for the data shown in Figures 6.3 and 6.4.

Chapter 7

Results from B98

BOOMERANG made its first long duration flight on December 29, 1998 from Williams Field at McMurdo Station Antarctica ($77°11'S, 167°5'E$). It circumnavigated the continent in 10.5 days landing about 30 miles from the launch site. It stayed within a couple degrees of latitude $78°S$ throughout the flight. We collected 259 hours of data with 187 hours spent in CMB scanning mode. Most of the remaining time was spent observing the galactic HII regions RCW38, RCW57 (a double source composed of NGC3603 and NGC3576), IRAS/08576, IRAS/1022, and the Carina Nebula. The clusters A3158, A3112, and A3226 were targeted in the hope of measuring the Sunyaev-Zel'dovich effect.

The receiver consisted of two 90 GHz channels, two single mode 150 GHz channels, and four 3-color photometers each with channels at 150, 240 and 410 GHz. See Crill et al. [22] for more detail on the in-flight performance and instrument characterization.

Channel	Band (GHz)	$NET_{CMB}(\mu K\sqrt{s})$	Beam FWHM (arc minutes)
B150A	148.0 - 171.4	130	9.2 ± 0.5
B150B	145.8 - 168.6	Variable	9.2 ± 0.5
B150A1	145.5 - 167.3	231	9.7 ± 0.5
B150A2	144.0 - 167.2	158	9.4 ± 0.5
B150B1	144.2 - 165.9	196	9.9 ± 0.5
B150B2	143.7 - 164.3	184	9.5 ± 0.5
90 (2 Chs)	79 - 95	140	18 ± 1
240 (3 chs)	228 - 266	200	14.1 ± 1
410 (4 chs)	400 - 419	~ 2700	12.1 ± 1

Table 7.1: Summary of relevant B98 instrument parameters (from Crill et al.[22]). The NET's are computed at 1 Hz. Channels B150A, B150A1, B150A2, and B150B2 were used for the CMB analysis presented here.

7.1 Scan Strategy

Because the flight takes place at high latitude in the Antarctic summer, the scan strategy is dominated by the position of the sun. In order to avoid solar contamination, the azimuth of the telescope is kept within $\pm 60^\circ$ of the anti-solar azimuth during our CMB scans. The elevation limits of the telescope are 35° to 55°. This anti-solar region simultaneously allows for observations of sources near the galactic plane and the CMB in a region away from the galactic plane.

Primary CMB observations were made using $\pm 30^\circ$ azimuthal scans at three elevations (40°, 45° and 50°). The elevation of the CMB scans was changed once per day. The azimuthal scan center was updated every 1 or 1.5 hours. As a systematic check, a $\pm 60^\circ$ scan was performed for 5 minutes prior to every update. The scan center was updated so that the scan center was kept at nearly the same Right Ascension ($RA \approx 85^\circ$). Two azimuthal scans speeds were used: 1 deg/s and 2 deg/s. Since the payload was at a latitude of $\approx 78^\circ$, a single elevation moved 24° in declination during 1 day. Sky rotation causes the scans are tipped by $\pm 12^\circ$ which provided good cross-linking (Figure 7.1).

Figure 7.2 shows the noise per pixel for the four 150 GHz channels (B150A, B150A1, B150A2, B150B2) used in the analysis. The region enclosed by the solid line is used for the CMB power spectrum analysis in Ruhl et al. [98]. This region covers 2.94% of the sky and can be defined as the intersection of:

- an ellipse centers on $RA = 88^\circ$, $Dec = -47^\circ$ with semi-axes $a = 25^\circ$ and $b = 19^\circ$. The short axis lies along the local celestial meridian.
- a strip with $-59^\circ < Dec < -29.5^\circ$
- and where the galactic latitude $b < -10^\circ$.

7.2 Maps

As mentioned in section 6.6, we used two pipelines (MADCAP and FASTER) to analyze the CMB power spectrum using the four 150 GHz channels. Before estimating the power spectra, maps need to be made. MADCAP produces a map of the 4 combined channels using 8 time-time noise correlations matrices (one for each channel at each of the two fundamental scan speeds). For the FASTER pipeline, the data is highpass filtered and a map is made for each channel. The individual maps are then coadded. For coadding the maps, each pixel is weighted by n_p^{-1}, where n_p is the number samples that hit the pixel. Also, each map is given an overall weight by the NET of the channel that produced it. Figure 7.3 shows the CMB maps for the MADCAP and FASTER pipelines. The MADCAP map shows more structure on large scales due to the fact that it uses much of the low frequency data that is filtered out of the naive maps.

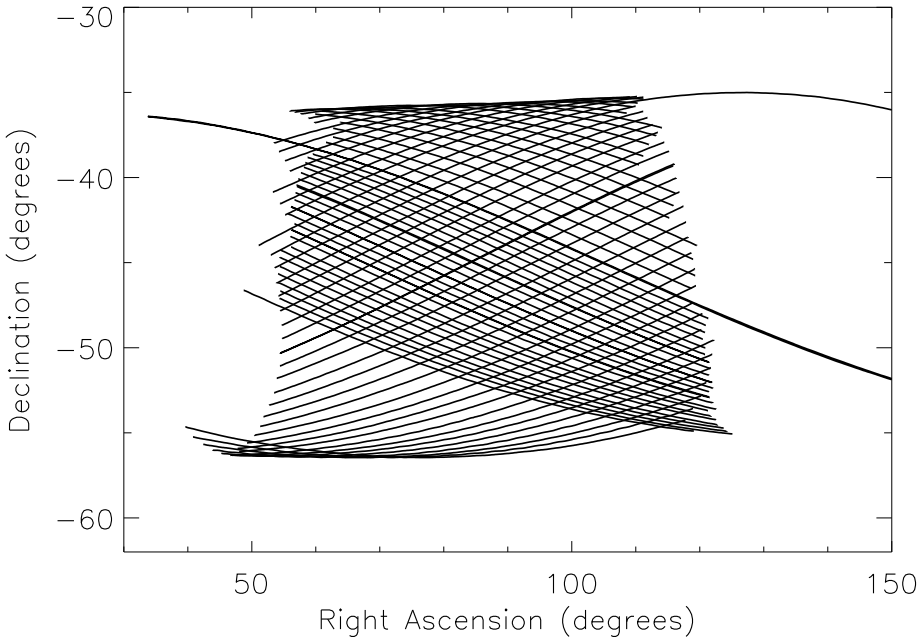

Figure 7.1: An example of the cross-linking in the B98 scans (from Crill et al.[22]). Every 20th scan is plotted during a 22.5 hour period of observation covering parts of the 4th and 5th day of observation. The elevation was fixed at 45° during this period. The closely placed scans are at 2 degrees/sec which was the scan speed during the first 5 hours of this period. During the rest of this period the speed was 1 degree/s.

As we will discuss in section 7.3, the B98 maps have a systematic error which manifests itself as stripes along lines of constant declination. For the FASTER pipeline these stripes are removed (the map is destriped) by projecting the map onto a plane and Fourier filtering out all modes on scales larger than 8.2° in the RA direction. The naive map shown has been destriped in that way. In the MADCAP map, the stripes are left in the map. These modes are marginalized over in the power spectrum estimation process by using constraint matrices.

7.3 Jackknife Tests

In order to check the data for systematic errors, a variety of tests are performed. These tests help to ensure confidence in the final result. The most powerful test is the null or jackknife test. The idea behind a jackknife tests is to split up the data into two halves which have roughly equal sky coverage and integration time. Ideally two halves of the data see the same sky signal; therefore the power

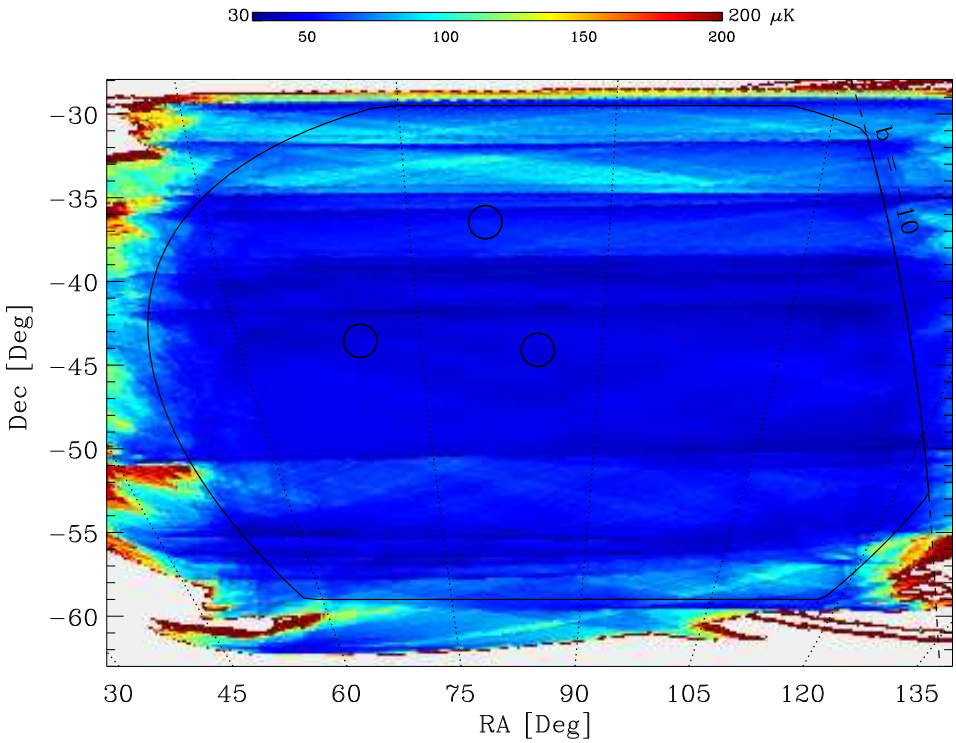

Figure 7.2: Plot of noise per 7′ Healpix pixel for the 4 coadded 150 GHz channels from Ruhl et al.[98]. The noise is from the diagonal component of the MADCAP noise covariance matrix ($n_p \approx NET_{tot}/T_{int}$). The region enclosed by the solid line is used for the power spectrum analysis in Ruhl et al. [98]. The circles denote three bright known quasars. Data within 0.5° of the quasars is not used for power spectrum analysis.

spectrum of the difference map should be consistent with zero. More concretely, if the data is split into two maps labeled Δ_A and Δ_B. The difference map is $\Delta_J = (\Delta_A - \Delta_B)/2$ (using only overlapping pixels). In the maximum likelihood power spectrum formalism (used in MADCAP), the noise correlation matrix of Δ_J is $C_N^J = (C_N^A + C_N^B)/4$. In the Monte Carlo formalism, the jackknife correlations are taken care of by splitting up the simulated timestreams in the same manner as the real data.

For B98 the most powerful jackknife test is to take the difference between the data taken with an azimuthal scan speed of 1 degree/sec (1 dps) and the data taken with a scan speed of 2 degree/sec (2 dps) (the so-called (1dps - 2dps)/2 test). The gondola was scanned at 2 dps (for 82 hours) in the first part of the

flight and 1 dps (for 105.8 hours) in the remaining part. This test is sensitive variations on long time scales such as the variation in the gondola position with respect to the Earth, changes in the position of scan region with respect to the Sun or non-stationary noise. Comparing data at different scan speed provides a check against systematic problems modulated by the scan speed, pointing reconstruction errors, and errors in the electronics transfer function or bolometer time constant measurements.

Other jackknife tests that we can do are the left-going vs right-going scans, the quadrant tests, and channel difference tests. For the quadrant tests, the 1 dps data is split into halves Q_1 and Q_2 and the 2 dps data is split into halves Q_3 and Q_4. Two quadrant tests can be done: $(Q_1+Q_3-Q_2-Q_4)/2$ and $(Q_1+Q_4-Q_2-Q_3)/2$. The quadrant tests should provide provide roughly the same long term stability information as the (1dps-2dps)/2 test, while providing a different way of dividing up the scan speed effects. The left-going vs right-going test checks for residual effects of scan synchronous noise. Channel difference tests insure that different channels see the same signal.

Figure 7.4 shows the (1dps-2dps)/2 maps for MADCAP (top) and FASTER (bottom). Although the FASTER power spectrum analysis was done at 3.5' both maps are shown at 7' resolution so that the noise properties are similar. The MADCAP map contains some constant declination stripes which are marginalized over for the power spectrum analysis. Figure 7.5 show the full and (1dps-2dps)/2 power spectra for MADCAP and FASTER. Constant declination stripes have been removed from all of the spectra.

Besides the removal of the constant declination stripes, another correction is done on the FASTER (1dps-2dps)/2 spectrum. Because of the timestream filtering, Monte Carlo simulations show that different scanning speeds and scan directions can lead to a leakage of CMB signals into a (1dps-2dps)/2 naive map. This signal is expected to be $\sim 10\mu K$ at $\ell \sim 200$ (near the first acoustic peak). The magnitude of the residual is calculated using signal-only Monte Carlo simulation. The FASTER (1dps-2dps)/2 spectrum is then corrected by subtracting out the mean residual and adding the variance of the residual to the FASTER (1dps-2dps)/2 spectrum error bars in quadrature. The FASTER (1dps-2dps)/2 spectrum shown in figure 7.5, is corrected for this effect.

One the corrections applied to the FASTER (1dps-2dps)/2 spectrum, we can check if the (1dps-2dps)/2 spectra are consistent with zero signal. To make a statistical comparison, we calculate the χ^2 per degree of freedom with respect to a zero-signal model. For the bins $\ell = 50$ to $\ell = 1000$, The χ^2 per degree of freedom equal to 1.34 for MADCAP and 1.28 for FASTER. The probabilities of exceeding this χ^2 are $P_> = 0.14$ for MADCAP and $P_> = 0.18$ for FASTER. Both are therefore consistent with zero when looking over the entire ℓ range. However looking at figure 7.5, it is clear the FASTER (1dps-2dps)/2 spectra has a residual signal near $\ell = 200$ which is not consistent with zero. For the 6 bins where $\ell \leq 300$,

the FASTER has a $\chi^2 = 3.7$ with $P_> = 0.001$, while MADCAP has $\chi^2 = 1.10$ with $P_> = 0.36$.

This localized residual in the FASTER difference spectra is quite small with a mean of $45\mu K^2$ in bins $\ell = 150, 200, 250, 300$. The CMB signal in this ℓ range is $\sim 5000\mu K^2$ and the sample variance dominated error on this signal is $\sim 400\mu K^2$. The residual systematic effect is roughly 10% of the errorbar in this range and roughly 1% of the signal. Even though this residual is not consistent with zero, it is a rather small effect.

Since the FASTER pipeline was completed before MADCAP was able to marginalize over constant declination stripes, much effort was undertaken to try to understand the nature of the residual signal. The (1dps-2dps)/2 residual signal was found in in three of the four 150 GHz channels used in the analysis. Table 7.2 shows the χ^2 and $P_>$ results for (1dps-2dps)/2 tests on the individual channels used in the analysis (these results are not corrected for the filter-induced signal residual, but that's a small perturbation).

	$\ell = 50 - 1000$		$\ell = 50 - 300$	
Channel	χ^2	$P_>$	χ^2	$P_>$
B150A	3.1	3.45e-6	7.355	7.0e-8
B150A1	1.39	0.1145	2.25	0.035
B150A2	1.83	0.0129	4.886	5.88e-5
B150B2	1.88	0.010	0.335	0.919

Table 7.2: Reduced χ^2 and $P_>$ for the (1dps-2dps)/2 jackknife tests for the four individual 150 GHz channels used in the analysis. These spectra are not corrected for the filter-induced signal residuals. Nonetheless, they provide an illustration of the excess signal in the (1dps-2dps)/2 spectra.

Many attempts were made to discover the cause of the jackknife failure. Nearly every variable parameter was tweaked to either try to fix the problem or to make it worse. These parameters included:

- Changing the size of flagged areas in the data stream.
- Inserting a gain offset between the 1 dps and 2 dps data.
- Inserting a pointing offset between the 1 dps and 2 dps data.
- Adding phase offsets to the electronics transfer function.
- Changing the number of hits required to keep a pixel in the map.
- Cutting chunks of data with bad 1/f noise.

- Changing parameters in the despiking code.
- Using more than the just two noise filters.

These effects were tested through direct applications to the real data and with Monte Carlo simulations with fake data. None of these proved to be the smoking gun we were looking for. Most of these test were done on channel B150A, since it was the most sensitive channel and had the most significant residual signal.

In the monte carlo formalism, the $\left\langle \widetilde{N}_\ell \right\rangle_{MC}$ and $\left\langle \widetilde{C}_\ell \right\rangle_{MC}$ are computed as the average of the monte carlo results and the variances are computed as $\sum_{MC}(x_i - \langle x \rangle)^2$. This is strictly true only if they are Gaussian distributed. One might expect sample variance to cause a deviation from Gaussianity. This was checked for noise-only and signal+noise simulations and the resulting distributions were found to be very close to Gaussian.

Given that MADCAP is able to pass the (1dps-2dps)/2 test, gain or pointing offsets and noise misunderestimation are unlikely to be the cause of the problem. A pointing offset had morphology which was most like the jackknife failure we see. The FASTER spectrum can also rule out the pointing offset, because the 0.6' offset necessary to cause a large enough (1dps-2dps)/2 signal, would kill off a fair amount of the high-ℓ power in the spectrum.

In trying to solve the jackknife residual issue, we implemented a method to calculate the cross spectrum using the monte carlo formalism. The cross spectrum is defined

$$X_l = \frac{1}{2l+1} \sum a_{lm} b^*_{lm} \tag{7.3.1}$$

where a_{lm} and b_{lm} are from different maps. Using this method we investigated correlations between the (1dps-2dps)/2 maps and the 1 dps, 2 dps, and (1dps+2dps)/2 maps. Ideally the (1dps - 2dps)/2 map, should have no signal left in it; therefore, the cross spectrum between the individual data maps and the (1dps - 2dps)/2 map should be consistent with noise. Figure 7.6 shows the results of the map destriping algorithm (used in the FASTER pipeline) on B150A. The top panel shows how destriping improves the (1dps - 2dps)/2 power spectra. The middle panel shows that the destriping has only a small effect on the 2dps data, while the bottom panel shows that the destriping had a significant effect on the cross spectrum between the 1dps and (1dps - 2dps)/2 maps. It appears that the destriping primarily cleans up contaminants in the 1dps data.

Figure 7.7 shows how the cross spectra can rule out an error like the small pointing offset between the 1dps and 2dps data. The top panel shows the full power spectra and the cross spectrum of the 1dps and 2dps maps for B150A. There is good agreement between the cross spectrum and the real spectrum. The bottom panel shows the effect of a $6'$ pointing offset between the 1dps and 2dps data on a fake data stream. In this case, the pointing offset causes a systematic decay in the cross spectrum power above $\ell \sim 550$. Comparing the fake data result

to B150A, we see that it is unlikely that there is any such pointing offset in the data.

Another attempt to test long term stability involved the previously discussed quadrant jackknife tests. These resulted in residuals similar to those found in the (1dps - 2dps)/2 test.

Although we are unable to resolve FASTER's failure in the (1dps - 2dps)/2 test, we were able to perform two other successful jackknife tests. One test was to make a maps of the difference of the left-going and right-going scans, the so called (L-R)/2 test. The other was to coadd two pairs of channels (B150A + B150A2)/2 and (B150A1 + B150B2)/2 and then take the power spectrum of the difference of the two coadded maps. Both of these tests had results consistent with zero signal. Table 7.3 shows the χ^2 results of the consistency tests and figure 7.8 shows the power spectra from the three tests done with FASTER

The failure of the FASTER (1dps - 2dps)/2 test is accounted for by adding the residual error in quadrature to the FASTER errors bars derived in the likelihood analysis. In the Fisher matrix, only to the diagonal elements are affected.

Test	Bins	Reduced χ^2	$P_>$
FASTER (L-R)/2	all	1.15	0.29
	1-6	0.96	0.45
FASTER [(B150A+B150A2)-(B150A1+B150B2)]/2	all	1.18	0.26
	1-6	1.25	0.28
FASTER (1dps-2dps)/2	all	1.28	0.18
	1-6	3.70	0.001
MADCAP (1dps-2dps)/2	all	1.34	0.14
	1-6	1.11	0.35

Table 7.3: Summary of the reduced χ^2 and $P_>$ calculated for the systematic tests performed on the data (reported in Ruhl et al. [98]). The FASTER results pass the the left-going minus right-going test and the two channel coadd difference test. FASTER formally passes the (1dps - 2dps)/2 test when all the bins are considered; however, it fails when only the first six bins are considered. The MADCAP results pass the (1dps-2dps)/2 test. Because of computational cost, this was the only jackknife performed using MADCAP.

7.4 Other Pipeline Consistency Checks

Besides the jackknife tests, we also tested robustness of the power spectrum results to changes in the data processing. Due to computational costs, the MADCAP analysis had to be limited to a 7' pixelization and due to it's architecture it needed to assume a common beam for all channels (an average beam weighted by the NET of each channel). For the final FASTER results, 3.5' pixels were used and the Monte Carlo formalism easily allowed the use of different beams for different channels.

Using the FASTER pipeline, we found that the $7'$ arcmin pixelization and the single beam model did not introduce a significant bias. The final FASTER result also included a signal variance + noise variance (S+N) weighting of the naive map and the removal of constant declination stripes. The removal of stripes and the weighting of the map change the information content of the map and could in principle change the output power spectrum. However, we found that their effect on the power spectrum was not significant when compared to the statistical error bars (see Figure 3 of Ruhl et al. [98]). Also the FASTER spectrum was not affected by variations in the choice of ℓ-bins.

The top panel of figure 7.5 shows the output power spectra from FASTER and MADCAP. Generally the agreement is pretty good given the difference in the number of effective signal modes in each pipeline. However, from the plot it appears that the MADCAP spectra is rising with respect to the FASTER spectrum as a function of ℓ. None of the effects discussed in the previous paragraph can account for this. The change could be accounted for by increasing MADCAP's effective beam by about 1/2 the beam uncertainty, but there is no reason to expect the pipelines to have different effective beams.

Another possible problem is the asymmetry of the HEALPIX pixels. FASTER is not sensitive to this because the calculation of the Monte Carlo transfer function should include any effects of asymmetric pixels. To understand the effect on MADCAP, we can estimate the effect of the asymmetric pixels on the window functions by comparing the window functions of individual pixels. Because this is a costly operation for $7'$ pixels, we can do this with $27'$ pixels and scale the result. In this case, the maximum deviation is about 10% in power at $\ell = 256$ (corresponding to $\ell = 1024$ for a $7'$ pixelization) over the whole celestial sphere. Since the full map has pixels of many different shapes, one would expect the actual error to be an average over pixel shapes which should be less than 2% in power.

7.5 Foreground Contamination

For any CMB experiment, galactic foreground contamination is always a concern. Using the B98 410 GHz channels, we estimated the power spectrum of the galactic dust in three circles of radius 9° centered at galactic latitudes

$b = -38°, -27°$ and $-17°$ [74]. In the circle center at $b = -38°$, the power spectrum is consistent with noise, while there is a detection of a dust signal in the circles centered at $b = -27°$ and $-17°$. The results at 410 GHz are scaled to 150 GHz using correlations between our maps and the 3000 GHz map from Finkbeiner et al ([24], model 8 in that paper). Figure 7.9 shows a comparison of the dust and the FASTER power spectra. The dust power spectra which peaks at $\ell < 400$ has a peak value $< 100\mu K^2$ which is $\sim 2\%$ of the CMB signal in that ℓ range.

MADCAP is able to marginalize over foreground templates. Figure 7.10 compares the MADCAP results with and without foreground marginalization. Dust and synchrotron templates are used for the foreground marginalization. The effect of foreground marginalization is small for $\ell > 200$ and has the largest effect on the first bin in the MADACAP spectrum. We use the foreground marginalized spectra as our final MADCAP result.

7.6 B98 Final Power Spectra at 150 GHz

With all systematic testing done, we can move on to the final FASTER and MADCAP results. Figure 7.11 shows the final results from Ruhl et al. [98]. Modes corresponding to constant declination stripes were removed from both spectra. The FASTER spectra is from the 3.5' pixelization and its error bars are corrected for the (1dps - 2dps)/2 failure. The final MADCAP spectrum is marginalized over templates for dust and synchrotron radiation. The final FASTER spectra is calculated for shaped bins, while the MADCAP spectra uses tophat bins. The plots do not show errors in the calibration and beam uncertainty. The $1-\sigma$ calibration uncertainty quoted in Ruhl et al. [98] is 20% in $(\Delta T)^2$ units; it acts to move the entire spectrum up and down. The $1-\sigma$ uncertainty on the FWHM beam of each channel is 1.4'. With the beam window function defined as $B_\ell(\sigma) = e^{-\ell(\ell+1)\sigma^2/2}$ (where $\sigma = \mathrm{FWHM}/2.355$), the effect of the beam uncertainty can be approximated by $B_\ell(\sigma+\delta\sigma)/B_\ell(\sigma) = e^{-\ell(\ell+1)\sigma\delta\sigma}$. Changing $\delta\sigma$ effectively applies an ℓ dependent tilt to nominal power spectrum. These errors can accounted for in cosmological parameter analysis or any other likelihood analysis involving the power spectrum.

For calculations involving the likelihood curve for the bandpowers $\mathcal{C}_b$, we use an offset lognormal function which provides a good approximation to the true likelihood [13]. The function $Z_b = ln(\overline{\mathcal{C}}_b + x_b)$ is a function of the maximum likelihood bandpower ($\overline{\mathcal{C}}_b$) and a parameter x_b. With these variables, Z_b has a Gaussian distribution (see [13] for more details).

7.7 Peaks and Valleys

One obvious feature of our power spectrum results is that there appear to be 3 peaks and 2 valleys. Inflation models with adiabatic initial density perturbations generically predict such a series of peaks and valleys. Characterizing the significance of these apparent peaks and valleys is an intuitive way to begin accessing how our results relate to various cosmological models. One generic prediction is that in flat universe models ($\Omega_{tot} = 1$) there will be a peak in the power spectrum at $\ell \sim 220$.

Here we restate the results from Ruhl et al. [98] which used the techniques presented in de Bernardis et al. (2002) [25] for analyzing the results in Netterfield et al. (2002)[86]. The method is based on fitting a parabola to small groups of contiguous ℓ bands. This provides a method of finding peaks and valleys independent of any cosmological models. The significance of the detection of a peak or valley depends on the range over which the fit is done. The reported results are from the ranges which gives the most significant results. We used $\ell = 100 - 300$ for the first peak, $\ell = 300 - 500$ for the first valley, $\ell = 400 - 650$ for the second peak, $\ell = 550 - 800$ for the second valley and $\ell = 750 - 950$ for the third peak. Table 7.4 show the results of the polynomial peaks and valleys analysis for the MADCAP results, the ensemble averaged peaks and valleys from a Bayesian analysis of adiabatic CDM models using a weak prior on cosmological parameters (see section 7.8), and the results from WMAP [89]. The WMAP results come from Gaussian fits as opposed to the polynomial fit used in B98 papers. In Page et al.[89], a Gaussian fit is done to the Ruhl et al. [98] data resulting in a first peak position $\ell_p = 219 \pm 5$ and $\Delta T_p = 73.8^{+8.5}_{-7.0}$ which should correspond to $C_p = 5446.4^{+1327}_{-984} \mu K^2$. For B98 , the error on the amplitude of the first peak is dominated by the 20% calibration uncertainty.

7.8 Cosmological Parameter Analysis

Even though different sets of cosmological parameters can generate nearly the same CMB power spetrum [32], we can still provide strong constraints on the certain parameters using CMB power spectrum measurements and other cosmological results. The large number of recent measurements of the CMB power spectrum has been the impetus for a correspondingly large number of cosmological parameter estimates [38, 101, 4, 54, 105, 8, 102, 95, 84, 69, 104].

The approach used for B98 was presented in Lange et al. (2001) [69] and is very similar (if not identical) to the method used in the parameter analysis presented for ACBAR [38] and CBI [101]. A large database of C_ℓ power spectra is built for a family of adiabatic cold dark matter models parametrized by seven fundamental parameters. Following a Bayesian prescription we calculate the likelihood of each model given the data. We can then marginalize over continuous parameters such

	MADCAP		Adiabatic CDM		WMAP	
Feature	ℓ_p	$C_p(\mu K^2)$	ℓ_p	$C_p(\mu K^2)$	ℓ_p	$C_p(\mu K^2)$
Peak 1	216^{+6}_{-5}	5480^{+1130}_{-1130}	223^{+4}_{-4}	6022^{+394}_{-370}	220.1^{+8}_{-8}	5583^{+73}_{-73}
Valley 1	425^{+4}_{-5}	1820^{+420}_{-410}	411^{+17}_{-17}	1881^{+152}_{-141}	$411.7^{+3.5}_{-3.5}$	1679^{+43}_{-43}
Peak 2	536^{+10}_{-10}	2420^{+620}_{-570}	539^{+19}_{-19}	2902^{+248}_{-229}	546^{+10}_{-10}	2318^{+83}_{-83}
Valley 2	673^{+18}_{-13}	2030^{+670}_{-560}	667^{+28}_{-27}	2122^{+302}_{-265}	-	-
Peak 3	825^{+10}_{-13}	2500^{+1100}_{-840}	812^{+26}_{-25}	3121^{+497}_{-429}	-	-

Table 7.4: Results of the peak and valley analysis (presented in Ruhl et al. [98]). Columns 2 and 3 shows the results for the MADCAP spectrum (The FASTER spectrum provides similar results but with slightly less significance.). Columns 4 and 5 show the prediction of peak and valley locations based on a Bayesian analysis (using the MADCAP spectrum and the COBE-DMR results) of adiabatic CDM models with a weak prior on cosmological parameters. Columns 6 and 7 show the results from WMAP which use a Gaussian fit for the peak position [89]. The errors on the amplitude or the first peak for the B98 data are largely due to the 20% calibration uncertainty.

as the calibration and beam uncertainties. By integrating over the database we can collapse the multidimensional likelihood to a one-dimensional likelihood curve for a given parameter.

Seven fundamental parameters accessible through our method are: $\Omega_k = 1 - \Omega_{tot}$, Ω_Λ, ω_{cdm}, ω_b, n_s, τ_c and $ln(\mathcal{C}_{10})$. Ω_{tot} is the ratio of the total energy density to the critical energy density ($\Omega_{tot} = \rho/\rho_{crit}$) and is the sum of all matter and energy in the universe

$$\Omega_{tot} = \Omega_\Lambda + \Omega_{cdm} + \Omega_b \tag{7.8.1}$$

where we have ignored the any contribution from possibly massive neutrinos whose effect on the power spectrum should be negligible over the B98 range of ℓ. If $\Omega_{tot} > 1$ then the curvature of space is positive (a closed universe), while for $\Omega_{tot} < 1$ space is negatively curved (an open universe). $\Omega_{tot} = 1$ is favored by inflationary models and corresponds to a spatially flat universe. Ω_Λ is the cosmological constant, Ω_{cdm} is the contribution of the cold dark matter to the density and Ω_b is the baryon density. With the Hubble constant defined as $H_0 = 100\ h\ km/s/Mpc$, we have $\omega_{cdm} = \Omega_{cdm}h^2$ and $\omega_b = \Omega_b h^2$. ω_{cdm} and ω_b are preferred over Ω_{cdm} and Ω_b because they are the physical densities which determine the temperature power spectrum at the time of decoupling [11].

The nature of primordial scalar fluctations is described by n_s. It parameterizes the scale dependence of these fluctuations. More precisely the n_s is related to the

power spectrum of the gravitational potential $\mathcal{P}_\Phi(k) \equiv d\sigma_\Phi^2/d(lnk)$ [12]. The tilt of scalar fluctuations is given by $\nu_s \equiv d\mathcal{P}_\Phi/d(lnk)$ with $n_s = 1 + v_s$. If $n_s = 1$ then $v_s = 0$ and the scalar fluctuations are scale invariant. It is also possible to have tensor fluctuations induced by gravity waves; their tilt would be described by n_t. Tensor modes are poorly constrained by temperature anisotropy measurements, but could possibly be detected through polarization measurements.

Based on measurements of the Gunn-Peterson effect [40], we know the universe was reionized when $z \geq 5$. The presence of free electrons leads to Thomson scattering of CMB photons which smoothes anisotropies on scales smaller than the causal horizon at the time of reionization. The surppression is characterized by τ_c, the optical depth to Thomson scattering in this epoch. Reionization surppresses CMB anisotropies on all scales by a factor $e^{-\tau_c}$; however, new anisotropies are generated on scales larger than the horizon size at the time of reionization. This effectively restores the lost power on large scales [120]. Reionization is worse on small angular scales with the net effect being surpression by a factor $e^{-2\tau_c}$. Recent WMAP measurements of the temperature-polarization cross spectra ($\langle TE \rangle$) show that $\tau_c = 0.17 \pm 0.04$ and $11 < z_{reion} < 30$ [64].

The last parameter $ln(\mathcal{C}_{10})$ (the amplitude of the power spectrum at $\ell = 10$) provides an overall amplitude for the power spectrum. Full sky experiments such as the COBE-DMR [5] and WMAP [6] are able to measure the low multipoles very well. However, even with low-ℓ measurements of the temperature power spectrum it is hard to actually measure the overall normalization. This is because $ln(\mathcal{C}_{10})$ and τ_c are nearly degenerate parameters [32]; their effects on the power spectrum nearly cancel out. The WMAP $\langle TE \rangle$ results are able to break this degeneracy. In our analysis, we use the COBE-DMR results to constrain the low-ℓ amplitude; however, our calibration uncertainty leads to our result (for $\ell > 25$) floating with respect to COBE-DMR meaning that $ln(\mathcal{C}_{10})$, τ_c and our calibration uncertainty are highly degenerate.

The Hubble expansion constant and the age of the universe can be derived from the fundamental parameters. With the parameterization $H_0 = 100h\ km/s/MPc$ we get

$$h = \sqrt{\frac{\omega_{cdm} + \omega_b}{\Omega_{tot} - \Omega_\Lambda}} \tag{7.8.2}$$

The age of the universe can be found by

$$t_0(Gyr) = \frac{9.778}{h} \int_0^1 \frac{2x^2}{\sqrt{\Omega_m + \Omega_k x^2 + \Omega_\Lambda x^3}} dx \tag{7.8.3}$$

ignoring the small effect of relativistic particles.

Since $ln(\mathcal{C}_{10})$ is an overall gain parameter we don't have to generate a new model for each different value we want to test. The other six parameters are discretized so that we can build the database in a reasonable time. For the B98 parameter estimations results [98, 86, 69], we used the following ranges

for the parameters: $-0.5 \leq \Omega_k \leq 0.9$, $0 \leq \Omega_\Lambda \leq 1.1$, $0.03 \leq \omega_{cdm} \leq 0.8$, $0.003125 \leq \omega_b \leq 0.2$, $0.5 \leq n_s \leq 1.5$ and $0 \leq \tau_c \leq 0.7$. See Table 6 of Ruhl et al. [98] for a description of the parameter grid.

To compare the model spectra with our results, we must account for the fact that our power spectrum was calculated using ℓ-bins with size $\Delta\ell > 1$. The model C_ℓ's can be related to measured band powers $\overline{\mathcal{C}}_b$ via

$$\mathcal{C}_b^T = \frac{\mathcal{I}[W_\ell^b \mathcal{C}_\ell^T]}{\mathcal{I}[W_\ell^b]} \tag{7.8.4}$$

where $\mathcal{C}_\ell^T = \ell(\ell+1)C_\ell^T/2\pi$, W_ℓ^b is the effective window function and

$$\mathcal{I}[f_\ell] = \sum_l \frac{\ell + \frac{1}{2}}{\ell(\ell+1)} \tag{7.8.5}$$

is the weighting prescription. This prescription can be understood intuitively. The factor $\ell(\ell+1)$ in the denominator converts $\mathcal{C}_\ell$ back to C_ℓ. The amount of power in a map for a given multipole is $(2\ell+1)C_\ell$ and this is what is measured over the bands in the theory correlation matrix. Therefore operator $\mathcal{I}[f_\ell]$ effectively converts $\mathcal{C}_\ell$ into the amount of power in the ℓ-band which is exactly what we need to make this comparison. In general the final answer is not strongly dependent on this choice , as long as the bins are small in ℓ [13]. With FASTER we are able to calculate W_ℓ^b, but for MADCAP we used tophat window functions.

Given one set of theoretical bandpowers $\mathcal{C}_b^T$, the likelihood of the model can be calculated by expanding the likelihood around its maximum value

$$ln\mathcal{L}(\mathcal{C}^T) = ln\mathcal{L}(\overline{\mathcal{C}}) - \frac{1}{2}\sum_{bb'}(Z_b - \overline{Z}_b)\mathcal{F}_{bb'}^{(z)}(Z_b' - \overline{Z}_b') \tag{7.8.6}$$

where $\overline{Z}_b = ln(\overline{C}_b + x_b)$ is the value of the lognormal variable at the point of maximum likelihood. $\mathcal{F}_{bb'}^{(z)} = (\overline{C}_b + x_b)\mathcal{F}_{bb'}^{(\mathcal{C})}(\overline{C}_b + x_b)$ is the transformation of the Fisher matrix into the lognormal basis. Marginalization over the continuous parameters is done for a given model by finding the maximum likelihood value of the amplitude ($ln(\mathcal{C}_{10})$ and calibration uncertainty) and the beam deviation ($\delta\sigma$) then calculating the Fisher matrix curvature at that point and integrating the likelihood with the assumption that these parameters are Gaussian variables. For the discrete parameters, we can calculate the joint probably distribution of any set of parameters $\vec{x}$ by integrating over the unwanted parameters $\vec{y}$

$$L(\vec{x}) = P(\vec{x}|\overline{C}_B) = \int P_{prior}(\vec{x},\vec{y})\mathcal{L}(\vec{x},\vec{y})d\vec{y} \tag{7.8.7}$$

where $P_{prior}(\vec{x},\vec{y})$ encodes the use of other cosmological data and the effective size of our database.

The prior probabilties are based on our knowledge of the comsological parameters from on other measurements. First and foremost there is a prior induced by the range of the parameters we choose in our database. A poor parametrization can lead to misleading results (i.e. the database prefers certain parameter values regardless of the data). Figure 3 of Lange et al. [69] shows the one-dimensional likelihoods for the database itself independent of the B98 data. The database for Ruhl et al. is similar but not exactly the same as the one in Lange et al. In Ruhl et al., we used four sets of priors which result from 7 separate constraints. Our "weak" prior excludes all models where h ($H_0 = 100\ h\ km/s/MPc$) is outside the range $0.45 < h < 0.90$, the age of the universe is less than 10^{10} years, or the matter density is low $\Omega_M < 0.1$. The Ω_M constraint is implemented in the building of the database. We use a strong prior on the Hubble constant $h = 0.72 \pm 0.08$ based on recent results from the Hubble key project [35]. We include a large-scale structure (LSS) prior which is a joint constraint on based on σ_8^2 and the shape parameter Γ_{eff}. σ_8^2 characterizes the linear density fluctuations on scales of $8h^{-1}$ MPc and Γ_{eff} characterizes the linear density power spectrum (see Bond et al. [9] for more details). The Type 1A supernova data [97, 92] provides constraints on $\Omega_\Lambda - \Omega_M$. Our last constraint comes from assuming the universe is flat ($\Omega_{tot} = 1$).

In table 7 of Ruhl et al. [98], we show the results from the following combinations: "Weak h + age", "Weak h + age + LSS", "HST results + age", and "Flat + Weak h + LSS + SN1A". Even without the LSS and SN1A priors our results significantly constrain Ω_k, $\Omega_b h^2$ and n_s. $\Omega_{cdm} h^2$ is somewhat constrained in the weak case, but more significantly determined when the LSS prior is added. Ω_Λ is well determined only when the LSS and/or the supernova priors are added. Our inability to measure $\Omega_{cdm} h^2$ and Ω_Λ is due to a fundamental degeneracy of their effects with regards to the CMB [32]. As mentioned earlier, τ_c is very hard to measure with temperature anisotropy data. With B98 we are only able to set upper limits for it. Interestingly the results "Flat + Weak h + LSS + SN1A" are a near perfect fit to the parameters in the generic ΛCDM model with $\Omega_b h^2 \simeq 0.023$, $\Omega_{cdm} h^2 \simeq 0.12$, $\Omega_\Lambda \simeq 0.70$, $h \simeq 0.7$, and an age of about 13.6 Gyr. Figure 7.12 shows the marginalized likelihood curves for the six parameters derived from the combination of the MADCAP and COBE-DMR power spectra.

Table 7.5 shows the 68% confidence intervals for the fundamental and derived parameters. The MADCAP and FASTER results are shown for the the strong Hubble constant and the "Weak h + age + LSS" priors. The agreement between their results show that the small differences in their power spectra do not affect the cosmological interpretation of the results. The 'Weak h + age + LSS" results from Goldstein et al. [38] are shown in the ACBAR+ column. The ACBAR+ result includes the power spectra data from many recent experiments [68, 7, 77, 42, 44, 39] and the COBE-DMR results. The ACBAR+ results do not strikingly improve the confidence intervals on the cosmological parameters. This

Priors →	($h = 0.72 \pm 0.08$) + age		Weak h + age + LSS			Flat ΛCDM
Pipeline →	MADCAP	FASTER	MADCAP	FASTER	ACBAR+	WMAP+
Parameters ↓						
Ω_{tot}	$1.00^{0.04}_{0.04}$	$0.99^{0.04}_{0.05}$	$1.03^{0.05}_{0.05}$	$1.03^{0.05}_{0.05}$	$1.03^{0.05}_{0.04}$	(1.00)
n_s	$1.02^{0.08}_{0.07}$	$1.06^{0.09}_{0.07}$	$1.01^{0.07}_{0.06}$	$1.03^{0.08}_{0.07}$	$0.98^{0.09}_{0.07}$	$0.99^{0.04}_{0.04}$
$\Omega_b h^2$	$0.023^{0.003}_{0.003}$	$0.023^{0.003}_{0.003}$	$0.023^{0.003}_{0.003}$	$0.024^{0.004}_{0.003}$	$0.022^{0.003}_{0.003}$	$0.024^{0.001}_{0.001}$
$\Omega_{cdm} h^2$	$0.13^{0.04}_{0.03}$	$0.14^{0.05}_{0.04}$	$0.11^{0.03}_{0.02}$	$0.11^{0.03}_{0.03}$	$0.11^{0.02}_{0.03}$	-
Ω_Λ	$0.64^{0.11}_{0.14}$	$0.62^{0.12}_{0.17}$	$0.66^{0.07}_{0.09}$	$0.68^{0.07}_{0.10}$	$0.64^{0.08}_{0.12}$	-
Ω_m	$0.38^{0.13}_{0.13}$	$0.39^{0.14}_{0.14}$	$0.38^{0.10}_{0.10}$	$0.36^{0.11}_{0.11}$	$0.41^{0.11}_{0.11}$	$0.29^{0.07}_{0.07}$
Ω_b	$0.053^{0.016}_{0.016}$	$0.055^{0.016}_{0.016}$	$0.065^{0.020}_{0.020}$	$0.066^{0.022}_{0.022}$	$0.067^{0.019}_{0.019}$	$0.047^{0.006}_{0.006}$
h	$0.66^{0.09}_{0.09}$	$0.67^{0.09}_{0.09}$	$0.61^{0.11}_{0.11}$	$0.63^{0.11}_{0.11}$	$0.59^{0.09}_{0.09}$	$0.72^{0.05}_{0.05}$
Age (Gyr)	$13.7^{1.3}_{1.3}$	$13.4^{1.3}_{1.3}$	$14.9^{1.7}_{1.7}$	$14.8^{1.7}_{1.7}$	$15.2^{1.4}_{1.4}$	$13.4^{0.3}_{0.3}$
τ_c	< 0.49	< 0.30	< 0.50	< 0.53	< 0.51	$0.166^{0.076}_{0.071}$

Table 7.5: Cosmological parameter estimates with the 68% confidence intervals. The B98 results are shown using both the FASTER and MADCAP results (along with COBE-DMR) for the strong Hubble constant prior and the "Weak h + age + LSS" prior (from Ruhl et al. [98]). The ACBAR+ data from [38] is for the "Weak h + age + LSS" prior and comes from the combined results of ACBAR [68], Archeops [7], B98 , COBE-DMR [5], CBI [77], DASI [42], Maxima [44] and VSA results [39]. The WMAP results are from tables 1 and 2 of [104] are the best fit parameters to the WMAP $\langle TT \rangle$ and $\langle TE \rangle$ data alone for a flat ΛCDM model. The WMAP results have $\Omega_m h^2 = 0.14 \pm 0.02$ but do not quote a value of $\Omega_{cdm} h^2$. They also do not quote a value of Ω_Λ.

is due to the fact that the CMB data alone is not able to perfectly constrain all the parameters. The last column shows results from the WMAP $\langle TT \rangle$ and $\langle TE \rangle$ spectra alone from Spergel et al. [104, 112] in the context flat ΛCDM models. In this case the constraints on h and the age of the universe are quite striking. They do not state a value for Ω_Λ, but one can infer a value $\Omega_\Lambda \simeq 1 - \Omega_m \simeq 0.71$. B98 gets similar results with the "Flat + Weak h + LSS + SN1A" prior. When considering non-flat models the WMAP data alone finds a 95% confidence interval of $0.98 < \Omega_{tot} < 1.08$ with an $h > 0.5$ prior.

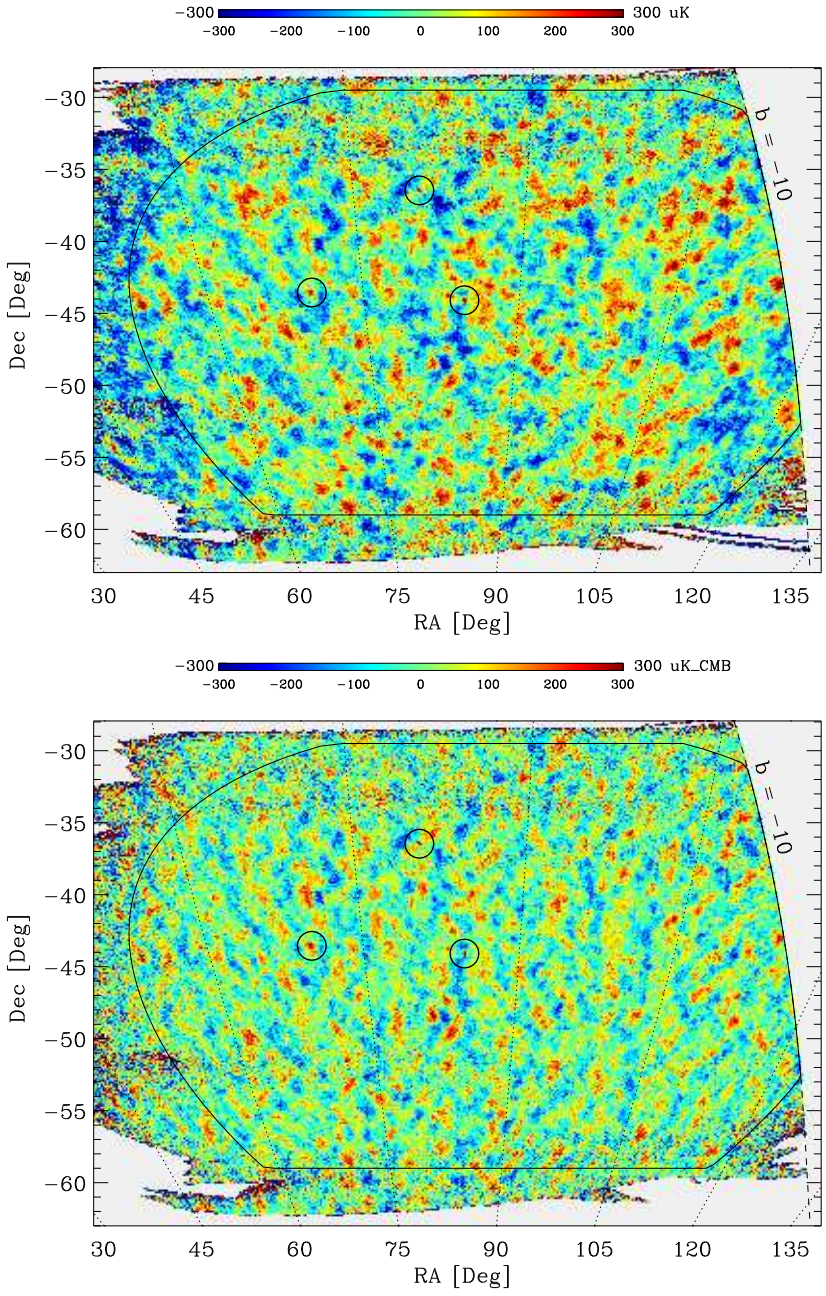

Figure 7.3: 150 GHz maps made from the MADCAP (top) and MASTER/FASTER pipelines (from Ruhl et al. [98]). To facilitate comparison, both maps are pixelized at 7'. The main difference between the maps is that MADCAP retains more information on long time scales which result is more large scale structure especially in the horizontal (RA) direction.

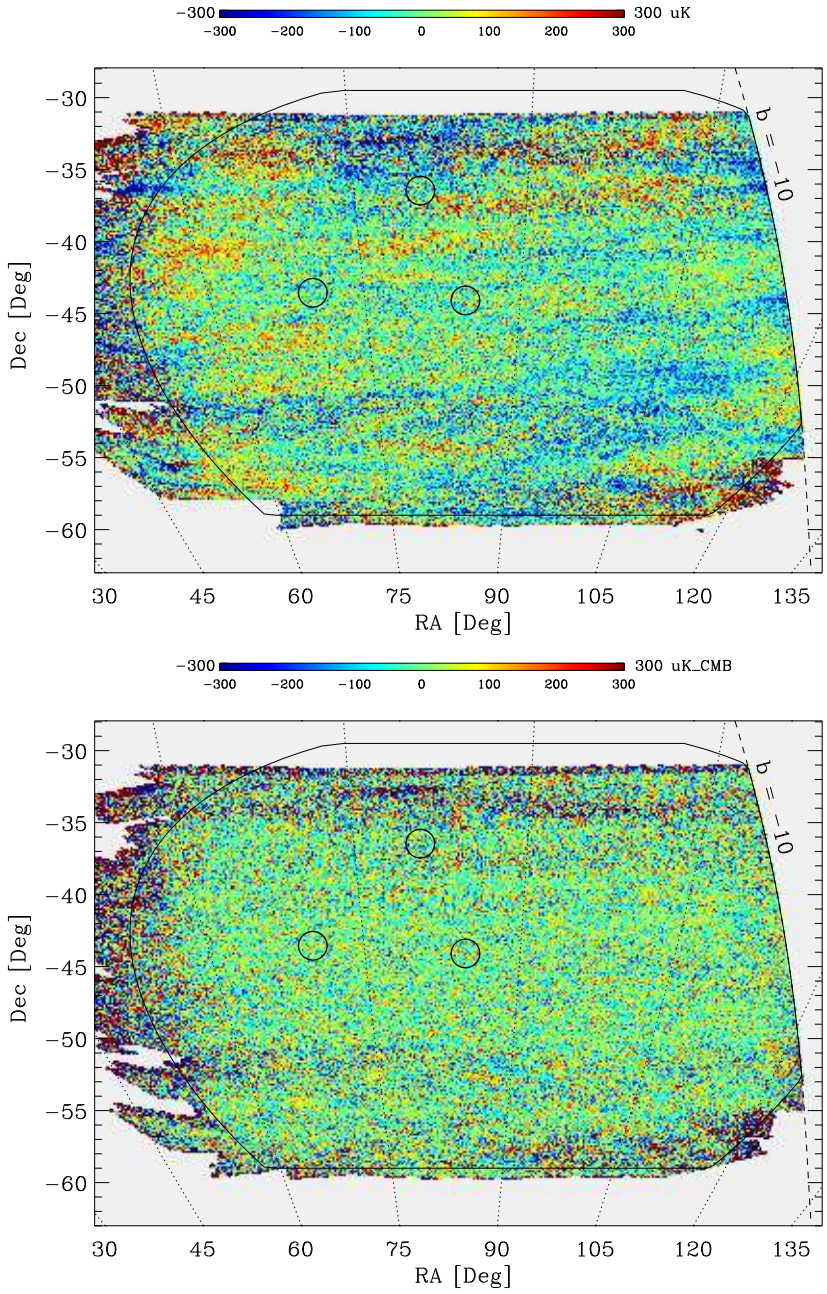

Figure 7.4: (1dps-2dps)/2 maps for MADCAP (top) and FASTER (bottom) both at 7' resolution (from Ruhl et al. [98]). The MADCAP map still has some constant declination stripes, but these modes are marginalized over in the power spectrum estimation.

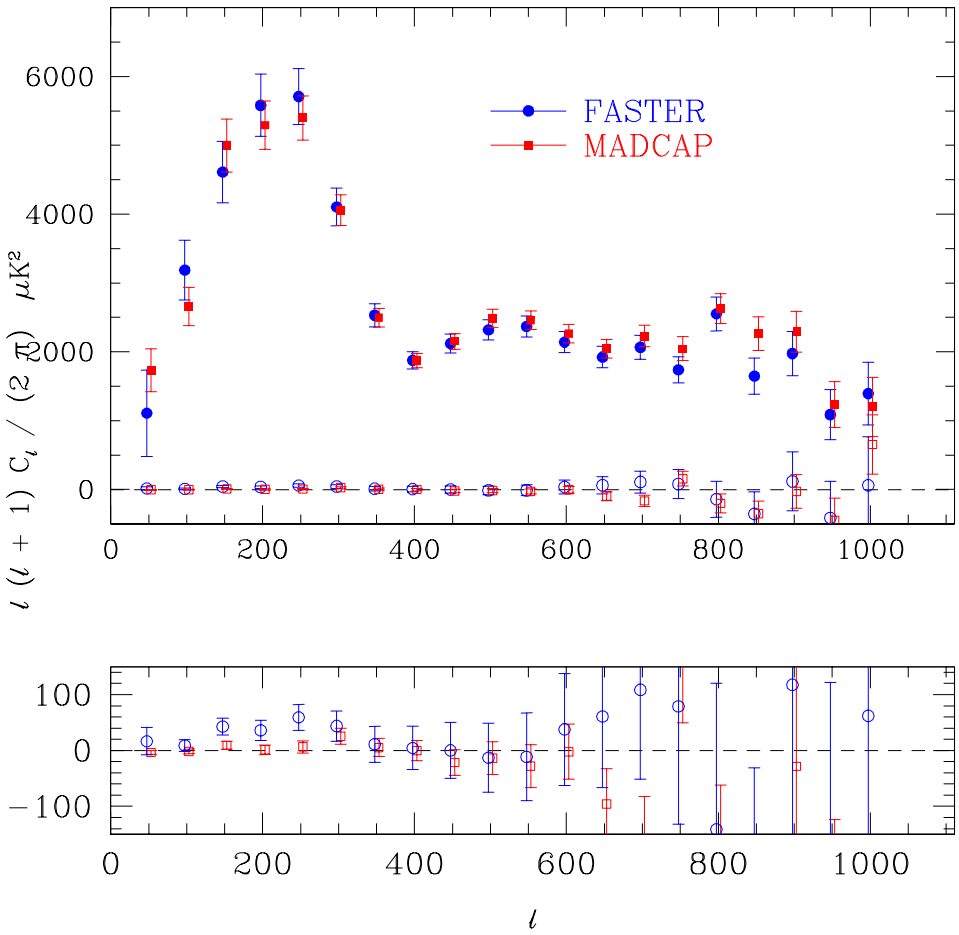

Figure 7.5: The MADCAP and FASTER full and (1dps-2dps)/2 power spectra (from Ruhl et al.[98]). The top panel shows the MADCAP (red) FASTER (blue) data (filled circles for the full spectrum and open circles for the (1dps-2dps)/2. The bottom panel shows a magnification of the (1dps-2dps)/2 results. Effects of constant declination stripes have been removed from all spectra. In this figure galactic foreground templates are not marginalized over in the MADCAP power spectra.

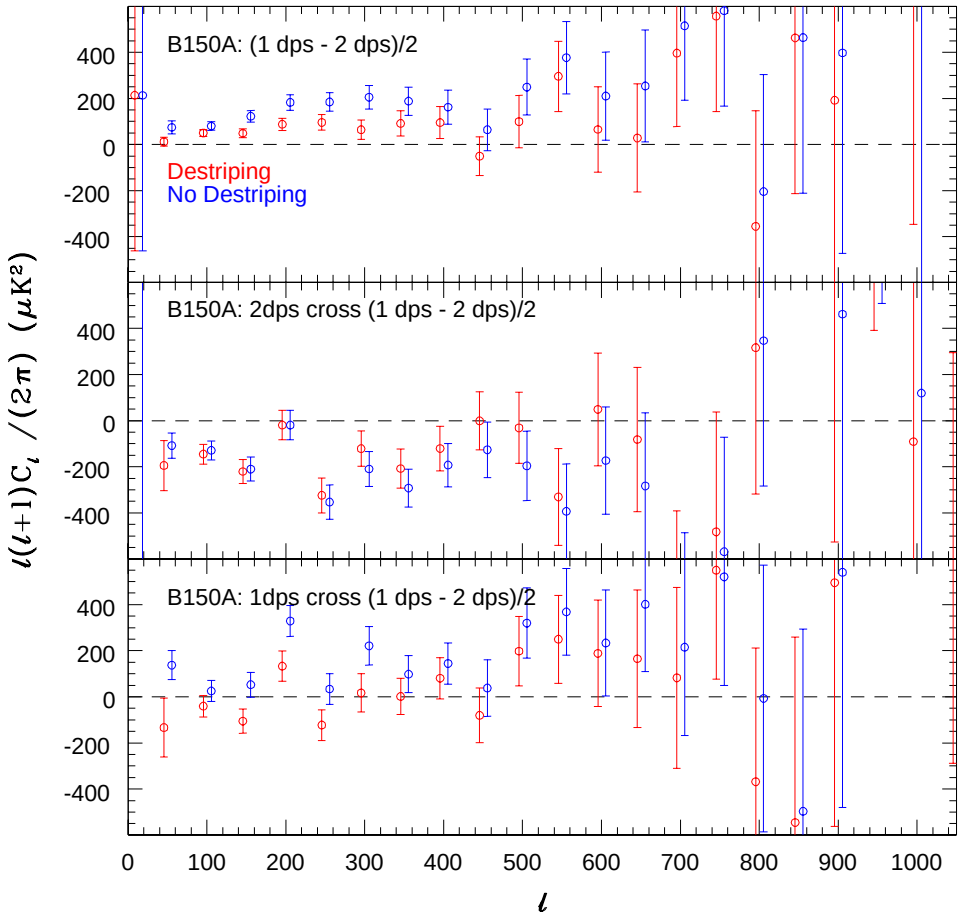

Figure 7.6: Comparison of destriped and non-destriped results for the (1dps - 2dps)/2 power spectrum and the cross spectra of the (1dps - 2dps)/2 map with the 2 dps and 1 dps maps for channel B150A. The destriped results are in red and the non-destriped results are in blue. The top panel shows the effect of destriping on the (1dps - 2 dps) maps. The middle panel shows the results for the cross spectrum of the 2dps and (1dps-2dps)/2. The bottom panel shows the results for the cross spectrum of the 1dps and (1dps - 2dps)/2. The destriping seems to primarily clean up contamination associated with the 1 dps map.

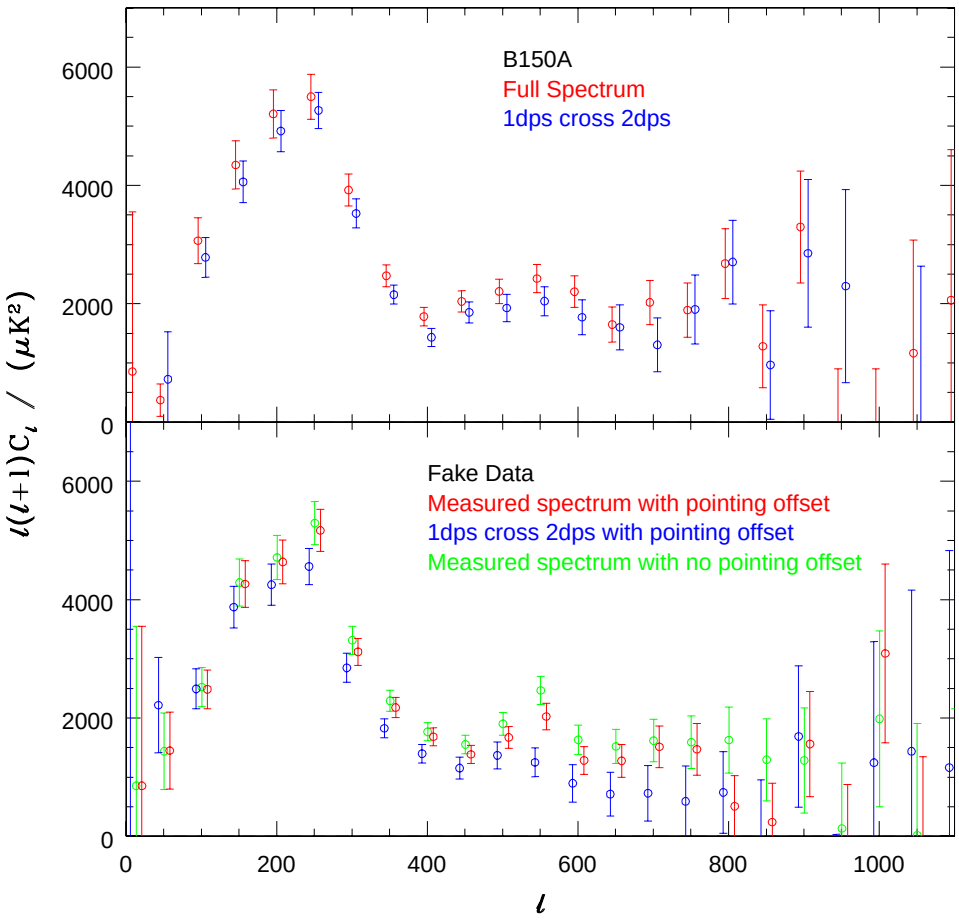

Figure 7.7: Comparison of cross spectra for B150A and a fake bolometer time stream using B150A's flags and pointing. The top panel shows a comparison of the B150A power spectra (red) and the cross spectrum of the 1dps and 2dps data (blue). The bottom panel shows what happens to fake data if we introduce a 6' declination offset in the pointing of the 2dps data.

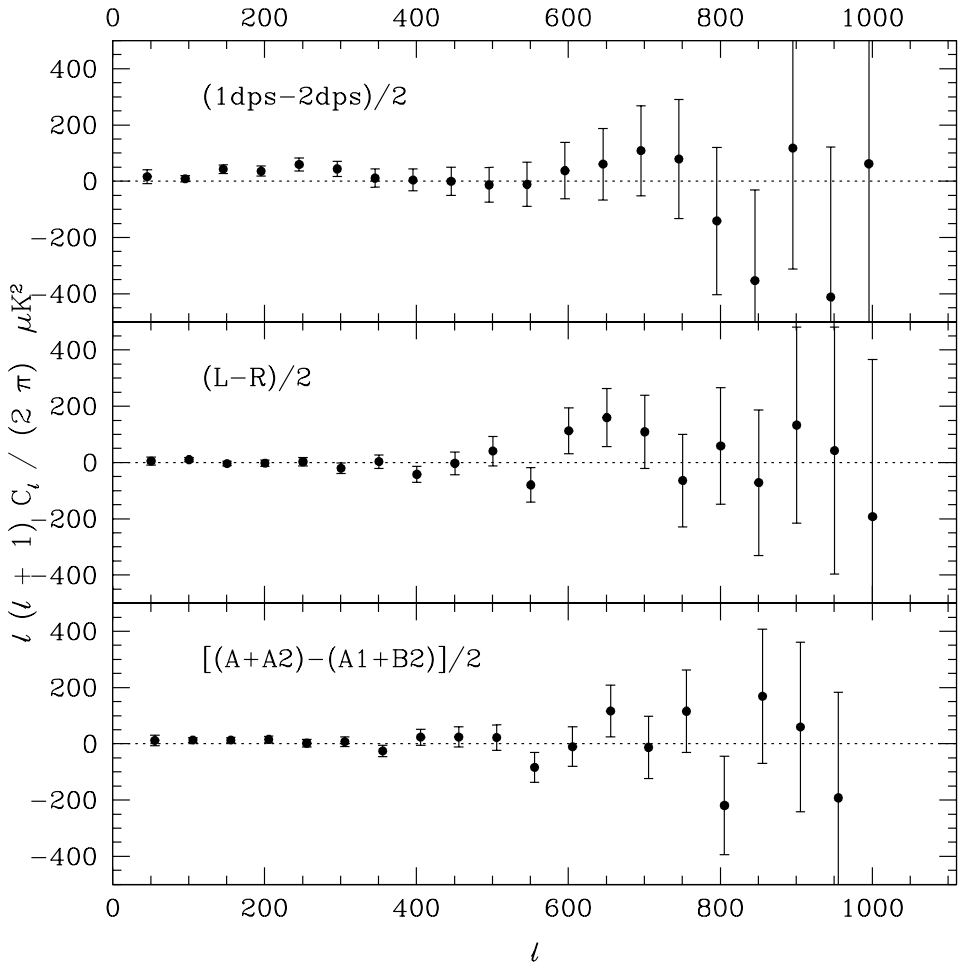

Figure 7.8: The power spectra of the three consistency tests done with the FASTER pipeline (from Ruhl et al. [98]). The top panel shows the (1dps - 2dps)/2 results. The middle panel shows the power spectra from a map made by differencing the left-going and right-going scans, (L-R)/2. The bottom panel shows the results from a map made by differencing to pairs of coadded channels ((B150A+B150A2)/2-(B150A2+B150B2)/2)/2.

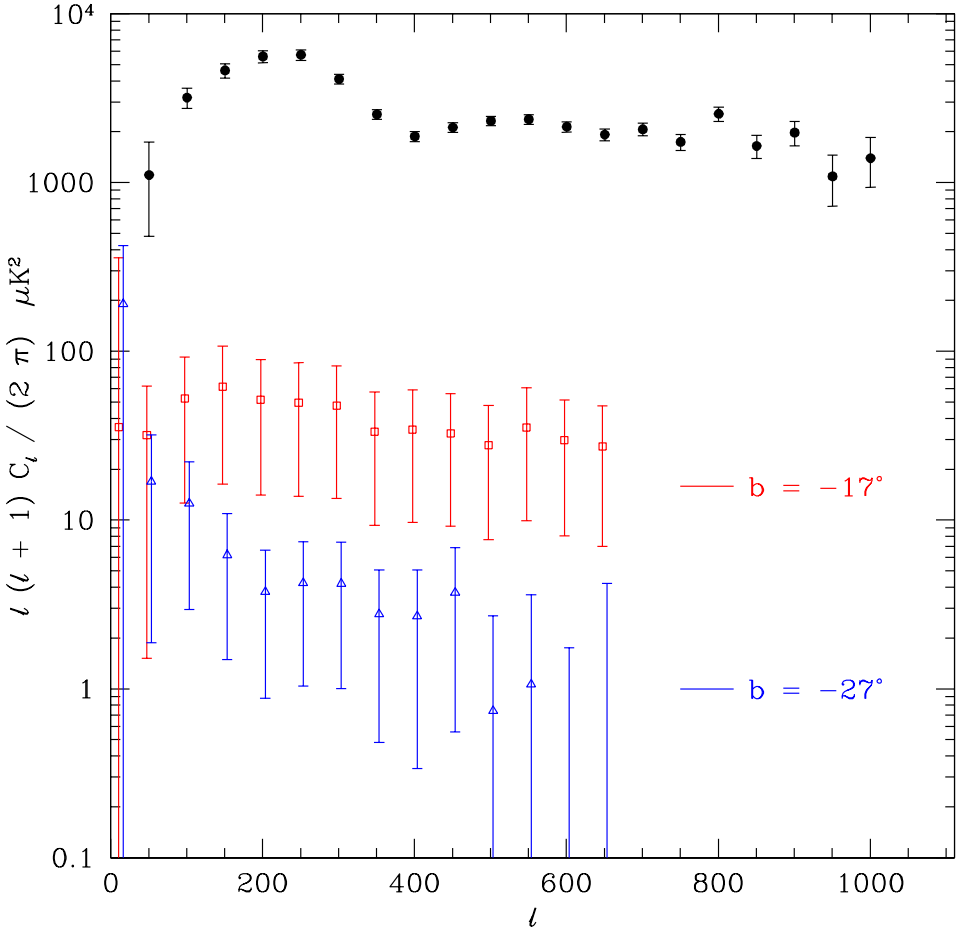

Figure 7.9: A comparison of the dust power spectrum and the FASTER spectrum (black squares) at 150 GHz (presented in Ruhl et al. [98]). The dust power spectrum is computed in two circles centered at $b = -17°$ (red open circles) and $-27°$ (blue triangles),see Masi et al. [**?**] for full details of this analysis.

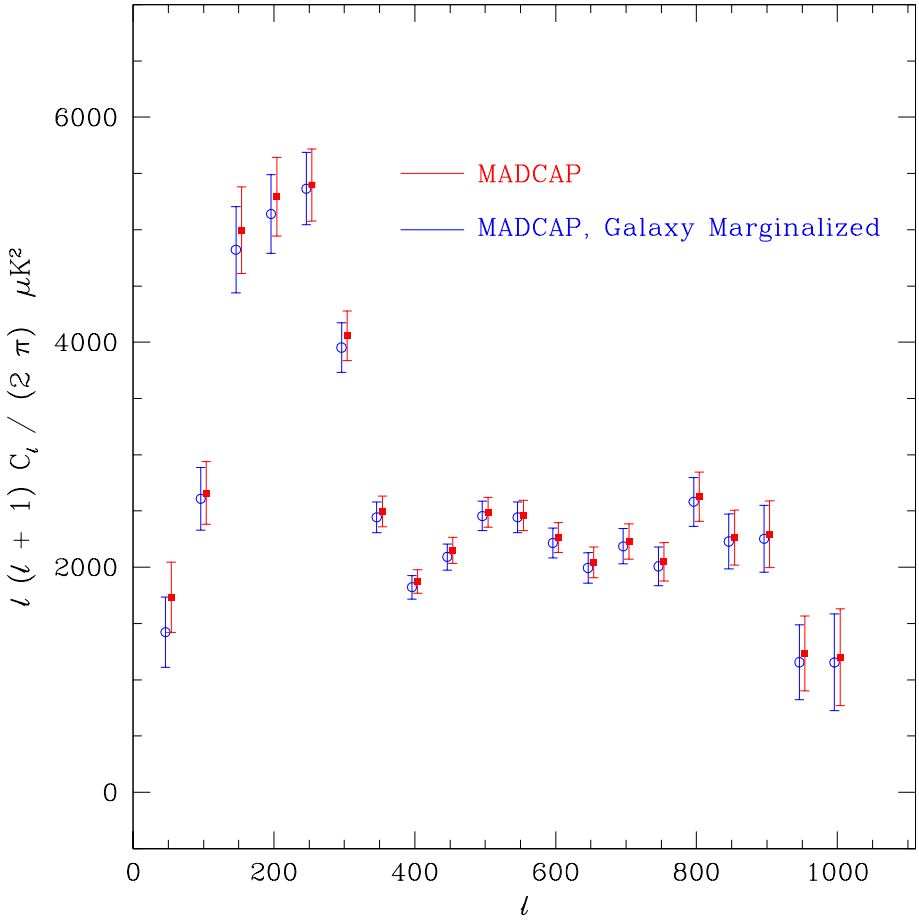

Figure 7.10: A comparison of the MADCAP power spectra with (blue open circles) and without (red squares) foreground marginalization (from Ruhl et al. [98]). It has a small effect for $\ell > 200$.

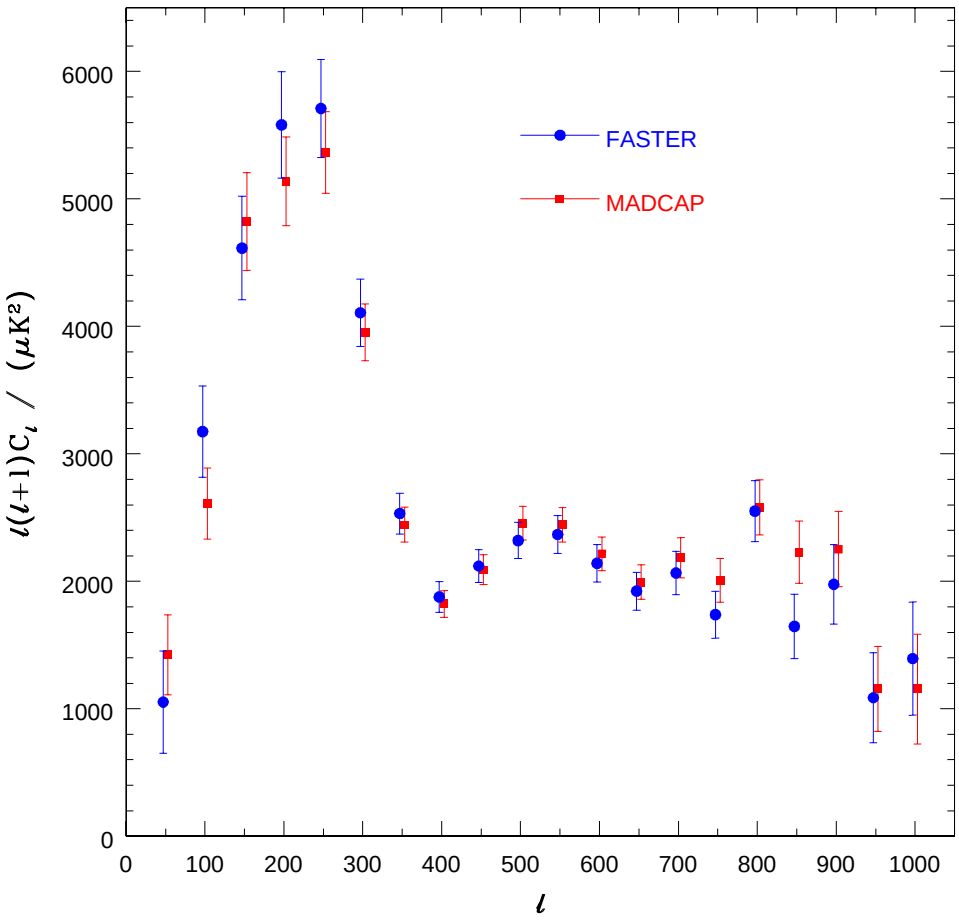

Figure 7.11: The final power spectra results from Ruhl et al.[98]. The solid blue circles are from FASTER and the solid red squares from MADCAP. Both pipelines removed constant declination modes and the MADCAP spectra was marginalized over two galactic foreground templates.

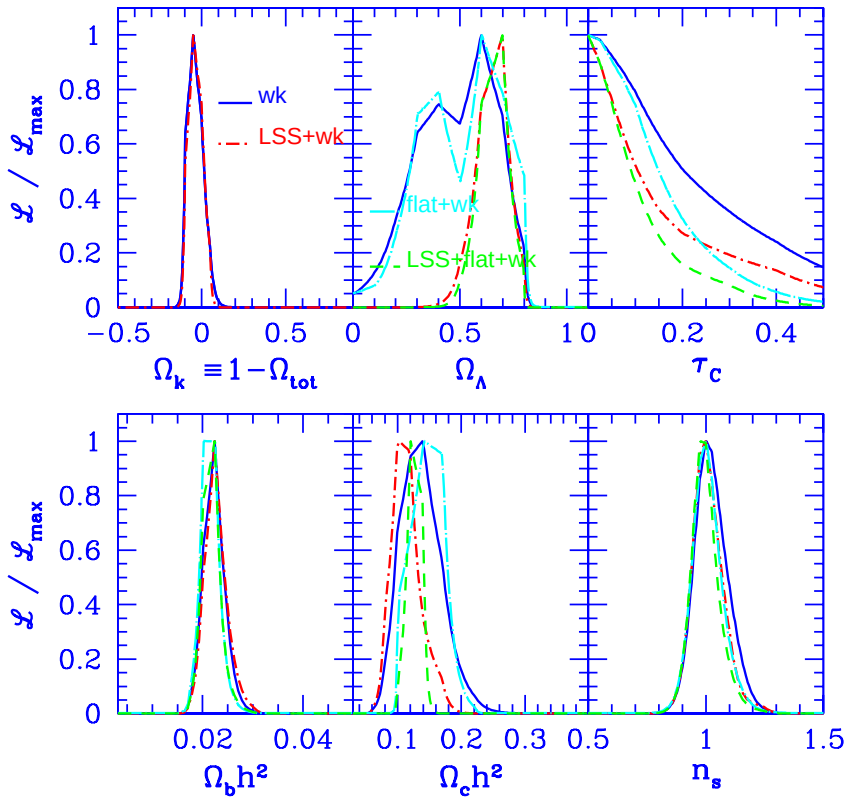

Figure 7.12: Likelihood curves for the comsological parameters: Ω_k, Ω_Λ, τ_c, $\Omega_b h^2$, $\Omega_{cdm} h^2$, and n_s (from Ruhl et al. [98]. The results are derived from the MADCAP power spectrum and the COBE-DMR results and are done using various priors. Using the FASTER spectrum instead of MADCAP, results in similar curves.

Chapter 8

BOOM03 Results

The second long duration flight of BOOMERANG was launched on January 6, 2003 from Williams Field at McMurdo Station Antarctica. The telescope was in the air for 15 days. The flight was terminated on January 21. As shown in figures 8.1 and 8.2, the BOOM03 flight did not have as smooth a ride as B98. Both the altitude and the flight path were sub-optimal. The average altitude began to drop after the first day; on day five, a ballast drop raised the altitude back to 120,000 ft but it kept losing altitude. The winds were such that it spent 5 days in nearly the same spot. Because of the altitude loss and slow winds the payload was terminated near Dome Fuji (a remote Japanese base) after 15 days. Thanks to heroic efforts from the Antarctic support crew, the pressure vessel containing the flight data was retrieved while the rest of the payload had to be left on the polar plateau.

Regardless of the altitude loss, the payload worked very well. After 10.9 days the Helium-3 refrigerator began to warm up. The fridge was re-cycled and we were able to get another 19 hours of data before we had power down the payload. We powered down at an altitude of 70,000 ft, because the air-pressure was too high to allow for attitude control of the payload. In the end, we have 11.7 days of useful data. The analysis of the flight data is still in its early stages. Here we summarize some of the early results and estimate our sensitivity to the temperature and polarization power spectra.

8.1 Scan Strategy

The polarization signal is approximately 10% of the temperature anisotropy signal, while our detector sensitivity is similar to those we had in B98. This leads to the naive expectation that it is best to concentrate the integration time on a small area. However, sample variance complicates this. It turns out that for our sensivities, a small region is best order to measure C_ℓ^E. To optimize the sensitivity to C_ℓ^{TE}, a larger area is necessary. Our scan strategy included both a

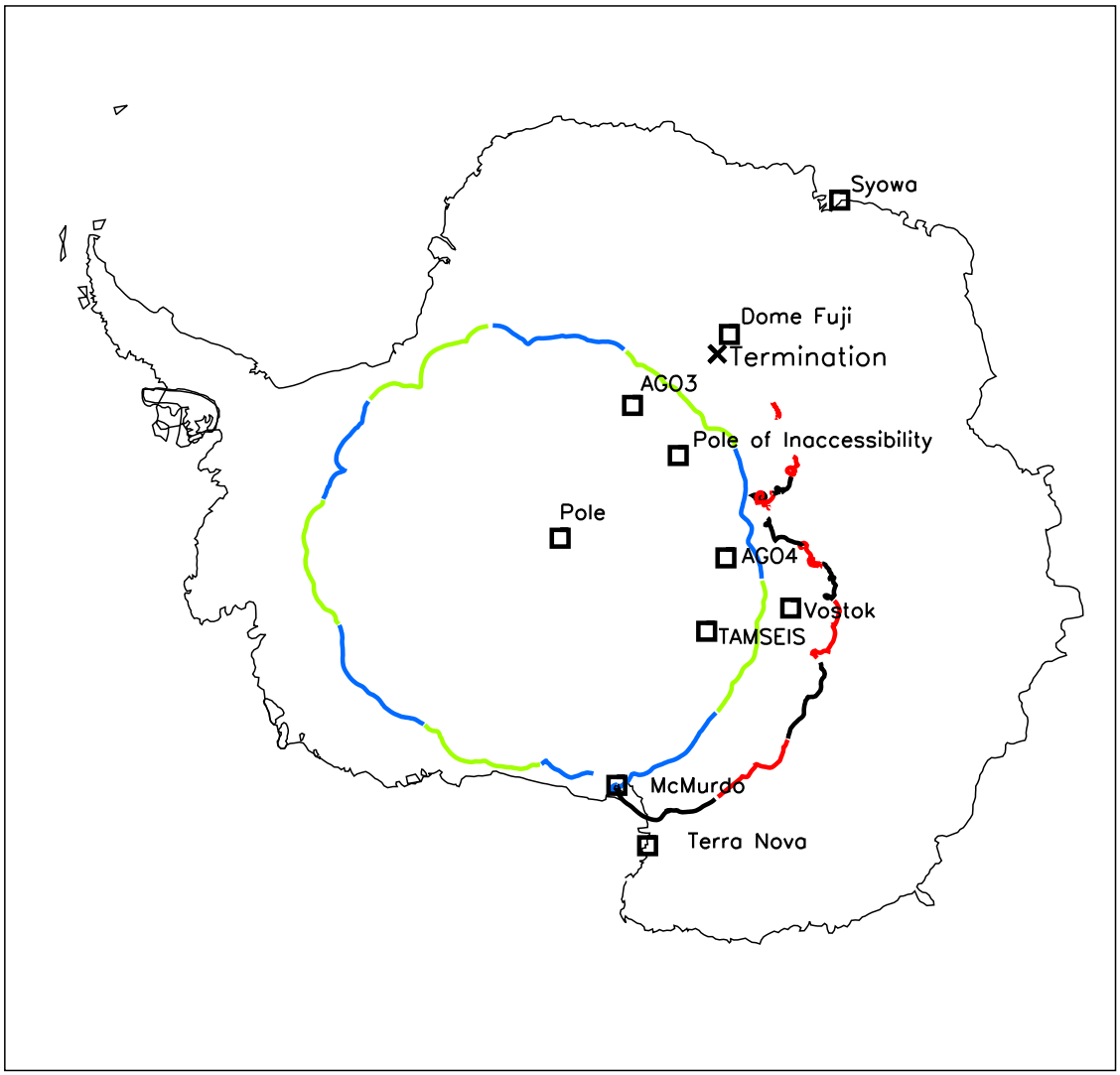

Figure 8.1: Flight paths of both of BOOMERANG LDB flights (made by B. Crill). The 1998 flight (BOOM03) is plotted in with blue and yellow on alternating days. The 2003 flight (BOOM03) is plotted with red and black on alternating days. Those with black and white printers should note that the B98 flight is the one which circumnavigated the continent, while the BOOM03 flight did not even travel halfway around.

large shallow region and small deep region so that we could optimize our sensitivity to both spectra. Figure 8.3 shows the coverage map from one of the PSB's pairs and table 8.1 lists the relevant data for each region. The total CMB scan region is 3.0% of the sky, slightly larger than the region used in Ruhl et al. We also mapped

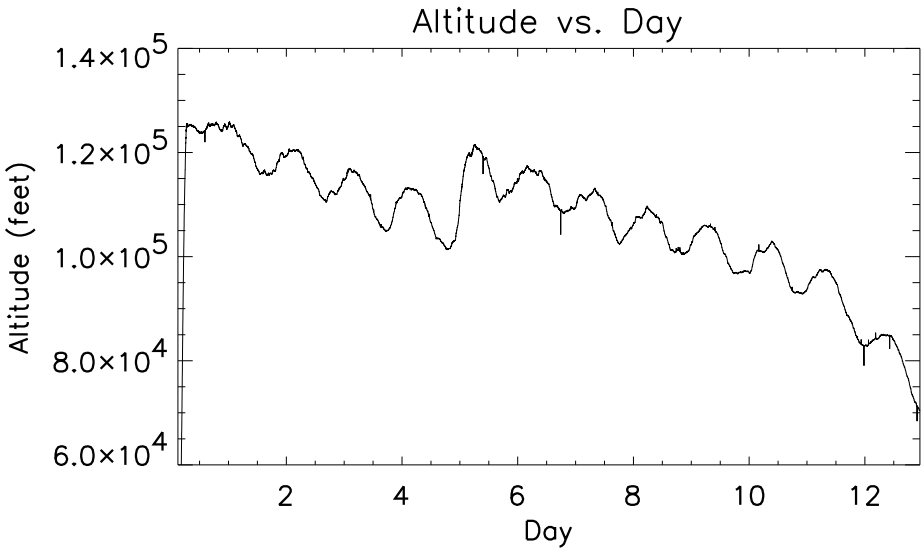

Figure 8.2: A plot of altitude vs. day for the BOOM03 flight. A ballast-drop on day 5 regained some of the lost altitude, but it continued to lose altitude. Once the altitude dropped to 70,000 ft, attitude control became very difficult and we had to power down the telescope.

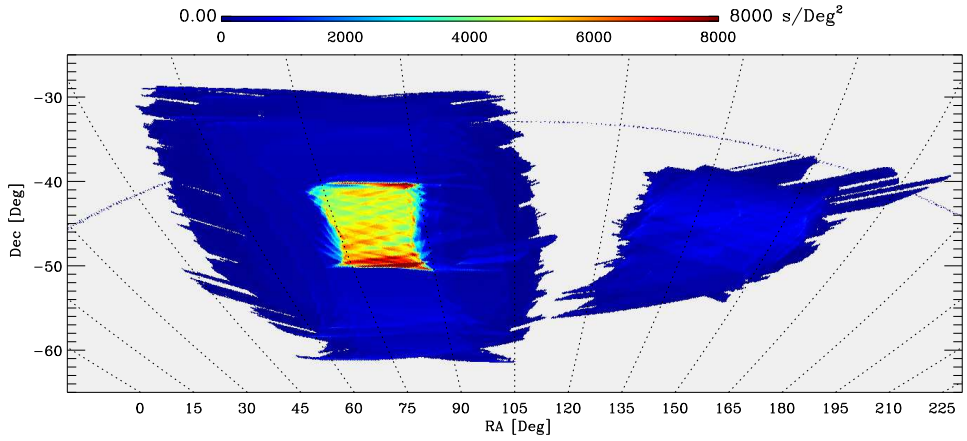

Figure 8.3: Sky coverage for channel B145W1.

nearly 400 deg^2 near the galactic plane, which should provide some insight into the nature of polarized foregrounds.

8.2 General Performance

The telescope worked quite well throughout most of the flight. However, there were a few problems with the pointing system. There was a communication problem in the attitude control system. When all the pointing sensors were operating, the flight logic computer was not able to keep up with the flow of incoming data. This problem became manageable when we turned off the pointed Sun sensor (PSS). A few days after turning off the PSS, the star camera stopped working (it got too cold). While the star camera was frozen, we could turn on the PSS without any problems. Eventually, the star camera came back to life, and we had to power down the PSS. In the end the star camera was functional for 65% of the flight, while the PSS was working properly for 25% of the flight. The fine Sun sensor and gryoscopes worked throughout the entire flight. The differential GPS array suffered a few outages (probably due to the low elevation of the GPS satelites), but worked much better than it did in the B98 flight.

The cryogenic system worked well throughout the flight. The ^{3}He refrigerator began to warm up at the end of the 11th day. We re-cycled the refrigerator and were able to get an additional 19 hours of data before the telescope was powered down. In fact, the cryostat was still cold when we powered down after 13 days in flight. Figure 8.4 shows the variation of the cryogenic temperature over the flight. The temperatures are strongly dependent on altitude. As the altitude dropped, the pressure and temperature of the ^{4}He bath increased with increasing atmospheric pressure. The ^{4}He bath is probably the dominant influence on the temperature of the ^{3}He stage. The liquid Nitrogen solidified after the first 2 days of the flight, due to the fact that the vent valve on the Nitrogen tank was open to the atmosphere.

Figure 8.5 shows the thermal performance of various parts of the telescope. The wide variation in temperatures is due to the fact that some parts are in the shade while other parts are constantly illuminated by the Sun. The thermal conduction between various components is also important. These temperatures are also strongly dependent on the altitude.

Figure 8.6, shows the variation in the DC bolometer voltages over the course of the flight. Not surprisingly, this data also correlated with the altitude. Ideally, the DC bolometer voltage is directly proportional to bolometer resistance. However, the phase shift on the lock-in reference (see section 4.4) complicates this. Nevertheless, changes in DC level do imply that the bolometer resistance is changing. This change in bolometer resistance could be due to either a change in the optical load or a change in the ^{3}He temperature. The lower right panel shows the ratio $\Delta V/V_{avg}$ for the four bias monitor channels. This gives us some handle on gain drifts in the electronics. In this case the gain drift is less than 1%, making it a relatively insignificant component of the drift in the bolometer DC levels.

8.3 Calibration Stability

Even though we continually lost altitude throughout the flight, the effect on our sensitivity should be small. Figure 8.7, shows the drift in responsivity over the flight (as measured by the calibration lamp). The responsivity tracks the altitude reasonably well with diurnal variations and a net downward slope. The responsivity loss is not very serious until we get below 100,000 ft at the end of day 10. Even so, we can easily correct for the responsivity change in our analysis. The responsivity change also correlates strongly with changes in DC bolometer readouts (Figure 8.6).

8.4 In-flight Noise

Figure 8.8 shows sample noise spectra for channels B145W1 and B145W2. This is the average spectra for a 50 minute chunk of data taken while we were scanning over the deep region. The data has been deconvolved with a transfer function measured by using cosmic rays (section 6.1.3). Also, spikes and glitches are removed and replaced by a constrained realization of the noise. The spectra rise sharply with frequency due to their long time constants (preliminary measurements find that B145W1 has a time constant of 90 ms and B145W2 has time constant of 50 ms). Figure 8.9 shows how the effective noise changes when the beam window function is convolved with the noise spectra. For this plot the conversion was done the following way:

$$\theta = \frac{v_{az}}{f}, \tag{8.4.1}$$

$$\ell \simeq \frac{180}{\theta} = \frac{180 f}{v_{az}}, \tag{8.4.2}$$

$$n_{eff}(\ell) = \frac{n(\ell)}{B_\ell}, \tag{8.4.3}$$

where v_{az} is the azimuthal scan speed, f is the frequency, and n is the noise spectra. The plot shows the the effective noise for the four primary scan speeds (0.35, 0.5, 0.7 and 1.0 deg/s) and the effect of the beam alone assuming that the noise spectra is flat. Even though B145W1 is quite slow, the beam and the time constant have a comparable effect at $\ell = 1000$ for the the scan speeds 0.35 deg/s and 0.5 deg/s.

8.5 Preliminary Maps

Although the data analysis is still in its early stages we can make some naive maps using the cleaned timestream and pointing solution. Figure 8.10 shows

the results for the channels B145W1 and B145W2. The top panel shows the average map (W1+W2)/2 and the bottom panel shows the difference map (W1-W2)/2. One would expect the residual signal to the polarized signal, but the parallactic angle is not accounted for in the difference map so the polarization signal is perhaps smeared out a bit.

8.6 Expected Results

Figure 8.11 shows some expected results for BOOM03 with eight channels at 145 GHz based on the model NET from table 4.1. The error bars are individually calculated for the shallow and deep regions using standard C_ℓ error estimation formulas [60, 120] then combined to give the final error bars. This estimate might prove somewhat optimistic since the long time constants increase the effective noise level at high-ℓ (Figure 8.9), a fact not accounted for in this error estimate. Also, this assumes all the 145 GHz channels have the same NET, which will not be true in practice. Any residual pointing and/or beam uncertainty can significantly effect the final results for $\ell > 1200$. Nevertheless, BOOM03 should produce results measuring C_ℓ^T to $\ell > 1100$, C_ℓ^E to $\ell \sim 1000$ and C_ℓ^{TE} to $\ell \sim 1000$.

Region	7' pixels	Area (deg^2)	Average Time (s)
CMB Deep	8700	114	60
CMB Shallow	86000	1128	3.3
CMB total	94700	1242	8.5
Galaxy	29900	393	4.67

Table 8.1: A list of the BOOM03 primary scan regions including the average amount of observation time per pixel per detector. The "CMB total" region, is the union of the shallow and deep regions where the average time per pixel is a bit skewed since the deep region pixels dominate the average.

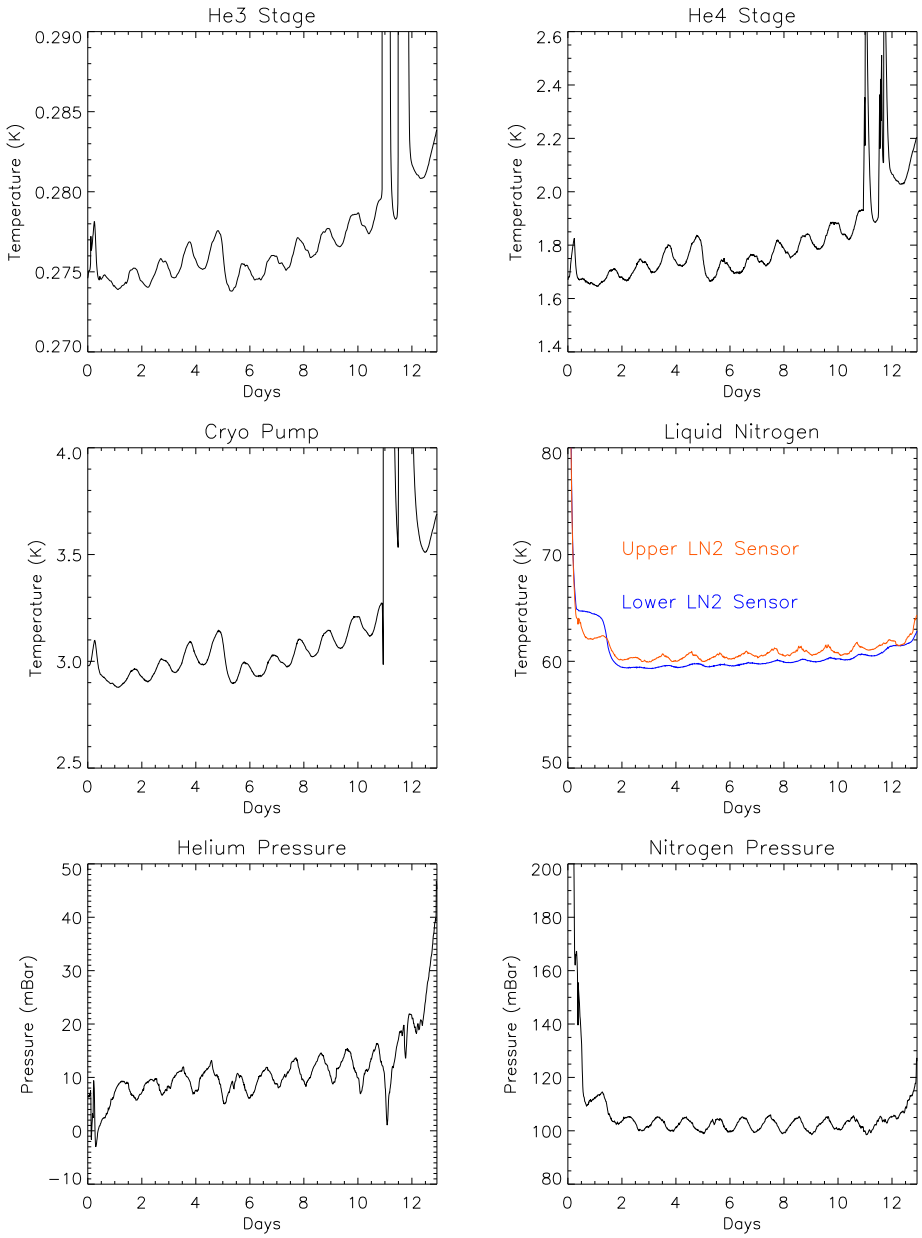

Figure 8.4: Plot of the cryogenic temperature over during the flight. All of the temperature display a diurnal variation. As the altitude dropped, the ^{4}He pressure rose with the rising pressure of the atmosphere (as can be seen in the plot of Helium pressure); it should be the dominant factor driving changes in the ^{3}He stage. The vent for the liquid Nitrogen tank was open to the atmosphere; this caused the liquid Nitrogen to become solid. The rise in temperature in the ^{3}He, ^{4}He stage and cryo pump on days 11 and 12 is due to the ^{3}He running out and the subsequent cycling of the ^{3}He refrigerator.

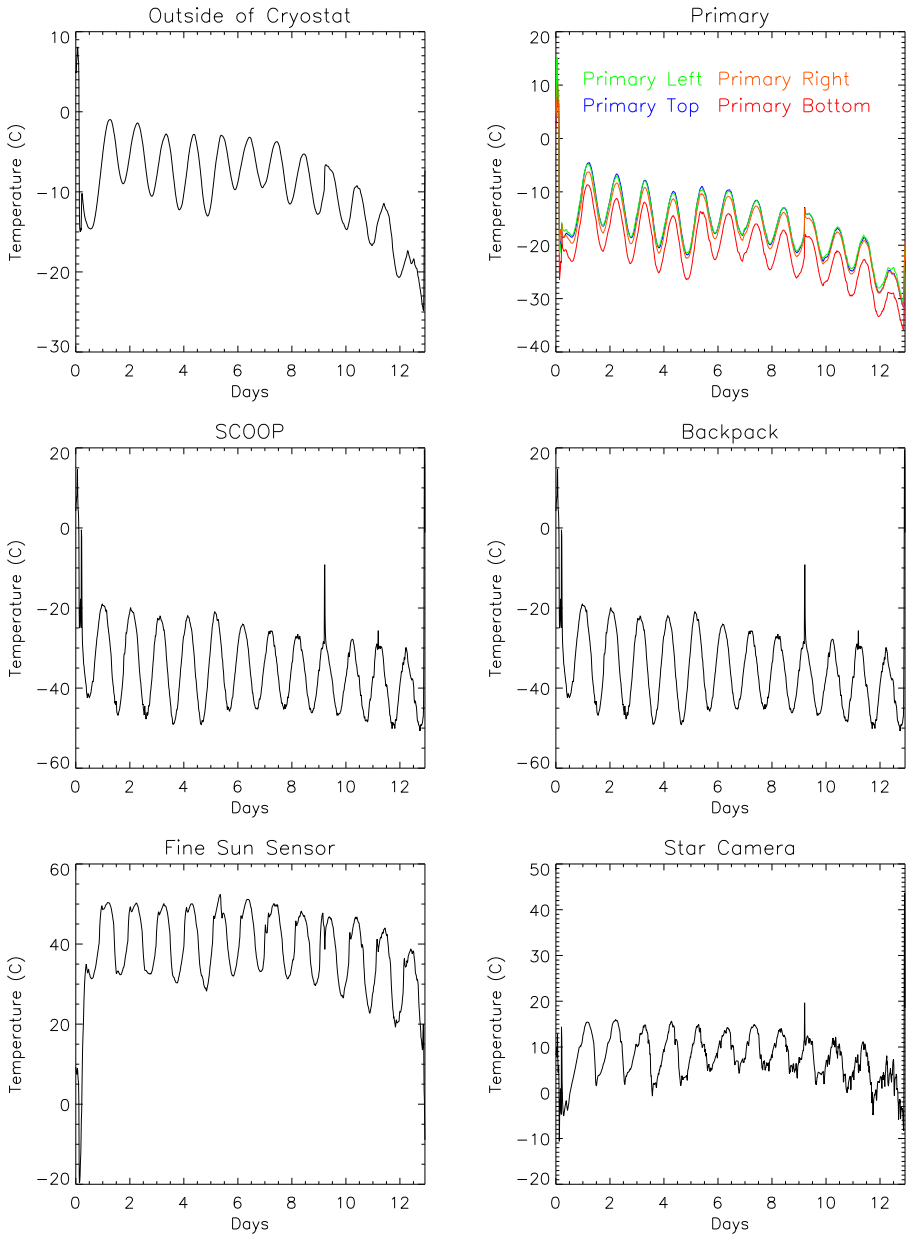

Figure 8.5: Plot of telescope temperatures over the flight. The wide variation in temperature is largely due to the fact that some parts of the telescope are shaded while other parts are directly in the Sun. Also, it depends on the thermal conduction between various parts of the telescope. As the altitude drops, there is more convection from cold air currents and radiation from the Sun decreases.

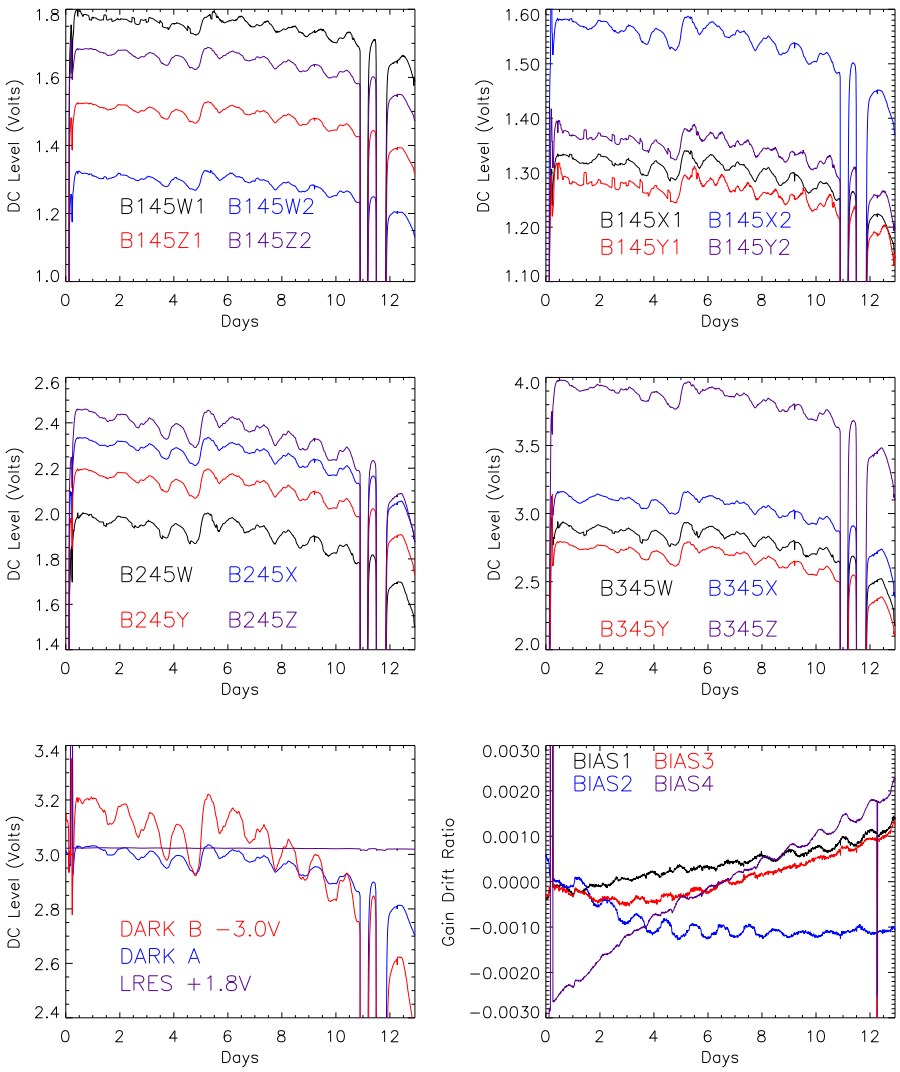

Figure 8.6: Plot of the DC bolometer voltage over the flight. As we discussed in section 4.4, the addition of the phase shift complicates our interpretation of the meaning of the DC bolometer data. However, changes in the DC bolometers values do imply that the bolometer resistance is changing. Similar to the cryogenic temperatures and the ambient telescope temperatures, the DC bolometer voltage are sensitive to changes in altitude. The change in the DC levels should track changes in bolometer responsivity. The dark bolometers (Dark A and Dark B) and the load resistor channel (LRES) are shown as well; offsets are removed from Dark B (3.0 V)and LRES (1.8 V) so that they can be shown on the same scale with Dark A. The BIAS monitor channels (BIAS1, BIAS2, BIAS3, BIAS4) are shown. Here the y-axis of this plot is $\Delta V/V_{avg}$ showing the gain drift of the electronics. The change in the bias monitors is quite small compared to the effect on the bolometers.

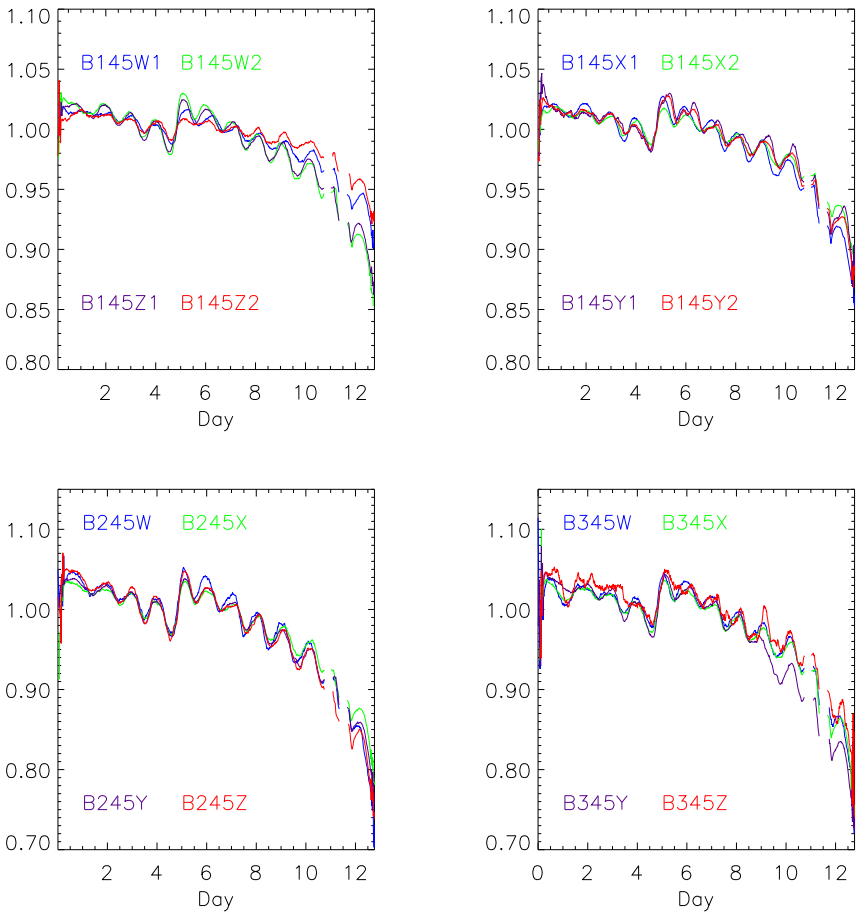

Figure 8.7: Plot of the responsivity change over the flight as measured by the calibration lamp. The gaps in the plot denote where the ^{3}He refrigerator was being cycled.

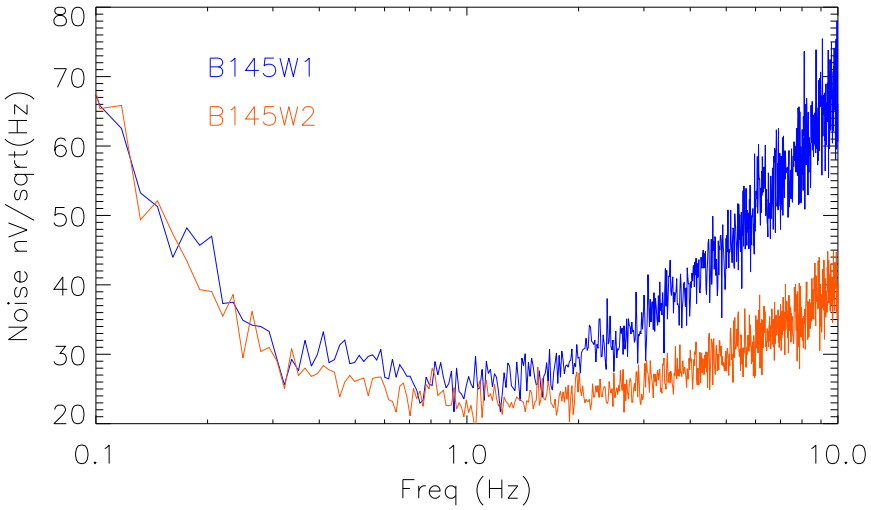

Figure 8.8: Noise spectra for the channels B145W1 and B145W2. The data for these spectra come from a 50 minute period while we were making small amplitude scans over the deep CMB region. The data has been deconvolved and despiked. The increased noise at high frequency is due to the bolometer time constant. From preliminary measurements, B145W1 has a time constant of 90 ms and B145W2 has a time constant of 50 ms.

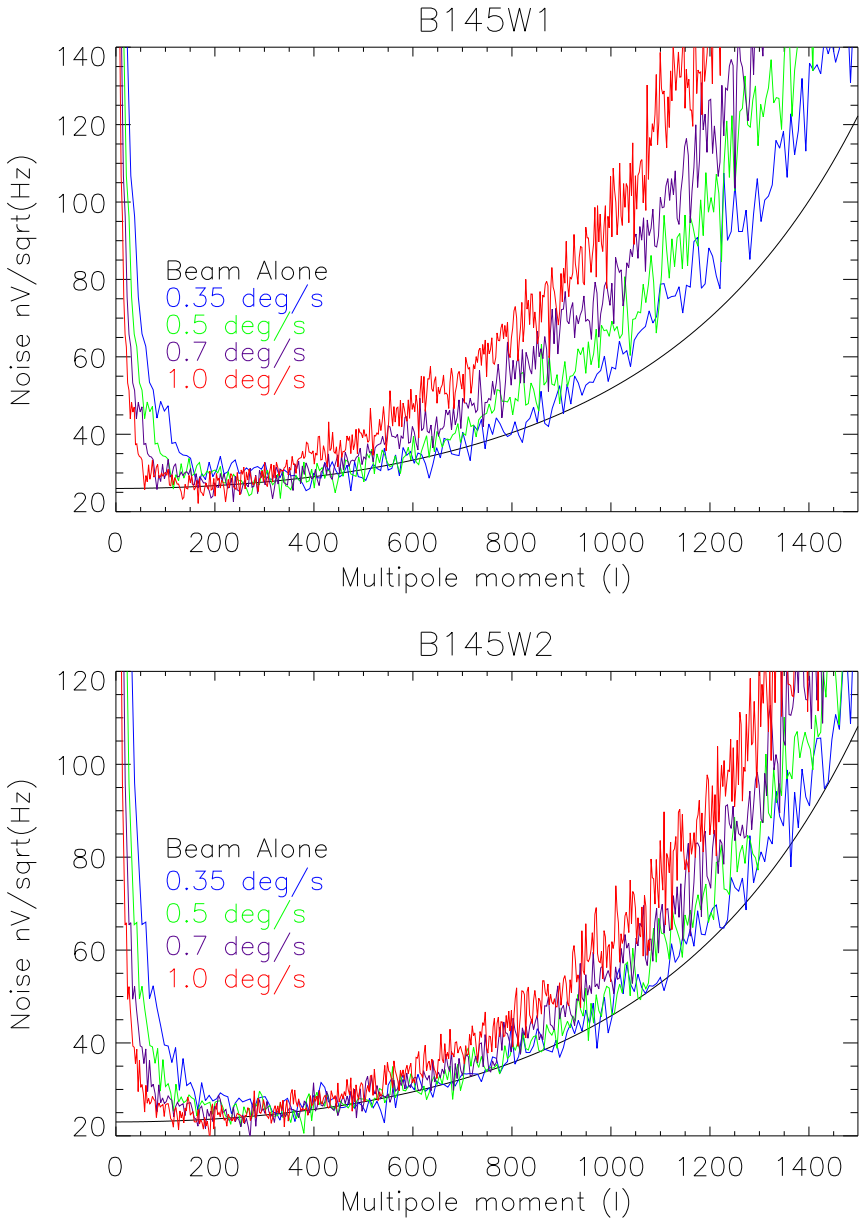

Figure 8.9: The noise spectra in Figure 8.8 are convolved with the experimental beam ($\sim 9.5'$). The conversion from frequency to ℓ is done for four scan speeds (0.35, 0.5, 0.7 and 1.0 deg/s). The "Beam Alone" curve is normalized by the noise level at 1 Hz.

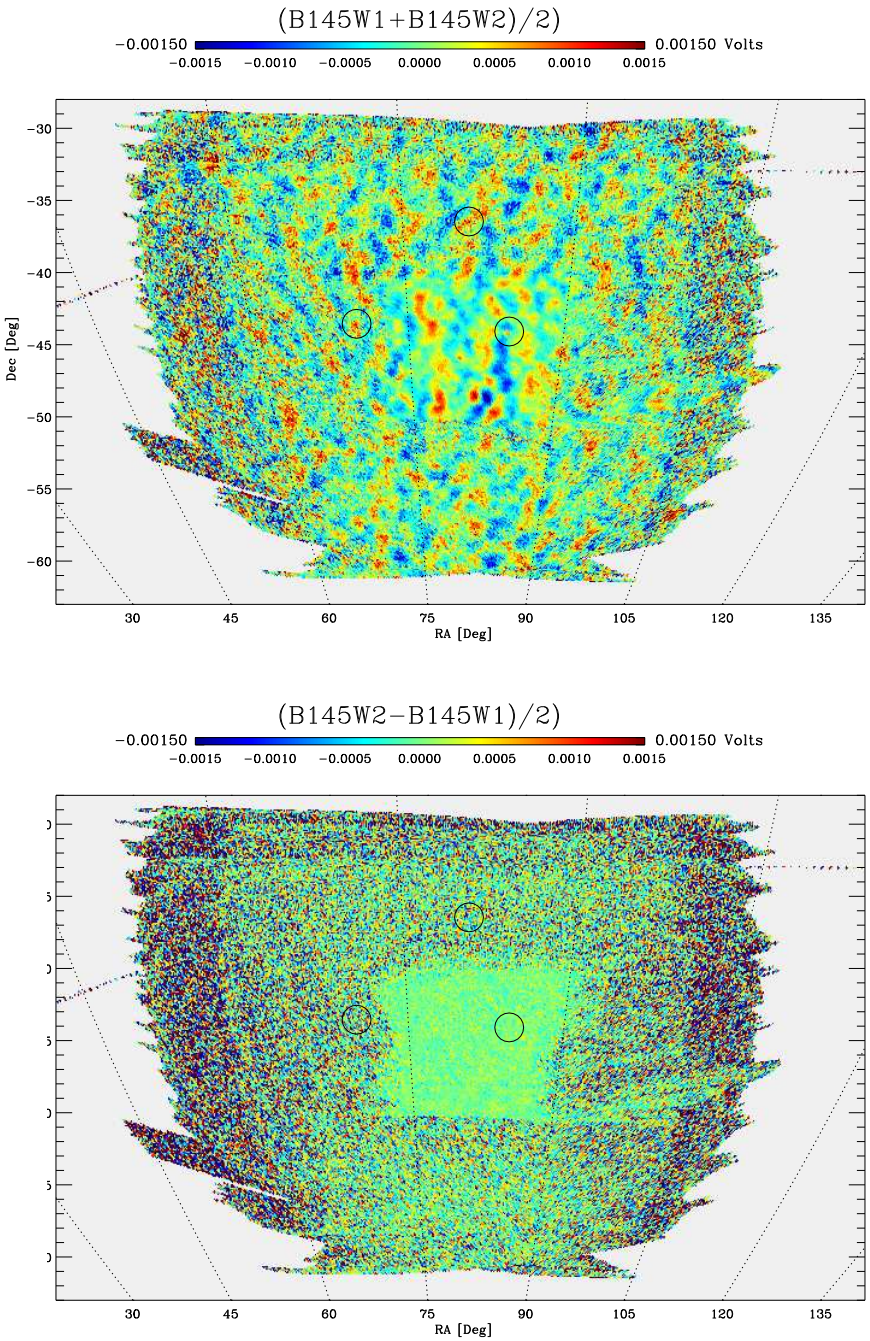

Figure 8.10: Preliminary maps from one 145 GHz PSB pair (B145W1 and B145W2) showing both the average (top panel) and one-half the difference (bottom panel) of the detectors.

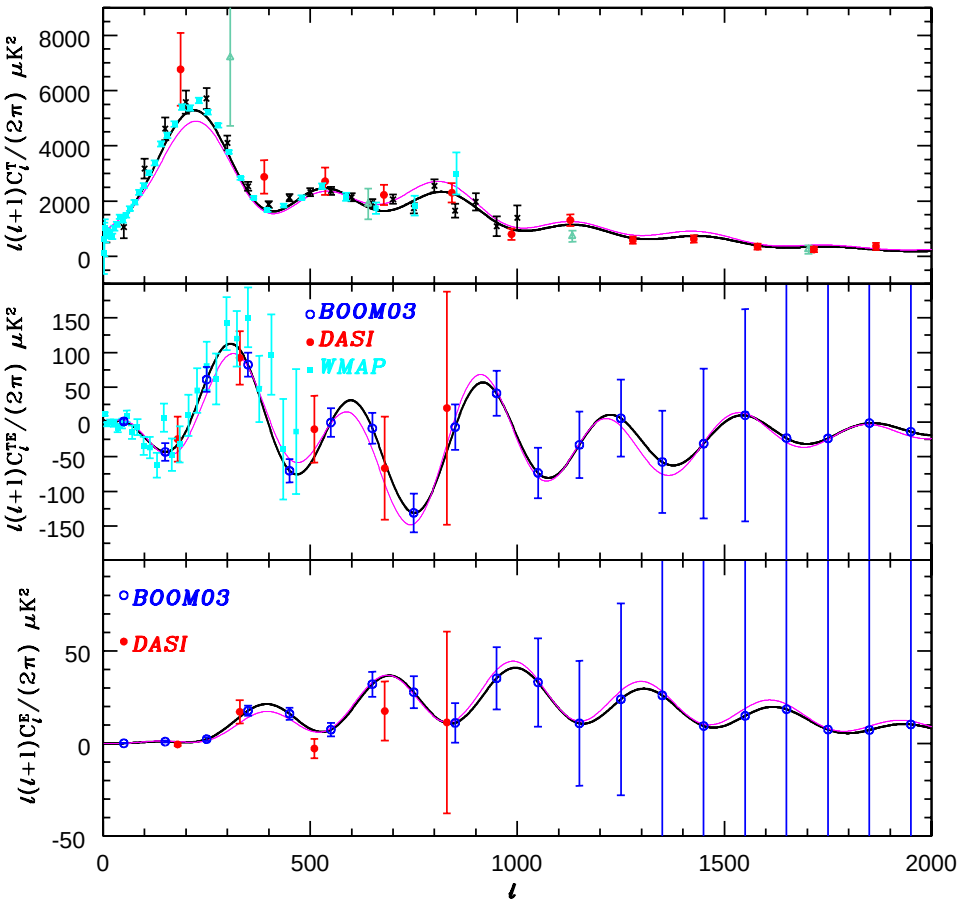

Figure 8.11: Forecasted results for BOOM03 at 145 GHz compared with some recent results and two theoretical models (Figures 1.1 and 1.5). The top panel shows C_ℓ^T, the middle shows C_ℓ^{TE}, and the bottom C_ℓ^E.

Chapter 9

Conclusion

With its two LDB flights, BOOMERANG has performed remarkably well. It has been part of the vanguard of modern experiments which have opened up a new era of precision cosmology. B98 has helped to provide strong constraints on the energy density of the universe and it's baryon content. BOOM03 had a very successful flight and should provide measurements of the CMB temperature and polarization.

Bibliography

[1] R. A. Alpher, R. Herman, and G. A. Gamow. Thermonuclear Reactions in the Expanding Universe. *Physical Review*, 74:1198–1199, nov 1948.

[2] E. M. Arnold et al. *Astronomy and Astrophysics*, 70:L1, 1978.

[3] N. A. Bahcall, R. Cen, R. Davé, J. P. Ostriker, and Q. Yu. The Mass-to-Light Function: Antibias and Ω_m. *Astrophysical Journal*, 541:1–9, September 2000.

[4] A. Balbi, P. Ade, J. Bock, J. Borrill, A. Boscaleri, P. De Bernardis, P. G. Ferreira, S. Hanany, V. Hristov, A. H. Jaffe, A. T. Lee, S. Oh, E. Pascale, B. Rabii, P. L. Richards, G. F. Smoot, R. Stompor, C. D. Winant, and J. H. P. Wu. Constraints on Cosmological Parameters from MAXIMA-1. *Astrophysical Journal Letters*, 545:L1–L4, December 2000.

[5] C. L. Bennett, A. J. Banday, K. M. Gorski, G. Hinshaw, P. Jackson, P. Keegstra, A. Kogut, G. F. Smoot, D. T. Wilkinson, and E. L. Wright. Four-Year COBE DMR Cosmic Microwave Background Observations: Maps and Basic Results. *Astrophysical Journal Letters*, 464:L1, June 1996.

[6] C. L. Bennett, M. Halpern, G. Hinshaw, N. Jarosik, A. Kogut, M. Limon, S. S. Meyer, L. Page, D. N. Spergel, G. S. Tucker, E. Wollack, E. L. Wright, C. Barnes, M. R. Greason, R. S. Hill, E. Komatsu, M. R. Nolta, N. Odegard, H. V. Peirs, L. Verde, and J. L. Weiland. First Year Wilkinson Microwave Anisotropy Probe (WMAP) Observations: Preliminary Maps and Basic Results. *Astrophysical Journal*, submitted, astro-ph/0302207, 2003.

[7] A. Benoît, P. Ade, A. Amblard, R. Ansari, É. Aubourg, S. Bargot, J. G. Bartlett, J.-P. Bernard, R. S. Bhatia, A. Blanchard, J. J. Bock, A. Boscaleri, F. R. Bouchet, A. Bourrachot, P. Camus, F. Couchot, P. de Bernardis, J. Delabrouille, F.-X. Désert, O. Doré, M. Douspis, L. Dumoulin, X. Dupac, P. Filliatre, P. Fosalba, K. Ganga, F. Gannaway, B. Gautier, M. Giard, Y. Giraud-Héraud, R. Gispert, L. Guglielmi, J.-C. Hamilton, S. Hanany, S. Henrot-Versillé, J. Kaplan, G. Lagache, J.-M. Lamarre, A. E. Lange, J. F. Macías-Pérez, K. Madet, B. Maffei, C. Magneville, D. P. Marrone,

S. Masi, F. Mayet, A. Murphy, F. Naraghi, F. Nati, G. Patanchon, G. Perrin, M. Piat, N. Ponthieu, S. Prunet, J.-L. Puget, C. Renault, C. Rosset, D. Santos, A. Starobinsky, I. Strukov, R. V. Sudiwala, R. Teyssier, M. Tristram, C. Tucker, J.-C. Vanel, D. Vibert, E. Wakui, and D. Yvon. The cosmic microwave background anisotropy power spectrum measured by Archeops. *Astronomy and Astrophysics*, 399:L19–L23, March 2003.

[8] A. Benoît, P. Ade, A. Amblard, R. Ansari, É. Aubourg, S. Bargot, J. G. Bartlett, J.-P. Bernard, R. S. Bhatia, A. Blanchard, J. J. Bock, A. Boscaleri, F. R. Bouchet, A. Bourrachot, P. Camus, F. Couchot, P. de Bernardis, J. Delabrouille, F.-X. Désert, O. Doré, M. Douspis, L. Dumoulin, X. Dupac, P. Filliatre, P. Fosalba, K. Ganga, F. Gannaway, B. Gautier, M. Giard, Y. Giraud-Héraud, R. Gispert, L. Guglielmi, J.-C. Hamilton, S. Hanany, S. Henrot-Versillé, J. Kaplan, G. Lagache, J.-M. Lamarre, A. E. Lange, J. F. Macías-Pérez, K. Madet, B. Maffei, C. Magneville, D. P. Marrone, S. Masi, F. Mayet, A. Murphy, F. Naraghi, F. Nati, G. Patanchon, G. Perrin, M. Piat, N. Ponthieu, S. Prunet, J.-L. Puget, C. Renault, C. Rosset, D. Santos, A. Starobinsky, I. Strukov, R. V. Sudiwala, R. Teyssier, M. Tristram, C. Tucker, J.-C. Vanel, D. Vibert, E. Wakui, and D. Yvon. Cosmological constraints from Archeops. *Astronomy and Astrophysics*, 399:L25–L30, March 2003.

[9] J. R. Bond, C. R. Contaldi, U. L. Pen, D. Pogosyan, Prunet S., M. I. Ruetalo, J. W. Wadsley, P. Zhang, B. S. Mason, S. T. Meyers, T. J. Pearson, A. C. S. Readhead, J. L. Sievers, and P. S. Udomprasert. The Sunyaev-Zeldovich effect in CMB-calibrated theories applied to the Cosmic Background Imager anisotropy power at l ¿ 2000. *Astrophysical Journal*.

[10] J. R. Bond and G. Efstathiou. Cosmic background radiation anisotropies in universes dominated by nonbaryonic dark matter. *Astrophysical Journal Letters*, 285:L45–L48, October 1984.

[11] J. R. Bond, G. Efstathiou, and M. Tegmark. Forecasting cosmic parameter errors from microwave background anisotropy experiments. *Mon. Not. R. Astron. Soc.*, 291:L33–L41, November 1997.

[12] J. R. Bond and A. H. Jaffe. Constraining large-scale structure theories with the cosmic background radiation. In *Large-Scale Structure in the Universe*, page 57, 1999.

[13] J. R. Bond, A. H. Jaffe, and L. Knox. *Physical Review D*, 57:2117–2137, 1998.

[14] J. R. Bond, A. H. Jaffe, and L. Knox. Radical Compression of Cosmic Microwave Background Data. *Astrophysical Journal*, 533:19–37, April 2000.

[15] J. Borrill. In *Proceedings of the 5th European SGI/Cray MPP Workshop, Bologna, Italy*, 1999.

[16] A. Boscaleri et al. *Measurement Science and Technology*, 5:190, 1994.

[17] M. Bucher, K. Moodley, and N. Turok. Constraining Isocurvature Perturbations with Cosmic Microwave Background Polarization. *Physical Review Letters*, 87:191301, November 2001.

[18] E. F. Bunn, M. Zaldarriaga, M. Tegmark, and A. de Oliveira-Costa. E/B decomposition of finite pixelized CMB maps. *Physical Review D*, 67:23501, January 2003.

[19] C. R. Contaldi et al. in preparation, 2003.

[20] F. Couchot, J. Delabrouille, J. Kaplan, and B. Revenu. Optimised polarimeter configurations for measuring the Stokes parameters of the cosmic microwave background radiation. *Astronomy and Astrophysics Supplement Series*, 135:579–584, March 1999.

[21] B. P. Crill. PhD thesis, California Institute of Technology, 2000.

[22] B. P. Crill, P. A. R. Ade, Artusa D. R., R. S. Bhatia, J. J. Bock, A. Boscaleri, P. Cardoni, S. E. Church, K. Coble, P. de Bernardis, G. De Troia, P. Farese, K. M. Ganga, M. Giacometti, C. V. Haynes, E. Hivon, V. V. Hristov, A. Iacoangeli, W. C. Jones, A. E. Lange, L. Martinis, S. Masi, P. V. Mason, P. D. Mauskopf, L. Miglio, T. Montroy, C. B. Netterfield, C. G. Paine, E. Pascale, F. Piacentini, D. Pogosyan, F. Pongetti, G. Polenta, F. Pongetti, G. Romeo, J. E. Ruhl, F. Scaramuzzi, D. Sforna, and A. D. Turner. BOOMERANG: A Balloon-borne Millimeter Wave Telescope and Total Power Receiver for Mapping Anisotropy in the Cosmic Microwave Background. *Astrophysical Journal*, 2002.

[23] R. A. C. Croft, W. Hu, and R. Davé. Cosmological Limits on the Neutrino Mass from the LyAlpha Forest. *Physical Review Letters*, 83:1092, August 1999.

[24] M. Davis D. P. Finkbeiner and D. J. Schlegel. *Astrophysical Journal*, 524:2, 1999.

[25] P. de Bernardis, P. A. R. Ade, J. J. Bock, J. R. Bond, J. Borrill, A. Boscaleri, K. Coble, C. R. Contaldi, B. P. Crill, G. De Troia, P. Farese, K. Ganga, M. Giacometti, E. Hivon, V. V. Hristov, A. Iacoangeli, A. H. Jaffe, W. C. Jones, A. E. Lange, L. Martinis, S. Masi, P. Mason, P. D. Mauskopf, A. Melchiorri, T. Montroy, C. B. Netterfield, E. Pascale, F. Piacentini,

D. Pogosyan, G. Polenta, F. Pongetti, S. Prunet, G. Romeo, J. E. Ruhl, and F. Scaramuzzi. Multiple Peaks in the Angular Power Spectrum of the Cosmic Microwave Background: Significance and Consequences for Cosmology.

[26] P. de Bernardis, P. A. R. Ade, J. J. Bock, J. R. Bond, J. Borrill, A. Boscaleri, K. Coble, B. P. Crill, G. De Gasperis, P. C. Farese, P. G. Ferreira, K. Ganga, M. Giacometti, E. Hivon, V. V. Hristov, A. Iacoangeli, A. H. Jaffe, A. E. Lange, L. Martinis, S. Masi, P. V. Mason, P. D. Mauskopf, A. Melchiorri, L. Miglio, T. Montroy, C. B. Netterfield, E. Pascale, F. Piacentini, D. Pogosyan, S. Prunet, S. Rao, G. Romeo, J. E. Ruhl, F. Scaramuzzi, D. Sforna, and N. Vittorio. A flat Universe from high-resolution maps of the cosmic microwave background radiation. *Nature*, 404:955–959, April 2000.

[27] P. de Bernardis and S. Masi. A Simple Evaluation of Offsets due to Intrumental Polarization. *Collaboration Internal Memo*, 2002.

[28] G. De Troia and P. Natoli. B2K Scan Strategy Optimization: Naive Error Bar Forecasting for the EE and TE Mode Power Spectra. *Collaboration Internal Memo*, 2002.

[29] R. H. Dicke, P. J. E. Peebles, P. G. Roll, and D. T. Wilkinson. Cosmic Black-Body Radiation. *Astrophysical Journal*, 142:414–419, July 1965.

[30] O. Doré, R. Teyssier, F. R. Bouchet, D. Vibert, and S. Prunet. MAPCUMBA: A fast iterative multi-grid map-making algorithm for CMB experiments. *Astronomy and Astrophysics*, 374:358–370, July 2001.

[31] C. D. Dowell, W. Collins, M. Gardner, A. Kovacs, D. C. Lis, T. G. Phillips, H. Yoshida, C. Allen, M. Jhabvala, S. H. Moseley, and G. Voellmer. SHARC II, a Second Generation 350 Micron Camera for the Caltech Submillimeter Observatory. *American Astronomical Society Meeting*, 198:0, May 2001.

[32] G. Efstathiou and J. R. Bond. Cosmic confusion: degeneracies among cosmological parameters derived from measurements of microwave background anisotropies. *Mon. Not. R. Astron. Soc.*, 304:75–97, March 1999.

[33] K. Enqvist, H. Kurki-Suonio, and J. Väliviita. Limits on isocurvature fluctuations from Boomerang and MAXIMA. *Physical Review D*, 62:103003, November 2000.

[34] Phillip Farese. PhD thesis, University of California, Santa Barbara, 2002.

[35] W. L. Freedman, B. F. Madore, B. K. Gibson, L. Ferrarese, D. D. Kelson, S. Sakai, J. R. Mould, R. C. Kennicutt, H. C. Ford, J. A. Graham, J. P. Huchra, S. M. G. Hughes, G. D. Illingworth, L. M. Macri, and P. B. Stetson. Final Results from the Hubble Space Telescope Key Project to Measure the Hubble Constant. *Astrophysical Journal*, 553:47–72, May 2001.

[36] B. D. Górski, K. M.and Wandelt, E. Hivon, F. K. Hansen, and A. J. Banday. The Healpix Primer.

[37] K. M. Górski, E. Hivon, and B. Wandelt. Analysis issues for large CMB data sets. In *Evolution of Large Scale Structure : From Recombination to Garching*, page 37, 1999.

[38] J. H. Goldstein, P. A. R. Ade, J. J. Bock, J. R. Bond, C. Cantalupo, C. R. Contaldi, M. D. Daub, W. L. Holzapfel, C. Kuo, A. E. Lange, Lueker M., M. Newcomb, J. B. Peterson, D. Pogosyan, J. E. Ruhl, M. C. Runyan, and E. Torbet. Estimates of Cosmological Parameters Using the CMB Angular Power Spectrum of ACBAR. *Astrophysical Journal*, submitted, astro-ph/0212517, 2002.

[39] K. Grainge et al. The CMB power spectrum out to l=1400 measured by the VSA. *Monthly Notices of the Royal Astronomical Society*, in press, astro-ph/0212495, 2002.

[40] J. E. Gunn and B. A. Peterson. On the Density of Neutral Hydrogen in Intergalactic Space. *Astrophysical Journal*, 142:1633–1636, November 1965.

[41] A. H. Guth. Inflationary universe: A possible solution to the horizon and flatness problems. *Physical Review D*, 23:347–356, January 1981.

[42] N. W. Halverson, E. M. Leitch, C. Pryke, J. Kovac, J. E. Carlstrom, W. L. Holzapfel, M. Dragovan, J. K. Cartwright, B. S. Mason, S. Padin, T. J. Pearson, A. C. S. Readhead, and M. C. Shepherd. Degree Angular Scale Interferometer First Results: A Measurement of the Cosmic Microwave Background Angular Power Spectrum. *Astrophysical Journal*, 568:38–45, March 2002.

[43] J. P. Hamaker and J. D. Bregman. Understanding radio polarimetry. III. Interpreting the IAU/IEEE definitions of the Stokes parameters. *Astronomy and Astrophysics*, 117:161–165, May 1996.

[44] S. Hanany, P. Ade, A. Balbi, J. Bock, J. Borrill, A. Boscaleri, P. de Bernardis, P. G. Ferreira, V. V. Hristov, A. H. Jaffe, A. E. Lange, A. T. Lee, P. D. Mauskopf, C. B. Netterfield, S. Oh, E. Pascale, B. Rabii, P. L. Richards, G. F. Smoot, R. Stompor, C. D. Winant, and J. H. P.

Wu. MAXIMA-1: A Measurement of the Cosmic Microwave Background Anisotropy on Angular Scales of $10' - 5^{circ}$. *Astrophysical Journal Letters*, 545:L5–L9, December 2000.

[45] M. M. Hedman, D. Barkats, J. O. Gundersen, J. J. McMahon, S. T. Staggs, and B. Winstein. New Limits on the Polarized Anisotropy of the Cosmic Microwave Background at Subdegree Angular Scales. *Astrophysical Journal Letters*, 573:L73–L76, July 2002.

[46] G. Hinshaw, D. N. Spergel, L. Verde, R. S. Hill, S. S. Meyer, C. Barnes, C. L. Bennett, M. Halpern, N. Jarosik, A. Kogut, E. Komatsu, M. Limon, L. Page, G. S. Tucker, J. L. Weiland, E. Wollack, and E. L. Wright. First Year Wilkinson Microwave Anisotropy Probe (WMAP) Observations: Angular Power Spectrum. *Astrophysical Journal*, submitted, astro-ph/0302217, 2003.

[47] E. Hivon, K. M. Górski, C. B. Netterfield, B. P. Crill, S. Prunet, and F. Hansen. MASTER of the Cosmic Microwave Background Anisotropy Power Spectrum: A Fast Method for Statistical Analysis of Large and Complex Cosmic Microwave Background Data Sets. *Astrophysical Journal*, 567:2–17, March 2002.

[48] W. S. Holland. Design and Development of Bolometric Detector Systems. *Ph.D. Thesis*, 1991.

[49] P. Horowitz and W. Hill. *The Art of Electronics*. University of Cambridge Press, Cambridge, UK, 1989.

[50] M. Houde, R. L. Akeson, J. E. Carlstrom, J. W. Lamb, D. A. Schleuning, and D. P. Woody. Polarizing Grids, Their Assemblies, and Beams of Radiation. *Proceedings of the Astronomical Society of the Pacific*, 113:622–638, May 2001.

[51] W. Hu, N. Sugiyama, and J. Silk. The Physics of Microwave Background Anisotropies. *NATURE*, 386:37–43, 1997.

[52] W. Hu and M. White. A CMB polarization primer. *New Astronomy*, 2:323–344, September 1997.

[53] W. T. Hu. Wandering in the Background: a Cosmic Microwave Background Explorer. *Ph.D. Thesis*, January 1995.

[54] A. H. Jaffe, P. A. Ade, A. Balbi, J. J. Bock, J. R. Bond, J. Borrill, A. Boscaleri, K. Coble, B. P. Crill, P. de Bernardis, P. Farese, P. G. Ferreira, K. Ganga, M. Giacometti, S. Hanany, E. Hivon, V. V. Hristov, A. Iacoangeli, A. E. Lange, A. T. Lee, L. Martinis, S. Masi, P. D. Mauskopf, A. Melchiorri,

T. Montroy, C. B. Netterfield, S. Oh, E. Pascale, F. Piacentini, D. Pogosyan, S. Prunet, B. Rabii, S. Rao, P. L. Richards, G. Romeo, J. E. Ruhl, F. Scaramuzzi, D. Sforna, G. F. Smoot, R. Stompor, C. D. Winant, and J. H. Wu. Cosmology from MAXIMA-1, BOOMERANG, and COBE DMR Cosmic Microwave Background Observations. *Physical Review Letters*, 86:3475–3479, April 2001.

[55] R. Clark Jones. *Journal of the Optical Society of America*, 43:1–14, 1953.

[56] W. C. Jones, R. S. Bhatia, J. J. Bock, and A. E. Lange. 'A Polarization Sensitive Bolometric Receiver for Observations of the Cosmic Microwave Background. In *Proceedings of SPIE Vol.* **4855** Millimeter and Submillimeter Detectors for Astronomy*, edited by T.G. Phillips, J. Zmuidzinas, (SPIE, Bellingham, WA)*, 2003.

[57] Coble K., P. A. R. Ade, J. J. Bock, J. R. Bond, J. Borrill, A. Boscaleri, C. R. Contaldi, B. P. Crill, P. de Bernardis, K. Ganga, M. Giacometti, E. Hivon, V. V. Hristov, A. Iacoangeli, A. H. Jaffe, W. C. Jones, A. E. Lange, L. Martinis, S. Masi, P. Mason, P. D. Mauskopf, A. Melchiorri, T. Montroy, C. B. Netterfield, L. Nyman, E. Pascale, F. Piacentini, D. Pogosyan, G. Polenta, F. Pongetti, S. Prunet, G. Romeo, J. E. Ruhl, and F. Scaramuzzi. Observations of Galactic and Extra-galactic Sources From the BOOMERANG and SEST Telescopes. *Astrophysical Journal Supplement*, 2003.

[58] M. Kamionkowski, A. Kosowsky, and A. Stebbins. Statistics of cosmic microwave background polarization. *Physical Review D*, 55:7368–7388, June 1997.

[59] B. G. Keating, C. W. O'Dell, A. de Oliveira-Costa, S. Klawikowski, N. Stebor, L. Piccirillo, M. Tegmark, and P. T. Timbie. A Limit on the Large Angular Scale Polarization of the Cosmic Microwave Background. *Astrophysical Journal Letters*, 560:L1–L4, October 2001.

[60] L. Knox. Determination of inflationary observables by cosmic microwave background anisotropy experiments. *Physical Review D*, 52:4307–4318, October 1995.

[61] L. Knox and M. S. Turner. Detectability of tensor perturbations through anisotropy of the cosmic background radiation. *Physical Review Letters*, 73:3347–3350, December 1994.

[62] A. Kogut, A. J. Banday, C. L. Bennett, K. M. Gorski, G. Hinshaw, P. D. Jackson, P. Keegstra, C. Lineweaver, G. F. Smoot, L. Tenorio, and E. L.

Wright. Calibration and Systematic Error Analysis for the COBE DMR 4 Year Sky Maps. *Astrophysical Journal*, 470:653, October 1996.

[63] A. Kogut, A. J. Banday, C. L. Bennett, K. M. Gorski, G. Hinshaw, G. F. Smoot, and E. I. Wright. Microwave Emission at High Galactic Latitudes in the Four-Year DMR Sky Maps. *Astrophysical Journal Letters*, 464:L5, June 1996.

[64] A. Kogut, D. N. Spergel, C. Barnes, C. L. Bennett, M. Halpern, G. Hinshaw, N. Jarosik, A. Kogut, M. Limon, S. S. Meyer, L. Page, G. S. Tucker, E. Wollack, and E. L. Wright. Wilkinson Microwave Anisotropy Probe (WMAP) First Year Observations: TE Polarization.

[65] E. W. Kolb and M. Turner. *The Early Universe*. Addison-Wesley, New York, 1990.

[66] A. Kosowsky. Introduction to microwave background polarization. *New Astronomy Review*, 43:157–168, July 1999.

[67] J. M. Kovac, E. M. Leitch, C. Pryke, J. E. Carlstrom, N. W. Halverson, and W. L. Holzapfel. Detection of polarization in the cosmic microwave background using DASI. *Nature*, 420:772–787, December 2002.

[68] C. L. Kuo, P. A. R. Ade, J. J. Bock, C. Cantalupo, M. D. Daub, J. H. Goldstein, W. L. Holzapfel, A. E. Lange, Lueker M., M. Newcomb, J. B. Peterson, D. Pogosyan, J. E. Ruhl, M. C. Runyan, and E. Torbet. High Resolution Observations of the CMB Power Spectrum with ACBAR.

[69] A. E. Lange, P. A. Ade, J. J. Bock, J. R. Bond, J. Borrill, A. Boscaleri, K. Coble, B. P. Crill, P. de Bernardis, P. Farese, P. Ferreira, K. Ganga, M. Giacometti, E. Hivon, V. V. Hristov, A. Iacoangeli, A. H. Jaffe, L. Martinis, S. Masi, P. D. Mauskopf, A. Melchiorri, T. Montroy, C. B. Netterfield, E. Pascale, F. Piacentini, D. Pogosyan, S. Prunet, S. Rao, G. Romeo, J. E. Ruhl, F. Scaramuzzi, and D. Sforna. Cosmological parameters from the first results of Boomerang. *Physical Review D*, 63:42001, February 2001.

[70] A. T. Lee, P. Ade, A. Balbi, J. Bock, J. Borrill, A. Boscaleri, P. de Bernardis, P. G. Ferreira, S. Hanany, V. V. Hristov, A. H. Jaffe, P. D. Mauskopf, C. B. Netterfield, E. Pascale, B. Rabii, P. L. Richards, G. F. Smoot, R. Stompor, C. D. Winant, and J. H. P. Wu. A High Spatial Resolution Analysis of the MAXIMA-1 Cosmic Microwave Background Anisotropy Data. *Astrophysical Journal Letters*, 561:L1–L5, November 2001.

[71] C. Lee, P. A. R. Ade, and C. V. Haynes. Self Supporting Filters for Compact Focal Plane Designs. *ESA SP-388*, page 81, 1996.

[72] E. M. Leitch, J. M. Kovac, C. Pryke, J. E. Carlstrom, N. W. Halverson, W. L. Holzapfel, M. Dragovan, B. Reddall, and E. S. Sandberg. Measurement of polarization with the Degree Angular Scale Interferometer. *Nature*, 420:763–771, December 2002.

[73] F. J. Low. Low-Temperature Germanium Bolometer. *Journal of the Optical Society of America*, 51:1300–1304, November 1961.

[74] S. Masi, P. A. R. Ade, J. J. Bock, A. Boscaleri, B. P. Crill, P. de Bernardis, M. Giacometti, E. Hivon, V. V. Hristov, A. E. Lange, P. D. Mauskopf, T. Montroy, C. B. Netterfield, E. Pascale, F. Piacentini, S. Prunet, and J. Ruhl. High-Latitude Galactic Dust Emission in the BOOMERANG Maps. *Astrophysical Journal Letters*, 553:L93–L96, June 2001.

[75] S. Masi et al. *Cryogenics*, 38:319, 1998.

[76] S. Masi et al. *Cryogenics*, 39:217, 1999.

[77] B. Mason, T. J. Pearson, A. C. S. Readhead, M. C. Shepherd, J. H. Sievers, P. S. Udomprasert, J. K. Cartwright, A. J. Farmer, S. Padin, S. T. Meyers, J. R. Bond, C. R. Contaldi, U. L. Pen, D. Pogosyan, Prunet S., J. E. Carlstrom, J. Kovac, E. M. Leitch, C. Pryke, N. W. Halverson, W. L. Holzapfel, P. Altamirano, L. Bronfman, S. Casassus, J. May, and M. Joy. The Anisotropy of the Microwave Background to l = 3500: Deep Field Observations with the Cosmic Background Imager. *Astrophysical Journal*, in press, astro-ph/0205384, 2002.

[78] J. C. Mather, E. S. Cheng, D. A. Cottingham, R. E. Eplee, D. J. Fixsen, T. Hewagama, R. B. Isaacman, K. A. Jensen, S. S. Meyer, P. D. Noerdlinger, S. M. Read, L. P. Rosen, R. A. Shafer, E. L. Wright, C. L. Bennett, N. W. Boggess, M. G. Hauser, T. Kelsall, S. H. Moseley, R. F. Silverberg, G. F. Smoot, R. Weiss, and D. T. Wilkinson. Measurement of the cosmic microwave background spectrum by the COBE FIRAS instrument. *Astrophysical Journal*, 420:439–444, January 1994.

[79] John C. Mather. Bolometer Noise: nonequilibrium theory. *Applied Optics*, 21:1125–1129, 1982.

[80] John C. Mather. *Applied Optics*, 23:584–588, 1984.

[81] P. D. Mauskopf. Measurements of Anisotropies in the Cosmic Microwave Background at Small and Intermediate Angular Scales with Bolometric Receivers at MM Wavelengths. *Ph.D. Thesis*, 1997.

[82] P. D. Mauskopf, P. A. R. Ade, P. de Bernardis, J. J. Bock, J. Borrill, A. Boscaleri, B. P. Crill, G. DeGasperis, G. De Troia, P. Farese, P. G. Ferreira, K. Ganga, M. Giacometti, S. Hanany, V. V. Hristov, A. Iacoangeli, A. H. Jaffe, A. E. Lange, A. T. Lee, S. Masi, A. Melchiorri, F. Melchiorri, L. Miglio, T. Montroy, C. B. Netterfield, E. Pascale, F. Piacentini, P. L. Richards, G. Romeo, J. E. Ruhl, E. Scannapieco, F. Scaramuzzi, R. Stompor, and N. Vittorio. Measurement of a Peak in the Cosmic Microwave Background Power Spectrum from the North American Test Flight of Boomerang. *Astrophysical Journal Letters*, 536:L59–L62, June 2000.

[83] P. D. Mauskopf et al. *Applied Optics*, 36:765, 1997.

[84] A. Melchiorri, P. A. R. Ade, P. de Bernardis, J. J. Bock, J. Borrill, A. Boscaleri, B. P. Crill, G. De Troia, P. Farese, P. G. Ferreira, K. Ganga, G. de Gasperis, M. Giacometti, V. V. Hristov, A. H. Jaffe, A. E. Lange, S. Masi, P. D. Mauskopf, L. Miglio, C. B. Netterfield, E. Pascale, F. Piacentini, G. Romeo, J. E. Ruhl, and N. Vittorio. A Measurement of Ω; from the North American Test Flight of Boomerang. *Astrophysical Journal Letters*, 536:L63–L66, June 2000.

[85] P. Natoli, G. de Gasperis, C. Gheller, and N. Vittorio. A Map-Making algorithm for the Planck Surveyor. *Astronomy and Astrophysics*, 372:346–356, June 2001.

[86] C. B. Netterfield, P. A. R. Ade, J. J. Bock, J. R. Bond, J. Borrill, A. Boscaleri, K. Coble, C. R. Contaldi, B. P. Crill, P. de Bernardis, P. Farese, K. Ganga, M. Giacometti, E. Hivon, V. V. Hristov, A. Iacoangeli, A. H. Jaffe, W. C. Jones, A. E. Lange, L. Martinis, S. Masi, P. Mason, P. D. Mauskopf, A. Melchiorri, T. Montroy, E. Pascale, F. Piacentini, D. Pogosyan, F. Pongetti, S. Prunet, G. Romeo, J. E. Ruhl, and F. Scaramuzzi. A Measurement by BOOMERANG of Multiple Peaks in the Angular Power Spectrum of the Cosmic Microwave Background. *Astrophysical Journal*, 571:604–614, June 2002.

[87] C. B. Netterfield, M. J. Devlin, N. Jarolik, L. Page, and E. J. Wollack. A Measurement of the Angular Power Spectrum of the Anisotropy in the Cosmic Microwave Background. *Astrophysical Journal*, 474:47, January 1997.

[88] C. W. O'dell, B. G. Keating, A. de Oliveira-Costa, M. Tegmark, and P. T. Timbie. CMB Polarization at Large Angular Scales: Data Analysis of the POLAR Experiment.

[89] L. Page, M. R. Nolta, C. Barnes, C. L. Bennett, M. Halpern, G. Hinshaw, N. Jarosik, A. Kogut, M. Limon, S. S. Meyer, H. V. Peirs, D. N. Spergel, G. S. Tucker, E. Wollack, and E. L. Wright. First Year Wilkinson Microwave Anisotropy Probe (WMAP) Observations: Interpretation of the TT and TE Angular Power Spectrum Peaks. *Astrophysical Journal*, 2003.

[90] P. J. E. Peebles. *Principles of Physical Cosmology.* Princeton University Press, Princeton, 1966.

[91] A. A. Penzias and R. W. Wilson. The Measure of Excess Antenna Temperature at 4080 mc/s. *Astrophysical Journal*, 142:419, 1965.

[92] S. Perlmutter, G. Aldering, G. Goldhaber, R. A. Knop, P. Nugent, P. G. Castro, S. Deustua, S. Fabbro, A. Goobar, D. E. Groom, I. M. Hook, A. G. Kim, M. Y. Kim, J. C. Lee, N. J. Nunes, R. Pain, C. R. Pennypacker, R. Quimby, C. Lidman, R. S. Ellis, M. Irwin, R. G. McMahon, P. Ruiz-Lapuente, N. Walton, B. Schaefer, B. J. Boyle, A. V. Filippenko, T. Matheson, A. S. Fruchter, N. Panagia, H. J. M. Newberg, W. J. Couch, and The Supernova Cosmology Project. Measurements of Omega and Lambda from 42 High-Redshift Supernovae. *Astrophysical Journal*, 517:565–586, June 1999.

[93] F. Piacentini, P. A. R. Ade, R. S. Bhatia, J. J. Bock, A. Boscaleri, P. Cardoni, B. P. Crill, P. de Bernardis, H. Del Castillo, G. De Troia, P. Farese, M. Giacometti, E. F. Hivon, V. V. Hristov, A. Iacoangeli, A. E. Lange, S. Masi, P. D. Mauskopf, L. Miglio, C. B. Netterfield, P. Palangio, E. Pascale, A. Raccanelli, S. Rao, G. Romeo, J. Ruhl, and F. Scaramuzzi. The BOOMERANG North America Instrument: A Balloon-borne Bolometric Radiometer Optimized for Measurements of Cosmic Background Radiation Anisotropies from 0.3d to 4°. *Astrophysical Journal Supplement Series*, 138:315–336, February 2002.

[94] S. Prunet, P. A. R. Ade, J. J. Bock, J. R. Bond, J. Borrill, A. Boscaleri, K. Coble, B. P. Crill, P. de Bernardis, G. de Gasperis, G. de Troia, P. C. Farese, P. G. Ferreira, K. Ganga, M. Giacometti, E. Hivon, V. V. Hristov, A. Iacoangeli, A. H. Jaffe, A. E. Lange, L. Martinis, S. Masi, P. Mason, P. D. Mauskopf, A. Melchiorri, L. Miglio, T. Montroy, C. B. Netterfield, E. Pascale, F. Piacentini, D. Pogosyan, F. Pongetti, S. Prunet, S. Rao, G. Romeo, J. E. Ruhl, F. Scaramuzzi, D. Sforna, and N. Vittorio. Noise Estimation in CMB Time-Streams and Fast Iterative Map-Making. In *Mining the Sky*, page 421, 2001.

[95] C. Pryke, N. W. Halverson, E. M. Leitch, J. Kovac, J. E. Carlstrom, W. L. Holzapfel, and M. Dragovan. Cosmological Parameter Extraction from the

First Season of Observations with the Degree Angular Scale Interferometer. *Astrophysical Journal*, 568:46–51, March 2002.

[96] B. Revenu, A. Kim, R. Ansari, F. Couchot, J. Delabrouille, and J. Kaplan. Destriping of polarized data in a CMB mission with a circular scanning strategy. *Astronomy and Astrophysics Supplement Series*, 142:499–509, March 2000.

[97] A. G. Riess, A. V. Filippenko, P. Challis, A. Clocchiatti, A. Diercks, P. M. Garnavich, R. L. Gilliland, C. J. Hogan, S. Jha, R. P. Kirshner, B. Leibundgut, M. M. Phillips, D. Reiss, B. P. Schmidt, R. A. Schommer, R. C. Smith, J. Spyromilio, C. Stubbs, N. B. Suntzeff, and J. Tonry. Observational Evidence from Supernovae for an Accelerating Universe and a Cosmological Constant. *Astronomical Journal*, 116:1009–1038, September 1998.

[98] J. E. Ruhl, P. A. R. Ade, J. J. Bock, J. R. Bond, J. Borrill, A. Boscaleri, C. R. Contaldi, B. P. Crill, P. de Bernardis, G. De Troia, K. Ganga, M. Giacometti, E. Hivon, V. V. Hristov, A. Iacoangeli, A. H. Jaffe, W. C. Jones, A. E. Lange, S. Masi, P. Mason, P. D. Mauskopf, A. Melchiorri, T. Montroy, C. B. Netterfield, E. Pascale, F. Piacentini, D. Pogosyan, G. Polenta, F. Pongetti, S. Prunet, and G. Romeo. Improved Measurement of the Angular Power Spectrum of Temperature Anisotropy in the CMB from Two New Analyses of BOOMERANG Observations. *Astrophysical Journal*, 2002.

[99] R. Sancisi and T. S. van Albada. Dark matter. In *IAU Symp. 124: Observational Cosmology*, pages 699–710, 1987.

[100] U. Seljak and M. Zaldarriaga. A Line-of-Sight Integration Approach to Cosmic Microwave Background Anisotropies. *Astrophysical Journal*, 469:437, October 1996.

[101] J. H. Sievers, J. R. Bond, J. K. Cartwright, C. R. Contaldi, B. S. Mason, S. T. Meyers, S. Padin, T. J. Pearson, U. L. Pen, D. Pogosyan, Prunet S., A. C. S. Readhead, M. C. Shepherd, P. S. Udomprasert, L. Bronfman, W. L. Holzapfel, and J. May. Cosmological Parameters from Cosmic Background Imager Observations and Comparisons with BOOMERANG, DASI, and MAXIMA. *Astrophysical Journal*, in press, astro-ph/0205387, 2002.

[102] A. Slosar et al. Cosmological parameter estimation and Bayesian model comparison using VSA data. *Monthly Notices of the Royal Astronomical Society*, in press, astro-ph/0212497, 2002.

[103] A. Sonnenschein, D. A. Bauer, D. O. Caldwell, H. Nelson, S. Yellin, P. L. Brink, B. Cabrera, R. M. Clarke, P. Colling, A. K. Davies, K. D. Irwin, S. W. Nam, M. J. Penn, D. S. Akerib, A. Bolodyaynya, T. A. Perera, R. W. Schnee, M. B. Crisler, R. Dixon, S. Eichblatt, A. da Silva, R. J. Gaitskell, S. R. Golwala, J. Jochum, P. D. Barnes, B. Sadoulet, T. Shutt, A. L. Spadafora, W. K. Stockwell, E. E. Haller, W. B. Knowlton, R. R. Ross, A. Smith, G. Smith, B. A. Young, B. Neuhausser, and F. Lipschultz. Results of the Cryogenic Dark Matter Search (CDMS) Obtained with Thermistor-Instrumented Germanium Calorimeters. In *The Identification of Dark Matter*, page 347, 1999.

[104] D. N. Spergel, L. Verde, H. V. Peirs, E. Komatsu, M. R. Nolta, C. L. Bennett, M. Halpern, G. Hinshaw, N. Jarosik, A. Kogut, M. Limon, S. S. Meyer, L. Page, G. S. Tucker, J. L. Weiland, E. Wollack, and E. L. Wright. First Year Wilkinson Microwave Anisotropy Probe (WMAP) Observations: Determination of Cosmological Parameters. *Astrophysical Journal*, submitted, astro-ph/0302209, 2003.

[105] R. Stompor, M. Abroe, P. Ade, A. Balbi, D. Barbosa, J. Bock, J. Borrill, A. Boscaleri, P. de Bernardis, P. G. Ferreira, S. Hanany, V. Hristov, A. H. Jaffe, A. T. Lee, E. Pascale, B. Rabii, P. L. Richards, G. F. Smoot, C. D. Winant, and J. H. P. Wu. Cosmological Implications of the MAXIMA-1 High-Resolution Cosmic Microwave Background Anisotropy Measurement. *Astrophysical Journal Letters*, 561:L7–L10, November 2001.

[106] R. V. Sudiwala, M. J. Griffin, and A. L. Woodcraft. *International Journal of Infrared and Millimeter Waves*, 23:545, 2002.

[107] P. L. Richards T. Timusk. *Applied Optics*, 20:1355–1360, 1981.

[108] M. Tegmark. How to Make Maps from Cosmic Microwave Background Data without losing Information. *Astrophysical Journal Letters*, 480:L87, 1997.

[109] M. Tegmark and A. de Oliveira-Costa. How to measure CMB polarization power spectra without losing information. *Physical Review D*, 64:63001, September 2001.

[110] M. S. Turner. Dark Matter and Dark Energy: The Critical Questions. In *To appear in "Hubble's Science Legacy: Future Optical-Ultraviolet Astronomy from Space", eds. K.R. Sembach, J.C. Blades, G.D. Illingworth, and R.C. Kennicutt, ASP Conference Series, astro-ph/0207297.*

[111] D. Tytler, J. M. O'Meara, N. Suzuki, and D. Lubin. Review of Big Bang Nucleosynthesis and Primordial Abundances. *Physics Scripta*, 85:12–31, 2000.

[112] L. Verde, H. V. Peirs, D. N. Spergel, M. R. Nolta, C. L. Bennett, M. Halpern, G. Hinshaw, N. Jarosik, A. Kogut, M. Limon, S. S. Meyer, L. Page, G. S. Tucker, E. Wollack, and E. L. Wright. First Year Wilkinson Microwave Anisotropy Probe (WMAP) Observations: Parameter Estimation Methodology.

[113] R. M. Wald. *General Relativity.* University of Chicago Press, Chicago, 1984.

[114] S. Weinberg. *The First Three Minutes.* Basic Books, New York, 1977.

[115] E. W. Woolard and G. M. Clemence. *Spherical Astronomy.* Academic Press, New York, 1966.

[116] M. Zaldarriaga. Cosmic Microwave Background Polarization Experiments. *Astrophysical Journal*, 503:1, August 1998.

[117] M. Zaldarriaga. Nature of the E-B decomposition of CMB polarization. *Physical Review D*, 64:103001, November 2001.

[118] M. Zaldarriaga and U. Seljak. All-sky analysis of polarization in the microwave background. *Physical Review D*, 55:1830–1840, February 1997.

[119] M. Zaldarriaga and U. Seljak. Gravitational lensing effect on cosmic microwave background polarization. *Physical Review D*, 58:23003, July 1998.

[120] M. Zaldarriaga, D. N. Spergel, and U. Seljak. Microwave Background Constraints on Cosmological Parameters. *Astrophysical Journal*, 488:1, October 1997.

Appendix A

Zemax and the Focal Plane

Zemax is a useful program which provides a lot of tools for quick analysis of optical systems. As with any complicated system, there are many specifications necessary to properly model the system. Here we describe the coordinate system used to design the BOOM03 focal plane.

Table A.1 lists the coordinates of the optimal focus positions in the focal plane. All coordinates are referred to the center of the tertiary mirror. Figure A.1 shows the focus positions, the coordinate reference frames in the focal plane and how they relate to the external gondola coordinates. The focal plane is symmetric in x and azimuth, so the x coordinates of the foci for the negative azimuth positions are just of the negative of corresponding positive azimuth coordinate. θ_z and θ_y reverse sign for the negative azimuth positions as well. The θ_z rotation is done first.

Position	Az (deg)	El (deg)	x (mm)	y(mm)	z(mm)	θ_z (deg)	θ_y (deg)
D	0.25	-0.25	10.149	-22.2100	300.687	114.5583	4.6428
B	0.25	0.25	10.292	-0.7750	308.9188	175.6936	1.9136
C	0.75	-0.25	30.594	-21.36	301.6522	145.0782	7.0514
A	0.75	0.25	31.033	0.1930	310.0551	180.3563	5.7157

Table A.1: Design parameters of the focal plane. Note these angles are defined with respect to the boresight of the telescope, the Zemax field angle convention is reversed in sign from this. The linear dimensions are with respect to the center of the BOOMERANGtertiary. θ_z and θ_y describe the rotations required to align the feed with the center of the tertiary. The θ_z rotation is done first. These are all positive rotations about their respective axes.

Ray tracing was used to determine the mapping of the electric field from the sky to each element in the focal plane. For each ray the electric field was referenced to the coordinate system defined by the central ray of that field angle. This right-handed coordinate system is defined so that the positive z-axis is propagating

Position	Az (deg)	El (deg)	E_x rotation	E_y rotation
D	0.25	-0.25	66.2700	156.2702
B	0.25	0.25	5.1409	95.1399
C	0.75	-0.25	37.4003	127.4012
A	0.75	0.25	2.1387	92.1357

Table A.2: Mapping of the electric field from the sky to the focal plane.

from the source to the primary; the y-axis is vertical and the x-axis point towards positive azimuth. The mapping was done by averaging the Stokes Q and U of the rays which originated from that field angle. Table A.2 shows how E_x and E_y are rotated when they arrive at the foci. After the feed horns are pointed towards the tertiary, these angles can be found by rotating about $\hat{z}$ in that coordinate system. E_x and E_y are not quite orthogonal. This is due a small amount of depolarization caused by the telescope. For the negative azimuth coordinates the E_x and E_y rotations go to $180 - \theta$.

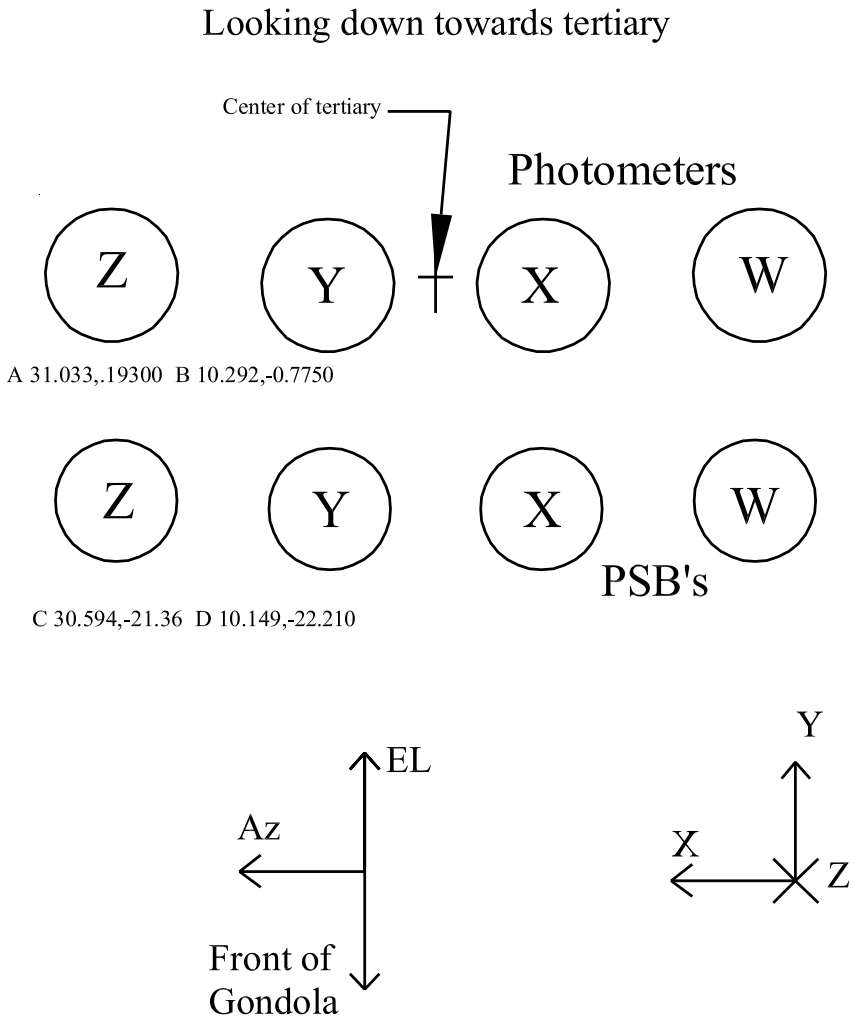

Figure A.1: Reference for coordinate systems in the focal plane. The z-axis points into the paper towards the tertiary. Initial rotations are referenced to this coordinate system. All horns point to the center of the tertiary. W, X, Y and Z refer to the respective channel, while A, B, C and D refer to the Zemax fields listed in Table A.1.

Appendix B

Calculating bolo resistance and the parasitic capacitance

In section 4.4, we derived equations for the complex impendance (4.4.2) and the complex transfer function (4.4.4)

$$Z = \frac{R_{bolo}}{2 + i\omega C R_{bolo}}, \tag{B.0.1}$$

$$T = \frac{V_{out}}{V_{in}} = \frac{Z}{R_{load}/2 + Z}. \tag{B.0.2}$$

Unlike simple RC filters where R and C are degenerate, here we can use the output voltage and input voltage for a single point to solve for R_{bolo} and C simultaneously. Solving B.0.2 for Z we get

$$Z = \frac{R_{load} V_{out}}{2(V_{in} - V_{out})}. \tag{B.0.3}$$

Letting $V_{out} = V_{out}^{Re} + iV_{out}^{Im}$, we can solve for the real and imaginary parts of Z

$$Z^{Re} = \frac{R_l(V_{out}^{Re}V_{in} - (V_{out}^{Re})^2 - (V_{out}^{Im})^2)}{(V_{in} - V_{out}^{RE})^2 + (V_{out}^{Im})^2}, \tag{B.0.4}$$

$$Z^{Im} = \frac{R_l V_{in} V_{out}^{Im}}{(V_{in} - V_{out}^{Re})^2 + (V_{out}^{Im})^2}. \tag{B.0.5}$$

At this point, it is most convenient to use equation B.0.2 and set

$$Z^{RE} + iZ^{Im} = \frac{R_{bolo}}{2 + i\omega C R_{bolo}}. \tag{B.0.6}$$

Cross multiplying and dividing into real and imaginary parts, we get

$$R_{bolo} = 2Z^{Re} - Z^{Im}\omega C R_{bolo}, \tag{B.0.7}$$

$$0 = 2Z^{Im} + Z^{Re}\omega C R_{bolo}. \tag{B.0.8}$$

Equation B.0.8 can be solved for $\omega C R_{bolo}$ and then equation B.0.8 can be solved for R_{bolo} and then for C.

$$\omega C R_{bolo} = \frac{-2Z^{Im}}{Z^{Re}}, \tag{B.0.9}$$

$$R_{bolo} = 2Z^{Re}(1 + \left(\frac{Z^{Im}}{Z_{Re}}\right)^2), \tag{B.0.10}$$

$$C = \frac{1}{\omega}\frac{-2Z^{Im}}{Z^{Re}}\frac{1}{2Z^{Re}(1 + \left(\frac{Z^{Im}}{Z_{Re}}\right)^2)}. \tag{B.0.11}$$

With these equations and the AC load curve data (taken at a bias frequency of 145 Hz) mentioned in section 4.4, we can calculate R_{bolo} and C at each point in the load curve. Ideally the value of C is the same at each point. In practice we found that our data gave us values of C which dropped monotonically as a function of bias. It turns out that applying an offset phase shift of a few degrees ($\sim -7^\circ$ for the PSB's), can produce more consistent results for C. However, it is hard to physically justify this offset. The optimal offset is found by minimizing the standard deviation of the calculated capacitances in a load curve. Using this method the same capacitance was found in both the room temperature and 77K AC-biased loadcurves. Table B.1 shows the calculated values of C for each channel.

In the end, the most important application of this process is to link the AC load curves to the DC load curves. By setting the DC bias current to be equal to the root mean square AC bias current, we can compare plots of R_{bolo} vs. I_{bias}. Figure B.1 shows the agreement between the AC and DC loadcurves. For the 145 GHz channels, adding an offset to the measured phase shifts helps the fit. It does not help for the 245 and 345 GHz channels.

Channel	Capacitance (pF)
B145W1	231
B145W2	238
B145X1	260
B145X2	245
B145Y1	245
B145Y2	226
B145Z1	244
B145Z2	250
B245W	na
B245X	190
B245Y	177
B245Z	163
B345W	179
B345X	172
B345Y	192
B345Z	174

Table B.1: Calculated value of capacitance from AC-biased load curve data. The loadcurves were taken at a bias frequency of 145 Hz.

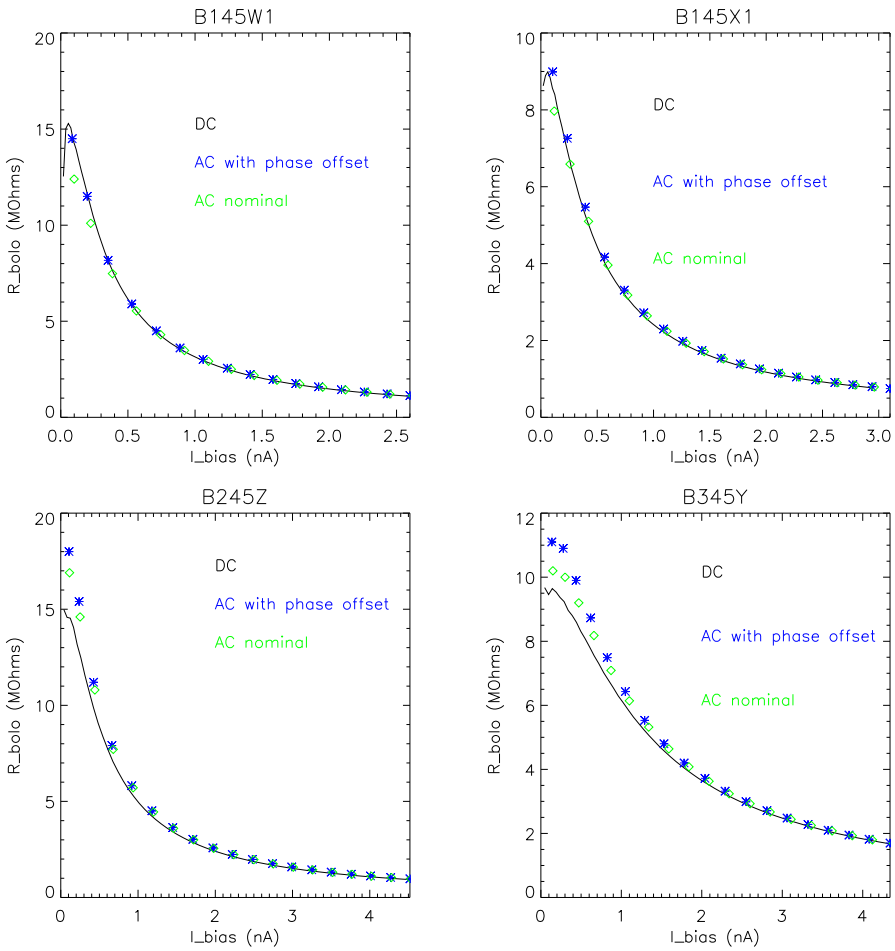

Figure B.1: Comparsion of R_{bolo} and I_{bias} for DC and AC load curves. The solid black line is the DC load curve data. The green points represent the nominal results for the AC loadcurves, while the blue points represent the results found by adding a phase offset to the raw data.

Appendix C

Deriving Load Curve Responsivity

R. Clark Jones [55] describes much of the underlying theory of bolometer dynamics. Although the work was quite comprehensive, some of the finer details are hard to discern (perhaps only to the author of this work). One part which has been difficult to understand is the derivation of the bolometer responsivity.

C.1 Jones' Derivation of DC Biased Responsivity

Central to the derivation is a dimensionless quantity H which can be rewritten in a number of ways

$$H(\omega) = \frac{d\log W}{d\log R_{bolo}}, \tag{C.1.1}$$

$$= \frac{Z_{bolo}(\omega) + R_{bolo}}{Z_{bolo}(\omega) - R_{bolo}}. \tag{C.1.2}$$

W is the incident power on the bolometer ($W = P_{elec} + Q$), $Z_{bolo}(\omega)$ is the dynamic impedance of the bolometer and ω is the angular frequency of the input power variation. Equation C.1.2 can be derived from equation C.1.2 by expanding the numerator and denominator of equation C.1.2 in terms of dV_{bolo}, dI_{bias}, V_{bolo} and I_{bias}. In order to find the bolometer responsivity ($S = dV/dQ$) from a loadcurve, we need to compare values of $H(\omega)$ using the above definitions

$$\frac{d\log\left(P_{elec} + Q\right)}{d\log R_{bolo}} = \frac{Z_{bolo}(\omega) + R_{bolo}}{Z_{bolo}(\omega) - R_{bolo}}. \tag{C.1.3}$$

This relationship allows us to characterize the response of the bolometer to any change in incident power (either electrical or optical). Expanding the left side of

C.1.3, we get

$$\frac{I_{bias}\ dV_{bolo} + V_{bolo}\ dI_{bias} + dQ}{I_{bias}\ dV_{bolo} - V_{bolo}\ dI_{bias}} = \frac{Z_{bolo}(\omega) + R_{bolo}}{Z_{bolo}(\omega) - R_{bolo}}. \tag{C.1.4}$$

Dividing the top and bottom of the left side by $I_{bias}\ dV_{bolo}$, we get

$$\frac{1 + R_{bolo}\frac{dI_{bias}}{dV_{bolo}} + \frac{1}{I_{bias}\ S(\omega)}}{1 + R_{bolo}\frac{dI_{bias}}{dV_{bolo}}} = \frac{Z_{bolo}(\omega) + R_{bolo}}{Z_{bolo}(\omega) - R_{bolo}}, \tag{C.1.5}$$

where $S(\omega) = dV_{bolo}/dQ$. Solving this equation for $S(\omega)$, we get

$$S(\omega) = \frac{1}{2I_{bias}} \frac{\frac{Z_{bolo}(\omega)}{R_{bolo}} - 1}{1 - Z_{bolo}(\omega)\frac{dI_{bias}}{dV_{bolo}}}. \tag{C.1.6}$$

This is now almost in the same form as equation 4.3.5. Now we need to calculate dI_{bias}/dV_{bolo}. This is a confusing quantity because at first glance it looks to be $Z_{bolo}(\omega)^{-1}$. The definition of $Z_{bolo}(\omega)$ is the derivative of V_{bolo} with respect to I_{bias} as V_{bias} is changed. In this particular case, we are looking for the change in I_{bias} due to a change in V_{bolo} (caused by a change in R_{bolo} not V_{bias}). dI_{bias}/dV_{bolo} can be easily derived:

$$V_{bolo} = V_{bias}\frac{R_{bolo}}{R_{load} + R_{bolo}}, \tag{C.1.7}$$

$$I_{bolo} = \frac{V_{bolo}}{R_{bolo}}, \tag{C.1.8}$$

$$\frac{dI_{bias}}{dV_{bolo}} = \frac{1}{R_{bolo}} - \frac{V_{bolo}}{R_{bolo}^2}\frac{dR_{bolo}}{dV_{bolo}}, \tag{C.1.9}$$

$$\frac{dV_{bolo}}{dR_{bolo}} = \left(\frac{dR_{bolo}}{dV_{bolo}}\right)^{-1}, \tag{C.1.10}$$

$$\frac{dV_{bolo}}{dR_{bolo}} = V_{bias}\frac{R_{load}}{(R_{load} + R_{bolo})^2}. \tag{C.1.11}$$

Expanding all the terms in equation C.1.9, we end up with a simple answer

$$\frac{dI_{bias}}{dV_{bolo}} = \frac{-1}{R_{load}}. \tag{C.1.12}$$

This allows us to recover equation 4.3.5

$$S(\omega) = \frac{1}{2I_{bias}} \frac{\frac{Z_{bolo}(\omega)}{R_{bolo}} - 1}{\frac{Z_{bolo}(\omega)}{R_{load}} + 1}. \tag{C.1.13}$$

C.2 An Alternate Derivation of Bolometer Responsivity

Starting with a more intuitive model for bolometer dynamics, we can also derive the bolometer responsivity. This is useful because it is more easily generalized to the case of AC bias. Beginning with equation 4.1.2, we have

$$\delta Q + \delta P_{elec} = G(T_{bolo})\delta T_{bolo} + C(T_{bolo})\frac{dT_{bolo}}{dt}. \tag{C.2.1}$$

If the input optical power is oscillating with angular frequency ω, we can write

$$Q = Q_0 + \Delta Q e^{i\omega t}, \tag{C.2.2}$$
$$T_{bolo} = T_{avg} + \Delta T e^{i\omega t}, \tag{C.2.3}$$

which can be inserted into equation C.2.1. However, we also need to account for the change in P_{elec} due to a change in T_{bolo}. Setting $P_{elec} = V_{bolo}^2/R_{bolo}$, we have

$$\frac{dP_{elec}}{dT_{bolo}} = \frac{dR_{bolo}}{dT_{bolo}}\left[\frac{2V_{bolo}}{R_{bolo}}\frac{dV_{bolo}}{dR_{bolo}} - \left(\frac{V_{bolo}}{R_{bolo}}\right)^2\right]. \tag{C.2.4}$$

The change in V_{bolo} due to a change in T_{bolo} is a useful derivative

$$\frac{dV_{bolo}}{dT_{bolo}} = \frac{dV_{bolo}}{dR_{bolo}}\frac{dR_{bolo}}{dT_{bolo}}. \tag{C.2.5}$$

By keeping only the time variable terms in equation C.2.1, we can solve for dT_{bolo}/dQ:

$$\frac{dT_{bolo}}{dQ} = \frac{1}{G - \frac{dP_{elec}}{dT_{bolo}} + i\omega C}. \tag{C.2.6}$$

The inclusion of dP_{elec}/dT_{bolo} provides electro-thermal feedback, meaning that the effective thermal conductivity is decreased. This has the effect of decreasing the bolometer responsivity, but it also reduces the time constant which leads to more bandwidth. Nominally the time constant is C/G, but the feedback changes it to $C/(G - dP_{elec}/dT_{bolo})$.

Since we actually measure bolometer voltage, the quantity of interest is the voltage responsivity of the bolometer (dV_{bolo}/dQ). This can be written as

$$\frac{dV_{bolo}}{dQ} = \frac{dV_{bolo}}{dT_{bolo}}\frac{dT_{bolo}}{dQ}. \tag{C.2.7}$$

Expanding dV_{bolo}/dT_{bolo} and inserting the expression for dT_{bolo}/dQ, we find

$$\frac{dV_{bolo}}{dQ} = \frac{dR_{bolo}}{dT_{bolo}}\frac{dV_{bolo}}{dR_{bolo}}\frac{1}{G - \frac{dP_{elec}}{dT_{bolo}} + i\omega C}. \tag{C.2.8}$$

It takes some work to relate this quantity to relate this to the quantity derived by Jones (equation C.1.13). First we need to relate G to Z_{bolo}. This is done by rewriting Z_{bolo} in a few different ways:

$$\begin{aligned} Z_{bolo} &= \frac{dV_{bolo}}{dI_{bias}}, && \text{(C.2.9)} \\ &= R_{bolo}\frac{d\log V_{bolo}}{d\log I_{bias}}, && \text{(C.2.10)} \\ &= R_{bolo}\frac{d(\log P_{elec}+\log R_{bolo})}{d(\log P_{elec}-\log R_{bolo})}, && \text{(C.2.11)} \\ &= R_{bolo}\frac{\frac{d}{dT_{bolo}}(\log P_{elec}+\log R_{bolo})}{\frac{d}{dT_{bolo}}(\log P_{elec}-\log R_{bolo})}, && \text{(C.2.12)} \\ &= R_{bolo}\left(\frac{G+\alpha P_{elec}}{G-\alpha P_{elec}}\right), && \text{(C.2.13)} \end{aligned}$$

where $G = dP_{elec}/dT_{bolo}$ and $\alpha = R_{bolo}^{-1}dR_{bolo}/dT_{bolo}$.

At this point the reader might begin to wonder if we are playing a bit too fast and loose with the derivatives. In equation C.2.4, there is an expression for dP_{elec}/dT_{bolo} (in that case the bias is fixed). A more precise way to define G might be to write

$$G = \left(\frac{dT_{bolo}}{dP_{tot}}\right)^{-1}. \qquad \text{(C.2.14)}$$

With this definition, we see that G is inversely related to the change in bolometer temperature due to a change in incident power (similar to the definition of electrical conductivity). The above equations show G as a function of P_{elec} only. This is because those equations are written in the context of a loadcurve done with a fixed optical load.

We can now rearrange equation C.2.13 to find G as a function of Z_{bolo} and R_{bolo}

$$G = \alpha P_{elec}\left(\frac{Z_{bolo}+R_{bolo}}{Z_{bolo}-R_{bolo}}\right). \qquad \text{(C.2.15)}$$

With this expression for G, we can recover equation C.1.13 for $\omega = 0$. To do this we evaluate the expressions dV_{bolo}/dT_{bolo} (equation C.2.5) and dP_{elec}/dT_{bolo} (equation C.2.4) for the case when the bolometer circuit consists of only a load resistor and the bolometer. The full complex form of equation C.2.8 explicitly shows the effective time constant of the bolometer (it can also be derived from Jones' expression). This equation should also cover the AC-biased case when there is no parasitic capacitance. The only caveats are that the bolometer must be much slower than the AC-bias frequency and Z_{bolo} is calculated as a function of the root mean square bias current.

Appendix D

Calculating the Polarization Angle

As discussed in section 1.6.1, the Stokes parameters are defined by

$$\begin{aligned} I &= \left\langle E_y^2 + E_x^2 \right\rangle, && \text{(D.0.16)} \\ Q &= \left\langle E_x^2 - E_y^2 \right\rangle, && \text{(D.0.17)} \\ U &= \left\langle 2E_y E_x cos(\delta_y - \delta_x) \right\rangle, && \text{(D.0.18)} \\ V &= \left\langle 2E_y E_x sin(\delta_y - \delta_x) \right\rangle, && \text{(D.0.19)} \\ \frac{U}{Q} &= tan(2\tau). && \text{(D.0.20)} \end{aligned}$$

In the linearly polarized case $\delta_x = \delta_y$, so the polarization angle τ is relatively trivial

$$\tan\tau = E_y/E_x, \qquad \text{(D.0.21)}$$

$$\tan 2\tau = \frac{2tan\tau}{1 - tan^2\tau} = \frac{E_x E_y}{E_x^2 - E_y^2} = \frac{U}{Q}. \qquad \text{(D.0.22)}$$

In the general case of an elliptically polarized field, finding τ is not quite so trivial. It can be defined as the rotation angle that changes the electric field into the form

$$\vec{E'} = e^{i\gamma}(Ae^{i\omega t}\hat{x'} + iBe^{i\omega t}\hat{y'}), \qquad \text{(D.0.23)}$$

where A and B are real. Because the total intensity is invariant under a coordinate rotation, we can set $A = I\cos\beta$ and $B = I\sin\beta$. It is also convenient to set $E_x = I\cos\alpha$ and $E_y = I\sin\alpha$.

After rotating the electric field by τ, we can write the components (ignoring e^{iwt}) as

$$\begin{aligned} E_{x'} &= I(\cos\tau\cos\alpha + e^{i\delta}\sin\tau\sin\alpha) = I\cos\beta e^{i\gamma}, && \text{(D.0.24)} \\ E_{y'} &= I(-\sin\tau\cos\alpha + e^{i\delta}\cos\tau\sin\alpha) = iI\sin\beta e^{i\gamma}. && \text{(D.0.25)} \end{aligned}$$

The unknowns are β, γ, and τ. Because of the complex components, there are four equations. Writing out all four equations separately we get (dropping the I's)

$$\begin{aligned}
\mathrm{R}e\ E_{x'}: &\quad \cos\tau\cos\alpha + \cos\delta\sin\tau\sin\alpha = -\cos\beta\cos\gamma, && \text{(D.0.26)}\\
\mathrm{I}m\ E_{x'}: &\quad \sin\delta\sin\tau\sin\alpha = \cos\beta\sin\gamma, && \text{(D.0.27)}\\
\mathrm{R}e\ E_{y'}: &\quad -\sin\tau\cos\alpha + \cos\delta\cos\tau\sin\alpha = -\sin\beta\sin\gamma, && \text{(D.0.28)}\\
\mathrm{I}m\ E_{y'}: &\quad \sin\delta cos\tau\sin\alpha = \sin\beta\cos\gamma. && \text{(D.0.29)}
\end{aligned}$$

The dependence on γ can be eliminated by solving D.0.27 and D.0.29 for $\sin\gamma$ and $\cos\gamma$ respectively and then substituting the results back into D.0.26 and D.0.28

$$\begin{aligned}
\cos\tau\cos\alpha + \cos\delta\sin\tau\sin\alpha &= -\cot\beta\cos\tau\sin\alpha\sin\delta, && \text{(D.0.30)}\\
-\sin\tau\cos\alpha + \cos\delta\cos\tau\sin\alpha &= -\tan\beta\sin\tau\sin\alpha\sin\delta. && \text{(D.0.31)}
\end{aligned}$$

Both these equations can be solved for $\tan\beta$ and set equal

$$\frac{\tan\alpha\sin\delta}{1+\tan\tau\tan\alpha\cos\delta} = \frac{\tan\tau-\tan\alpha\cos\delta}{\tan\tau\tan\alpha\sin\delta}. \qquad \text{(D.0.32)}$$

Cross multiplying and simplifying, we find

$$\frac{\tan\tau}{1-\tan^2\tau} = \frac{\tan\alpha\cos\delta}{1-\tan^2\alpha}. \qquad \text{(D.0.33)}$$

By substituting in $E_y/E_x = \tan\alpha$ and rearranging, we recover

$$\tan 2\tau = \frac{2E_xE_y\cos\delta}{E_x^2-E_y^2} = \frac{U}{Q}. \qquad \text{(D.0.34)}$$